The Henryk Niewodniczański Institute of Nuclear Physics

Polish Academy of Sciences

Investigation of plasma compression in the PF-24 device with the use of different Z working gases

Łukasz Marciniak

Thesis submitted for the Degree of Doctor of Philosophy in Physics

Prepared under the supervision of

Assoc. Prof. Agnieszka Kulińska (thesis supervisor)

Ph. D. Eng. Urszula Wiącek (auxiliary supervisor)

Kraków 2019

Acknowledgements

The author would like to give special thanks to the following people:

Agnieszka Kulińska
Mohamad Akel
Sing Lee
Marek Scholz
Hans-Joachim Kunze
Sor Heoh Saw
and
Anna Marciniak

The authour would also like to thank the National Science Centre in Poland for the financial support of the research project number 2018/29/N/ST2/02804 (PRELUDIUM 15). The results of investigations presented in this PhD dissertation are part of this research project.

NATIONAL SCIENCE CENTRE
POLAND

Abstract

The work addresses the problem of radiative compression of electron-ion plasma occurrence and conditions during electric discharges in the z-pinch type devices. Also, the issue of the plasma radiative compression influence on the total neutron emission from nuclear fusion of deuterium nuclei is addressed. The plasma radiative compression is the phenomenon which should theoretically appear during high current conducting electric discharges in working gases having relatively high Z atomic number in comparison to deuterium ($Z = 1$), which are pinched with self-generated magnetic field pressure. When these types of gases are used the X-ray radiation losses during discharge are significant leading to cooling of the plasma, smaller internal pressures and possibly enable the compression to smaller sizes and higher densities. Moreover, the discharges in the mixtures of deuterium with noble gases, in which strong radiative compression has developed, may potentially produce more neutrons from the fusion of deuterium nuclei on average, despite the lower initial D_2 pressure.

The conducted researches are based on: 54 theoretical discharges, 123 experimental discharges and 123 computed discharges in D_2, Ar and D_2+Ar mixtures under constant initial total pressure of about 2.9 mbar. The experimental discharges were performed in the plasma-focus PF-24 device, which is a type of dynamic non-cylindrical z-pinch type plasma generator and the nuclear fusion device with magnetic confinement, under the 17 kV of charging voltage and the 16.8 kJ of energy storage. During the experimental part of research 3 diagnostic systems were used: the Rogowski coil, the magnetic probe and the neutron counter. They were used to obtain: the total discharge current trace, the derivative of total discharge current over time trace and the total number of counts, during each experimental discharge. The obtained electric traces and number of counts enabled to determine the 6 different measured parameters describing behavior of plasma during each discharge. On the other hand, the theoretical and computed discharges were performed using the 5-phase Lee model code, which enables simulation of approximately all phases of discharge in any plasma-focus type device. Wherein, the 123 computed discharges have been connected to experimental discharges (123 coupled experimental-computed discharges) using the total discharge current fitting technique. The results obtained using the 5-phase Lee model code enabled to determine the 37 computed parameters and the 6 computed radiative compression indicators describing the behavior of plasma for each investigated discharge.

The obtained theoretical results showed strong plasma radiative compression phenomenon occurrence for discharges in the 1.70-4.20 mbar of initial Ar pressures and in x = 50-95% of Ar fraction in the $(100\text{-}x)D_2+x$Ar mixtures. While for all the theoretical discharges in D_2, in 0.50-1.60 mbar and 4.50-5.00 mbar of initial Ar pressures and in x = 1-45% of Ar fractions in the $(100\text{-}x)D_2+x$Ar mixtures weak or non-existent radiative compression phenonmenon was stated. Moreover, the obtained experimental-computed results showed strong radiative compression phenomenon occurrence for only half of discharges in about 1.2 mbar of Ar. While for all the discharges in D_2, the other half of discharges in Ar (also about 1.2 mbar) and in all the discharges in x = 3-60% of Ar fractions in $(100\text{-}x)D_2+x$Ar mixtures weak or non-existent radiative compression phenomenon was stated. The main reason of this state is to be the too low total X-ray line radiation emission power. The main parameters influencing strong radiative compression occurrence were stated as: the total yield of X-ray line radiation, the initial plasma pinch radius, the initial ion temperature and the initial ion number density. These parameters determine the radiative compression phenomenon occurrence during single discharge including its strength. Thus, they should be more accurate in comparison to the standard indicators used: the reduced Pease-Braginskii current, the radiation depletion time, etc. Also, no increase in the average total yield of fusion neutrons was stated for discharges in 3-60% of Ar fraction in $(100\text{-}x)D_2+x$Ar mixtures under constant initial pressure. The main reason of this is the decrease in deuterium ion number densities due to the decrease in initial pressures and deuterium fractions and the special changes in electro-kinetics/dynamics of discharges.

Streszczenie

Praca dotyczy problemu występowania kompresji radiacyjnej plazmy elektronowo-jonowej i warunków podczas wyładowań elektrycznych w urządzeniach typu z-pinch. Poruszono również kwestię wpływu kompresji radiacyjnej plazmy na całkowitą emisję neutronów z syntezy jąder deuteru. Kompresja radiacyjna plazmy jest zjawiskiem, które teoretycznie powinno pojawić się podczas wyładowań elektrycznych przewodzących wysoki prąd w gazach roboczych o względnie wysokiej liczbie atomowej Z w porównaniu do deuteru ($Z = 1$), które są ściskane przez samoistnie generowane ciśnienie pola magnetycznego. Gdy stosuje się tego rodzaju gazy, straty na promieniowanie rentgenowskie podczas wyładowania są znaczne, co prowadzi do chłodzenia plazmy, mniejszych ciśnień wewnętrznych i ewentualnie umożliwia kompresję do mniejszych rozmiarów i wyższych gęstości. Ponadto wyładowania w mieszaninach deuteru z gazami szlachetnymi, w których rozwinęła się silna kompresja radiacyjna, mogą potencjalnie, średnio wytwarzać więcej neutronów z syntezy jąder deuteru, pomimo niższego początkowego ciśnienia D_2.

Przeprowadzone badania opierają się na: 54 wyładowaniach teoretycznych, 123 wyładowaniach eksperymentalnych i 123 wyładowaniach obliczeniowych w D_2, Ar i mieszaninach D_2+Ar pod stałym, całkowitym, początkowym ciśnieniem około 2.9 mbar. Wyładowania eksperymentalne przeprowadzono w urządzeniu plasma-focus PF-24, które jest rodzajem dynamicznego, niecylindrycznego generatora plazmy typu z-pinch i urządzenia do syntezy jądrowej z magnetycznym pułapkowaniem plazmy, pod napięciem ładowania 17 kV i magazynowaniem energii 16.8 kJ. Podczas części eksperymentalnej badań wykorzystano 3 układy diagnostyczne: cewkę Rogowskiego, sondę magnetyczną i licznik neutronów. Wykorzystano je do uzyskania: przebiegu całkowitego prądu wyładowania, przebiegu pochodnej całkowitego prądu wyładowania po czasie oraz całkowitej liczby zliczeń, podczas każdego eksperymentalnego wyładowania. Uzyskane przebiegi elektryczne i liczby zliczeń umożliwiły określenie 6 różnych mierzonych parametrów opisujących zachowanie plazmy podczas każdego wyładowania. Z drugiej strony wyładowania teoretyczne i obliczeniowe przeprowadzono przy użyciu 5-fazowego kodu modelu Lee, który umożliwia symulację w przybliżeniu wszystkich faz wyładowania w dowolnym urządzeniu typu plasma-focus. Przy czym, 123 obliczeniowe wyładowania zostały połączone z wyładowaniami eksperymentalnymi (123 sprzężone wyładowania eksperymentalno-obliczeniowe) przy użyciu techniki dopasowania całkowitego prądu wyładowania. Wyniki uzyskane przy użyciu 5-fazowego kodu modelu Lee umożliwiły określenie 37 obliczeniowych parametrów i 6 obliczeniowych wskaźników kompresji radiacyjnej opisujących zachowanie plazmy, dla każdego badanego wyładowania.

Uzyskane wyniki teoretyczne wykazały zachodzenie silnego zjawiska kompresji radiacyjnej plazmy dla wyładowań w początkowych ciśnieniach Ar 1.70-4.20 mbar i x = 50-95% zawartości Ar w mieszaninach (100-x)D_2+xAr. Podczas gdy, dla wszystkich teoretycznych wyładowań w D_2, w 0.50-1.60 mbar i 4.50-5.00 mbar początkowych ciśnień Ar i w x = 1-45% zawartości Ar w mieszaninach (100-x)D_2+xAr słabe lub nieistniejące zjawisko kompresji radiacyjnej zostało stwierdzone. Ponadto uzyskane wyniki obliczeniowo-eksperymentalne wykazały silne zjawisko kompresji radiacyjnej tylko dla połowy wyładowań w około 1.2 mbar Ar. Podczas gdy, dla wszystkich wyładowań w D_2, drugiej połowie wyładowań w Ar (również około 1.2 mbar) i we wszystkich wyładowaniach w x = 3-60% zawartości Ar w mieszaninach (100-x)D_2+xAr słabe lub nieistniejące zjawisko kompresji radiacyjnej zostało stwierdzone. Głównym powodem tego stanu jest zbyt niska całkowita moc emisji liniowego promieniowania X. Główne parametry wpływające na występowanie silnej kompresji radiacyjnej określono, jako: całkowita wydajność promieniowania liniowego X, początkowy promień pinchu plazmowego, początkowa temperatura jonów i początkowa gęstość liczby jonów. Parametry te określają zjawisko kompresji radiacyjnej podczas pojedynczego wyładowania w tym jego nasilenie. Tak, więc powinny być one dokładniejsze w porównaniu ze stosowanymi standardowymi wskaźnikami: zmniejszonym prądem Pease'a-Braginskiego, czasem wytracania promieniowania, itp. Nie stwierdzono również wzrostu średniej, całkowitej wydajności neutronów z syntezy, dla wyładowań w 3-60% zawartości Ar w mieszaninach (100-x)D_2+xAr pod stałym, początkowym ciśnieniem. Głównym powodem tego jest spadek gęstości ilości jonów deuteru spowodowany zmniejszeniem początkowych ciśnień i zawartości deuteru oraz specjalnymi zmianami w elektro-kinetyce/dynamice wyładowań.

Table of contents

List of abbreviations

D-D nuclear fusion – nuclear fusion of deuterium nuclei

EMF – electromotive force

MCF – magnetic confinement fusion

MHD – magnetohydrodynamic

P-B current – Pease-Braginskii current

PF – plasma-focus

SHR – specific heat ratio

SXR – soft X-ray

VUV – vacuum ultra violet

1. Introduction

In the XX century a significant development of plasma physics, electron-ion plasma generators and confiment devices took place. Devices such as tokamaks, stellarators, micro-fusion facilities and plasma-focuses were designed. The main drive for the development of this type of devices was nuclear fusion research and assessment of the capabilities of these devices as future thermonuclear power reactors [Lerner 1980], [Haines 1982], [Liberman 1999], [Sadowski 2005].

The plasma-focus (PF) devices (also known as dense plasma-focus or DPF) were invented in the 1960s [Filippov 1962], [Mather 1964]. These devices belong to the family of z-pinches [Liberman 1999], [Haines 2011], [Sadowski 2012] and for some time were considered as one of the most promising future nuclear fusion power reactors [Mather 1971], [Lerner 1980], [Haines 1982] [Rawat 2015]. However, to this day no one has successfully achieved break-even conditions in a PF device. Nowadays, PFs are viewed and used mostly as efficient sources of different types of radiation which can be used in many branches of science, technology and industry [Raspa 2008], [Gribkov 2008], [Rawat 2015].

The scientific research of dynamic and short lived plasma generated in z-pinches as well as occurring mechanisms of nuclear fusion during z-pinch discharges proved to be very difficult especially on the experimental site [Liberman 1999] [Ryutov 2000] [Haines 2011] [Sadowski 2012]. Moreover, the race to achieve nuclear fusion power reactor based on z-pinch caused relatively fast and significant changes of direction of research not spending enough time and effort to study thoroughly all given effects. And due to lack of achievement of break-even conditions and the growing popularity of other devices for magnetic confined fusion (MCF) in many laboratories around the world research on physical mechanisms occurring during discharges in PF and z-pinch were abandoned. This all resulted in the existence of many unknowns concerning physical processes that take place inside of these devices during discharges [Liberman 1999] [Ryutov 2000] [Haines 2011] [Sadowski 2012]. One of such processes still not fully investigated both experimentally and theoretically is the plasma radiative compression phenomenon.

The plasma radiative compression phenomenon was predicted initially by R. S. Pease [Pease 1957] and S. I. Braginskii [Braginskii 1958] independly in: 1957 and 1958, respectively. This phenomenon involves the compression of high current conducting plasma by means of the magnetic field pressure and Ampere's force as a result of the decrease of plasma internal pressure caused by radiation losses [Shearer 1976]. The radiation losses have been predicted to be mainly losses of soft X-ray (SXR) line radiation and also vacuum ultra violet (VUV) – energy range from about 10 eV to 5000 eV [Liberman 1999].

The work describes the results of a coupled experimental-theoretical study of the plasma radiative compression phenomenon using the plasma-focus PF-24 device [Marciniak 2016] and the 5-phase Lee model code [Lee 2014] [Lee 2017]. The theoretical predictions obtained using the 5-phase Lee model code have suggested, that during the discharges in noble gases and their mixtures with deuterium in the PF-24, phenomenon of radiative compression should take place. Wherein, the noble gases used should have high enough atomic Z number like for example argon. Thus, argon (atomic number Z = 18) and mixtures of argon with deuterium (total atomic number Z = 1.17-11.20) under constant total pressure were used for coupled experimental-theoretical investigation.

The work is divided into ten chapters.

Chapter 1 is the introduction.

Chapter 2 contains a description of plasma radiative compression phenomenon including history and scientific status of research. The z-pinch and PF devices are introduced in this chapter.

Chapter 3 provides information about neutron emission from the nuclear fusion reactions of deuterium nuclei (D-D nuclear fusion) as a result of discharges in z-pinches and plasma-focuses. The information about total fusion neutron emission during discharges in plasma-focuses operated with mixtures of deuterium and other heavier gases are provided.

Chapter 4 presents the aims of the thesis.

Chapter 5 introduces modern, 100 kJ, Mather type, electron-ion plasma generator called PF-24 and 3 different diagnostic systems used: the Rogowski coil, the magnetic probe and the neutron counter [Marciniak 2016] [Bienkowska 2014]. By using these three diagnostic systems 6 different experimental parameters describing the behavior of moving current conducting plasma structure and generated plasma pinch (column) can be determined. These experimental parameters are used for: the determination of optimum initial D_2 pressure for the highest neutron emission on average, the verificaction of increase of the average total neutron yields with Ar fraction increase, the evaluation of the fitting procedure of current traces performed during simulation of discharges with the Lee model code and general assessment of the compatibility of measured and computed results.

Chapter 6 presents the hybrid 5-phase Lee model code used for simulation of a single discharge in the plasma-focus PF-24 device. The general informations about the model are given and all important equations are presented. The process of fitting of measured current trace with computed current trace is specified. The input parameters and output data of the code are listed and described. The determined parameters (output parameters), describing moving plasma structure and generated plasma pinch (column), based on the output data, are presented and characterized.

Chapter 7 introduced all performed: experimental, simulated and computed discharges, their identifiers, the parameters of working gas (its initial pressures and composition), the computed nominal inductance and resistance of the PF-24 device, and so called model parameters of the Lee model code. This chapter is divided into three sections. The first section presents the theoretical discharges in D_2 and Ar under variable initial pressure and the theoretical discharges in mixtures of D_2 and Ar under constant initial total pressure. The second section presents coupled experimental-computed (fitted) discharges in D_2 under variable initial pressure. And the third section presents coupled experimental-computed (fitted) discharges in D_2, Ar and mixtures of D_2 and Ar.

Chapter 8 presents the results of the analysis of 6 different measured parameters, 37 different computed parameters and 6 computed radiative compression indicators. This chapter is divided into eight sections, in which each section relates to the different type of parameters and indicators: the kinetic parameters, the electric parameters, the radiative compression indicators – currents, – times, the plasma pinch parameters – dimensions, – densities, – temperatures and the total radiation yields and the ohmic heating yield. All of the above parameters and indicators are determined on the basis of discharges presented in chapter 7.

Finally, chapter 9 is dedicated to summary and conclusions. It is divided into 4 sections, in which each refers to the different aim of the thesis.

And, chapter 10 contains the list of all references.

2. Plasma radiative compression phenomenon in z-pinch

2.1. Plasma radiative compression phenomenon

2.1.1. Bennett equilibrium pinch and radiative compression concept

The electron-ion plasma can be generated in many types of modern plasma generators that take advantage of non-stationary processes. When plasma is generated for example as a result of linear high voltage gas discharge it conducts electric current and can become magnetized (magnetic field is strong enough to significantly alter particle trajectories). The plasma for example in the form of a column conducting electric current along its length creates a magnetic field around that column. When this magnetic field is strong enough it can pinch the column forcing it to compress to a smaller radius. This type of effect called “plasma pinching” or “pinch effect” was described originally by W. H. Bennett in 1934 [Bennett 1934]. More precisely, Bennett stated that streams of fast electrons which can accumulate positive ions in sufficient quantity to have a linear density of positives about equal to the linear density of electrons, along the streams, become magnetically self-focusing when the current exceeds a value which can be calculated from the initial stream conditions. Bennett performed calculations leading to his law (presently known as Bennett law or relation) in conditions of dynamic equilibrium (Bennett equilibrium pinch). The analyzed theoretically streams had a cylindrical symmetry having the z axis as the axis of symmetry. The electrons moved parallel along z axis direction and ions moved similar but in opposite direction. The densities of both species were assumed small and collisions of particles were assumed infrequent. The distribution of velocities of particles was described with Maxwellian distribution function (equilibrium distribution constant in time) both for electrons and ions. Also effects connected with plasma streams contact with electrodes were neglected.

The phenomenon predicted by Bennett became the basis of operation of z-pinch devices as well as plasma-focus devices (described in the section 2.2. of this work). The hot, dense and magnetized plasma object which is created in these devices is often called “plasma pinch” or simply “pinch”. In the z-pinch devices discharge is usually performed in deuterium in gas form. Because of presence of deuterium nuclei in hot and dense plasma, which is generated as a result of some type of high current electric discharge, D-D nuclear fusion (nuclear fusion of deuterium nuclei) can take place [Liberman 1999], [Sadowski 2005], [Velikovich 2007]. In general, the higher is the plasma density, temperature and confiment time the higher is the fusion reaction efficiency. And stronger plasma compression can lead to higher density of plasma particles as well as longer interaction times between particles and longer stability. Mainly because of these facts and the possibility of achieving break-even conditions, the plasma compression phenomenon (and other accompanying phenomena) in z-pinches was studied for many decades. However, after years of research break-even conditions were not achieved in any z-pinch device. And there are still many physical processes that occur in z-pinches which are not fully understood and/or their existence has not been confirmed and investigated properly. One of such effects is the plasma radiative compression phenomenon.

For the plasma radiative compression phenomenon in z-pinches it was predicted theoretically that the concentration of plasma particles density can rise to extremely high values (10^{29} particles/cm^3) while the plasma pinch radius drops to very low values (10^{-7} cm) in some devices [Robson 1989a]. However, to achieve this extreme compression plasma must be approximately in a state of pressure equilibrium (balance of magnetic pressure and internal plasma pressure forces) as well as a current higher than the so called Pease-Braginskii (P-B) current must flow through plasma [Shearer 1976]. The P-B current is a characteristic value, per given plasma type, and is calculated for conditions of thermodynamic equilibrium [Pease 1957], [Braginskii 1958], [Shearer 1976]. Namely, when P-B current flows through plasma the power of the bremsstrahlung radiation losses and the power of the ohmic heating (Joule heat) are in balance – equilibrium current. When the current flowing in plasma exceeds P-B current value the power of radiation losses will exceed the power of ohmic heating [Shearer 1976]. Because of this plasma will start to cool down and internal pressure will drop. So, an external power source must supply additional energy to sustain pressure equilibrium. And supplying additional energy into the system results in increase of magnetic pressure and this leads to further plasma compression. The compression will continue until the moment when internal pressure rise will cause degeneration of electron states in the area of high densities or when plasma will start to be optically thick (self-absorption of plasma radiation) or when instabilities of different kind appear and start to destroy the mechanical pressure balance and disrupt (break) the plasma column [Stepniewski 1995], [Liberman 1999], [Haines 2011].

The first estimations of P-B current values were made by two scientists working independently in 1956 and 1957 – R. S. Pease [Pease 1957] and S. I. Braginskii [Braginskii 1958]. Afterwards, in 1976 J. W. Shearer showed analysis of plasma pinch generated in z-pinch in pressure equilibrium state including higher current values than P-B current [Shearer 1976]. These early estimates of P-B current and conditions for achieving plasma radiative compression in z-pinches were rather inaccurate. In later studies scientist investigating plasma compression in z-pinch devices took into consideration additional effects, such as: plasma density profiles, axial outflow of plasma, plasma anomalous resistivity, plasma opacity and coupling of the pinch formation into a realistic electrical RLC circuit (for more realistic power source condition) [Stepniewski 1995], [Liberman 1999], [Haines 2011]. Also, one of the biggest breakthroughs was caused by taking into account radiation losses from X-ray line radiation and recombination radiation. These types of radiation losses are insignificant for plasma ions of low atomic Z numbers (for example deuterium plasma). However, if gases with higher Z numbers are present in plasma the line radiation losses can become the dominating ones [Vikhrev 1978a], [Pereira 1988], [Koshelev 1991], [Stepniewski 1995], [Liberman 1999], [Haines 2011], [Lee 2013]. Thus, the value of P-B current can be reduced – reduced P-B current – significantly when the powers of ohmic heating, bremsstrahlung radiation losses, line radiation losses and recombination radiation losses are included all together in the estimates while plasma is composed of higher Z nuclei. Moreover, even if the line radiation losses are significant, there is still the effect of the time of plasma pinch existence in pressure equilibrium versus the time of radiation emission during given z-pinch discharge. Only if the characteristic depletion time of radiation per given plasma type is significantly shorter than the time of the pinch existence in pressure equilibrium, plasma radiative compression can develop during discharge [Shearer 1976], [Stepniewski 1995], [Liberman 1999], [Haines 2011], [Lee 2016]. In next subsection most important equations concerning plasma compression for equilibrium z-pinch state are presented and described.

2.1.2. Basic equations of equilibrium pinch

The plasma column is generated as a result of electric discharge between electrodes. Effects at end of electrodes are neglected. Dynamic pressure equilibrium conditions are assumed. Plasma column conducts uniform electric current through unit of surface in *z* axis direction (figure 2.1.1).

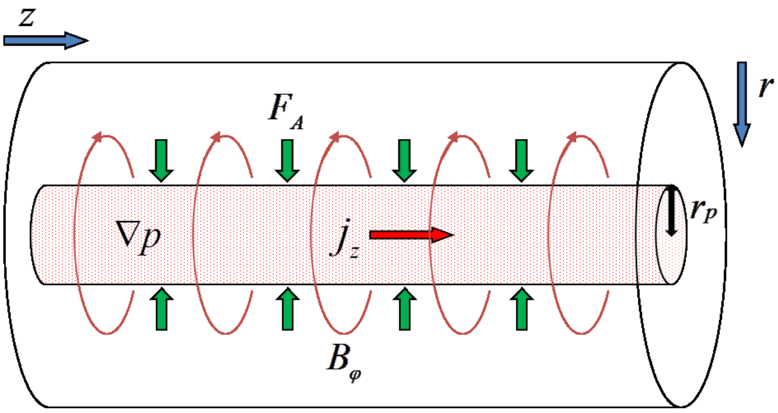

Figure 2.1.1. Schematic diagram of plasma column (z-pinch discharge). z – axial direction/component in cylindrical system of coordinates (blue arrow), r – the radial direction/component in cylindrical system of coordinates, r_p – the radius of plasma column (pinch), ∇p – the gradient of internal plasma pressure, j_z – current density z component (red arrow), B_φ – magnetic field induction φ component (red circles with arrows) and F_A –Ampere's force extered on the column (green arrows). The ∇p, j_z, B_φ and F_A are constant along z direction.

The uniform current density j_z (z axis direction) creates uniform magnetic field B_φ (azimuthal direction) along the entire length of the column. This magnetic field exerts pressure on the plasma (magnetic pressure) through Ampere's force F_A. The dependence of plasma internal pressure gradient from self magnetic pressure gradient can be described as [Bodin 1971], [Liberman 1999], [Haines 2011]:

$$\nabla p = \frac{dp}{dr} = \frac{1}{c} j_z B_\varphi \tag{2.1.1}$$

In equation (2.1.1), $\frac{dp}{dr}$ is the r component of the internal plasma pressure gradient (in CGS units) and c is the speed of light. The right side of equation (2.1.1) is the magnetic pressure gradient. Thus, this equation describes the equilibrium of pressures. Moreover, the equation (2.1.1) is actually the special case of the ideal magnetohydrodynamic (MHD) equation of momentum [Bodin 1971], [Liberman 1999].

The relation between current density and magnetic filed inductance can also be expressed using Ampere's law in magnetostatic form (CGS units): $\vec{\nabla} \times \vec{B} = \frac{4\pi\vec{j}}{c}$ [Liberman 1999], [Haines 2011]. When this equation is introduced into cylindrical system of coordinates then z component of current density can be expressed as [Liberman 1999], [Haines 2011]:

$$j_z = \frac{c}{4\pi r} \frac{d}{dr} \left(r B_\varphi \right) \tag{2.1.2}$$

In equation (2.1.2), r is the radial length (coordinate). The use of equation (2.1.2) is motivated by the fact that the force acting on the plasma column is actually the Ampere's force F_A. The external Ampere's force F_A acting on an element of surface of plasma column can be expressed as: $F_A = - p(r_p) l r_p d\varphi$, where l is the length of an element of column, $r_p d\varphi$ is the width of an element of column and $p(r_p)$ is the uniform external magnetic pressure exterted on the surface of the column.

When equation (2.1.2) is combined with equation (2.1.1) the dependence of magnetic pressure at the surface of pinch from magnetic field inductance can be found. Assuming the plasma column radius is equal to r_p and resultant pressure at the border of the pinch is equal to 0 then [Liberman 1999], [Stepniewski 1995]:

$$p(r_p) = \frac{B_\varphi^2(r_p)}{8\pi} \tag{2.1.3}$$

The value at the right side of equation (2.1.3) is often called the magnetic pressure. Thus, the Ampere's force F_A acting on an element of surface of plasma column is expressed as [Anderson 1958]:

$$F_A = -\frac{B_\varphi^2(r_p)}{8\pi} l r_p d\varphi \tag{2.1.4}$$

On the other hand, the internal pressure of the plasma column composed of ions and electrons can be expressed by the sum of partial pressures exerted by electrons and ions alone [Stepniewski 1995], [Haines 2011]:

$$p = p_e + p_i = n_p k\left(ZT_{pe} + T_{pi}\right) \tag{2.1.5}$$

In equation (2.1.5), p_e is the electron plasma pressure, p_i is the ion plasma pressure, $n_p = n_{pi}$ is the ion number density ($Zn_{pi} = n_{pe}$ – the electron number density), k is the Boltzmann's constant, T_{pe} is the electron temperature, T_{pi} is the ion temperature and Z is the ion charge number (atomic number for low Z gas).

When equation (2.1.2) and (2.1.3) are combined as well as it is assumed that $B_0 = B_\varphi(r_p) = 2I_{pp}/cr_p$ (I_{pp} is the uniform current flowing through pinch) then the so called Bennett relation can be presented in the best known form as [Thornhill 1989], [Stepniewski 1995], [Liberman 1999], [Haines 2011]:

$$I_{pp}^2 = 2c^2 N_p k T_p (1 + Z) \tag{2.1.6}$$

In equation (2.1.6), T_p is the temperature of particles in plasma column ($T_p = T_{pe} = T_{pi}$) and N_p is the ion line number density of plasma column (number of ions per unit of pinch length). This equation binds together the current flow I_{pp} through pinch with one of the most important plasma parameters – N_p, T_p and Z. Wherein, the ion line number density N_p is connected with plasma volumetric ion number density n_p through the equation (2.1.7) [Liberman 1999]:

$$N_p = \int_0^{r_p} 2\pi n_p r dr \tag{2.1.7}$$

Moreover, the equation (2.1.6) does not give information about plasma profiles – the T_p and Z parameters are assumed to be uniform in the entire plasma volume and N_p is integrated along r, but $B_\varphi(r)$, $p(r)$ and $n_p(r)$ are in general not uniform along r component. The magnetic field distribution B_φ along r can be described as (using equation (2.1.2) and assuming $I_{pp} = j_z \pi r_p^2$) [Thornhill 1989], [Stepniewski 1995]:

$$B_\varphi(r) = \begin{cases} B_0 \frac{r_p}{r}, r \geq r_p \\ B_0 \frac{r}{r_p}, r < r_p \end{cases} \tag{2.1.8}$$

The pressure p distribution inside plasma column along r can be described as (combining equation (2.1.1) and (2.1.2) for $p \neq 0$ and using equation (2.1.8)) [Thornhill 1989], [Stepniewski 1995], [Liberman 1999]:

$$p(r) = \frac{B_0^2}{4\pi}\left(1 - \frac{r^2}{r_p^2}\right) \tag{2.1.9}$$

And the distribution of particle ion number density n_p along r can be in general described as [Thornhill 1989], [Stepniewski 1995], [Liberman 1999]:

$$n_p(r) = \frac{2N_p}{\pi r_p^2}\left(1 - \frac{r^2}{r_p^2}\right) \tag{2.1.10}$$

The plasma pinch which is described using equations from (2.1.1) to (2.1.10) is called equilibrium pinch or quasi-stationary pinch with parabolic profiles (Bennett profiles). This pinch is characterized by: the dynamic pressure equilibrium, the uniform current flow, the uniform drift speed (constant electron speed in comparison to ion speed), the quasi-electrical plasma, the high heat conductivity as well as the parabolic profiles of density and pressure. Moreover, the above relations can be extended to cover the general case of any current density distribution (and any profiles of other physical quantities) which is constant along z axis and in time for a z-pinch discharge under pressure equilibrium [Haines 2011].

In the quasi-stationary pinch approximation it is also possible to determine the velocity profiles in the column for uniform compression or expansion – velocity of compression or expansion of given plasma sheet at distance r from the center of column (z axis) along radial direction [Thornhill 1989], [Stepniewski 1995]. This requires making an assumption that characteristic speed of compression or expansion is smaller than speed of sound in plasma (no shock waves) which is true for equilibrium pinch approximation.

When pressure equilibrium sets on further evolution of the plasma column is driven only by the processes of energy transport. But in z-pinches pressure equilibrium is hard to sustain because of plasma instabilities and possible existence of complex internal structures like magnetic flux loops of different shape [Bodin 1971], [Haines 1982], [Rudakov 1997], [Liberman 1999], [Haines 2011] [Sadowski 2012]. In general the stability of the z-pinch is still subject of extensive research [Liberman 1999], [Haines 2011].

2.1.3. Pease-Braginskii current

Apart from the pressure equilibrium also the thermodynamic equilibrium plays an important role in the system – the P-B current is derived in the thermodynamic equilibrium state. In order to derive the P-B current equations global conditions of power balance are usually used. In order to express the power balance, processes responsible for decreasing of plasma column energy such as the emission of bremsstrahlung radiation as well as the emission of X-ray line radiation and X-ray recombination radiation (when significant number of ions with high Z number are present in plasma), must be considered. Other mechanisms responsible for the decreasing of plasma energy are electrons and ions interacting with the cold electrodes of the devices or not ionized gas as well as plasma outflow in form of plasma waves, streams of charged particles or jets. On the other hand, the main process responsible for increasing plasma energy which should be considered is the ohmic heating. Other process responsible for the increase of plasma column energy is the heating with nuclear fusion products when significant number of light nuclei like deuterium and tritium is present in the plasma.

The basic equation of power balance of quasi-stationary plasma column is shown below (equation (2.1.11)) – only the power of bremsstrahlung radiation losses and power of ohmic heating are included [Robson 1989a], [Haines 1989], [Stepniewski 1995]. All other processes are considered insignificant.

$$\frac{dE}{dt} = p\frac{dV}{dt} + \frac{dU_{int}}{dt} = P_{ohm} - P_{brem} \tag{2.1.11}$$

In equation (2.1.11), dE/dt is the change of total energy of system, pdV/dt is the change of energy of system connected with the change of volume of plasma column, dU_{int}/dt is the change of internal energy of system, P_{ohm} is the change of energy of the system due to the ohmic heating (power of ohmic heating) and P_{brem} is the change of energy of the system due to the bremsstrahlung radiation losses (power of bremsstrahlung radiation emission). This equation was derived from law of energy conservation.

From equation (2.1.11) the relation describing P-B current can be derived. This can be done assuming the case where $P_{ohm} = P_{brem}$ (the power of bremsstrahlung radiation losses and ohmic heating are in balance), $p\frac{dV}{dt} = 0$ (constant plasma column radius), $\frac{dU_{int}}{dt} = 0$ (pressure balance condition as well as constant current and constant number of particles conditions) and equation (2.1.6) is used for the calculation of temperature T_p. All things considered the equation for P-B current can be expressed as [Robson 1989a], [Stepniewski 1995], [Haines 2011]:

$$I_{P-B}(MA) \approx 0.499\frac{1+Z}{2Z}\left(\frac{1}{\alpha^{1/2}}\right)(ln\Lambda)^{1/2} \tag{2.1.12}$$

In equation (2.1.12), Z is the ion charge number (or atomic number for low Z gas), α is the dimensionless quantity that depends on the radial plasma density profile and $ln\Lambda$ is the so called Coulomb logarithm. This equation bases on the original considerations of Pease and Braginskii.

The equation for P-B current value can be also enhanced taking into account: parabolic density profile, Spitzer resistivity of the plasma and plasma opacity factor f_o [Robson 1989a], [Bernal 2002], [Lee 2013]:

$$I_{P-B}(MA) \approx 0.23\left(1 + \frac{1}{Z}\right)(ln\Lambda)^{1/2}\frac{1}{f_o^{1/2}} \tag{2.1.13}$$

Furthermore, the value of P-B current can be considered as a constant, for given plasma type which is optically transparent, since the Coulomb logarithm is a weekly dependent function of density and temperature and it is commonly assumed that $ln\Lambda \approx 10$ for hot and dense plasma generated in z-pinches [Pease 1957], [Pereira 1988], [Robson 1989a], [Koshelev 1991], [Bernal 2002]. On the other hand, the plasma opacity represented by the f_0 parameter can change vastly during single discharge and has significant influence on the P-B current values. Thus, in general the P-B current values with opacity factor included are not constant during single discharge.

2.1.4. Basic analysis of compression conditions

In order to find the dependency of plasma column radius from the power of ohmic heating and the power of bremsstrahlung radiation losses the equation (2.1.11) can be used.

The equation (2.1.11) for $P_{ohm} \neq P_{brem}$ and plasma column radius $r_p \neq const$ (general solution), can be transformed into [Shearer 1976], [Robson 1989a], [Stepniewski 1995]:

$$\frac{1}{r_p}\frac{dr_p}{dt} = \frac{P_{brem}c^2}{I_{pp}^2}\left(\frac{P_{ohm}}{P_{brem}} - 1\right) \tag{2.1.14}$$

In equation (2.1.14), r_p is the plasma column radius dependent on time t, P_{ohm} is the power of the ohmic heating, P_{brem} is the power of bremsstrahlung radiation losses, I_{pp} is the current flowing through plasma column (in z axis direction) and c is the speed of light. Equation (2.1.14) shows that when $P_{ohm} > P_{brem}$ plasma column will increase radius (expansion). On the other hand, when $P_{ohm} < P_{brem}$ plasma column will decrease radius (compression). And for $P_{ohm} = P_{brem}$ the plasma column radius is constant. The equation (2.1.14) can also be presented in a different form [Shearer 1976], [Haines 1989], [Robson 1989a], [Stepniewski 1995]:

$$\frac{1}{r_p}\frac{dr_p}{dt} = \frac{3}{4\tau_{brem}}\left(\frac{I_{P-B}^2}{I_{pp}^2} - 1\right) \tag{2.1.15}$$

In equation (2.1.15), τ_{brem} is the characteristic time of bremsstrahlung radiation losses ($\tau_{brem} = U_{int}/P_{brem}$ and U_{int} is the internal plasma column energy) and I_{P-B} is the Pease-Braginskii current. Similarly as in equation (2.1.12): when $I_{pp} < I_{P-B}$ plasma column radius increases, when $I_{pp} > I_{P-B}$ plasma column radius decreases and when $I_{pp} = I_{P-B}$ plasma column radius is constant. This type of analysis of the pinch in pressure equilibrium was done originally by Shearer [Shearer 1976].

The equation (2.1.15) can be also used to derive the dependence of plasma column radius r_p from time t when I_{P-B} and I_{pp} are constant [Shearer 1976], [Robson 1989a], [Haines 1989], [Stepniewski 1995]. This analysis shows that when $I_{pp} > I_{P-B}$ plasma column radius tends to zero and plasma density tends to infinity in a finite time (characteristic time of compression). However, in reality even if the I_{P-B} and I_{pp} were constant during the entire compression process (which is in general not true) and there would be no significant outflow of plasma particles, the compression would stop at some point because of the degeneration of electron states (plasma degeneration) or self-absorption of radiation or development of plasma instabilities [Haines 1989], [Robson 1989a], [Robson 1989b], [Chittenden 1990], [Cochran 1990], [Stepniewski 1995], [Rudakov 1997], [Liberman 1999], [Haines 2011]. Thus, if the plasma radiative compression was to be successful the characteristic time of compression (dependent on the characteristic time of radiation emission) must be smaller than the lifetime of the plasma column in mechanical pressure balance. And the lifetime of the plasma column is usually believed to be determined by the development of the MHD instabilities [Shearer 1976], [Haines 1989], [Robson 1989a], [Cochran 1990], [Koshelev 1991], [Rudakov 1997]. To be more precise, the main MHD instability responsible for breaking of the plasma column is belived to be the so called sausage instability (instability with azimuthal wave number $m = 0$) [Bodin 1971]. The development of sausage instability in plasma column is presented in figure 2.1.2, together with MHD kink instability ($m = 1$).

The MHD sausage instability, together with other instabilities (like MHD kink instability) including micro-instabilities, leads to destruction of global mechanical pressure balance, breaking of column, plasma outflow and cooling because of plasma particle’s interaction with the electrodes of the device. Wherein, in the micro-instabilities the local radiative collapse can occure [Pereira 1988], [Koshelev 1991], [Hebach 1993], [Lebert 1995]. Furthmore, the presence of MHD instabilities may also result in formation of complex internal structures like tangled loops of magnetic flux [Rudakov 1997] or increase plasma resistivity (micro-instabilities like lower-hybrid-drift instability) [Robson 1989b], [Robson 1991].

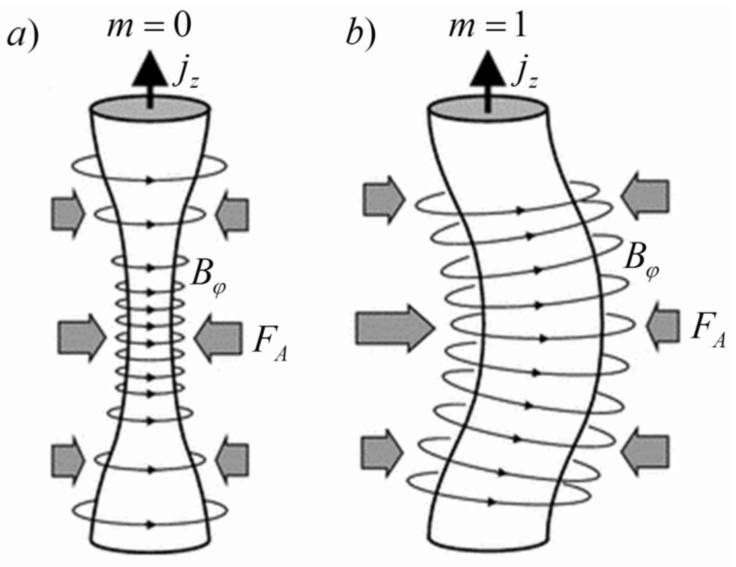

Figure 2.1.2. **a)** Scheme illustrating the development of MHD a) sausage instability (azimuthal wave number $m = 0$) and **b)** kink instability (azimuthal wave number $m = 1$) in plasma column [Piel 2017]. The symbols are: j_z – current density z component (black arrow), B_φ – magnetic field induction φ component (circles with arrows) and F_A –Ampere's force extered on the column (gray arrows). The j_z, B_φ and F_A are not constant along z direction.

2.1.5. Reduced Pease-Braginskii current and characteristic time of radiation depletion

The observed fast development of instabilities in plasma generated in z-pinch and the fulfillment of the fast compression condition (short characteristic time of compression and radiation emission) were stated to be the main reasons why plasma radiative compression in pure hydrogen or deuterium pinch was not observed in some experiments (even when current flowing through plasma column exceeded the P-B current) [Robson 1989a], [Robson 1989b], [Stepniewski 1995]. And it has been shown theoretically that decreasing of characteristic time of radiation emission (depletion) can be shorter due to the presence of admixtures in plasma which have a higher atomic Z number [Pereira 1988], [Koshelev 1991], [Haines 2011], [Lee 2013], [Lee 2016a]. In general, the higher is the power of radiation emission, the shorter is the time of radiation depletion and also the P-B current value is lower – reduced P-B current. However, it is difficult to analytically derive the reduced P-B current equation and characteristic time of radiation depletion equation when bremsstrahlung radiation, X-ray line radiation and recombination radiation losses are included. Nevertheless, few groups reported calculation of P-B current values under these conditions with the help of numerical computations (see section 2.3). Furthermore, in the articles S. Lee et al. [Lee 2013], [Lee 2016] suggest that it is possible to approximate the reduced P-B current value using P-B current value (calculated for ohmic heating and bremsstrahlung radiation only) and using powers of bremsstrahlung radiation losses, line radiation losses and recombination radiation losses. This idea was initially proposed by V. V. Vikhrev [Vikhrev 1978] and developed by K. N. Koshelev [Koshelev 1991] and N. R. Pereira [Pereira 1988]. Below the equation for the reduced P-B current $I_{P\text{-}Breduced}$ is presented [Lee 2013], [Lee 2016], [Akel 2016a]:

$$I_{P-Breduced}{}^2 = I_{P-B}^2 \frac{Z'}{K} \tag{2.1.16}$$

$$K = \frac{P_{line}+P_{rec}+P_{brem}}{P_{brem}} \tag{2.1.17}$$

$$Z' = \frac{1}{4}\left(1+\frac{1}{Z_{eff}}\right)^2 \tag{2.1.18}$$

In equations (2.1.16), (2.1.17) and (2.1.18), $I_{P\text{-}B}$ is the P-B current from equation (2.1.12), K is the coefficient representing the ratio of the sum of line radiation power P_{line}, recombination radiation power P_{rec} and bremsstrahlung radiation power P_{brem} to bremsstrahlung radiation power P_{brem} and Z' is the coefficient introducing correction associated with the effective ion charge number Z_{eff} of plasma (important when plasma is composed of ions with higher atomic numbers Z). The powers of radiation losses from plasma column in equation (2.1.16) and (2.1.17) as well as ohmic heating power P_{ohm} can be presented as [Lee 2016], [Akel 2016a]:

$$P_{line} \approx 4.6 \times 10^{-31} \frac{1}{T_p} n_p^2 Z^4 Z_{eff} \pi r_p^2 z_p \tag{2.1.19}$$

$$P_{rec} \approx 5.92 \times 10^{-35} \frac{1}{T_p^{1/2}} n_p^2 Z_{eff}^5 \pi r_p^2 z_p \tag{2.1.20}$$

$$P_{brem} \approx 1.6 \times 10^{-40} T_p^{1/2} n_p^2 Z_{eff}^3 \pi r_p^2 z_p \tag{2.1.21}$$

$$P_{ohm} \approx 1300 \frac{1}{T_p^{3/2}} Z_{eff} I_{pp}^2 \frac{z_p}{\pi r_p^2} \tag{2.1.22}$$

In equations from (2.1.19) to (2.1.22), T_p is the plasma column temperature, $n_p = n_{pi}$ is the ion number density of plasma column, Z is the atomic number of gas, Z_{eff} is the effective ion charge number (as in equation (2.1.18)), I_{pp} is the uniform current flowing through plasma column along z axis, r_p is the plasma column radius (the same as r_p in equation (2.1.14) and (2.1.15)) and z_p is the plasma column length. It is also worth to mention that the equation (2.1.22) is based on the Spitzer resistivity formula [Lee 2014].

The overall characteristic time of radiation losses t_Q (or radiation depletion) can be described using P_{ohm}, P_{line}, P_{rec}, P_{brem} and U_{int} values [Lee 2016]:

$$t_Q = \frac{U_{int}}{P_{line}+P_{rec}+P_{brem}-P_{ohm}} \tag{2.1.23}$$

In equation (2.1.23), U_{int} is the internal energy of the plasma column (the same as in equation (2.1.11)). The U_{int} is given as [Lee 2016]:

$$U_{int} = \frac{1}{\gamma-1} kT_p n_p \left(1+Z_{eff}\right) \pi r_p^2 z_p = \frac{f}{2} kT_p n_p \left(1+Z_{eff}\right) \pi r_p^2 z_p \tag{2.1.24}$$

In equation (2.1.24), $\gamma = C_p / C_v$ is the specific heat ratio (SHR) of plasma (C_p is the specific heat capacity at constant pressure and C_v is the specific heat capacity at constant volume), k is the Boltzmann constant and f is the number of degrees of freedom of plasma particles ($\gamma = (2+f)/f$ so that $1/(\gamma-1) = f/2$).

Additionaly, since the $I_{P\text{-}B}(t)$, $I_{P\text{-}Breduced}(t)$ and $I_{pp}(t)$ are in general not constant during z-pinch discharges the radiative compression lifetime (t_{rcl}) can be introduced into considerations. The t_{rcl} is entire period of time during stable phase of z-pinch discharge for which $I_{P\text{-}Breduced}(t) < I_{pp}(t)$. And since $I_{P\text{-}Breduced}(t)$ is sensitive to changes of f_0 the t_{rcl} is entire period of time when plasma is optically transparent (or at least not significantly optically dense) and is able effectively emit X-ray radiation. So, when t_{rcl} is higher than positive t_Q the radiative compression should be possible.

Summarizing section 2.1, the radiative compression phenomenon occurrence requires that the current flowing through plasma pinch (I_{pp}) must be higher than the reduced P-B current ($I_{P\text{-}Breduced}$) and the plasma pinch lifetime (t_{pl}) has to be longer than characteristic time of radiation depletion (t_Q). Additionaly, the radiative compression lifetime (t_{rcl}) can be also introduced and used as another indicator since pinch plasma current ($I_{pp}(t)$) and reduced P-B current ($I_{P\text{-}Breduced}(t)$) are in general not constant during discharge. Wherein, one must remember that the P-B current, the reduced P-B current, the characteristic time of radiation depletion and the radiative compression lifetime are only basic approximated indicators informing on the possibility of any radiative compression occurrence (even very weak and insignificant). And in order to achieve strong raditive compression it is possible that additional indicators or parameters should be taken into account, as was done in previous works and simulations (see section 2.3). However, up to this day there is no agreement on which other indicators and parameters should be actually taken into account when investigating plasma radiative compression phenomenon – different authors reached different conclusions. Finally, there are phenomenons which may occurre during z-pinch discharges, like for example different instabilities development, hot spots and filamentary structure formation, which significantly alter plasma behaviour during discharges and prevent the occurrence of global or even local radiative compression.

2.2. Z-pinch and plasma-focus devices

2.2.1. Concept and types of z-pinch devices

The officially accepted starting date of z-pinch research is 1934. In this year W. H. Bennett [Bennett 1934] described the effect of pinching of uniform charged particle streams with self generated magnetic field. On the basis of the principles described by Bennett new devices were constructed and modified. The development of great power pulse current generators in XX century also contributed to this. For past 80 years many different z-pinch constructions were invented. Still, their basis of operation remains the same. The operation of each z-pinch is based on the current flow in *z* axis direction through plasma and compression using self generated magnetic field (as described in Chapter 2.1) [Liberman 1999], [Ryutov 2000], [Haines 2011] [Sadowski 2012]. To achieve this type of discharge in plasma different non-stationary processes can be utilized. In view of different possibilities of discharge generation – place of the initial discharge in the system, medium and way of further discharge development – there are many possibilities of assignment of individual z-pinches into smaller groups. Examples of such categories were mentioned by Stępniewski in [Stepniewski 1995]: linear z-pinch, plasma-focus, gas-puff, exploding wires, micro-pinch (vacuum spark) and discharges using thin dielectric fibers. Another classification was presented by Liberman [Liberman 1999]: dynamic z-pinch, equilibrium z-pinch, vacuum arcs and plasma-focus, or by Sadowski [Sadowski 2012]: single-channel z-pinches, wire-array z-pinches, x-pinch configurations, gas-puffed z-pinches and non-cylindrical z-pinches (often called dense plasma focus).

The important fact about all z-pinch is that two discharges are never exactly the same, even if they are performed in the same device, under the same operation conditions and in the same working gas under the same pressure (the same initial condition). This is due to the fact that z-pinch discharge depends on the local concentration of gas particles at given time (as in atmospheric discharges) and there are many non-linear effects which can develop differently (like instabilities) in relatively short periods of time (dynamic and turbulent behaviour of plasma). Thus, there are many possibilities of mass and charge/current flow between electrodes during entire discharge. So, the information acquired from a given diagnostic system during given discharge should not be used as complementary information for the second discharge, in general. In other words, all necessary diagnostic systems used during investigation of z-pinch discharges should be used simultaneously for all planned discharges/experiments.

2.2.2. Plasma-focus devices – basics of contruction and phases of discharge

In subsection 2.2.1 two classifications of z-pinch devices were given. In both of them (as well as in many other) special type of z-pinch called plasma-focus (or dense plama-focus) is mentioned. The PF is a type of dynamic, non-cylindrical plasma generator and magnetic confiment fusion device of z-pinch type [Mather 1971], [Liberman 1999]. The device usually consists of: condenser bank and switches (battery), transmission cables, collector and experimental chamber with electrodes [Mather 1971], [Decker 1976], [Liberman 1999]. The condenser bank of the device stores the energy in form of electromagnetic field and releases it all instantly (for example using spark-gaps) after charging of battery ends. The transmission cables transmit electric energy from the condenser bank to the collector. The collector collects the electric energy and ensures homogeneous current flow from the condenser bank to the electrodes of the device. The experimental chamber is a vacuum tight container with electrodes and isolator inside. There are two standard configurations of the electrode’s and isolator’s layout in PFs as described by Filippov [Filippov 1962] and Mather [Mather 1965].

Phases of discharge (experimental) in plasma-focus device

The discharge in PF device can be divided into two or three main phases occurring one after another [Bernard 1998] [Scholz 2004] – see figure 2.2.1 [Abdallah 1999].

Phase I – breakdown and build-up (ignition)

The first phase of discharge is the breakdown between coaxial electrodes over the isolator (insulator) in working gas and build-up (initial forming) of the approximately symmetrical, uniform and thin plasma current sheet.

Phase II – axial acceleration (run-down)

The second phase of discharge, taking place only in Mather type of PF’s, is the run-down of the current sheet (acceleration phase) in the axial direction. In this phase the current sheet is accelerated along electrodes (along z axis) through the Ampere’s force (see subsection 2.1.2). The sheet quickly reaches supersonic velocity and shock wave in front of structure appears. Because of this high velocity of movement, strong conductivity of electric current, generation of self magnetic field and symmetry the plasma structure is able to “sweep”, ionize and accelerate the neutral gas in front – part of previously neutral gas becomes ionized and joins moving plasma structure. This is why the plasma sheet structure is often called magnetic piston. Moreover, this type of sweeping is similar to a moving snow plough or a growing balloon. Thus, this phase of discharge is often described using so called snow-plough model [Anderson 1958], [Gross 1971], [Potter 1971], [Pereira 1988], [Liberman 1999], [Haines 2011].

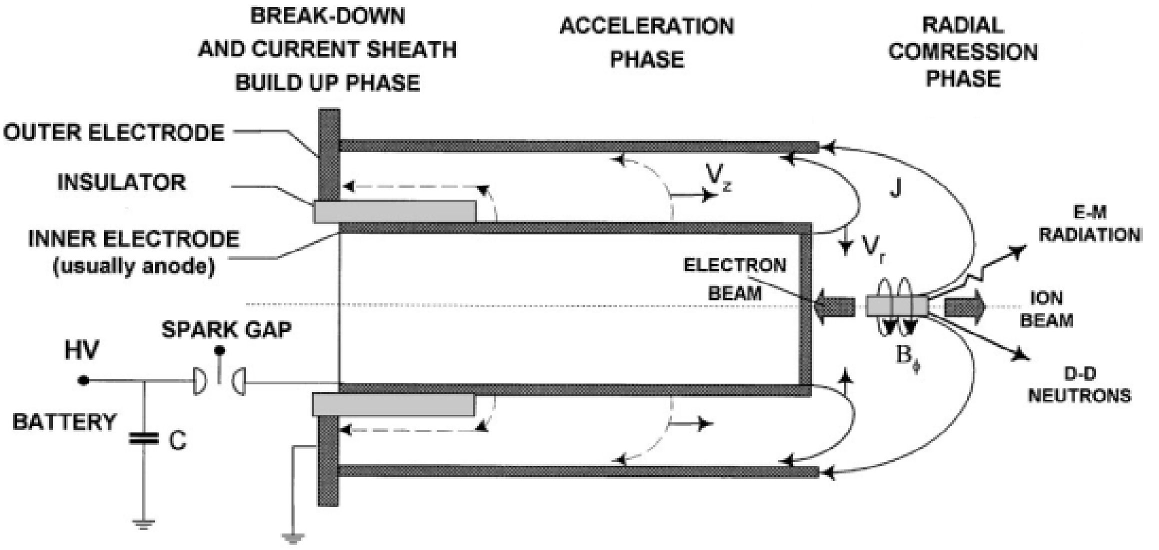

Figure 2.2.1. Phases of discharge in Mather type plasma-focus and basis of operation [Abdallah 1999]. The symbols are: C – the total capacitance of battery, v_z – the velocity of plasma structure (magnetic piston with shock) along z direction, v_r – the velocity of plasma structure (magnetic piston with shock) along r direction, J – the density of current flowing through plasma structure and B_φ – the φ component of magnetic field induction around generated plasma column (plasma pinch).

Phase III – radial compression (run-in and pinch)

The third phase of discharge is the radial compression of the current sheet (magnetic piston) with shock wave in front. In this phase the current sheet is compressed towards the center of electrodes (into z axis) also using the Ampere’s force (see figure 2.2.1). The radial movement of magnetic piston with shock wave in front of it can be described in approximation using so called slug model [Potter 1978], [Liberman 1999], [Haines 2011]. During this phase the current sheet coincides close to the z axis forming plasma pinch – see figure 2.2.1. The plasma pinch is a relatively small and short lived object shaped similarly to a funnel or to a column. It has been stated in previous research that it can exist in approximation from a few to a few hundred nanoseconds (in largest PF devices) [Mather 1971], [Decker 1976], [Bernard 1998], [Liberman 1999], [Scholz 2004], [Kubes 2011]. The plasma volume in the pinch varies between few cubic millimeters and dozens of cubic centimeters (in largest devices) [Mather 1971], [Decker 1976], [Bernard 1998], [Liberman 1999]. The typical ion average pinch temperature achieved in PF devices is about 1 keV and typical ion number density is about 10^{18} per cubic centimeter [Mather 1971], [Decker 1976], [Bernard 1998], [Liberman 1999]. In general, conditions achieved in the plasma pinch enable nuclear fusion of light nuclei – for example nuclear fusion of D nuclei if deuterium is the working gas filling experimental chamber

[Bernstein 1970], [Lee 1971], [Bernard 1977], [Bernard 1998] [Sadowski 2012]. The plasma pinch is also the source of other type of radiation: electromagnetic radiation (mainly in the X-ray range), ion streams, electron streams, plasma waves and plasma jets [Mather 1965] [Bernard 1998] [Sadowski 2010] [Sadowski 2012] [Rawat 2015]. Moreover, the time period starting from the moment when plasma pinch is generated is often called pinch phase [Bernard 1998] [Scholz 2004]. This pinch phase of discharge can be also divided into three subphases – quiet phase, unstable phase and late phase (best seen in large plasma-focus devices) [Bernard 1998] [Scholz 2004] [Kubes 2010]. In quiet pinch phase plasma column is believed to be approximately stable and can still expand globally. In this phase neutron production and emission is stated in large plasma-focus devices (first pulse) [Bernard 1998] [Scholz 2006] [Schmidt 2006] [Kubes 2010]. In unstable pinch phase neutron production and emission is continued (second pulse in large PF devices) and MHD instablities (see figure 2.1.2) and/or micro-instabilities (also called hot-spots) can develop inside plasma column [Koshelev 1991], [Pereira 1988], [Lebert 1995], [Bernard 1998], [Kies 1998], [Scholz 2004], [Scholz 2006], [Schmidt 2006], [Kubes 2010], [Kubes 2012], [Sadowski 2015], [Kubes 2019a]. In fact, it was stated that entire plasma column can be transformed globally into a group of micro-instabilities placed along *z* axis [Pereira 1988], [Koshelev 1988], [Lebert 1995], [Decker 1996], [Sadowski 2015]. In the late phase plasma decays after the break-up of plasma column, rapidly expands and cools down (regardless of whether it is a column or a group of hot-spots). Furthermore, during pinch phase complex internal structures like magnetic flux loops of different shape or current filaments can also develop inside column [Rudakov 1997], [Soto 2014], [Sadowski 2015], [Kubes 2017], [Kubes 2019a].

2.2.3. Equivalent electric circuit of plasma-focus

It is worth to mention that a discharge in plasma-focus devices can be described in approximation as a discharge in a dynamic and damped RLC circuit [Mather 1971], [Bernard 1998], [Scholz 2004]. The scheme of electric discharge in such equivalent RLC circuit is presented in figure 2.2.2.

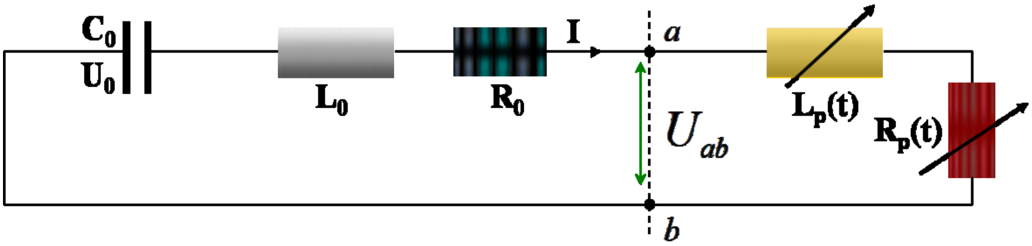

Figure. 2.2.2. Equivalent circuit for a discharge in plasma-focus. The U_{ab} is the total voltage between the electrodes and I is the total current flowing in the circuit. The C_0, L_0, R_0, are the total capacitance, the total inductance and the total resistance of the plasma-focus device, respectively. The L_p is the dynamic plasma inductance and R_p is dynamic plasma resistance [Mather 1971], [Bernard 1998].

The equivalent electric circuit shown in figure 2.2.2 consists of elements which during discharge usually have static values in approximation: the total capacitance of the device – C_0, the total (nominal) inductance of the device – L_0 and the total (nominal) resistance of the device – R_0. The total capacitance of the device is basically the total capacitance of condenser bank. And L_0 and R_0 elements represent inductance and resistance of all parts of plasma-focus device which conduct electric current during each discharge – condensers, spark-gaps, transmission cables, collector plates and isolator between electrodes covered with thin current conducting sheet in the experimental chamber. Furthermore, L_p and R_p is the dynamic plasma inductance and the dynamic plasma resistance, respectively. This is connected with the fact that in PF devices plasma closes the electric circuit and conducts electric current. So, L_p inductance is connected with motion of the current sheet and geometry of electrodes and R_p is the ohmic plasma resistance of the moving sheet. The change of voltage in such a system is represented by U_{ab} (total discharge voltage) and the current flowing through the circuit is represented by I (total discharge current). Below, equation describing the equivalent electric RLC circuit from figure 2.2.2 was presented [Mather 1971], [Bernard 1998], [Scholz 2004]:

$$U_0 - \frac{1}{C_0}\int I dt - L_0\frac{dI}{dt} - IR_0 = U_{ab} = I\frac{dL_p}{dt} + L_p\frac{dI}{dt} + IR_p \qquad (2.2.1)$$

In equation (2.2.1) all symbols are the same as in figure 2.2.2. Wherein, I, L_p, R_p and U_{ab} are time t dependent functions.

2.3. History and status of research on plasma radiative compression phenomenon in z-pinch

2.3.1. Original research of Pease and Braginskii – characteristic current concept

Research concerning plasma radiative compression started in 1957-1958 when R. S. Pease and S. I. Braginskii published first articles stating the existence of characteristic current [Pease 1957], [Braginskii 1958]. Pease investigated axially-symmetrical discharges, in long straight tubes (cylindrical symmetry) and under stationary conditions. The calculations were to meet the requirements of a power-producing thermonuclear reactor. Pease considered first of all: the validity of the diffusion conditions implied in the initial equations, the transport properties of the plasma and the cyclotron radiation arising from thermal motion in the self-magnetic field. His results showed that in a stationary state a pinch discharge will exist with radiative cooling and that a maximum current will be encountered. This maximum current will dependent on pinch parameters and the characteristic current of ionized gas. The value of this maximum current was to be about 1.7×10^6 A (between one and two million ampers for assumed conditions). Furthermore, it was stated that the discharge does not have to become heated to an “unpinchable” temperature in order to dissipate the energy fed in, and that the most obvious and serious obstacle to achieve discharge conditions in which performed calculations would be applicable lies in the instabilities known to exist in current-carrying plasmas [Pease 1957]. Similarly, Braginskii considered the discharges developing in a cylindrical pinch in a quasi-stationary state in completely ionized and quasi-neutral plasma. His calculations were based mainly on the power balance and the assumption, that the plasma pressure is balanced by the electrodynamic forces generated by the current flowing through the pinched plasma. The gradients of all quantities were directed along the radius r and the electric current flow was along the z axis while the magnetic field was directed azimuthally. The end effects (electrode effects) were neglected in his calculations. The results showed that in a stationary mode there are possible energy losses via radiation (bremsstrahlung). When the power of these energy losses is equal to the power of Joule heating, the maximum and the characteristic current of a discharge can be calculated. This value of the characteristic current for the given assumptions was about

1.4×10^6 A. If the current flowing through pinch is smaller than this characteristic current, part of the generated Joule heat is radiated and the remaining part is removed by conductivity. It was also stated that an increase in the electric field in the filament (pinch) would lead to further compression and increased radiation emission because the temperature and current do not change (stationary mode with maximum current and temperature). Furthermore, for the non-stationary pinch mode simple calculations were also performed showing that change of filament radius is possible in time and it is connected with the current value and how fast the current changes [Braginskii 1958].

2.3.2. Original research of Shearer – radiative compression concept

By showing independently simple analysis Pease and Braginskii created the basis of the plasma radiative compression theory. However, the full theory of this phenomenon was not completed until 1976 when J. W. Shearer presented relations with currents exceeding P-B current for z-pinch type of discharge and thus created generalized conditions (see also section 2.1) [Shearer 1976]. Shearer assumed equilibrium model of the radial motion of z-pinches for his calculations. This model was based on Bennett relation, radiation losses and Ohmic heating. In his work Shearer commented that in classical z-pinch discharge the P-B current is constant, independent of density, temperature and radius. This would imply that the pinch is in full equilibrium only when its current is equal to P-B current. However, in reality the pinch plasma current will differ from the P-B current. Thus, the analysis needs to be generalized permitting gain or loss of energy by the pinch. Shearer in his calculations considered that Bennett equation is always valid so the processes that occur are isothermal for given constant line density of particles as well as instabilities are ignored. Results of Shearer calculations showed that if $I_{pp} < I_{P\text{-}B}$ the plasma column expands and if $I_{pp} > I_{P\text{-}B}$ the plasma column contracts (see section 2.1). In this second case, the self-constricting pinch force keeps the pinch density high and the radiation loss rate exceeds the Joule heating. Shearer commented that in the z-pinch devices equilibrium motion of the pinch (dynamic balance) should be possible for these cases where the radial motion time constant is shorter than the instability growth times. For a pure deuterium plasma pinch, this is fulfilled only for extremely dense, low-temperature conditions that usually do not match the experimental ones. But if the deuterium plasma contains some impurity ions the radiation losses are enhanced and the consistency with conditions achieved in the experiment is improved. Finally, Shearer stated that this model predicts that the pinch radius will approach to zero when the current is higher than the P-B current but one would expect that many additional effects exist that would terminate the contraction or disturb it [Shearer 1976]. Next 42 years of research gave some interesting and controversial results. The selected important ones are mentioned below.

2.3.3. Modeling of plasma radiative compression – Vikhrev code

In 1977 V. V. Vikhrev published an article describing relatively simple 0/1-dimensional computer code [Vikhrev 1977]. The code (including next versions) enabled effective simulation of plasma radiative compression development in a dynamic z-pinch operated with hydrogen or deuterium including small admixtures of high Z working gases [Vikhrev 1978a], [Vikhrev 1978b], [Vikhrev 1980], [Vikhrev 1986]. This model was next developed by Vikhrev and K. N. Koshelev enabling simulations of discharges in vacuum spark systems [Vikhrev 1982], [Koshelev 1985]. The codes were based on a model which assumed that after a first compression due to an $m = 0$ MHD instability energy losses caused by line radiation and by plasma outflow lead to a further rapid compression, accompanied by a strong increase of electron temperature and density. The computations included following effects: the inertia of the radial motion of the matter, approximated plasma outflow (decrease of plasma particle number and plasma column energy), lowering of current as a result of growth of inductance and resistance of plasma column, anomalous plasma heating (anomalous resistance) as a result of micro-instabilities development in the column (for instabilities with lowest excitation threshold), viscous heat release, bremmstrahlung radiation transport in "gray body" approximation (kinetic and transport coefficient are independent of radiation frequency), pressure of degenerated electron gas and plasma heating with nuclear fusion products. The results from the Vikhrev codes suggested that plasma radiative compression develops only in pinch where the initial linear concentration of particles is higher than 10^{21} per cm. The significant grow of concentration of particles in plasma pinch occurs when the power of radiation losses exceeds the power connected with plasma particles outflow. And the radiative compression can be stopped when one of the the following is valid: plasma becomes degenerated, significant growth of plasma opacity (growth of optical density) will take place and significant growth of anomalous plasma resistance will occur [Vikhrev 1978a], [Vikhrev 1978b], [Vikhrev 1980], [Vikhrev 1982], [Koshelev 1985], [Stepniewski 1995].

2.3.4. Microstructures in z-pinch discharges

In 1988 articles concerning formation of micro-pinch structures during plasma-focus discharges in the presence of small impurities of heavy gas were published by Koshelev et al. [Koshelev 1988] as well as I. V. Volobuev et al. [Volobuev 1988]. The articles suggested that formation of hot-spots can be the effect of local radiative compression.

Koshelev et al. [Koshelev 1991] and N. R. Pereira et al. [Pereira 1988] presented the experimental and computation results of the plasma radiative compression in vacuum spark systems. They observed small glowing spots: the small plasma dots (a few microns in size, a high density of about 10^{23} particle/cm^3 and electron temperature equal or above 1 keV) and the large plasma speckles/dots (one order of magnitude larger in size and two order of magnitude lower densities then the small one). Koshelev reported formation of micro-pinch like structures (hot-spots) in wire-array, gas-puff and plasma-focus systems and noted that many characteristics of the plasma points are successfully reproduced by the Vikhrev model. Moreover, it was stated that the final pinch structure changes significantly with different z-pinch device used and with admixture of elements with higher Z. For example in vacuum sparks strong X-ray line radiation emission from helium-like and hydrogen-like ions was registered during experiments with admixture of Mg, Al and S. Additionally, if total power of X-ray line radiation and recombination radiation is K times bigger than total power of radiation emission from pure hydrogen plasma then the P-B current should decrease $K^{0.5}$ times (suggested also by Vikhrev computations).

Pereira [Pereira 1988] summarized the recent experimental data from reliable z-pinch experiments (with well-defined parameters) and presented an overview of theoretical issues concerning radiation production in the pinch plasma including micro-pinch discharges and their radiation output. He suggested that in z-pinches (except vacuum sparks) the mechanical balance is difficult to achieve and sustain and radiation losses are relatively slow in time. Nevertheless, some data and photos in XUV and soft X-ray radiation showing plasma pinch compression from discharges in Kr confirmed a high compression, small pinch radius and large emission of EM radiation. Wherein, in presented discharges in the final stage plasma column transformed into micro-pinches and no analysis of radius values were given.

The codes developed by Vikhrev et al. [Vikhrev 1982] and by Koshelev et al. [Koshelev 1985] were used also by M. Hebach et al. [Hebach 1993]. Hebach compared the computed (based on Vikhrev code [Vikhrev 1982], [Koshelev1985]) and the experimental results from micro-pinch discharges. The soft X-ray radiation (as a function of time) from small magnesium glowing points (helium-like) was registered using a streak camera. The micro-pinch discharges were performed in classical linear z-pinch, gas-puff and plasma-focus systems operated with heavy gases or with addition of heavy gases to a light discharge gas. Pinhole pictures revealed that the most intense X-rays were emitted from several or even a series of bright spots situated along the axis of the plasma column. The registered glowing points consisted of hot plasma and had subnanoseconds lifetimes. Very good match of measured and computed data was achieved concerning times of radiation emission and sizes of glowing points – the local plasma radiative compression was believed to be observed.

The effect of transition of plasma column into micro-pinch structures was also studied later by R. Lebert et al. [Lebert 1995] during discharges in pure high Z gases. Lebert stated that for element with $Z < 18$ (nitrogen or neon) K-shell emission is observed from column-like volumes several 100 µm in diameter and several mm in length (bulk or column mode). For $Z > 18$ (krypton or xenon) only emission of electromagnetic radiation with energy above 1 keV was observed from micro-pinches. And for $Z = 18$ (argon) both modes of operation could be observed. Lebert tried to find criterion for transition into different modes. He presented photos acquired using temporal integrated pinhole images of the SXR emission as well as streak images of SXR emission. Both micro-pinch and column modes were observed. Lebert stated that the transition into modes is connected with characteristic currents: the pinch current (determining the kinetic energy of the collapsing ions), the critical current which is a generalized Pease-Braginskii current for not totally ionized plasma (determining whether radiative collapse can be achieved) and the shell current estimated from Bennett equilibrium (determining whether a closed electron shell is ionize in the initial bulk plasma). If the pinch current is larger than the P-B current, then the radiative collapse is possible and if pinch current is larger than the shell current (characteristic for K, L and M shells), then the shell is ionized. Moreover, Lebert suggested coupling of these currents into one dimensionless parameter. If this parameter was bigger than 1 column mode would appear (global radiative compression of entire column) and if the parameter was smaller than 1 micro-pinch mode would appear (local radiative compression).

2.3.5. Modeling of plasma radiative compression – Apruzese and Kepple

J. P. Apruzese and P. C. Kepple [Apruzese 1989] published results of computations concerning plasma radiative compression and reduced P-B current in z-pinches. Their code included a detailed radiation transport model (X-ray line radiation) including 511 independent spectral lines and the possibility of self-absorption of each type of line. Computed dependence of the P-B current from particle concentration for few different plasma temperatures was presented by the authors. The computed P-B current in Kr discharges was about 100 kA for 10^{19} particles per cm^3 for all presented plasma temperatures (0.4-1.0 keV) thus a radiative compression was possible (the computed values of the P-B current were significantly smaller than those in pure H or D). Furthermore, the P-B current values increased in this model with increase of the plasma concentration (even up to 1 MA for 0.4 keV temperature and 10^{22} particles per cm^3).

2.3.6. Analysis of radiative compression by Meierovich

B. Meierovich in a series of articles published results of MHD computations concerning the plasma radiative compression effect in some astrophysical situations using his dynamical model [Meierovich 1982], [Meierovich 1984], [Meierovich 1985], [Robson 1989a], [Stepniewski 1995], [Haines 2011]. In this model Meierovich considered plasma radiative compression on the assumption that the current flowing through the plasma column is far greater than the P-B current as well as that a relative drift velocity is much greater than the thermal speed of plasma particles. Thanks to these assumptions he managed to achieve self-similar solutions describing the dynamic of compression and equilibrium conditions of the last stadium of evolution of heavily degenerated plasma. However, further investigation of other authors undermined Meierovieh work criticizing his main assumption of $I_{pp} >> I_{P\text{-}B}$ [Robson 1989a], [Stepniewski 1995]. Still, the published articles suggested that relativistic beams lead to a breakdown of quasi-neutrality state, but they are also likely to lead to micro-instabilities and anomalous resistivity [Haines 2011].

2.3.7. Modeling of plasma radiative compression – Jach

In results of computations presented in an article by K. Jach from 1991 no radiative compression was observed [Jach 1991] despite the fact of an exceeding P-B current value. The computations were performed for discharges in gas-puff systems operated with neon. In the averaged transport model which was used plasma entered quickly the higher opacity state (smaller radiation losses), and plasma dynamic was driven by the development of MHD instabilities [Jach 1991], [Stepniewski 1995].

2.3.8. Experiments in gas-puff system by Bailey

In the 1980s J. Bailey et al. published results on experimental observation of plasma compression and compared them with a simple model (calculations). The experiments were carried out in a gas-puff device operated with D_2 and a mixtures of D_2 with Ar [Bailey 1982], and He, Kr and mixtures of He with Kr [Bailey 1986]. In the first article the authors did not mention plasma radiative compression in pure D_2, and for D_2+Ar mixtures separation of D and Ar plasma in the pinch was stated (D in inner column and Ar in outer ring). The mechanism of separation was not explained. The authors reported stability of plasma column for about 40 ns time in total and decreasing of the plasma pinch radius with increasing of Ar doping. Adding small amounts of Ar percentage resulted in a more uniform, efficient and stable pinch. Still, there was no hint of plasma radiative compression and P-B current calculation [Bailey 1982]. On the other hand, the results from pure Kr and He+Kr mixtures are interpreted as the occurrence of plasma radiative compression. The data achieved using X-ray diodes and a Mach-Zehnder interferometer showed the increase in plasma concentration and the reduction in pinch radius. It was also stated that the results are in agreement with simple calculations based on an energy balance equation which enabled time-resolved estimation of the plasma temperature. The model showed that the measured radiation from the He-Kr mixture is sufficient to cause the temperature of the mixture plasma to increase more slowly than with pure helium plasma. And the slower temperature increase resulted in smaller finite plasma column radius (because the magnetic pressure compresses the plasma until the temperature is high enough to cause internal plasma pressure balances the magnetic pressure). In this work P-B current was not calculated – author based also only on power of radiation losses [Bailey 1986].

2.3.9. Experimental discharges in thin frozen deuterium fibers

The effect of plasma radiative compression was also considered during discharges in linear thin frozen deuterium fibers. Sethian et al. in the article [Sethian 1987], J. Hammel in the article [Hammel 1989] and P. Sheehey et al. in article [Sheehey 1992] presented results of such discharges. These experiments turned out to be different from standard z-pinch discharges in gases – there was no gas sweeping through current sheet and no compression phase as in gas z-pinches. The pinch radius of the fiber changed insignificantly during current increase, while the calculated times from the hydrodynamic equations predicted significantly shorter plasma pinch existence. In fact, results presented by Sethian showed that as long as the current derivative over time increased the fiber plasma was stable – about 130 ns time of stability was maximally achieved for the 80 μm fibber in radius and 640 kA of maximum current [Sethian 1987]). However, when the current reached its maximum the $m = 0$ MHD instability appeared, high neutron yield was produced and compression ended (regardless of the current magnitude and time to reach the maximum). The initial assumption presented by Hammel showed that the P-B current should be reached during the discharge through a frozen deuterium fiber of 30 μm in radius (about 1.4 MA) [Hammel 1989]. During the experiments a very fast current rise to its maximum (about 100 ns only) was observed. A very dense plasma and a Bennet equilibrium temperature of about 10 keV should be achieved for a 1.4 MA reached. However, ultimately a dense plasma was achieved for a short time but no radiative collapse or at least a contraction was clearly identified [Sheehey 1992], [Stepniewski 1995], [Akel 2016b]. The 1/2-dimensional resitive MHD simulations performed together with experiments showed that when the fiber was becoming fully ionized a rapidly developing $m = 0$ instability appeared, which originated in the corona surrounding the fiber, driving intense nonuniform heating, rapid expansion of the plasma column and dropping densities orders of magnitude below the near-solid densities desired for fusion conditions [Sheehey 1992].

2.3.10. Computations concerning radiative collapse in z-pinch including discharges in thin frozen deuterium fibers

Computations of discharges in z-pinch configuration including equivalent electric circuit equation were published in 1989 by M. Haines using analytic 0-dimensional model [Haines 1989] and by A. Robson [Robson 1989a] for discharges in hydrogen and helium as well as by W. Thornhill et al. [Thornhill 1989] for frozen deuterium fibers with relatively slowly rising current. The computations included in the models following effects: change of plasma temperature, change of plasma concentration/density, plasma self-absorption, degeneration of electron states.

The results of simulations present by Robson suggested that the maximum plasma density during discharge increases by the addition of series inductance inside the vacuum chamber. And in most cases the maximum density was limited by the pinch becoming optically thick, although for low line densities and large series inductance the maximum density was determined by onset of electron degeneracy. Robson's computations also suggested that the pinching effect in hydrogen plasma leads to denser collapsed states than in helium plasma. Moreover, Robson presented graphs showing a dependence of the P-B current from pinch radius for different linear plasma particles concentrations [Robson 1989a]. The curves suggested the existence of a minimum of the P-B current (not for the value of minimum pinch radius). And for smaller linear concentration there was bigger chance of plasma instabilities development and thus increase of resistance – smaller compression not possible. And for higher linear concentrations compression was weaker because of plasma internal pressure increase. Nevertheless, significant plasma pinch radius decrease was achieved in computations – 6.5×10^{-7} cm – for 17.1 keV of plasma temperature and constant *dI/dt* = 10 kA/ns in hydrogen. This decrease of pinch radius was accompanied with an increase of the plasma ion number density up to 10^{29} particles per cm^3 [Robson 1989a].

The result obtained by Haines [Haines 1989] using his 0-dimensional model suggested P-B current value of about 1 MA and a maximum current equal to $3^{0.5}I_{P\text{-}B}$ when *dI/dt* is constant. However, in reality when an external circuit equation was included into the computations it prevented the occurrence of such high current due to too low voltage of the power source. Maximum ion number densities achieved by Haines were at the level of $10^{26}/cm^3$ while the P-B current was reached. The maximum densities were limited by the resistance and inductance of the narrow column. The minimum current following the maximum density (drop of current at the beginning of radiative compression after P-B current was exceeded) was shown to be higher than $I_{P\text{-}B}/2$. Degeneracy effects were not included into the model.

The results obtained by Thornhill were performed for slowly rising current of about 3 kA/ns which was theoreticly powered by constant generator voltage of 200 kV during discharge in thin frozen deuterium fiber. Electron degeneracy was accounted for in the pressure. But the resistivity was taken (Spitzer resistivity) as purly classical – no anomalus resistivity. Moreover, transition of bremstrahlung spectrum from thin to thick during collapse was present in the computations. The computed total yield of X-ray radiation under 10^{18} line density was stated as equal to about 60-80 kJ with energies of about 3 keV during radiative collapse. The current was maximally equal to 1 MA and constant until radiative compression and the minimum pinch radius during discharge of about 10^{-5} meter was acquired. The simulated discharges were characterized by relatively long implosion time, which gave rise to a slower heating and compression of plasma. Robson commented that higher plasma temperatures and consequently more high-energy photons is acheived with discharges in deuterium than in the same discharges in higher Z materials. Although, plasma during discharges in higher *Z* material begins to radiativly collapse earlier since high *Z* plasma emits more efficiently X-ray radiation. Furthermore, discharges at given line density and external power source parameters were not very sensitive to the initial temperature and density of the fiber. The changes of the line density resulted in significant changes of the profile of the radiation spectrum but not of the total emitted radiation. Ultimately, the results were based on the assumption of stable plasma compression (Bennet equilibrium conditions) throughout entire plasma pinch evolution (as was during simulations of Haines and Robson).

The computations performed by Haines, Robson and Thornhill included some unrealistic conditions and differed from results achieved by Vikhrev. In fact, there was a non-physical result present in these computations – drift velocity of particles at the border of the pinch was increasing to infinity (assuming constant current density). In order, to get rid of this effect Robson made the assumption that anomalous plasma resistivity modifies the plasma density and current profiles in such a way that the drift velocity is everywhere smaller than the characteristic velocity of sound [Robson 1989b], [Robson 1991], [Stepniewski 1995]. Introducing this assumption into his code Robson created an averaged code. Results achieved from this code showed that P-B current value is higher than the previously calculated classical value and it is dependent on plasma particles line density. To achieve plasma radiative compression threshold value of constant current growth had to be also exceeded. Hence, the value of *dI/dt* increased with decreasing of plasma linear concentration [Robson 1991], [Stepniewski 1995].

The effect of plasma radiative compression was also modeled by J. P. Chittenden et al. and it was dedicated mostly to frozen deuterium fibers. The computations were based on 1-dimensional MHD equations coupled with the equation of equivalent electric circuit of the z-pinch device [Chittenden 1989], [Chittenden 1990], [Stepniewski 1995]. This model enabled tracing of pinch evolution from early cryogenic stadium up to degeneration of electron states and ion component becoming strongly non-ideal. A number of atomic and plasma effects were included in the model but the anomalous plasma heating was not included. Presented results suggested that increase of inductance alone does not stop the compression. The compression is stopped because of increase in plasma optical density and internal plasma pressure. For the lower linear initial concentration (smaller radius of fiber) compression is faster but the maximum compression state is shorter. Increasing length of fiber increases plasma pinch inductance and makes it more difficult to reach P-B current value but ultimately it leads to higher compression (bigger concentration of particles). Best compression parameters achieved using this model is: about 10^{-6} cm of minimum pinch radius and up to 10^{27} particles per cubic cm [Chittenden 1989], [Chittenden 1990], [Stepniewski 1995].

2.3.11. Modeling of plasma radiative compression – Bernal and Bruzonne

In 2003 also I. Bernal and H. Bruzonne published an article [Bernal 2002] in which the problem of radiative collapse with axial mass losses was approached one more time theoretically. Their approach was based on using 1/2-dimensionall numerical model with pure bremsstrahlung as the source of radiation including, anomalous resistivity and axial mass losses. The results showed both upper and lower limit value of the pinch current for plasma radiative collapse occurrence. The authors also stated that there is a minimum initial pinch radius required (which depends on the initial particle density) to obtain radiative compression. Moreover, authors stated that the axial mass losses make it more difficult for radiative collapse to occur because they enhance anomalous resistivity heating.

2.3.12. Experiments in linear z-pinch by Bogomaz

In 2008 A. A. Bogomaz et al. in [Bogomaz 2008] article stated the attainment of Pease-Braginskii current in an ultra high pressure discharge. The experiments were performed using deuterium and helium at current amplitudes of 0.5 MA to 1.6 MA and 5 MPa to 35 MPa of pressure. Linear z-pinch configuration was used and streak camera for pinch imaging. Contraction of the current channel was observed and was explained as result of exceeding of Pease–Braginskii critical current. Bogomaz also stated that theoretical value of the P-B current for discharges in vacuum is about 100–200 kA. The increase in the critical current to about 1 MA for given experiments is attributed to the absorption of channel radiation in the dense ambient gas (hydrogen and helium) as well as by an increase in the number of metal ions per unit length of the discharge channel. Moreover, the presence of a dense gas shell around the discharge channel was stated as well as formation of high-temperature zones. The mechanism responsible for the formation of these zones was to be similar to that responsible for the generation of hot-spots in vacuum discharges.

2.3.13. Modeling and experiments of plasma radiative compression – Lee, Akel and Saw

In 2013 S. Lee and M. Akel started their theoretical investigations of plasma radiative compression using newly developed 0/1-dimensional 5-phase Lee model code which simulates discharges in plasma-focus systems. In the published articles in 2013 [Lee 2013] [Akel 2013] authors described conditions during radiative compression in plasma-focus systems operated with argon, krypton and xenon. It was stated that in pure hydrogen or deuterium pinch the radiation-cooled threshold current is about 1.6 MA. However, when discharges are performed in gases undergoing line radiation strongly the radiation-cooled threshold current is considerably lowered. Authors showed that equations used in Lee model code can be used to approximately compute this lowering and to show the effect of radiation cooling leading to radiative collapse. Numerical experiments based on previously experimentally fitted model parameters were carried out and demonstrated that during plasma-focus discharges in Ar, Kr and Xe radiative collapse of column can be observed while pinch current is equal to about 50-100 kA only.

In 2016 Akel et al. publish experimental results concerning plasma radiative compression in plasma-focus PF-1000 device operated with D_2, He, Ne and mixtures of D_2 and Ne [Akel 2016b]. The results of the experiments presented some measured values of plasma pinch radius acquired through means of laser interferometery for 18 discharges in total. The measured values of minimum pinch radius were also computed using Lee model code. For discharges in Ne plasma radiative compression was stated. However, no reconstructed images from interferometer or information about contraction was given – did the entire column contracted or just the micro-pinch appeared. Moreover, the computed results using the code were partially in agreement with the measurements – the computed values of plasma pinch radius were usually bigger than measured.

Additionally, three more articles concerning theoretical and experimental studies of plasma radiative collapse in PF-1000 device as well as in PF400 and INTI PF were published in 2016 by Lee [Lee 2016], Akel [Akel 2016a] and S. H. Saw [Saw 2016]. In the first article [Lee 2016] results of numerical experiments carried out using the Lee model code operated as PF-1000 facility were presented. The computations included theoretical discharges in PF-1000 in D_2, He, Ne, Ar, Kr and Xe. The characteristic time of radiation depletion was defined and used as an indicator for the expectation of radiative collapse together with the reduced P-B current. The simulation indicated that during discharges in D_2 and He the radiation powers were small resulting in such long depletion times that no radiative collapse may be expected in the lifetime of the focus pinch. On the other hand, during discharges in Ne significantly more radiation is emitted in form of line and recombination radiation (bigger total power of radiation emission) resulting in relatively small but visible radiative radiative compression. Moreover, for discharges in Ar, Kr and Xe the characteristic time of radiation depletion was only but a small fraction of the estimated pinch duration in pressure balance. Thus, strong radiative collapse was anticipated for PF-1000 operated using these gases. Furthermore, in performed computations radiative collapse was stopped mainly because of plasma self-absorption. Authors also mentioned that the code enables only contraction of the entire plasma column without any breakups or existence of hot-spots which was observed in different previous experiments. Such breakups may lead to localized enhanced compression and may tend to make it easier for radiative collapse to occur (locally).

In the second article [Akel 2016], Akel investigated theoretically using Lee model code effects of power terms and thermodynamics on the contraction of plasma pinch in different plasma-focus devices (PF-1000, PF400 and INTI PF) operating at different bank energies. The power terms included Joule heating and X-ray bremsstrahlung, line and recombination radiation emission. The simulations were carried out for different filling gases – N_2, O_2, Ne, Ar, Kr and Xe. Results showed that plasma radiation losses enhance the contraction of plasma pinch within suitable pressure ranges characteristic for each machine and for each working gas discussed in the article. The radiation enhancement of compression increases with the atomic number of gas. And by comparing the radius ratio versus pressure curves in each gas for each of the three devices, it is noticed that the operational, geometrical and electrical parameters of the devices have an important role in determining the degree of radiative compression and the operational regimes.

In the third article by Saw [Saw 2016], comparison of computed and measured current traces was performed. However, no information was given on the number of discharges which were actually compared. The article reports that good match between computed and measured current traces were achieved in the important part of current waveforms. The article also confirms the computed values of the P-B current and the reduced P-B current for different gases (D_2, He, Ar, Kr, Xe) – similar as in other publish articles of Lee and Akel. But the experiments were actually carried out only in Kr in the small energy bank PF machine (INTI PF). The so called cut-off radius effect was successfully removed from the Lee model code in the presented results of computations. The final results show radiative compression of Kr plasma up to a minimum of 0.0013 cm in radius and 3.7×10^{26} m^{-3} in ion number density.

Summarizing section 2.3, many different simulations and modeling were performed during past 43 years of research for different z-pinch systems and working gases (or thin frozen fibers). The used models were developed by different authors and often included different effects introduced over the decades of research. Also, different indicators and parameters of plasma radiative compression were investigated over the decades of research like: the P-B current, the reduced P-B current, the maximum discharge current during plasma radiative compression, the minimum discharge current during radiative compression, the pinch current, the shell current, the value of constant current increase with time, the characteristic bremstrahlung radiation emission yield and spectrum, the characteristic radiation depletion time, the characteristic compression time, the characteristic pinch lifetime, the characteristic time of MHD instabilities development, the initial linear plasma density, initial volumetric plasma density, initial plasma pinch radius and initial pinch length. Most of performed computations concerning plasma radiative compression were performed using 0/1-dimensional computer codes. Some of the computations predicted the plasma radiative compression effect occurrence (especially for micro-pinch discharges) while other did not. The results of computations based on 0/1-dimensional Vikharev and Koshelev codes simulating micro-pinch discharges appear to give one of the most compatible results with the experimental results so far (perhaps the most compatible of all). Presently, results of computations based on modern models, which appear to include most of important effects, often predict occurrence of plasma radiative compression in z-pinch systems (when high Z working gases are used). For example the 0/1-dimensional Lee model code, which simulates discharges in plasma-focus devices, predicts the possibility of occurrence of strong plasma radiative compression phenomenon. In general, the achieved experimental results are even more contradictory as well as insufficient in number and presented data – inconclusive. Thus, the question about plasma radiative compression phenomenon occurrence and conditions achieved during z-pinch discharges is still open and needs further investigation.

3. Fusion neutron emission from z-pinch and plasma-focus devices

In the 1950s, the concept of nuclear fusion reactor based on z-pinch type of devices was strongly investigated. Since then, general interest in fusion neutron production and emission from z-pinch became very high [Velikovich 2007] [Sadowski 2012]. The most often investigated reaction in z-pinch has been nuclear fusion of deuterium nuclei. The main branches of this reaction are following [Sadowski 2005]:

$$^{2}\mathrm{D} + {}^{2}\mathrm{D} \rightarrow {}^{3}\mathrm{T}\ (3.02\ \mathrm{MeV}) + \mathrm{p}\ (1.01\ \mathrm{MeV}) + 4.03\ \mathrm{MeV},$$

$$^{2}\mathrm{D} + {}^{2}\mathrm{D} \rightarrow {}^{3}\mathrm{He}\ (0.82\ \mathrm{MeV}) + \mathrm{n}\ (2.45\ \mathrm{MeV}) + 3.27\ \mathrm{MeV},$$

In the above reactions, ^{2}D is deuterium nucleus, ^{3}T is tritium nucleus, ^{3}He is helium-3 nucleus, p is proton and n is fast neutron. The probability of occurrence of each reaction branch is equal. In order to perform this type of fusion reaction deuterium nuclei need to have kinetic energies high enough in order not to be repelled by the Coulomb repulsion forces. The two general mechanism of fusion (neutron production) are beam-target and thermonuclear. In z-pinch devices both of these mechanisms appear to be possible and present. In plasma-focus discharges usually the beam-target mechanism is stated to be the dominating one (responsible for production and emission of most of fusion neutrons during discharge) and different models and possibilities of ion acceleration have been studied [Bernstein 1970], [Jager 1987], [Bernard 1998], [Scholz 2006], [Schmidt 2006], [Gribkov 2007], [Kubes 2010], [Kubes 2019a], [Kubes 2019b]. However, in general to this day there is no agreement in which mechanism is actually the dominating one in the z-pinch and under what conditions of discharge which mechanism should become the dominating one [Anderson 1958], [Bernstein 1970], [Velikovich 2007], [Klir 2018], [Zhang 2019]. This problem is important since it determines the conditions/parameters of plasma which must be obtained during the discharge in order to perform controlled nuclear/thermonuclear fusion more efficiently and possibly create a fusion power reactor based on a z-pinch device – total neutron yield has been stated to be one of the main indicators of performance of plasma fusion devices.

3.1. Fusion neutron emission from z-pinch discharges in D_2

Among many facts concerning fusion neutron production and emission in z-pinch devices, which have been determined during decades of research, one of the most important is the change of dependency of total D-D fusion neutron emission with initial deuterium pressure and existence of maximum [Anderson 1958], [Rapp 1973], [Jager 1987], [Lee 2009], [Abdou 2012]. These types of dependencies are presented in Figure 3.1.1 and 3.1.2 as an example.

The effect presented in figure 3.1.1 and 3.1.2 has been observed in many different z-pinch devices during different experiments and is still reported [Anderson 1958], [Rapp 1973], [Jager 1987], [Lee 2009], [Abdou 2012]. Also, the author of this thesis presented similar experimental results in the article [Marciniak 2018]. Wherein, in the results presented in [Marciniak 2018] sudden drop of the average D-D fusion total neutron yield was observed for higher initial deuterium pressure – see subsection 8.7.2. This suggested rather the change of character of neutron production and/or it may be connected with higher compression due to shift of the plasma column structure into the hole at the center of the anode for most of discharges for lower initial pressures than 3.0 mbar (see subsection 8.7.2).

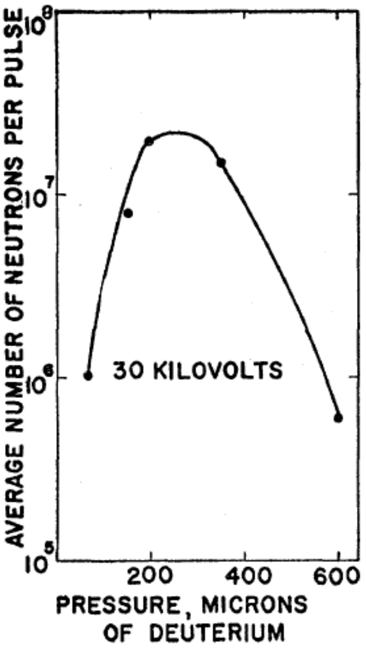

Figure 3.1.1. Average total D-D neutron yield versus initial deuterium pressure during discharges in linear z-pinch operated with 30 kV of charging voltage [Anderson 1958].

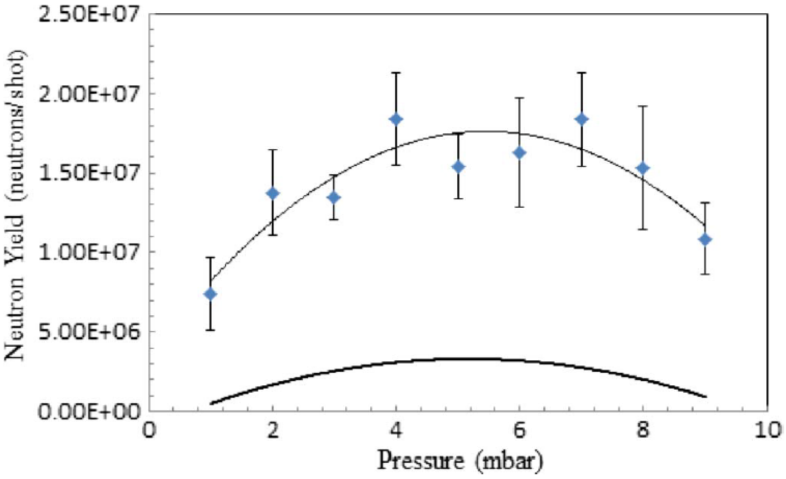

Figure 3.1.2. Total D-D neutron yield dependence on initial deuterium pressure for discharges in KSU plasma-focus [Abdou 2012].

In general, the effect presented in figure 3.1.1 and 3.1.2 is still not fully investigated and understood – change of the dependency and reasons for decrease of average total neutron yield during discharge under higher initial D_2 pressures. Regardless of what is the precise mechanism, it appears that there is always some optimum initial deuterium pressure and connected transfer of kinetic and magnetic energy from dynamic plasma structure into the plasma column resulting in optimum parameters/conditions for D-D fusion neutron production and emission. For example, in the Mather type of plasma-focus devices after the break-down and build up of plasma sheet the magnetic piston moves along the anode ionizing and sweeping the neutral gas in front (see subsection 2.2.2) similar to a snow plough. The velocity of magnetic piston according to the snow-plough model [Anderson 1958], [Gross 1971], [Potter 1971], [Liberman 1999] [Scholz 2004] (see subsection 2.2.2) is determined by the total mass or density of gas between and in fron of electrodes. So, the higher pressures of given gas type inside the experimental chamber lead in general to slower sheet-shock structure movement. Moreover, during single discharge under given initial total gas pressure the magnetic piston is acclearated along anode due to Ampere's force (back electromotive force working on the magnetic piston). This accleration process along anode is stated for smaller and optimum initial pressures of given working gas like deuterium (and under other constant operation parameters of the PF device). However, if the pressure of a given working gas is increased above some optimum value then the magnetic piston accleration along anode will not occure to full extent. This means, that the magnetic piston will be acclerated along a part of anode's length but at some point it will again start to slow down (under given operation conditions of the PF device). This is belived to be the effect of too high mass inside the sheet-shock structure and in front of it – the back electromotive forces (EMF) are unable to accelerate the piston to higher velocities. During this process also the percentage of mass sweeping by the magnetic piston and amount of mass left behind the structure may change. The changes of magnetic piston velocity influences the plasma (discharge tube) inductance – higher velocity leads to higher values of plasma inductance. And the increase of plasma inductance leads to decrease of discharge current. This is why the maximum discharge current values increases with increase of initial working gas pressure under given operation conditions of the device (assuming the device is operating below optimum or at the optimum pressure). Summarizing, there is some optimum initial working gas pressure for which the magnetic piston accelerates along entire length of anode resulting in highest maximum current during discharge (achived at the end of run-down phase) and connected optimum transfer of kinetic and magnetic energy into plasma pinch. If the working gas is deuterium then this optimum transfer will result in the highest total fusion neutron emission on average. Also, for the discharges with optimum mass (density) between and in fron of the electrodes the sharp and narrow jump of discharge current derivative over time and voltage during the radial compression phase appears suggesting good plasma compression and confiment (well pinched plasma). And this again should result in optimum transfer of kinetic and magnetic energy into plasma pinch and optimum values of all parameters describing neutron emission like: maximum pinch plasma current, maximum pinch ion temperature, maximum pinch ion density, minimum pinch radius, maximum pinch length, etc, in reference to the highest average D-D fusion total neutron yield. In the graph below three exemplary measured discharge current traces and corresponding three measured discharge current derivative over time traces are presented – each set of I and dI/dt is ploted for given discharge under given initial deuterium pressure while the rest of operation parameters of PF device are kept constant.

The three presented discharges – #17060101, #17052303 and #17063019 – in figure 3.1.3 were carried in the PF-24 device (see section 5.1) under given constant operation parameters. Theoreticaly the only parameter which changed during discharges was the initial deuterium pressure p_0 (in practice also L_0 and R_0 appear to have changed insignificantly – see section 7.2). The optimum pressure for the PF-24 device was stated as about 3 mbar (about 0.4 mg of D_2 between electrodes) – see subsection 8.7.2 (under given operation parameters). The total neutron yield per discharge (Y_n) values were determined using beryllium activation counter (see section 5.2). For the discharge #17052303 in 3.00(±0.01) mbar of initial D_2 pressure the highest value of $Y_n = 9.5(\pm 0.2) \times 10^9$ n/discharge was stated in comparison to the discharges #17060101 and #17063019. Also, for the discharge #17052303 the highest maximum discharge current and the smallest discharge current derivative over time minimum was registered (“sharpest” dI/dt jump) in comparison to discharges #17060101 and #17063019. The maximum current value for discharge #17060101 and #17052303 is achieved approximately just before current drop (at end of axial phase and at end of electrodes – see section and subsections 2.2.2., 5.3, 6.4.1 and 6.4.2) while for the discharge #17063019 the maximum current value is achieved earlier, after about 1.48 μs.

Furthermore, because of this effect presented in figure 3.1.1, 3.1.2 as well as 3.1.3, PF devices which have optimized operation parameters (primarily anode length inside the experimental chamber, charging voltage and total capacitance of battery) and operate under optimum initial deuterium pressure and mass/density inside the experimental chamber (assuming constant operation parameters) in reference to the highest average total D-D neutron emission are known as “neutron-optimized” or simply “optimized”.

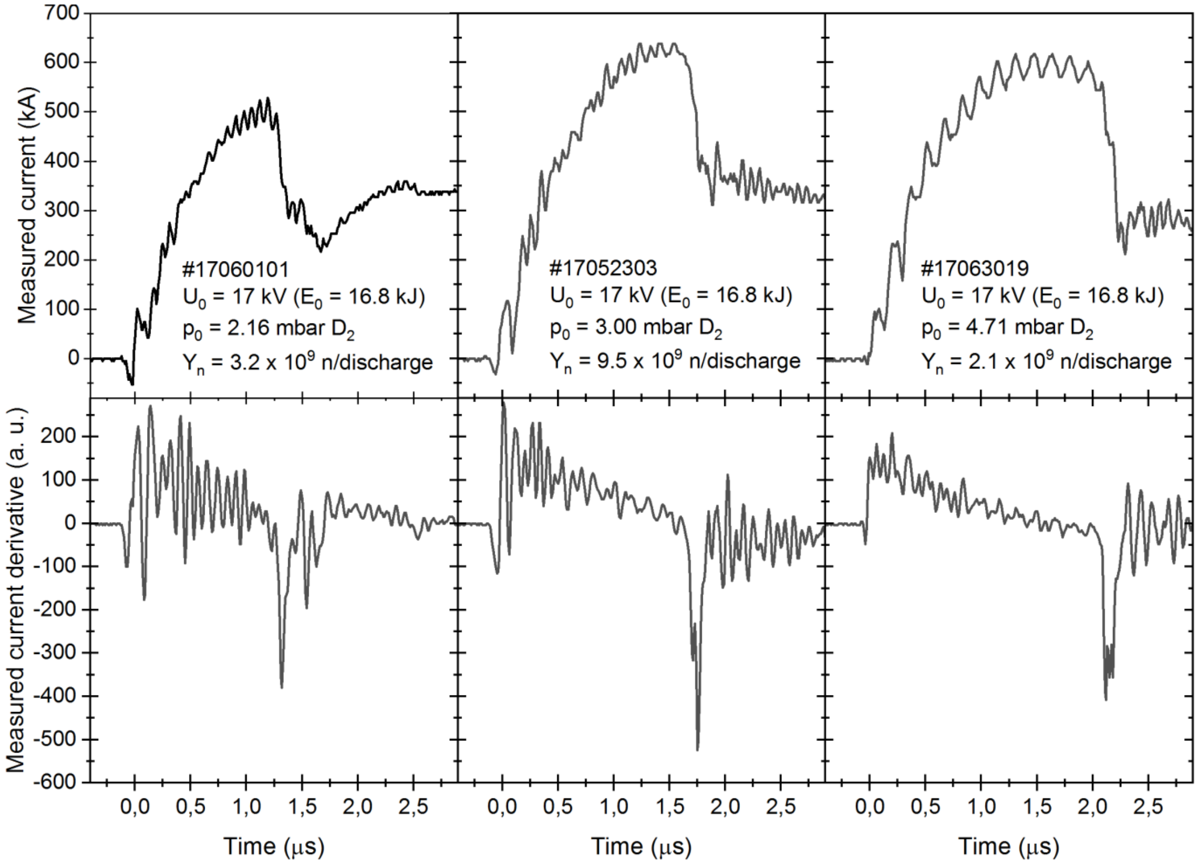

Figure 3.1.3. Measured discharge current (*I*) and discharge current derivative over time (*dI/dt*) for discharges: #17060101, #17052303 and #17063019. The discharge #17052303 was carried under 3.00(±0.01) mbar which was stated as the optimum deuterium pressure under given operation parameters of the PF-24 device.

3.2. Fusion neutron emission from plasma-focus discharges in gas mixtures

Fusion neutron emission from z-pinch devices has been also studied during discharges in gas mixtures with deuterium (usually under constant initial total gas pressure or constant initial total mass). The results of investigations of plasma-focus discharges in mixtures of deuterium with noble gas appear to have given some contradictory and questionable results. In part of carried experiments the decrease of the average total neutron yield with noble gas fraction (or pressure) was stated. On the other hand, in other experiments increase in the average total neutron yield values was stated when the noble gas fraction was increased in reference to the deuterium. The increase of the average total neutron yield with noble gas fraction is rather questionable effect since it is believed that only the deuterium ions are fully ionized and have enough kinetic energy to be the fuel for nuclear fusion. So, simultaneous increase of the amount of noble gas and decrease of the amount of deuterium (for example under constant total pressure of gas mixture) should rather result in smaller average total neutron yield values since the amount of fusion fuel decreases. However, there are other possibilities/concepts showing how the simultaneous decrease in fraction of deuterium and increase in fraction of noble gas can increase the average total neutron yield. Below discussion with a list of important results is given.

The influence of the gas mixture ratios on the structure of pinches [Bayley 1991], [Antsiferov 1995], plasma density [Brzosko 1991], stabilized pinch column effects

[Kies 1998], [Kies 2000] has been investigated and discussed. Moreover, experiments on the 3.3 kJ plasma-focus device operated with deuterium and deuterium-argon admixtures revealed an enhancement of the neutron yield by more than 80% as compared to pure deuterium discharges when the deuterium filling gas is doped with 30% to 40% of argon by mass [Yap 2005]. The presence of small amounts of high *Z* gas in the deuterium discharge may induce the radiative collapse phenomena, resulting in the stronger pinching action. A good compression and tighter pinch would lead to an effective increase in the interaction time between the energetic ions and the hot plasma. The onset of instabilities and formation of local necking in the plasma column after the focus phase can cause a severe disruption and further enhances the acceleration of the deuteron beam [Gribkov 2007]. The maximum neutron yield was achieved with 3% krypton seeding on the 90 kJ Filippov device and it was found an order of magnitude increase in neutron yield with krypton admixtures [Mohammadi 2011]. The results of the experiments on the Dena PF have shown that the use of admixture gas can increase the numbers of neutron productions [Talaei 2010]. The registered increment was three times the value without the added particles for 1% of krypton. It was postulated that by controlling the velocity of added particles one can increase the current and decrease the plasma confinement time. It was further postulated that the neutron production depends strongly on the pinch plasma current and weakly on the confinement time [Gribkov 2007], [Lee 2008a]. Rossel and Choi [Aliaga-Rossel 1998] used the DPF-78 device (60 kV, 28 kJ) with different admixtures of noble gases (Ne, Ar or Kr with D_2) and found a reduction in neutron yield for all admixture ratios. They also observed an increase in the neutron emission anisotropy and changes in the pinching phase according to the atomic number of doping. Furthermore, no correlation was observed between the total neutron yield and the appearance of hot spots. For sub-kJ plasma-focus devices, the neutron yield appears to be strongly consolidated compared to pure deuterium operation. Verma et al. [Verma 2008] concluded that the addition of krypton gas resulted in higher radiation emission, tighter compression and therefore a smaller final pinch radius. The higher plasma density in the radiatively-collapsed pinched column for deuterium–krypton admixture operation leads to neutron yield enhancement. For the 200 J FMPF-1 device, they reported a maximum of 30-fold increase. For a 500 J PF device, it was found an increase of 5-fold and 8-fold for neon and argon doping respectively [Bures 2009] and 3.6-fold on argon and krypton doping [Bures 2010]. On the other hand, another carefully designed experiment showed no such enhancement. A sub-kilo-Joule plasma-focus device (FMPF-3, 14 kV/235 J) was operated with deuterium–krypton admixtures (of 1%, 2% and 5% Kr by volume) to study the influence of the admixture ratio on the neutron yield. Experiments were performed for different insulator sleeve lengths and cathode geometries. The results revealed that for carefully optimized electrode geometry the highest average neutron yield is obtained with pure deuterium as the operating gas, whereas krypton seeding leads to a reduction in the neutron yield. Talebitaher et al. [Talebitaher 2016] argue that the electrode geometry and electrical coupling play critical roles in determining the influence of gas admixtures; and that for an optimized plasma-focus device D_2+Kr admixtures may give little or no neutron yield enhancement relative to pure D_2 operation and so the admixture operation is an evaluation methodology to determine the level of optimization of device geometry. One possible mechanism for enhancement is that the krypton seeding could enhance the density of the pinch, by making the pinch more compressible by the dual effect of radiative cooling [Lee 2013] and specific heat ratio [Talebitaher 2016]. Since, the krypton ions are not fully ionized they contribute an inordinate proportion to the thermodynamic degree of freedom of the ensemble, which reduces the SHR of the mixture to significantly less than 5/3 of pure deuterium case [Lee 1983], [Lee 2013], [Saw 2014]. This increases the compressibility of the krypton-doped deuterium. Furthermore, the presented results by Veloso et. al. [Veloso 2014] on 400 J plasma-focus showed that the argon doping on deuterium discharges reduces the breakdown voltage needed to originate the initial plasma sheet over the insulator surface. These obtained results are independent on the mixed gas pressure and the load mass density. They also illustrated that the average axial velocities of the plasma sheet and its geometrical shape and curvature remain nearly constant, which point out that the global dynamics of the discharge remains invariable with the argon doping; but the energy of the plasma components alters. This difference can be possibly related to the differences on the final neutron emission of such configurations. Besides, summary of the neutron yield variations emitted from the plasma-focus operated with different admixtures of gases (He, Ne, Ar or Kr with D_2) was also displayed [Veloso 2014].

Summarizing, it is possible that the radiative compression phenomenon can cause an increase in the average total neutron yield (in reference to the discharges in pure deuterium) because of the significant increase in the ion number density of deterium and decrease in the plasma pinch radius. Wherein, some researchers anticipate this effect for the non-optimized devices since for these devices the initial total mass of gas mixture between the electrodes is not optimum for the transfer of kinetic and magnetic energy into plasma pinch during discharges in pure D_2. However, under higher doping (assuming constant operation parameters of the device) the total mass can become again optimal since the Ar ions are about 20 times heavier than D ions – systematic decrease of D_2 fraction and increase of Ar fraction under the same pressure increases the total mass in experimental chamber and between electrodes. Thus, when the optimum total mass of gas mixture is used the kinetic and magnetic energy transfer to the plasma pinch should be optimum and the plasma may be better compressed and confined resulting in possibly higher total X-ray emission which is especially important to radiative compression. Still, it is not clear whether discharges in optimum or non-optimum deuterium pressure should cause increase in $<Y_n>$ as well as should they be performed under constant total pressure of mixture or not (under constant total pressure of gas mixture the amount of deuterium decreases with doping of noble gas). Moreover, the doping with noble gas should change the specific heat ratio of the plasma possible making it more compressible (easier to compress). In addition, the stability and interaction time between plasma and beam of fast ions may increase when deuterium is doped with noble gases, which should also influence the neutron emission.

4. Aims of the thesis

After decades of research the behaviour of electron-ion plasma during z-pinch type of electric discharges is still not fully understandable. One of the interesting topics which still needs further investigation is the compression of plasma during discharges in pure noble gases and in mixtures of noble gases with light gas like deuterium. During discharges in such gases or gas mixtures the so called plasma radiative compression phenomenon, described in the chapter 2 of this work, may occur under appropriate conditions [Shearer 1976], [Stepniewski 1995], [Liberman 1999], [Haines 2011], [Lee 2016]. Another interesting topic is the total emission of neutrons from the fusion of deuterium nuclei from the PF devices operated with gas mixtures. Few authors stated the increase of the total average neutron emission when deuterium was doped with different noble gases under constant total pressure or constant total mass of mixture [Yap 2005] [Verma 2008] [Bures 2009] [Bures 2010] [Veloso 2014] [Talebitaher 2016] – described in the chapter 3 of this work. The explanation of this may be connected with the occurrence of the plasma radiative compression phenomenon. Thus, the author formulates the following thesis: **plasma radiative compression phenomenon can occure during discharges in the plasma-focus PF-24 device operated with high *Z* gas and mixtures of deuterium with high *Z* gas**. This thesis assumes the four following aims:

1) Validation of the occurrence of the plasma radiative compression phenomenon in the plasma-focus PF-24 device (presented in the chapter 5) through determination of the approximated plasma parameters achieved during discharges in the PF-24 – the achieved minimum plasma pinch radius, the total change in plasma pinch radius, the highest plasma pinch density, the total change in plasma pinch density, etc (assuming plasma pinch in a form of a cylinder in the dynamic pressure balance).
2) Determination of the indicators and parameters needed for the occurrence of the strong plasma radiative compression phenomenon. This includes answering the question: are the P-B current, the reduced P-B current, the current flowing through plasma pinch, the characteristic time of radiation depletion, the radiative compression lifetime and the pinch lifetime sufficient to make accurate predictions concerning relatively strong plasma radiative compression occurrence (in reference to discharges without plasma radiative compression occurrence – presumably discharges in pure D_2)? And also answering the question: are there other parameters which play an important role in determining the occurrence and strength of the plasma radiative compression phenomenon?
3) Verification if some increase in the average total neutron yield is observed when D_2 is doped with Ar under constant total pressure of D_2+Ar gas mixture. This assumes also showing how much influence on the emission of D-D fusion neutrons has the doping with argon and the radiative compression phenomenon.
4) Making an attempt of validation of the results acquired using the 5-phase Lee model code. This includes answering the question: can the results of the study of the plasma radiative compression phenomenon based on the theoretical and computed discharges performed using the 5-phase Lee model code be able to describe well enough the real conditions achieved during the discharges in the PF-24 device? This aim is important because the results of plasma radiative compression investigation presented in this work are based on the so called 5-phase Lee model code.

5. Experimental setup and experimental plasma parameters

5.1. Plasma-focus PF-24 device

All experimental results presented in this work were obtained using plasma-focus PF-24 device operating in the Institute of Nuclear Physics Polisch Academy of Sciences in Cracow in Poland [Marciniak 2016] – see figure 5.1.1. The device was constructed in 2013 and upgraded in the following years.

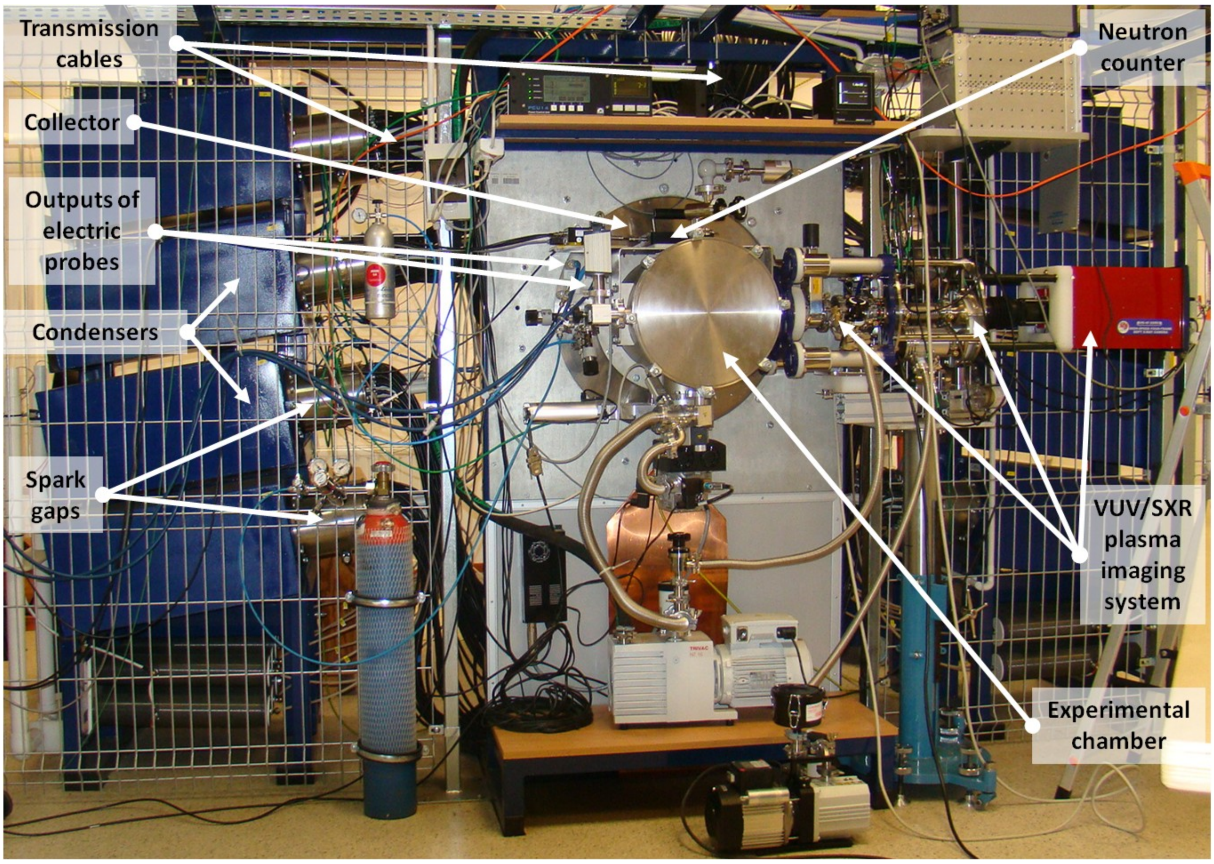

Figure 5.1.1. The front view of the plasma-focus PF-24 device in the laboratory hall in the Institute of Nuclear Physics Polish Academy of Sciences in Cracow in Poland.

5.1.1. Condensers and spark-gaps

The condenser bank of the PF-24 consists of 24 pulse condensers type IK-5/40 connected parallel. Each condenser in connected through a single spark-gap with the anode plate (see figure 5.1.1 and 5.1.2). The total capacitance of the condenser bank ($\boldsymbol{C_0}$) is equal to **116.12 μF** and it can be charged with voltage ($\boldsymbol{U_0}$) from 16 kV to 40 kV. Thus, the total energy that can be stored in the bank (E_0) is in the range of about 15 kJ to 93 kJ [Marciniak 2016]. The inductance of the single condenser was determined as 40 nH. Hence, the resultant total inductance of the bank L_b = 40 nH/24 = 1.67 nH.

The spark-gap of the field distortion [Hussain 2007] IFD-40 type was developed and integrated with the condenser IK-5/40. The integration involves the use of a condenser construction as a spark-gap component. This idea is shown in figure 5.1.1. The brass rods of the shape shown in figure 5.1.2 were used as the electrodes of the spark-gaps. The steering electrode (trigger electrode) made of cooper wire was placed at 1/3 of the distance from the upper electrode. This type of integrated construction of condensers and spark-gaps should ensure approximately simultanious energy release from all condensers in bank with jitter up to about 50 ns.

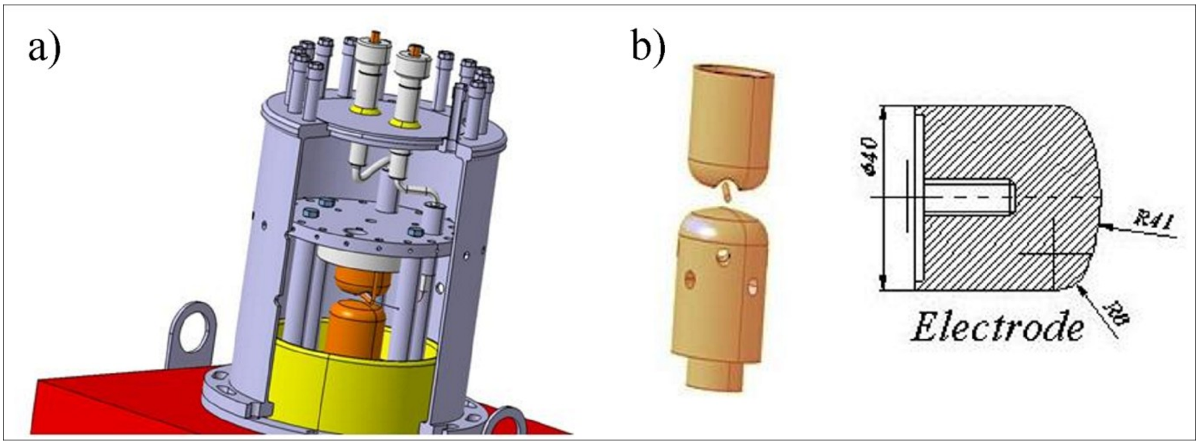

Figure 5.1.2. a) Projection of the three-dimensional model illustrating connection of the spark-gap IFD-40. **b)** Projection of the three-dimensional model and diagram showing profile of the electrodes used for construction of the three-electrode spark-gap IFD-40.

The spark-gap is a closed construction, able to work with gas pressure up to 1.6 bar. The breakdown voltage dependence on the pressure has a linear character – for example at the pressure of 0.2 bar and 1.2 bar the breakdown voltage is equal to about: 24 kV and 34 kV, respectively. Presently, the 0.11 bar of atmospheric dried pressure is used and 23 kV. The inductance of single spark gap was determined as 30 nH. Hence, the resultant inductance of all spark gaps L_s = 30 nH/24 = 1.25 nH.

5.1.2. Transmission cables and collector

The connection of the condensers and spak-gaps with the collector (see figure 5.1.1 and 5.1.3) is made by 3.5 m long coaxial wire (type RG 213/U – 2.25/7.25). In order to reduce the transmission path inductance, each of the condensers is connected with 18 cables grouped in the three modules, six cables each. The inductance of each single cable is determined as 875 nH. Hence, the resultant inductance of all transmission lines (single connection path) achieved L_t = 875 nH/(18 × 24) = 2.03 nH.

The schematic diagram of the collector, the vacuum chamber and the electrodes of the PF-24 plasma focus device is presented in figure 5.1.3. The collector is built with two parallel stainless steel plates, separated by an isolator. The first plate has the same electric potential as the anode and the second plate has the same electric potential as the cathode (common ground). The inductance of the collector L_c = 2.52 nH.

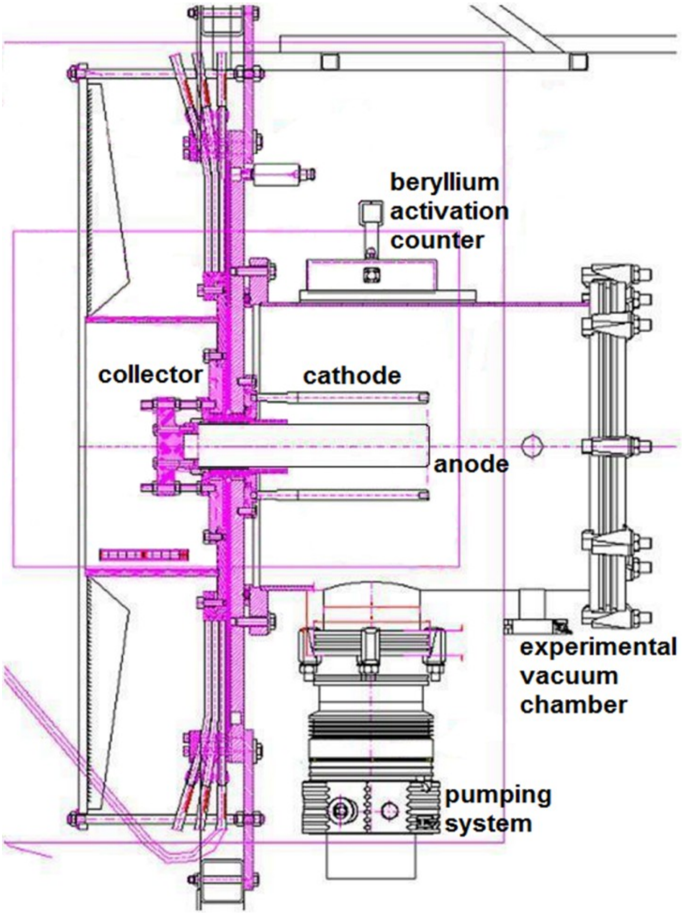

Figure 5.1.3. The scheme of system of the collector, the vacuum chamber and the electrodes of the PF-24 device (side view).

5.1.3. Experimental chamber with electrodes

The experimental chamber is a stainless steel vacuum vessel (see figure 5.1.1, 5.1.3 and 5.1.4) 40 cm long and 32 cm in diameter. The pumping system ensures a high vacuum in the chamber at the level of 10^{-6} mbar.

The PF-24 device has Mather type of electrode layout inside the vacuum chamber – see figure 5.1.4. The anode (inner electrode) is made of one single solid anaerobic copper rod placed in the center of the chamber. The rod is 25 cm long and **3.1 cm** in radius (***a_0***). Wherein, the effective length of the anode inside the chamber is equal to about **17 cm** (***z_0***). The cathode (outer electrode) is made of 16 stainless steel rods placed uniformly on the circumference of the circle. The radius of the circle is 5.5 cm and each rod has a diameter of 1.2 cm and length of 17.4 cm (the effective length inside the chamber is about 17 cm). The cathode radius minus the radius of single cathode rod is called the reduced cathode radius (***b_0***) and is equal to **4.9 cm**. The anode and the cathode are separated using Al_2O_3 ceramic isolator in form of a ring placed on the anode next to the collector (back wall of the experimental chamber) – see figure 5.1.3 and 5.1.4. The isolator is 6 cm long (about 4 cm of length inside the chamber) and about 0.4 cm thick. The inductance of the isolator covered with thin current sheet is established as $L_{is} = 1.20$ nH.

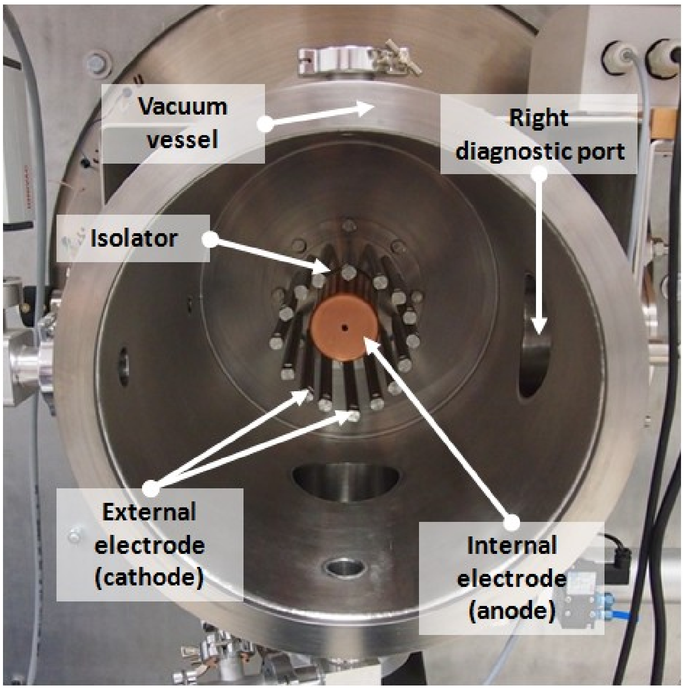

Figure 5.1.4. The open experimental chamber of the plasma-focus PF-24 device.

5.1.4. Total static inductance and resistance

The nominal, total, static inductance of PF-24 device L_0^{mea} can be considered as the sum of L_b, L_s, L_t, L_c and L_{is}. Thus, the $\boldsymbol{L_0^{mea}}$ = **8.66 nH**. This result was confirmed with the short-circuit tests connected with damped RLC circuit calculations (see subsection 2.2.3) [Mather 1971], [Bernard 1998], [Karimi 2017]. The short-circuit tests were carried out with 16 kV of charging voltage and D_2 pressure from 20 mbar to 25 mbar. The calculations based on short-circuit tests gave in the idealized case (simultaneous release of entire energy from all condensers and discharge in one current channel) the value of the nominal, total, static inductance $\boldsymbol{L_0^{mea}}$ = **8.5(±3.1) nH** and the nominal, total, static resistance $\boldsymbol{R_0^{mea}}$ = **3.1(±2.3) mΩ** for the PF-24 [Krol 2015]. Thus, for 17 kV of charging voltage, the quarter period time ($t_{1/4}$) should be equal to about 1.4 μs and short circuit-current ($I_{S\text{-}C}$) should be about 1.5 MA.

5.2. Neutron counter and total neutron yield

The phenomena accompanying plasma compression can be studied using fusion neutrons emitted from the plasma. A neutron activation counter consisting of a beryllium plate was used to measure a total yield of fast neutrons (Y_n^{mea}) emitted during a single discharge [Bienkowska 2014]. The device registers characteristic 2.45 MeV neutrons from D-D nuclear fusion emitted from the experimental chamber of the PF-24 device. The counter operation bases on the following nuclear reaction and decays: ^{9}Be(n,α)^{6}He → ^{6}Li + β^-. The cross section for the ^{9}Be(n,α)^{6}He activation reaction results in a maximum sensitivity to neutrons with 2.5 MeV energy and practically no sensitivity to neutrons with energies less than 1 MeV. The ^{6}He isotope decays to ^{6}Li with a half-life time of 0.807 s through β^- decay. Then the electrons can be easily registered using a large gas area SP-126C proportional counter (produced by Canberra).

The counter was calibrated by means of Monte Carlo simulations (MCNP code) and the measurements with Pu-Be source in order to assess the total number of neutrons emitted during single PF-24 discharge: Y_n^{mea} [Bienkowska 2014]. The calibration coefficient is equal to 2.00(±0.04)×10^5 n/count [Bienkowska 2014]. The sensitivity threshold of the counter is at the level of about 10^6-10^7 n/discharge.

5.3. Electric diagnostic systems – determination of experimental plasma parameters

5.3.1. Electric probes and acquired electric traces

The phenomena accompanying plasma compression can be studied using the changes of electric current flow in the system. The plasma-focus PF-24 device was equipped with two electric indeptendent diagnostic systems – the Rogowski coil and the magnetic probe. Both electric probes are standard equipment in PF laboratories. The Rogowski coil is a type of coreless transformer where a primary winding is the conductor and secondary winding is the Rogowski coil. The voltage induced in the secondary winding is proportional to the current derivative over time. Thus, by using electric integrating system configuration the current singnal can be obtained. The accuracy of measurements depends on the resistivity of the coil and scaling of the circumference of the ring. In the PF-24 system Rogowski coil is placed in the collector area – the coil is wound around entire collector area. It is used to measure the total discharge current that flows through the collector. The calibration factor of Rogowski coil in the PF-24 system is equal to 26.4 kA/V [Marciniak 2016]. The operation of magnetic probe is similar wherein, the magnetic probe covers only part of the collector area (corresponding to connection of transmission cables from 3 condensers).

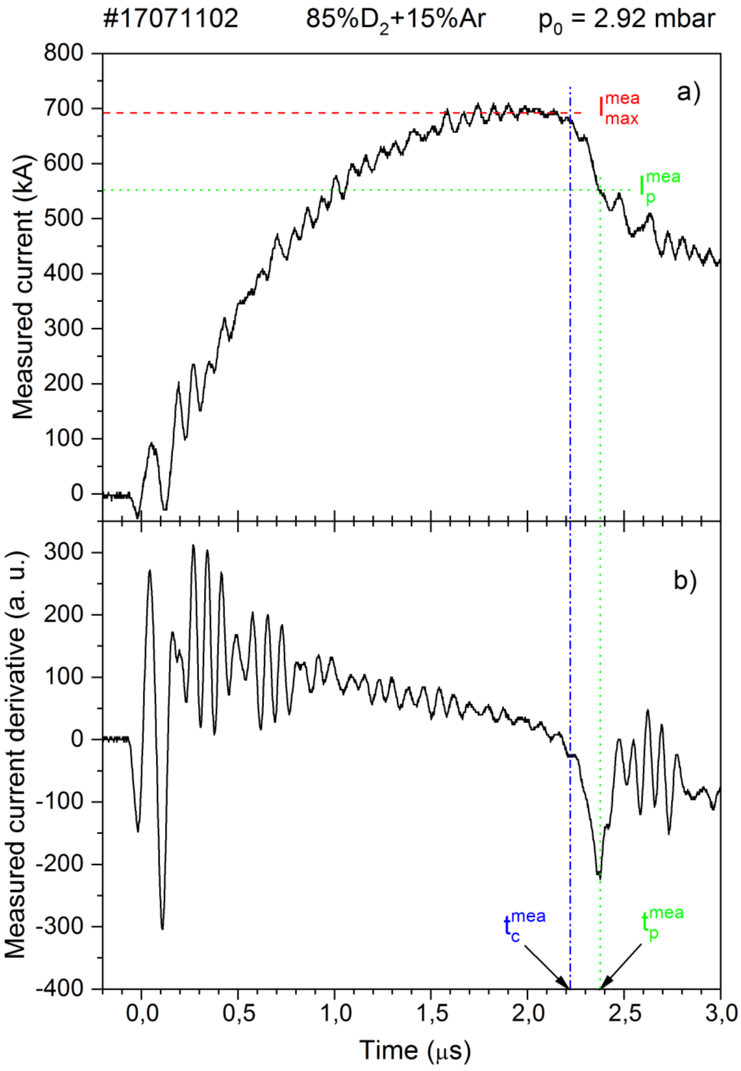

Figure 5.3.1. a) The measured total discharge current (upper trace) and **b)** the current derivative over time (bottom trace) of the PF-24 discharge: #17071102; U_0 = 17 kV; 85%D$_2$+15%Ar mixture; p_0 = 2.92(±0.09) mbar. The values of: the maximum current I_{max}^{mea}, the pinch current I_p^{mea}, the compession time t_c^{mea} and the pinch time t_p^{mea} were determined as indicated on the graph.

Both mounted probes in the PF-24 system measure the electric traces with single nanosecond time resolution. The typical (characteristic) current trace and its time derivative trace registered during discharge #17071102 in the PF-24 system are presented in figure 5.3.1. For this discharge the charging voltage U_0 was set to 17 kV and initial total pressure of 85%D_2+15%Ar mixture was 2.92(±0.09) mbar.

5.3.2. Electro-kinetic parameters

Using total discharge current trace and its time derivative trace, as shown in figure 5.3.1, a set of plasma parameters can be determined:

I. **Kinetic parameters**:
- $\boldsymbol{t_c^{mea}}$ (μs) – **compression time** – the time of run-down of magnetic piston along anode (axial direction of movement) and the moment of beginning of radial compression at the end of anode – the approximated time of beginning of "sharp" current drop.
- $\boldsymbol{t_p^{mea}}$ (μs) – **pinch time** – the time to plasma pinch generation – the approximated time to minimum of *dI/dt*.
- $\boldsymbol{v_z^{mea}}$ (cm/μs) – **average axial velocity** – the average velocity of magnetic piston moving along anode (average velocity during the axial phase of discharge).

II. **Electric parameters**:
- $\boldsymbol{I_{max}^{mea}}$ (kA) – **maximum current** – the maximum total current registered during discharge (measured in the collector area of the PF-24).
- $\boldsymbol{I_p^{mea}}$ (kA) – **pinch current** – the total discharge current registered approximately at the minimum of *dI/dt* (measured in the collector area of the PF-24) – corresponding to the t_p^{mea} time.

The parameters: t_c^{mea}, t_p^{mea}, I_{max}^{mea} and I_p^{mea} are marked in figure 5.3.1. The average measured velocity of magnetic piston along the anode can be determined as: $v_z^{mea} = z_0/t_c^{mea}$.

5.3.3. Determination of electro-kinetic parameters and errors

The precise determination of the experimental plasma parameters based on the measured electric traces is important, but also a challenging task due the fluctuations of the registered signal. The fluctuations are caused by the fluctuations of mass and charge flow during discharge as well as by different non-linear effects which may result in the significantly altered registered traces. The procedure of determination of: I_{max}^{mea}, t_c^{mea}, t_p^{mea}, I_p^{mea} and v_z^{mea} parameters and their errors: ΔI_{max}^{mea}, Δt_c^{mea}, Δt_p^{mea}, ΔI_p^{mea} and Δv_z^{mea} used in this work is explained below based on an example of discharge #17071102 (figure 5.3.1).

The first step of the procedure, invented by the author of this thesis, is to determine the I_{max}^{mea}+/-ΔI_{max}^{mea}. The I_{max}^{mea} value is based on the maximum and minimum values of observed fluctuations of current in the registered trace (with 10 ns time resolution) in the investigated area where maximum current value should be found – see figure 5.3.2. Based on maximum (I_{maxflu}^{mea}) and minimum (I_{minflu}^{mea}) value of current fluctuations: $\Delta I_{max}^{me} = (I_{maxflu}^{mea} - I_{minflu}^{mea})/2$. Thus, the $I_{max}^{mea} = I_{maxflu}^{mea} - \Delta I_{max}^{mea} = I_{minflu}^{mea} + \Delta I_{max}^{mea}$. For the presented discharge in figure 5.3.1 and 5.3.2, determined I_{max}^{mea} = 691(±14) kA.

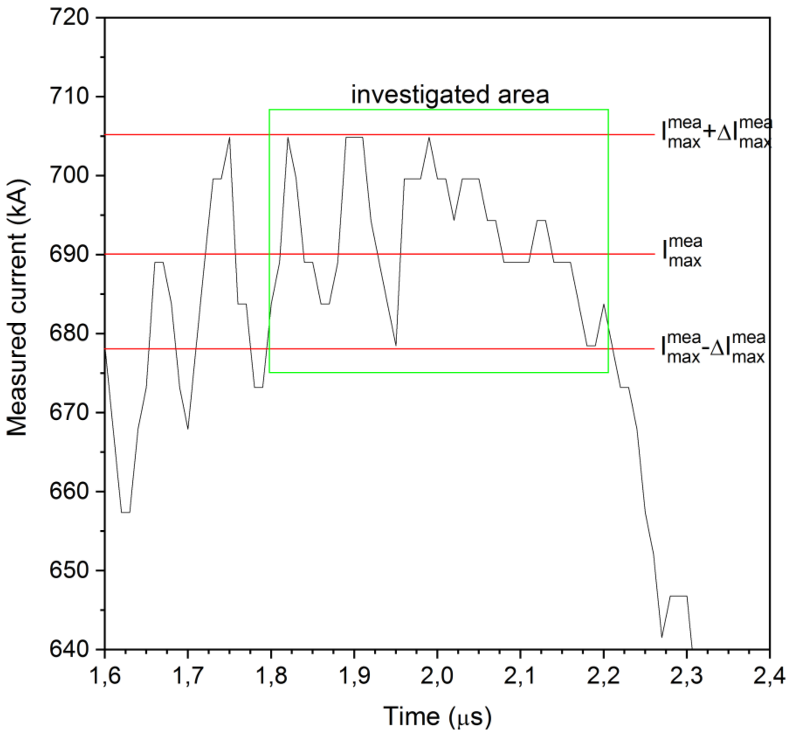

Figure 5.3.2. Part of registered electric total current trace during discharge #17071102 (see also figure 5.3.1). The presented time step of the trace is equal to 10 ns. The determined maximum current value $I_{max}^{mea} \pm \Delta I_{max}^{mea}$ = 691(±14) kA. The investigated area is marked with green color.

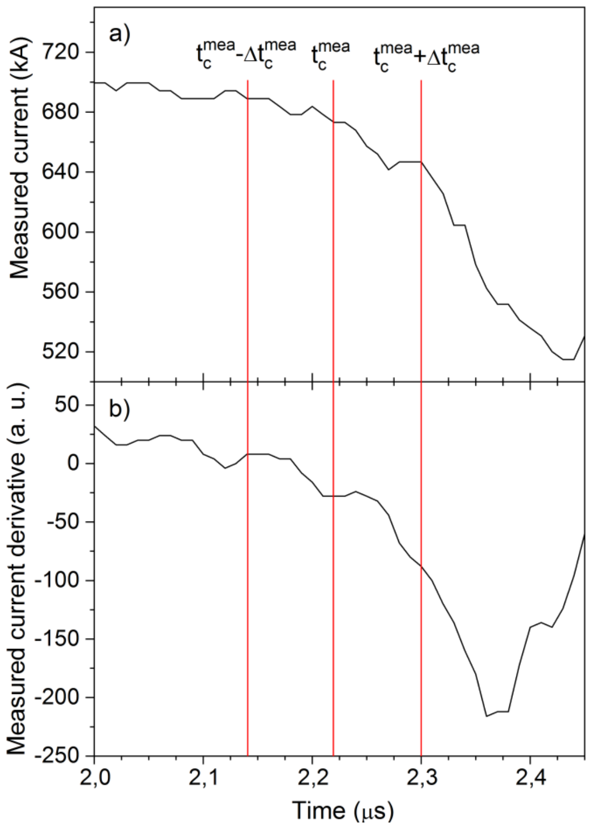

Figure 5.3.3. Part of registered electric a) total current trace and b) total current derivative over time trace during discharge #17071102 (see also figure 5.3.1). The presented time step of the trace is equal to 10 ns. The determined compression time value $t_c^{mea} \pm \Delta t_c^{mea}$ = 2.22(±0.08) μs.

The second step of procedure is to determine the t_c^{mea} parameter and its error Δt_c^{mea}. The t_c^{mea} value is based on the earliest and latest point which can be considered as t_c^{mea} time (with 10 ns time resolution) considering both current and current derivative trace – see figure 5.3.3. In other words, two points are searched for which current trace and current derivative trace appears to start the rapid decrease. Based on earliest (t_{minc}^{mea}) and latest (t_{maxc}^{mea}) values of time: $\Delta t_c^{mea} = (t_{maxc}^{mea} - t_{minc}^{mea})/2$. Thus, the $t_c^{mea} = t_{maxc}^{mea} - \Delta t_c^{mea} = t_{minc}^{mea} + \Delta t_c^{mea}$. For the presented discharge in figure 5.3.1 and 5.3.3, determined $t_c^{mea} = 2.22(\pm 0.08)$ µs.

The third step of procedure is to determine the t_p^{mea} parameter and its error Δt_p^{mea}. The t_p^{mea} value is based on two points which determine approximately half the high of *dI/dt* jump (with 10 ns time resolution) – see figure 5.3.4. Based on the earliest (t_{p1}^{mea}) and latest (t_{p2}^{mea}) points describing half high of *dI/dt* spike: $\Delta t_p^{mea} = (t_{p1}^{mea} - t_{p2}^{mea})/2$. Thus, the $t_p^{mea} = t_{p1}^{mea} + \Delta t_p^{mea} = t_{p2}^{mea} - \Delta t_p^{mea}$. For the presented discharge in figure 5.3.1 and 5.3.4, determined $t_p^{mea} = 2.38(\pm 0.06)$ µs.

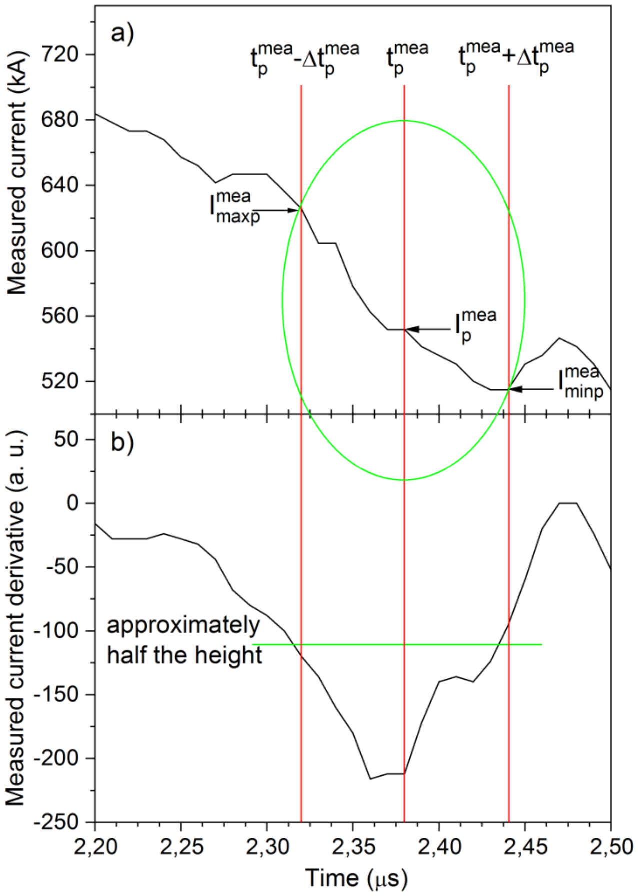

Figure 5.3.4. Part of the registered electric a) total current trace and b) total current derivative over time trace during discharge #17071102 (see also figure 5.3.1). The presented time step of the trace is equal to 10 ns. The determined pinch time value: $t_p^{mea} \pm \Delta t_p^{mea} = 2.38(\pm 0.06)$ µs. The determined pinch current value (measured in the collector area): $I_p^{mea}(t_p^{mea}) = 552$ kA. The determined error of I_p^{mea}: $\Delta I_p^{mea} = (I_{maxp}^{mea} - I_{minp}^{mea})/2 = 56$ kA. The green circle indicates the part of current trace from which highest and smallest value of *I* should be determined and taken.

The fourth step of procedure is to determine the I_p^{mea} parameter and its error ΔI_p^{mea}. The value of I_p^{mea} is determined on the basis of t_p^{mea} time: $I_p^{mea}(t_p^{mea})$ – see figure 5.3.4. And the ΔI_p^{mea} is determined on the base of the maximum (I_{maxp}^{mea}) and the minimum

(I_{minp}^{mea}) pinch current values in given range which is determined by t_{p1}^{mea} and t_{p2}^{mea} times – see figure 5.3.4. Thus, $\Delta I_p^{mea} = (I_{maxp}^{mea} + I_{minp}^{mea})/2$. For the discharge in figure 5.3.1 and 5.3.4, determined $I_p^{mea} = 552(\pm 56)$ kA.

Finally, the $v_z^{mea} = z_0/t_c^{mea}$. And based on the law of transfer of uncertainty: $\Delta v_z^{mea} = z_0 \Delta t_c^{mea}/(t_c^{mea})^2$. For the discharge in figure 5.3.1 and 5.3.3, determined $v_z^{mea} = 7.7(\pm 0.3)$ cm/μs.

6. Simulation of discharge in plasma-focus device

6.1. General information about Lee model

The Lee model code was created in 1985 by prof. Sing Lee originally as a 2-phase code and has been constantly developed since then. The 2007 version of the code (RADPFV5.15de) is an open source program developed in the Visual Basic and implemented as a Macro into Excel Sheet for easy data acquisition and visualization. It was described in details in [Lee 2014], [Lee 2017] and published online in: http://plasmafocus.net. The RADPFV5.15de version of the code has 5-phases and enables simulation of PF discharges in only single working gas. In the recent years, the upgraded version of the code enabling simulations of PF discharges in mixtures of two gases (RADPFV5.013.9b) has been developed and is currently being tested. The RADPFV5.013.9b version was made available by prof. Lee to the author of thesis for joined research.

The Lee model code is a relatively simple, efficient, 0/1-dimensional, hybrid code based on the 0/1-dimensional snow-plough model (combined with 0/1-dimensional shock model) and the 0/1-dimensional slug model (developed snow-plough and shock model for radial compression approximation of sheet-shock movement). The snow-plough model was described originally by M. Rosenbluth et al. in 1954 [Rosenbluth 1954] and described in details by D. E. Potter in 1971 [Potter 1971] as 2-dimensional snow-plough fluid (MHD) model. The 0-dimensional slug model was originally described by Potter in 1978 as 0/1-dimensional hybrid model [Potter 1978], [Haines 2011].

The Lee model code combines the electric RLC replacement circuit with plasma-focus dynamics, thermodynamics and radiation emitted. It is energy-, momentum-, charge- and mass-consistent and accounts for the effects of the finite transit times of small disturbances (based on shock wave theory [Gross 1971]) and plasma self-absorption. It has been used in design and interpretation of Mather type plasma-focus experiments and as a complementary facility to provide diagnostic reference numbers in deuterium, noble gases and more [Lee 2014], [Lee 2017]. Several effects have been studied using the code: the axial and radial plasma dynamics, the SXR emission and yield, the ion beam and electron beam emission, the fast plasma streams emission, the neutron yield computations, the current and neutron yield limitations, the deterioration of neutron scaling (neutron saturation), the radiative collapse, the speed-enhanced PF, the current-stepped PF and the extraction of diagnostic and anomalous resistance data from current signals [Lee 2014], [Lee 2017]. The summary of most important aspect of the code is presented in figure 6.1.1.

A few phases of discharge can be distinguished in each version of the Lee model code. The two superior phases which are distinguished in the 5-phase code are: axial and radial. These two phases can be further divided into five phases. Moreover, three superior phases can be distinguished in the upgraded 6-phase code: axial, radial and anomalous resistance. These three phases can also be further divided into six phases. Wherein, the 6-phase version of the code enables simulations of the discharges in PF devices with higher total inductance while the 5-phase version is used to simulate discharges in PF devices with lower total inductance. Since, the PF-24 device has relatively low total static inductance (see subsection 5.1.4) only the 5-phase code was used for simulations of all discharges presented in this work.

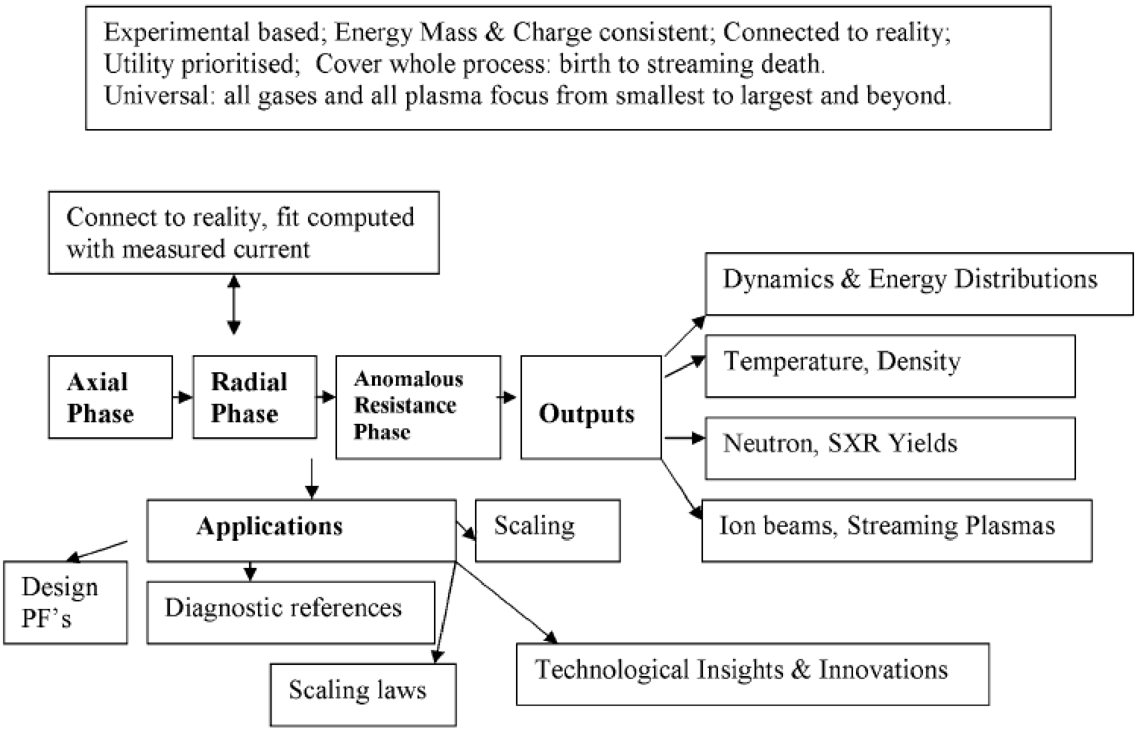

Figure 6.1.1. The philosophy, the phases, the outputs and applications of the Lee model code [Lee 2014].

6.2. Phases of discharge (theoretical) in the 5-phase Lee model code and equations

The 5-phase Lee model code (both RADPFV5.15de and RADPFV5.013.9b versions) describes discharge in the Mather type plasma-focus device in five particular phases: I – axial, II – radial inward shock, III – radial reflected shock, IV – slow compression (pinch) and V – expanded column axial [Lee 2014], [Lee 2017]. Phase I and V are axial phases while phase II, III and IV are radial phases. In each phase, a specific set of differential equations is used to compute velocity and relative position of magnetic piston (or for current sheet and shock wave seperatly) as well as total current flow. Moreover, the code computes also other data like: plasma (tube) inductance, discharge (tube) voltage, plasma (ion) density, plasma resistance (Spitzer resistivity), plasma (ion) temperature, small disturbance speed (acustic speed in plasma), effective charges of plasma (for ionized gases in Corona model), specific heat ratios (for ionized gases in Corona model), ohmic heating power, X-ray bremsstrahlung emission power, X-ray line emission power, X-ray recombination emission power, thermonuclear neutron yield and beam-target neutron yield [Lee 2014], [Lee 2017]. In the axial phases no radiation emission is allowed, while in radial phases ionization effects are all considered and during pinch phase (part of radial phase) the equations of motion are changed into radiation-coupled dynamics equations and radiation emission is allowed.

6.2.1. Phases I – axial

The axial phase description is based on the 0/1-dimensional snow-plough model combined with shock model [Lee 2014], [Lee 2017], [Haines 2011]. It is related to the movement of the magnetic piston (infinitesimally thin and highly conductive) along the *z* axis, starting from the base of the electrodes (back of the experimental chamber). Two differential equations are used to describe its axial velocity (and relative position) and current effectively “driving” it [Lee 2014] [Lee 2017]:

$$\frac{d^2z}{dt^2} = \frac{\frac{\mu \ln\left(\frac{b_0}{a_0}\right)}{4\pi^2 f_m \rho_0 \left(\left(\frac{b_0}{a_0}\right)^2 - 1\right)} \left(\frac{f_c I}{a_0}\right)^2 - \left(\frac{dz}{dt}\right)^2}{z} \tag{6.2.1}$$

$$\frac{dI}{dt} = \frac{U_0 - \frac{1}{C_0}\int I dt - R_0 I - f_c I \frac{\mu}{2\pi} \ln\left(\frac{b_0}{a_0}\right) \frac{dz}{dt}}{L_0 + f_c \frac{\mu}{2\pi} \ln\left(\frac{b_0}{a_0}\right) z} \tag{6.2.2}$$

In equation (6.2.1) and (6.2.2), z is the relative axial position of magnetic piston (variable) – axial position of both sheet and shock, I is the total discharge current (current flowing in the equivalent electric circuit based on the equation (2.2.1) and figure 2.2.2) (variable), t is time (variable), f_c is the axial current factor (described in subsection 6.3.2), f_m is the axial mass factor (described in subsection 6.3.2), ρ_0 is the total ambient density for gas or gas mixture initially between electrodes (taken as density o ideal gas of given type in normal conditions), a_0 is the anode radius, b_0 is the reduced cathode radius, U_0 is the charging voltage of the device, C_0 is the total capacitance of the device, R_0 is the nominal resitance of the device, L_0 is the nominal inductance of the device and μ is the magnetic permeability of vacuum. Wherein, the product of If_c and $\rho_0 f_m$ is: the current effectively “driving” the magnetic piston and the gas density being effectively sweeped by the piston, respectively. The equation (6.2.1) is the motion equation describing the rate of change of momentum to the Ampere’s force. And the equation (6.2.2) is the modified dynamic RLC replacement circuit equation (see figure 2.2.2) [Lee 2014] [Lee 2017]. Both equations (6.1.1) and (6.2.2) are coupled with each other through the same variables and parameters. The scheme of magnetic piston movement in phase I is presented in figure 6.2.1.

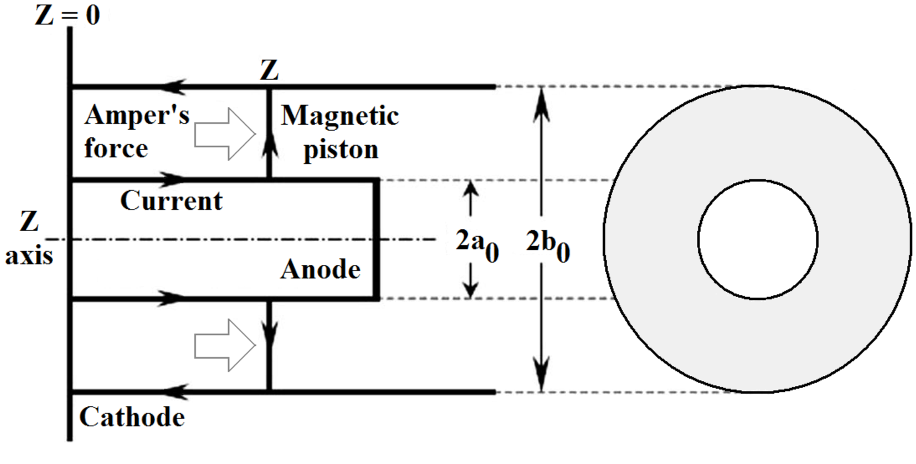

Figure 6.2.1. Scheme of the phase I (axial) of discharge in the Lee model code. The symbols are: z – the position of the plasma current sheet-shock structure (z = 0 – starting position), a_0 – anode radius, b_0 – cathode reduced radius. The arrows indicate: the direction of current flow, the Ampere’s force working on the plasma structure and the dimensions [Lee 2014], [Lee 2017].

The axial phase ends when magnetic piston reaches the end of anode. In this moment the radial inward shock phase starts.

6.2.2. Phases II – radial inward shock

The radial inward shock phase is described with the elongating slug model [Potter 1978], [Haines 2011], [Lee 2014], [Lee 2017]. In this phase the movement of magnetic piston continues (with parameters achieved at the end of phase I) but in both radial and axial directions. The elongating slug model assumes that there is some space between current sheet and shock wave and that the current sheet and shock wave can move with different velocities (the shock wave is always ahead of the current sheet) towards the center of the anode – see figure 6.2.2. The position of the shock wave and the current sheet is determined in reference to this center. It is also assumed that the z_f position of the sheet-shock changes with time (piston still moves along the z axis) in reference to the anode face.

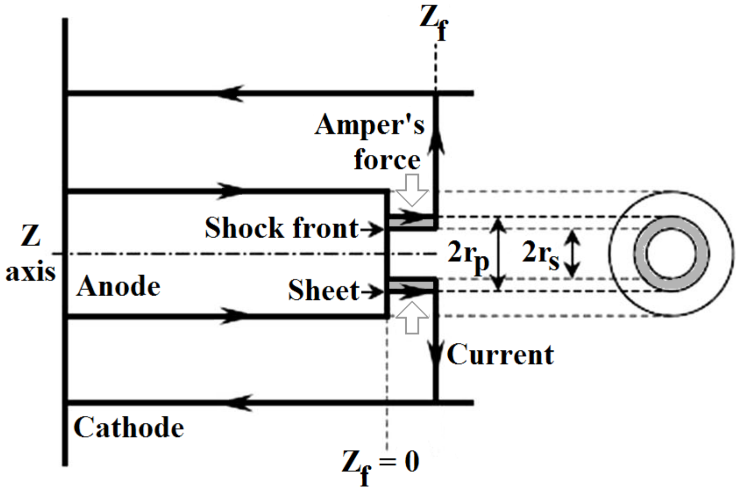

Figure 6.2.2. Scheme of the phase II (radial inward shock) of discharge in the Lee model code. The symbols are: z_f – the position of the plasma current sheet-shock front structure (in reference to the anode face), r_s – the position of the inward moving shock wave front (in reference to the anode center) and r_p – position of the inward moving current sheet (in reference to the anode center). Between r_s and r_p is the radially imploding slug elongating with the z_f length. The arrows indicate: the direction of current flow, the Ampere's force working on the plasma structure and the dimensions [Lee 2014], [Lee 2017].

Four differential equations are used to describe: the shock wave velocity (and relative position) in radial direction, the current sheet velocity (and relative position) in radial direction, the sheet-shock velocity (and relative position) in axial direction and the current effectivly flowing through the sheet [Lee 2014], [Lee 2017].

$$\frac{dr_s}{dt} = -\left[\frac{\mu(\gamma+1)}{f_{mr}\rho_0}\right]^{1/2} \frac{f_{cr}I}{4\pi r_p} \tag{6.2.3}$$

$$\frac{dr_p}{dt} = \frac{\frac{2}{\gamma+1}\frac{r_s}{r_p}\frac{dr_s}{dt} - \frac{r_p}{\gamma I}\left(1-\frac{r_s^2}{r_p^2}\right)\frac{dI}{dt} - \frac{1}{(\gamma+1)}\frac{r_p}{z_f}\left(1-\frac{r_s^2}{r_p^2}\right)\frac{dz_f}{dt}}{\frac{\gamma-1}{\gamma} + \frac{1}{\gamma}\frac{r_s^2}{r_p^2}} \tag{6.2.4}$$

$$\frac{dz_f}{dt} = -\left(\frac{2}{\gamma+1}\right)\frac{dr_s}{dt} \tag{6.2.5}$$

$$\frac{dI}{dt} = \frac{U_0 - \frac{1}{C_0}\int I dt - R_0 I - f_{cr} I \frac{\mu}{2\pi}\ln\left(\frac{b_0}{r_p}\right)\frac{dz_f}{dt} + f_{cr} I \frac{\mu}{2\pi}\frac{z_f}{r_p}\frac{dr_p}{dt}}{L_0 + f_{cr}\frac{\mu}{2\pi}\ln\left(\frac{b_0}{a_0}\right) z_0 + f_{cr}\frac{\mu}{2\pi}\ln\left(\frac{b_0}{r_p}\right) z_f} \tag{6.2.6}$$

In equation (6.2.3), (6.2.4), (6.2.5) and (6.2.6), r_s is the relative position of the front of radial shock wave (variable), r_p is the relative radial current sheet position (variable) – piston position, z_f is the relative axial sheet-shock position (variable), I is the total discharge current (current flowing in the equivalent electric circuit based on the equation (2.2.1) and figure 2.2.2) (variable), t is time (variable), f_{mr} is the radial mass factor (described in subsection 6.3.2), f_{cr} is the radial current factor (described in subsection 6.3.2), γ is the total specific heat ratio of plasma inside the sheet-shock structure (presented in subsection 6.2.8), ρ_0 is the total ambient density for gas or gas mixture initially between electrodes (taken as density of ideal gas of given type in normal conditions), a_0 is the anode radius, b_0 is the reduced cathode radius, z_0 is the anode length inside the experimental chamber, U_0 is the charging voltage of the device, C_0 is the total capacitance of the device, R_0 is the nominal resitance of the device, L_0 is the nominal inductance of the device and μ is the magnetic permeability of vacuum. Wherein, the product of If_{cr} and $\rho_0 f_{mr}$ is: the current effectively driving the sheet and the gas density being effectively sweeped by the sheet, respectively.

The equation (6.2.3) is used to compute the radial inward shock wave velocity from the driving magnetic pressure. This equation is based on the change of shock wave pressure due to the magnetic pressure which depends on the drive current value and current sheet position. The equation (6.2.4) is used to compute the velocity of the current sheet allowing it to separate from shock wave front by applying an adiabatic approximation. This equation is determined by the first law of thermodynamic applied to the effective increase in volume between shock wave front and current sheet created by the incremental motion of the shock wave front. The equation (6.2.5) is used to compute the axial elongation velocity of the current sheet-shock. This equation is based on the magnetic pressure which is similar as driving the inward radial shock wave – the compression has effects in both r and z directions (magnetic pressure can exert changes both in radial and axial direction). And the equation (6.2.6) is the modified dynamic RLC replacement circuit equation. Thermodynamic effects due to ionization and excitation are incorporated into these equations (effects important for gases with higher atomic Z number than hydrogen or deuterium) as well as into analogic equations describing phase III and IV. And communication delay between shock wave front and current sheet due to the finite small disturbance velocity (defined in subsection 6.2.9) is applied and introduced into these equations. The correction from small disturbance velocity is taken assumed as modified acoustic velocity in plasma based on shock wave theory [Gross 1971], [Potter 1978]. The scheme of phase II was presented in figure 6.2.2.

The radial inward shock phase ends when symmetrical parts of shock wave coming from opposite directions meet at the anode center (on the z axis) and are reflected off each other. In this moment the radial reflected shock phase starts.

6.2.3. Phases III – radial reflected shock

The radial reflected shock phase is also described with the elongating slug model [Potter 1978], [Liberman 1999], [Haines 2011]. However, in this phase the shock wave move towards the cathode while the current sheet still moves towards the anode center – they move towards each other – see figure 6.2.3.

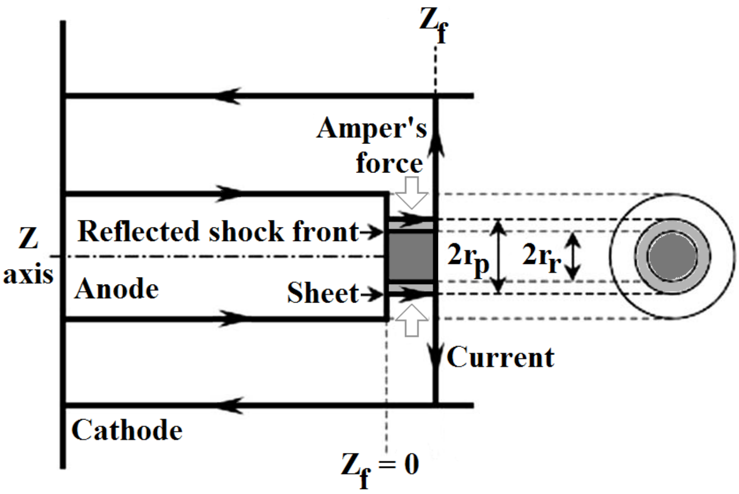

Figure 6.2.3. Scheme of the phase III (radial reflected shock) of discharge in the Lee model code. The symbols are: z_f – the position of the plasma current sheet-shock front structure (in reference to the anode face), r_r – the position of the outward moving shock wave front (in reference to the anode center) and r_p – the position of the inward moving current sheet (in reference to the anode center). Between r_r and r_p is the radially imploding slug elongating with the z_f length. The plasma column (unstable) is generated with r_r radius and z_f length. The arrows indicate: the direction of current flow, the Ampere's force working on the plasma structure and the dimensions.

Behind the moving slug (in the central region) plasma column is generated (not stable). Four differential equations describe the dynamics of this phase [Lee 2014], [Lee 2017]. The equation enabling computation of the radial outward shock velocity (and relative position) assumes constant value which depends on the final value of radial inward shock velocity (achived on z axis) [Lee 2014], [Lee 2017].

$$\frac{dr_r}{dt} = -0.3\left(\frac{dr_s}{dt}\right)_{on-axis} \tag{6.2.7}$$

$$\frac{dr_p}{dt} = \frac{-\frac{r_p}{\gamma I}\left(1-\frac{r_r^2}{r_p^2}\right)\frac{dI}{dt} - \frac{1}{(\gamma+1)}\frac{r_p}{z_f}\left(1-\frac{r_r^2}{r_p^2}\right)\frac{dz_f}{dt}}{\frac{\gamma-1}{\gamma}+\frac{1}{\gamma}\frac{r_r^2}{r_p^2}} \tag{6.2.8}$$

$$\frac{dz_f}{dt} = -\left(\frac{2}{\gamma+1}\right)\left(\frac{dr_s}{dt}\right)_{on-axis} \tag{6.2.9}$$

$$\frac{dI}{dt} = \frac{U_0 - \frac{1}{C_0}\int I dt - R_0 I - f_{cr} I \frac{\mu}{2\pi}\ln\left(\frac{b_0}{r_p}\right)\frac{dz_f}{dt} + f_{cr} I \frac{\mu}{2\pi}\frac{z_f}{r_p}\frac{dr_p}{dt}}{L_0 + f_{cr}\frac{\mu}{2\pi}\ln\left(\frac{b_0}{a_0}\right)z_0 + f_{cr}\frac{\mu}{2\pi}\ln\left(\frac{b}{r_p}\right)z_f} \tag{6.2.10}$$

In equations (6.2.7), (6.2.8), (6.2.9) and (6.2.10), r_r is the radial position of the reflected shock wave front, $(dr_s/dt)_{on-axis}$ is the final velocity of shock wave achived on the z axis and all other symbols are the same as in equation (6.2.3), (6.2.4), (6.2.5) and (6.2.6).

The radial reflected shock phase of discharge ends when the shock wave meets with the current sheet at some position determined with both shock wave and current sheet velocities (positions). This is the moment when slow compression (pinch) phase starts.

6.2.4. Phases IV – slow compression (pinch)

In the slow compression (pinch) phase a stable plasma pinch (column) is assumed to be generated with borders composing of current conducting sheet and plasma inside – see figure 6.2.4. This pinch is assumed to have average and uniform properties along dimensions such as current flow, ion density and ion temperature in entire plasma volume at given time. Furthermore, the pinch is still able to compress (inward movement) but relatively slowly.

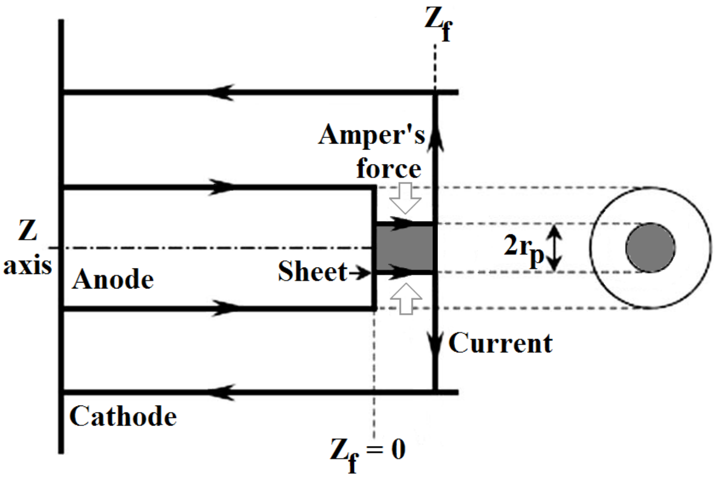

Figure 6.2.4. Scheme of the phase IV (pinch) of discharge in the Lee model code. The symbols are: z_f – the position of the current sheet-shock front structure (in reference to the anode face) and r_p – the position of the inward (relatively slow) moving current sheet (in reference to the anode center). The plasma column (stable) is generated with r_p radius and z_f length. The arrows indicate: the direction of current flow, the Ampere's force working on the plasma structure and the dimensions.

Three coupled differential equation are used to describe this phase: the radial sheet motion (radial velocity of the sheet), the pinch column elongation (axial velocity of sheet-shock) and the RLC equivalent circuit (current effectively flowing through sheet) [Lee 2014], [Lee 2017].

$$\frac{dr_p}{dt} = \frac{-\frac{r_p}{\gamma I}\frac{dI}{dt} - \frac{1}{\gamma+1}\frac{r_p}{z_f}\frac{dz_f}{dt} + \frac{4\pi(\gamma-1)}{\mu\gamma f_{cr}^2 I^2}\frac{r_p}{z_f}\frac{dQ}{dt}}{\frac{\gamma-1}{\gamma}} \tag{6.2.11}$$

$$\frac{dz_f}{dt} = \left[\frac{\mu}{f_{mr}(\gamma+1)\rho_0}\right]^{1/2}\frac{f_{cr}I}{2\pi r_p} \tag{6.2.12}$$

$$\frac{dI}{dt} = \frac{U_0 - \frac{1}{C_0}\int I dt - R_0 I - f_{cr}I\frac{\mu}{2\pi}\ln\left(\frac{b_0}{r_p}\right)\frac{dz_f}{dt} + f_{cr}I\frac{\mu}{2\pi}\frac{z_f}{r_p}\frac{dr_p}{dt} - R_S f_{cr} I}{L_0 + f_{cr}\frac{\mu}{2\pi}\ln\left(\frac{b_0}{a_0}\right)z_0 + f_{cr}\frac{\mu}{2\pi}\ln\left(\frac{b_0}{r_p}\right)z_f} \tag{6.2.13}$$

In equation (6.2.1), dQ/dt is the energy gain/loss term determined as: $dQ/dt = P_{ohm} - P_{brem} - P_{line} - P_{rec}$, wherein the P_{ohm}, P_{brem}, P_{line} and P_{rec} symbols are described by equations from (2.1.19) to (2.1.22) (see also subsection 6.2.11). And in equation (6.2.13), R_s is the Spitzer resitivity (presented in subsection 6.2.11). The rest of parameters describing the equations (6.2.11), (6.2.12) and (6.2.13) are the same as in equations (6.2.3), (6.2.4), (6.2.5) and (6.2.6).

The equation (6.2.11) describing the dynamic of current sheet (which forms the plasma pinch) is modified through including energy gain/loss term (*dQ*/*dt*) [Lee 2014], [Lee 2017]. This energy term can have positive or negative value. The positive value is connected with dominant Ohmic heating (equation (2.1.22)) and will result in tendency to push the sheet outwards (slower compression). And negative term is connected with dominant emission of bremsstrahlung (equation (2.1.21)), line radiation (equation (2.1.19)) and recombination radiation (equation (2.1.20)) and will result in tendency to push the sheet inwards (faster compression). Thus, if the power of radiation emission exceeds the power of Ohmic heating the final compression will be greater (assuming similar pinch lifetime).

Moreover, the emission of radiation from plasma pinch can be significantly reduced due to the increase of plasma opacity. To include this effect plasma self-absorption correction factor is also computed during this phase of discharge (this is the f_0 parameter from equation (2.1.13)) and transition from volumetric emission to surface emission is assumed and included [Lee 2014], [Lee 2017] – see subsection 6.2.12.

The duration of the pinch phase (lifetime of pinch and slow compression) is set as the time of transit of small disturbances across the entire pinched plasma column – see subsection 6.2.9 [Lee 2017]. Afterwards, the expanded column axial phase starts.

6.2.5. Phases V – expanded column axial

At the beginning of the expanded column axial phase the plasma column is assumed to rapidly expand (due to to loss of good confiment) to have diameter equal to the diameter of the anode [Lee 2014], [Lee 2017]. This diameter is set as constant until the end of discharge (simulation) – see figure 6.2.5. Thus, further increase of column volume takes place only along *z* axis direction.

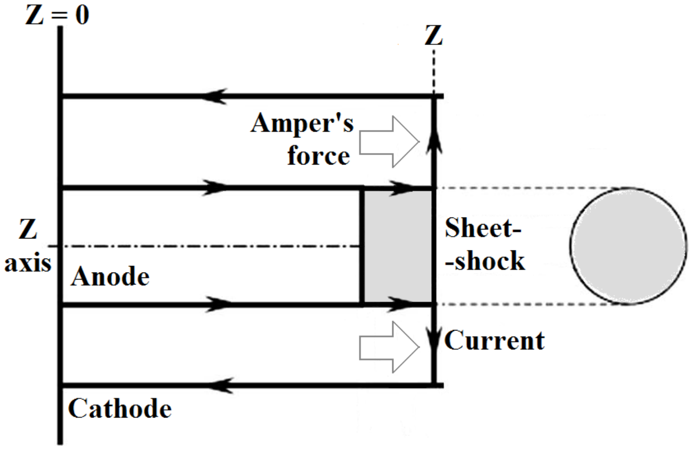

Figure 6.2.5. Scheme of the phase V (expanded column axial) of discharge in the Lee model code. The symbols are: *z* – the position of the sheet-shock front structure (in reference to the back of experimental chamber). The plasma column has constant radius equal to the anode radius and expands only in axial direction. The arrows indicate: the direction of current flow, the Ampere's force working on the plasma structure and the dimensions.

This axial movement of the plasma sheet-shock structure (column top) is described using two differential equations – motion equation and circuit equation (similar as in phase I) [Lee 2014], [Lee 2017].

$$\frac{d^2z}{dt^2}=\frac{\frac{\mu\ln\left(\frac{b_0}{a_0}\right)}{4\pi^2 f_m\rho_0\left(\left(\frac{b_0}{a_0}\right)^2-1\right)}\left(\frac{\ln\left(\frac{b_0}{a_0}\right)+\frac{1}{4}}{\ln\left(\frac{b_0}{a_0}\right)}\right)\left(\frac{f_c I}{a_0}\right)^2-\left(\frac{\left(\frac{b_0}{a_0}\right)^2}{\left(\frac{b_0}{a_0}\right)^2-1}\right)\left(\frac{dz}{dt}\right)^2}{z_0+\left(\frac{\left(\frac{b_0}{a_0}\right)^2}{\left(\frac{b_0}{a_0}\right)^2-1}\right)^2(z-z_0)} \tag{6.2.14}$$

$$\frac{dI}{dt}=\frac{U_0-\frac{1}{C_0}\int I dt-R_0 I-f_c I\frac{\mu}{2\pi}\ln\left(\frac{b_0}{a_0}\right)\left(\frac{\ln\left(\frac{b_0}{a_0}\right)+\frac{1}{2}}{\ln\left(\frac{b_0}{a_0}\right)}\right)\frac{dz}{dt}}{L_0+f_c\frac{\mu}{2\pi}\ln\left(\frac{b_0}{a_0}\right)z_0+f_c\frac{\mu}{2\pi}\ln\left(\frac{b_0}{a_0}\right)\left(\frac{\ln\left(\frac{b_0}{a_0}\right)+\frac{1}{2}}{\ln\left(\frac{b_0}{a_0}\right)}\right)(z-z_0)} \tag{6.2.15}$$

The symbols in the equations (6.2.14) and (6.2.15) are the same as in equations (6.2.1) and (6.2.2). Moreover, as previously, the initial conditions for parameters in the motion equation (6.2.14) and circuit equation (6.2.15) are taken from the values achieved at the end of previous phase of discharge (phase IV).

The expanded column axial phase ends when the discharge has proceeded to a half cycle (the half period of first oscillation of dynamic RLC damped circuit) [Lee 2017].

6.2.6. Additional relations and data used in the Lee model code – characteristic axial transit time and velocity

Except the above mentioned differential equations describing the dynamic of sheet-shock structure (including pinch) and current flow there are additional many relations and data used in the model for computations of different data and parameters describing plasma in different phases including radiation emission. The important ones will be presented in this and next subsections.

The characteristic axial transit time (t_a) of magnetic piston along the anode (phase I) is determined as [Lee 2014], [Lee 2017]:

$$t_a=\left[\frac{4\pi^2\left(\left(\frac{b_0}{a_0}\right)^2-1\right)}{\mu\ln\left(\frac{b_0}{a_0}\right)}\right]^{1/2}\frac{\sqrt{f_m}}{f_c}\,\frac{z_0}{\frac{I_0}{a_0\sqrt{\rho_0}}} \tag{6.2.16}$$

In equation (6.2.16), b_0 is the reduced cathode radius, a_0 is the anode radius, z_0 is the length of the anode inside the experimental chamber, f_m is the axial mass factor (described in subsection 6.3.2), f_c is the axial current factor (described in subsection 6.3.2), ρ_0 is the total ambient density for gas or gas mixture initially between electrodes (taken as density of ideal gas of given type in normal conditions), μ is the magnetic permability of vacuum and $I_0 = U_0 / Z_0 = U_0 (C_0 / L_0)^{0.5}$ is the maximum amplitude of oscillations of damped RLC circuit. Where, U_0 is the charging voltage of the device, C_0 is the total capacitance of the device and L_0 is the nominal inductance of the device.

The characteristic axial transit velocity is determined as [Lee 2014], [Lee 2017]:

$$v_a=\frac{z_0}{t_a}=\left[\frac{\mu\ln\left(\frac{b_0}{a_0}\right)}{4\pi^2\left(\left(\frac{b_0}{a_0}\right)^2-1\right)}\right]^{1/2}\frac{f_c}{\sqrt{f_m}}\,\frac{I_0}{a_0\sqrt{\rho_0}} \tag{6.2.17}$$

Also the α_a scalling parameter is determined as [Lee 2014]. [Lee 2017]:

$$\alpha_a = \frac{t_0}{t_a} = \frac{\sqrt{L_0C_0}}{t_a} = \left[\frac{\mu\ln\left(\frac{b_0}{a_0}\right)}{4\pi^2 f_m \rho_0\left(\left(\frac{b_0}{a_0}\right)^2 - 1\right)}\right]^{1/2} \frac{f_c U_0 C_0}{z_0 a_0} \tag{6.2.18}$$

The α_a scalling parameter in equation (6.2.18) is the ratio of the characteristic electrical discharge time (characteristic time of oscillating RLC circuit) $t_0 = (L_0C_0)^{0.5}$ to the characteristic axial transit time t_a (equation (6.2.16)). Thus, the α_a scalaing parameter is actually an indicator of the matching of electrical drive time to the axial transit time for efficient magnetic and kinetic energy transfer from magnetic piston to the plasma pinch (when $\alpha_a = 1$ most efficient transfer of magnetic and kinetic energy into plasma pinch is predicted).

The last part of the equation (6.2.18) is known as the speed or drive factor (*SF or S or RF* symbols are used) of the plasma-focus (determined for all eletromagneticly driven devices). This factor is expressed as [Lee 2014], [Lee 2017]:

$$SF = \frac{I_0}{a_0\sqrt{\rho_0}} \tag{6.2.19}$$

All symbols in equation (6.2.19) are the same as in equation (6.2.16).

6.2.7. Additional relations and data used in the Lee model code – inductances and voltages

In the phase I and V of discharge (axial phases) the dynamic plasma inductance is described as [Lee 2014] [Lee 2017]:

$$L = \frac{\mu}{2\pi}\ln\left(\frac{b_0}{a_0}\right) z \tag{6.2.20}$$

In equation (6.2.20), μ is the magnetic permability of vacuum, b_0 is the reduced cathode radius, a_0 is the anode radius and z is the axial position of magnetic piston.

In the phase II, III and IV (radial phases) the dynamic plasma inductance is described as [Lee 2014] [Lee 2017]:

$$L = \frac{\mu}{2\pi}\ln\left(\frac{b_0}{a_0}\right) z_0 + \frac{\mu}{2\pi}\ln\left(\frac{b_0}{r_p}\right) z_f \tag{6.2.21}$$

In equation (6.2.21), z_0 is the length of the anode inside the experimental chamber, r_p is the radial position of magnetic piston and z_f is the axial position of magnetic piston.

Using the dynamic plasma inductance from equation (6.2.20) the total voltage for the phase I and V is determined as [Lee 2014] [Lee 2017]:

$$U = \frac{d}{dt}(Lf_cI) = f_c\frac{\mu}{2\pi}\ln\left(\frac{b_0}{a_0}\right)\left(I\frac{dz}{dt} + z\frac{dI}{dt}\right) \tag{6.2.22}$$

In equation (6.2.22), f_c is the axial current factor (described in subsection 6.3.2), *dz/dt* is the axial velocity of magnetic piston, *I* is the total discharge current and *dI/dt* is the time derivative of the total discharge current.

Using the dynamic plasma inductance from equation (6.2.21) the total voltage for the phase II and III is determined as:

$$U = \frac{d}{dt}(Lf_{cr}I) = f_{cr}\frac{\mu}{2\pi}\left[I\left(-\frac{z_f}{r_p}\frac{dr_p}{dt} + \ln\left(\frac{b_0}{r_p}\right)\frac{dz_f}{dt}\right) + \left(\ln\left(\frac{b_0}{a_0}\right)z_0 + \ln\left(\frac{b_0}{r_p}\right)z_f\right)\frac{dI}{dt}\right] \qquad (6.2.23)$$

In equation (6.2.21), f_{cr} is the radial current factor (described in subsection 6.3.2) and I is the total discharge current.

In phase IV, the equation (6.2.23) is modified using Spitzer resistivity. So, the voltage across tube terminals is computed as:

$$U = f_{cr}\frac{\mu}{2\pi}\left[I\left(-\frac{z_f}{r_p}\frac{dr_p}{dt} + \ln\left(\frac{b_0}{r_p}\right)\frac{dz_f}{dt}\right) + \left(\ln\left(\frac{b_0}{a_0}\right)z_0 + \ln\left(\frac{b_0}{r_p}\right)z_f\right)\frac{dI}{dt}\right] + f_{cr}IR_S \qquad (6.2.24)$$

In equation (6.2.24), R_S is the Spitzer resistivity (see subsection 6.2.11).

6.2.8. Additional relations and data used in the Lee model code – effective charges and specific heat ratios

The data concerning the ionization effects in plasma are in general based on the corona model which in an approximated plasma model for spectroscopy [Elton 1971], [Anders 1990]. In the corona plasma model lower densities of plasma are assumed and the ionization coeeficients depend only on plasma temperature (temperature of ionized gas). The data from the corona model which are stored within the Lee model code and used are: ionization curves and ionization energies. Based on ionization curves and ionization energies: the effective charges, the specific heat ratios and the characteristics of soft X-ray emission are computed in the Lee model code (emission powers and yields). Moreover, the atomic information about working gases were obtained from the NIST database and also stored within the code [NIST 2019].

The effective charge of plasma particles composed of single gas species of type j is expressed as [Ching 2010], [Akel 2019]:

$$Z_{eff,j} = \frac{N_{electron,j}}{N_{ion,j}} = \frac{\sum_{z=0}^{Zn-j} zN_{z,j}}{\sum_{z=1}^{Zn-j} N_{z,j}} \qquad (6.2.25)$$

In equation (6.2.25), the $N_{z,j}$ is the number of ions type j (deuterium or argon) in the z-th state. Wherein, the summation is carried out starting from $z = 0$ or $z = 1$ state up to Zn-th state of ion type j. The equation (6.2.25) was developed based on the ratio of $N_{electron,j}$ to $N_{ion,j}$ which are the total number densities of: electrons and ions, respectively, in all states derive from atoms of type j.

If mixture of two gases is used than for each ionized gas type effective charge is computed based on equation (6.2.25) resulting in: Z_{eff1} and Z_{eff2} values. Both values Z_{eff1} and Z_{eff2} are used for computation of the total effective charge of plasma composing of gas mixture as: $Z_{eff} = v_1Z_{eff1} + v_2Z_{eff2}$. This relation is also used for obtaining the total atomic number of gas mixture used in calculations: $Z = v_1Z_1 + v_2Z_2$. Wherein, the v_1 and v_2 are the relative volumetric fractions of gas 1 and 2 (assuming ideal gas model).

The specific heat ratio γ of plasma composed of ionized gas type j is expressed using number of degree of freedom f_j of gas particles as: $\gamma_j = (2+f_j)/f_j$. The degree of freedom for single gas species j is expressed as [Ching 2010] [Akel 2019]:

$$f_j = 3 + \frac{U_{ie,j}}{\frac{1}{2}kT(1+Z_{eff,j})} \tag{6.2.26}$$

In equation (6.2.26), k is the Boltzmann's constant, T is plasma (ion) temperature (average and uniform temperature of ionized gas or gas mixture – see subsection 6.2.10), $Z_{eff,j}$ is the effective charge of plasma type j (from equation (6.2.25)) and $U_{ie,j}$ is the effective ionization energy of ions type j. The effective ionization energy of ions type j is computed as [Ching 2010], [Akel 2019]:

$$U_{ie,j} = \sum_{z=1}^{Zn-j} N_{z,j} U_{ie,z,j} \tag{6.2.27}$$

In equation (6.2.27), N_z is the number of ions of type j in the z-th ionized state and $U_{ie,z,j}$ is the amount of energy required to ionize a neutral gas atom of type j to z-th state. Wherein, the summation is carried out starting from $z = 1$ state up to Zn-th state of ion type j.

For the two gas mixture with volumetric fractions v_1 and v_2 the total degree of freedom f is expressed as [Ching 2010], [Akel 2019]:

$$f = 3 + \frac{v_1 U_{ie1} + v_2 U_{ie2}}{\frac{1}{2}kT[v_1(1+Z_{eff1}) + v_2(1+Z_{eff2})]} \tag{6.2.28}$$

In equation (6.2.28), k is the Boltzmann's constant, T is plasma temperature (average and uniform temperature of ionized gas or gas mixture – see subsection 6.2.10), Z_{eff1} and Z_{eff2} are effective charges of plasma composed of ions type 1 and 2 (based on eqution (6.2.25)) and U_{ie1} and U_{ie2} are the effective ionization energies of ions type 1 and 2 (based on equation (6.2.27)). Using the total degree of freedom the total specific heat ratio is expressed as: $\gamma = (2+f)/f$.

6.2.9. Additional relations and data used in the Lee model code – small disturbance speed

In the slug model describing all radial phases of the Lee model code the shock wave theory is applied [Gross 1965], [Lee 1970], [Gross 1971], [Hintz 1971], [Potter 1978]. Thanks to the shock wave theory and an adiabataic approximation used in the Lee model code shock wave can be distringuished from the current sheet and uniform plasma pressure between shock and sheet can be determined. This results in so called infinite acoustic speed approximation or infinite small disturbances speed approximation. In other words, in the slug model it is assumed that the pressure exerted by the magnetic piston is instantaneously felt by the shock front. Likewise, the shock speed is instantaneously felt by the current sheet. This leads to too high values of sheet and shock velocities. However, since the small disturbance speed is actually finite there should be some nonzero time lapse Δt_{SDS} communicating between shock front and current sheet. This communication delay was incorporated into the Lee model as: $\Delta t_{SDS} = (r_p - r_s) / v_{SDS}$. Wherein, r_p is the relative current sheet (piston) position, r_s is the relative shock postion (r_r in phase III) and v_{SDS} is the small disturbance speed. In order to compute the finit *SDS* correction, following relation describing small disturbance speed is used [Lee 2014], [Lee 2017]:

$$v_{SDS} = C_S = \left(\frac{\partial P}{\partial \rho}\right)^{1/2} = \left(\frac{\gamma P}{\rho}\right)^{1/2} = \left(\frac{\gamma R D_C T}{MW}\right)^{1/2} \tag{6.2.29}$$

In equation (6.2.29), $v_{SDS} = C_s$ is the small disturbance speed as acoustic (sound) velocity in ionized gas, γ is the total specific heat ratio of gas or gas mixture (see subsection 6.2.8), ρ is total the ambient density of gas or gas mixture inside the moving slug (between sheet and shock), R is the universal gas constant, MW is the total molecular weigh of gas or gas mixture, D_c is the departure cooeficent, T is the (shocked) plasma temperarure (see subsection 6.2.10) and P is the shock pressure (pressure between sheet and shock) [Gross 1965], [Lee 1970], [Lee 2014], [Lee 2017].

The total molecular weight of gas mixture in equation (6.2.29) is expressed as: $MW = v_1MW_1 + v_2MW_2$, where v_1 and v_2 are volumetric fractions of gas type 1 and 2 and MW_1 and MW_2 are molecular weights of gas type 1 and 2.

The departure coefficient in equation (6.2.29) is expressed as: $D_c = DN(1+Z_{eff})$, wherein Z_{eff} is the total effective charge number of gas or gas mixture (see subsection 6.2.8) and DN is the total dessociation number of gas or gas mixture. The total dessociation number of gas mixture is expressed as: $DN = v_1DN_1 + v_2DN_2$, where v_1 and v_2 are volumetric fractions of gas type 1 and 2 and DN_1 and DN_2 are dessociation numbers of gas type 1 and 2.

Moreover, any irregularity (e. g. small kink MHD instability) will transmit (information about the conditions related to the kink) across a plasma column (phase IV) at the small disturbance speed. When that information has transmitted across the column, the whole column may become kinked, disrupt and no longer remain a stable form. Thus, generally the lifetime of stability of a plasma column in phase IV (t_{pl}) is taken to be limited by the tranisit time of small disturbance speed as: $t_{pl} = 2\ r_p\ /\ v_{SDS}$ (r_p is the plasma column radius taken as piston relative position describing the border of column). And this is the minimum time needed for the development of instabilities inside the stable plasma column in mechanical pressure balance, since there might be other effects present stabilizing, like for example large Larmor radius effect [Liberman 1999], [Haines 2011].

6.2.10. Additional relations and data used in the Lee model code – temperatures and densities

The plasma ion temperature and volumetric ion number density, in phases of discharge II and III, are obtained from the shock wave theory (shock-jump equations) [Gross 1965], [Lee 1970], [Gross 1971], [Hintz 1971], [Potter 1978]. The shocked plasma temperature (shock heating) of moving slug in phase II is expressed as [Ching 2010], [Lee 2014], [Lee 2017]:

$$T = \frac{MW}{RD_c}\frac{2(\gamma-1)}{(\gamma+1)^2}\left(\frac{dr_s}{dt}\right)^2 \tag{6.2.30}$$

The shocked plasma temperature of moving slug in phase III is expressed as [Ching 2010], [Lee 2014], [Lee 2017]:

$$T = \frac{MW}{RD_c}\frac{2(\gamma-1)}{(\gamma+1)^2}\left(\frac{dr_r}{dt}\right)^2 \tag{6.2.31}$$

And the shocked plasma volumetric ion number density of gas type j in moving slug in phases II and III is expressed as [Ching 2010], [Lee 2014], [Lee 2017]:

$$n_j = v_j n_0 f_{mr}\frac{(\gamma+1)}{(\gamma-1)} \tag{6.2.32}$$

In equation (6.2.30), (6.2.31) and (6.2.32) MW is the total molecular weigh of gas or gas mixture (as in subsection (6.2.9)), R is the universal gas constant, D_c is the departure cooeficent (as in subsection (6.2.9)), γ is the total specific heat ratio of gas or gas mixture (see subsection 6.2.8), r_s is the relative position of the shock wave in phase II, r_r is the relative position of the shock wave in phase III, v_j is the volumertric fraction of gas type j in mixture, f_m is the axial mass factor (see subsection 6.3.2), f_{mr} is the radial mass factor (see subsection 6.3.2) and n_0 is the total ambient number density (initial volumetric ion number density of gas or gas mixture). Wherein, $n_0 = 6 \times 10^{26} \rho_0/MW$, where ρ_0 is the total ambient density for gas or gas mixture initially between electrodes and in experimental chamber (taken as density of ideal gas in normal conditions based on initial pressure value) and MW is the total molecular weigh of gas or gas mixture (as in subsection (6.2.9)).

Furthermore, in the pinch phase of discharge (phase IV) the plasma ion temperature T_p is computed using modified Bennett equation (based on equation (2.1.6)) – ohmic heating of plasma pinch [Ching 2010], [Lee 2014], [Lee 2017]:

$$T_p = \frac{\mu}{8\pi^2 k} \frac{f_{cr}^2 I^2}{D_c n_0 a_0^2 f_{mr}} \tag{6.2.33}$$

And the plasma volumetric ion number density $n_{p,j}$ of gas type j in the pinch phase (phase IV) of discharge is computed using mass conservation equation resulting in [Ching 2010], [Lee 2014], [Lee 2017]:

$$n_{p,j} = v_j n_0 f_{mr} \left(\frac{a_0}{r_p}\right)^2 \tag{6.2.34}$$

In equation (6.2.33) and (6.2.34), μ is the magnetic permeability of vacuum, k is the Boltzmann's constant, I is the total discharge current ($f_{cr}I = I_{pp}$ is the current flowing through plasma pinch), a_0 is the anode radius, r_p is the radius of plasma column (relative position of current sheet in phase IV). The rest of symbols are the same as in equations from (6.2.30) to (6.2.32).

The total ion number density n in all phases of discharge, for plasma composed of two types of ions, is expressed as: $n = n_1 + n_2$ ($n_p = n_{p1} + n_{p2}$ in phase IV). Wherein, n_1 and n_2 are ion number densities of plasma type 1 and 2 (n_{p1} and n_{p2} are ion number densities of plasma type 1 and 2 in phase IV). Thus, $n_1 = v_1 n$ and $n_2 = v_2 n$ ($n_{p1} = v_1 n_p$ and $n_{p2} = v_2 n_p$ in phase IV). Also, for the plasma composed of two species, temperatures are always equal: $T = T_1 = T_2$, where T_1 is plasma temperature of ionized gas type 1 and T_2 is plasma temperature of ionized gas type 2 ($T_p = T_{p1} = T_{p2}$ in phase IV).

6.2.11. Additional relations and data used in the Lee model code – Ohmic heating, resistivity and X-ray emission

In equation (6.2.11), the component responsible for power of ohmic heating and X-ray emission dQ/dt is introduced. This component is the difference between total power of ohmic heating and total power of X-ray emission: $dQ/dt = P_{ohm} - P_{brem} - P_{line} - P_{rec}$. Wherein, the ohmic heating term (Joule heat) presented in equation (2.1.22) comes from the following relation (generalized Ohm's law) [Lee 2014], [Lee 2017]:

$$P_{ohm} = \frac{dQ_J}{dt} = R_S f_{cr}^2 I^2 \tag{6.2.35}$$

In equation (6.2.35), the f_{cr} is the radial current factor (see subsection 6.3.2), I is the total discharge current ($f_{cr}I = I_{pp}$ is the current flowing through plasma pinch) and R_S is the plasma resistivity. The plasma resitivity in the Lee model code is described by Spitzer resitivity equation in the following form [Lee 2017]:

$$R_S = \frac{1290 Z_{eff} z_f}{\pi r_p^2 T_p^{3/2}} \tag{6.2.36}$$

In equation (6.2.36), Z_{eff} is the total effective charge of plasma (see subsection 6.2.8), z_f is the relative axial position of sheet-shock, r_p is the relative current sheet position (plasma column radius) and T_p is the plasma temperature (see subsection 6.2.10).

The X-ray emission power terms for the dQ/dt are described by equations (2.1.19), (2.1.20) and (2.1.21). In these equations the T_p is the plasma pinch temperature from equation (6.2.33), n_p is the plasma pinch total ion number density based on equation (6.2.34), Z_{eff} is the total effective charge of plasma (as in subsection 6.2.8), $Z = v_1Z_1 + v_2Z_2$ is the total atomic number of gas or gas mixture (where v_1 and v_2 are volumetric fractions of gas type 1 and 2), $I_{pp} = f_{cr}I$ is the current flowing through plasma pinch (based on equations from subsection 6.2.4), f_{cr} is the radial current factor and I is the total discharge current), r_p is the plasma column radius (relative radial current sheet position based on equations from subsection 6.2.4) and $z_p = z_f$ is the plasma column length (z_f is the relative axial position of sheet-shock based on equations from subsection 6.2.4). Wherein, because of the plasma self absorption and transit from volumetric X-ray emission to surface emission (see subsection 6.2.12) the equation (2.1.19) describing line (soft) X-ray emission power can change into [Lee 2014], [Lee 2017]:

$$P_{line} = \frac{dQ_{line}}{dt} = 4.62 \times 10^{-16}\, Z_{eff}^{0.5} Z^{3.5} r_p z_p T_p^4 \tag{6.2.37}$$

All symbols in equation (6.2.37) are the same as in equations (2.1.19), (2.1.20) and (2.1.21) (as described above).

6.2.12. Additional relations and data used in the Lee model code – plasma opacity

Plasma self absorption [Robson 1989a] and transition from volumetric X-ray emission to surface X-ray emission in plasma column are implemented inside the Lee model code. This implementation uses photonic excitation number P_{en} written as [Lee 2014], [Lee 2017]:

$$P_{en} = \frac{1.66 \times 10^{-15} r_p Z^{0.5} n_p}{Z_{eff} T_p^{1.5}} \tag{6.2.38}$$

In equation (6.2.38), r_p is the plasma column radius (relative radial current sheet position based on equations from subsection 6.2.4), $Z = v_1Z_1 + v_2Z_2$ is the total atomic number of gas or gas mixture (where v_1 and v_2 are volumetric fractions of gas type 1 and 2), n_p is the total plasma pinch ion number density (based on equation (6.2.34)), T_p is the plasma pinch ion temperature (from equation (6.2.33)) and Z_{eff} is the total plasma effective charge (as in subsection 6.2.8). Thanks to the photonic excitation number P_{en} the volumetric plasma self-absorption correction factor f_0 (as in equation (2.1.13)) is determined [Lee 2014], [Lee 2017]:

$$f_0 = \left(\frac{T_p^{3.5}}{1+10^{-14} n_p Z_{eff}}\right)^{1+P_{en}} \tag{6.2.39}$$

Transition from volumetric to surface emission occurs when f_0 goes down from 1 to smaller values than 1/2.718 (when $f_0 = 1$ there is no self absorption and when $f_0 = 0$ the radiation is fully self absorbed). Moreover, when the emission becomes surface like the equation (2.1.19) describing line (soft) X-ray emission changes into (6.2.37).

6.2.13. Additional relations and data used in the Lee model code – neutron emission

In the Lee model code two different equations describing neutron emission are used. The first one describes the neutron yield based on the thermonuclear fusion model. In this model plasma is composed of uniformly spread deuterium ions having the same average energy. If the energy per ion is high enough fusion can be achived. The neutron equation based on this model can be described as [Lee 2014], [Lee 2017]:

$$dY_{th} = 0.5 n_{pD}^2 \pi r_p^2 z_p \langle \sigma v \rangle \Delta t \tag{6.2.40}$$

In equation (6.2.40), dY_{th} is the neutron yield based on the thermonuclear fusion model emitted during single time interval, n_{pD} is the ion number density of deuterium inside plasma pinch in given time (averaged and uniform along pinch dimensions) (from equation (6.2.34)), r_p is the plasma pinch radius at given time (assuming column shape) (based on equations from subsection 6.2.4), $z_p = z_f$ is the plasma pinch length at given time (assuming column shape) (based on equations from subsection 6.2.4), $<\sigma v>$ is the thermalized fusion cross-section-velocity product corresponding to the plasma temperature for the time interval under consideration and Δt is the investigated time interval [Lee 2014]. The total neutron yield value based on the thermonuclear fusion model Y_{th} is computed by summing up over all time intervals during the pinch phase of discharge (summing over all dY_{th}).

The second equation describes the neutron yield based on the beam-target nuclear fusion model. It is phenomenological equation based on the vacuum (plasma) diode mechanism. In this model a beam of fast deuteron ions is produced by a vacuum diode in a thin layer close to the anode, with plasma disruptions generating the necessary high voltages. The generated deuteron beam interacts with the hot dense plasma (plasma ions are uniformy spread and have the same average energy) of the focus pinch column to produce the fusion neutrons. The neutron yield based on beam-target fusion model (Y_{b-t}) was deduced [Lee 2008a], [Lee 2008b], [Lee 2014], [Lee 2017] as:

$$Y_{b-t} = C_n \, n_{pmaxD} \, I_{pp}^2 \, z_{pmax}^2 \ln\left(\frac{b_0}{r_{pmin}}\right) \sigma_{3Umax} \, U_d^{-0.5} \tag{6.2.41}$$

In the equation (6.2.41), the C_n is the scaling constant (calibrated from available global data), the n_{pmaxD} is the maximum ion number density of deuterium in plasma pinch during discharge (average and uniform along pinch dimensions), the $I_{pp} = f_{cr} I$ is the initial (maximum) current flowing through the plasma pinch (uniform along pinch dimensions) (f_{cr} is radial current factor), the r_{pmin} is the final (minimum) plasma pinch radius during discharge (assuming column shape), the z_{pmax} is the final (maximum) pinch length during discharge (assuming column shape), the b_0 is the reduced cathode radius, the σ_{3Umax} is the cross-section of the D-D fusion reaction (for the beam of deuterons with energy equal to three times maximum discharge voltage induced during discharge – U_{max}) in n-branch and the U_d is the disruption-caused diode voltage [Gribkov 2007]. Data fitting gave

$U_d = 3U_{max}$, where U_{max} is the maximum voltage induced by the radially collapsing current sheet during discharge (maximum tube voltage induced). The $C_n = 8.54 \times 10^8$ is a global constant which was calibrated [Lee 2008b] at an experimental point of 0.5 MA from a graphical presentation of all available measured total neutron yield data (Y_n) from the experiments on the different plasma-focus devices.

The beam-target neutron yield in the Lee model code is additionaly also computed as time function:

$$dY_{b-t}(t) = C_n \, n_{pD}(t) \, I_{pp}^2(t) \, z_p^2(t) \ln\left(\frac{b_0}{r_p(t)}\right) \sigma_{3Umax} \, U_d^{-0.5} \Delta t \tag{6.2.42}$$

In equation (6.2.42), the $dY_{b-t}(t)$ is the beam-target neutron yield computed for given time step of the code, the $n_{pD}(t)$ is the ion number density of deuterium, the $I_{pp}(t) = f_{cr}I(t)$ is the current flowing through plasma pinch (f_{cr} is radial current factor), the $z_p(t)$ is the plasma pinch length, the $r_p(t)$ is the plasma pinch radius and Δt is the investigated time interval. The rest of the symbols are the same as for equation (6.2.41).

Based on the equation (6.2.40) and (6.2.41) the total neutron yield per discharge (Y_n) can be expressed as: $Y_n = Y_{th} + Y_{b-t}$. And based on the equation (6.2.40) and (6.2.42) total neutron yield per given time step (dY_n) can be expressed as: $dY_n = dY_{th} + dY_{b-t}$. Wherein, it is worth to mention that the results of computations based on the above equations show that the computed Y_{b-t} and dY_{b-t} values are practically always much larger than the computed Y_{th} and dY_{th} values. Thus, the total neutron yield per discharge can be approximately described as: $Y_n \approx Y_{b-t}$. And total neutron yield per given time step as: $dY_n \approx dY_{b-t}$.

6.3. Input and output parameters of the 5-phase Lee model code

6.3.1. Input parameters

There are 20 input parameters in the RADPFV5.013.9b version of 5-phase Lee model code [Ching 2010] [Lee 2014] [Lee 2017] [plasmafocus.net 2019]:

I. Operation parameters:

1) $\boldsymbol{C_0}$ (μF) – total capacitance of the condenser bank of the device.
2) $\boldsymbol{L_0}$ (nH) – total (nominal) static inductance of the device.
3) $\boldsymbol{R_0}$ (mΩ) – total (nominal) static resistance of the device.
4) $\boldsymbol{b_0}$ (cm) – cathode reduced radius (cathode radius minus the radius of single cathode rod) of the device.
5) $\boldsymbol{a_0}$ (cm) – anode radius of the device.
6) $\boldsymbol{z_0}$ (cm) – length of anode (inside the experimental chamber) of the device.
7) $\boldsymbol{U_0}$ (kV) – charging voltage of the device.

II. Gas parameters:

8) $\boldsymbol{p_0}$ (Torr) – total pressure of gas mixture.
9) $\boldsymbol{MW_1}$ – atomic mass (molecular weight) of the first working gas.
10) $\boldsymbol{A_1}$ – atomic number of the first working gas.
11) ***At-1_mol2*** or $\boldsymbol{DN_1}$ – dissociation number of the first working gas (monatomic or diatomic gas).
12) $\boldsymbol{v_1}$ – fraction of volume of the first working gas in relation to the volume of entire gas mixture (the same as the fraction by pressure assuming ideal gas).

13) **MW_2** – atomic mass (molecular weight) of the second working gas.
14) **A_2** – atomic number of the second working gas.
15) ***At-1_mol2*** or **DN_2** – dissociation number of the second working gas (monatomic or diatomic gas).
16) **v_2** – fraction of volume of the second working gas in relation to the volume of entire gas mixture (the same as the fraction by pressure assuming ideal gas).

III. Model parameters:
17) **f_m** – axial mass factor.
18) **f_c** – axial current factor.
19) **f_{mr}** – radial mass factor.
20) **f_{cr}** – radial current factor.

The operation parameters (C_0, L_0, R_0, b_0, a_0, z_0, U_0) characterize the PF device – they enable Lee model code to operate as given PF device. The gas parameters (p_0, MW_1, A_1, DN_1, v_1, MW_2, A_2, DN_2, v_2) describe the mixture of working gases filling the experimental chamber of PF device. The model parameters (f_m, f_c, f_{mr}, f_{cr} – described in details in next subsection) enable to conclude approximately diffrent effects during PF discharge which are not included in the 0/1-dimensional snow-plough and slug model's description used in the code and which influence the current and mass flow in the system (they enable different scenarios of discharge under the same initial conditions). The model parameters together with L_0 and R_0 parameters are adjusted during fitting procedure of current traces – measured current trace is fitted with simulated current trace (described in subsection 6.4.5). The procedure of fitting of current traces enables the Lee model code to reproduce in approximation the real discharge that occurred in given PF device under given operation and gas parametrers conditions [Lee 2014]. All 20 input parameters determine the entire simulation process of the single PF discharge.

6.3.2. Input parameters – model parameters

The f_m, f_c, f_{mr} and f_{cr} parameters appear in all equations describing the dynamic of current sheet and shock motion as well as in other relations describing operation of the Lee model code (as was presented in subsections from 6.2.1 to 6.2.13) [Lee 2014], [Lee 2017]. These parameters were introduced into the Lee model to approximate the various effects occurring during the discharges, thus allowing various possible scenarios for the development of a single discharge.

The parameters f_m and f_{mr} describe the fraction of gas mass that was effectively swept, ionized and became plasma in the magnetic piston during the axial and radial phases of discharge, respectively. These fractions refer to the total mass of gas mixture that was present across the current sheet-shock way (in each moment of time as well as during entire axial phase and radial phase). Using these two parameters the effects that influence the effective mass sweep into the plasma structure such as: porosity of current sheet, inclination (curvature) of the moving current sheet-shock, boundary layer effects and axial mass streaming are accounted approximately (as well as all other effects that influence the effective mass sweep into plasma structure including the unkown ones) [Lee 2014], [Lee 2017].

Similarly, the f_c and f_{cr} parameters describe the fraction of current that effectively flows through the piston structure ("drives" it) during the axial and radial phases, respectively. These fractions refer to the total current flowing between the electrodes in the experimental chamber (in each moment of time as well as during entire axial and radial phases). Using these two parameters effects such as: current shedding at/or near the back-wall, current sheath inclination, current shunting, current fragmenting, current sheet bifurcation, plasma/current necking (constriction) and disruptions leading to axial acceleration and ejection of mass are approximated (as well as all other effects that influence the effective current flow in the moving plasma structure including the unkown ones) [Lee 2014], [Lee 2017].

The change of gas mass sweeping and current flow cause changes in the dynamic of the current sheet and shock movement as well as in the thermodynamics and radiation process influencing the generated plasma pinch behaviour [Lee 2014], [Lee 2017].

6.3.3. Output data and parameters

Among the many output data of the RADPFV5.013.9b version of 5-phase Lee model code, only important for this work are listed [RADPF 2019]:

- $I(t)$ (kA) – (total discharge) current,
- $U(t)$ (kV) – (total plasma/tube/discharge) voltage,
- $z(t)$ (cm) – axial position of sheet-shock,
- $v_z(t)$ (cm/µs) – axial velocity of sheet-shock,
- $r_s(t)$ (mm) – radial shock position,
- $r_p(t)$ (mm) – radial current sheet (magnetic piston) position,
- $z_f(t)$ (mm) – axial position of sheet-shock (referenced to the anode end),
- $v_s(t)$ (cm/µs) – radial shock speed,
- $v_p(t)$ (cm/µs) – radial current sheath (magnetic piston) speed,
- $v_f(t)$ (cm/µs) – elongation speed of sheet-shock,
- $r_r(t)$ (mm) – reflected shock radial position,
- $T(t) = T_i(t)$ (K) – plasma (ion) temperature,
- $P_{Ohm}(t)$ (W) – ohmic (Joule) heating power,
- $P_{brem}(t)$ (W) – bremsstrahlung (X-ray) emission power,
- $P_{rec}(t)$ (W) – recombination (X-ray) emission power,
- $P_{line}(t)$ (W) – line (X-ray) emission power,
- $E_{Ohm}(t)$ (J) – time integrated Ohmic (Joule) heating power,
- $E_{brem}(t)$ (J) – time integrated bremsstrahlung (X-ray) emission power,
- $E_{rec}(t)$ (J) – time integrated recombination (X-ray) emission power,
- $E_{line}(t)$ (J) – time integrated line (X-ray) emission power,
- $E_{tot}(t)$ (J) – total energy of X-ray radiation emitted,
- $\Delta E_{tot}(t)$ (J) – total energy gain/loss,
- $f_0(t)$ – plasma self-absorption corrected coefficient,
- $P_{rad}(t)$ (W) – plasma radiation power (if black body),
- $\gamma(t)$ – total specific heat ratio,
- $Z_{eff}(t)$ – total effective plasma charge number,
- $dY_{th}(t)$ – thermal neutron yield,
- $dY_{b-t}(t)$ – beam-target neutron yield,
- $dY_n(t)$ – total neutron yield,
- $n_1(t) = n_{1i}(t)$ (1/m^3) – volumetric plasma (ion number) density of first ionized gas,
- $n_2(t) = n_{2i}(t)$ (1/m^3) – volumetric plasma (ion number) density of second ionized gas.
- $n(t) = n_i(t)$ (1/m^3) – total volumetric plasma (ion number) density,
- $P_{Vrad}(t)$ (W) – volume radiation power,
- $P_{Srad}(t)$ (W) – surface radiation power.

The position of the above presented data inside the main worksheet of Excel ("Sheet1") of the Lee model code is described in: [RADPF 2019]. The data which describe discharge and plasma are time functions – given type of data (parameter) is computed for each following time step during Lee model code operation. Some parameters are computed only during radial or pinch phase of discharge – see [RADPF 2019]. Moreover, other important plasma parameters are also computed, which are not time functions, like: the thermal total neutron yield per discharge (Y_{th}), the beam-target total neutron yield per discharge ($Y_{b\text{-}t}$) and the total neutron yield per discharge (Y_n). They are displayed in row 17 of the main worksheet of Excel. Based on the presented data user can determine 43 computed plasma parameters and radiative compression indicators important to plasma compression investigation:

I. Kinetic parameters:

1) t_c^{comp} (μs) – **compression time** – the time of run-down of magnetic piston along anode (axial direction of movement) and the moment of beginning of radial compression at the end of anode.
2) t_p^{comp} (μs) – **pinch time** – the time to plasma pinch generation.
3) v_z^{comp} (cm/μs) – **average axial velocity** – the average velocity of magnetic piston movement along anode (average velocity during the axial phase of discharge).
4) v_{zmax}^{comp} (cm/μs) – **maximum axial velocity** – the maximum velocity of magnetic piston moving along anode (maximum velocity during the axial phase of discharge).
5) v_{rmax}^{comp} (cm/μs) – **maximum radial velocity** – the maximum velocity of magnetic piston along face of anode (maximum radial velocity during the radial phases of discharge).

II. Electric parameters:

6) I_{max}^{comp} (kA) – **maximum current** – the maximum total current during discharge.
7) I_{maxpis}^{comp} (kA) – **maximum piston current** – the maximum current flowing through (driving) magnetic piston during discharge.
8) I_p^{comp} (kA) – **pinch current** – the total discharge current at the beginning of pinch phase of discharge (initial and maximum pinch current) corresponding to the t_p^{comp} time.
9) I_{pp}^{comp} (kA) – **pinch plasma current** – the current flowing through (driving) plasma pinch at the beginning of pinch phase of discharge (initial and maximum pinch plasma current uniformed along pinch dimensions) corresponding to the t_p^{comp} time.
10) U_{max}^{comp} (kV) – **maximum voltage** – the total maximum voltage induced by radially compressing current sheet during discharge.

III. Radiative compression indicators – currents:

11) $I_{P\text{-}Breduced}(t_1)^{comp}$ (kA) – **reduced P-B current at t_1** – the smallest value of reduced P-B current (see equation (2.1.16)) achieved during discharge (this value is reached at the t_1 time).
12) $I_{P\text{-}B}(t_1)^{comp}$ (kA) – **P-B current at t_1** – the P-B current (see equation (2.1.13)) at the moment when the smallest value of reduced P-B current is achieved (P-B current at t_1 time).
13) $I_{pp}(t_1)^{comp}$ – **pinch plasma current at t_1** – the current flowing through the plasma pinch (uniform current along pinch dimensions) at the moment when the smallest value of computed reduced P-B current is achieved (pinch plasma current at the t_1 time).

IV. Radiative compression indicators – times:

14) t_{pl}^{comp} (μs) – **pinch lifetime** – the stable plasma pinch lifetime (and duration of entire pinch phase of discharge).
15) t_{rcl}^{comp} (μs) – **radiative compression lifetime** – the entire period of time in which $I_{P\text{-}Breduced}^{comp}(t) < I_{pp}^{comp}(t)$.

16) t_Q^{comp} (μs) – **characteristic time of radiation depletion** – the characteristic time of radiation depletion per discharge (see equation (2.1.23)).

V. Plasma pinch parameters – dimensions:

17) r_{pmin}^{comp} (cm) – **minimum pinch radius** – the stable plasma pinch radius during the maximum compression moment (final and minimum pinch radius assuming cylindrical shape).
18) r_{p0}^{comp} (cm) – **initial pinch radius** – the stable plasma pinch radius at the beginning of pinch phase of discharge (initial and maximum pinch radius assuming cylindrical shape).
19) z_{pmax}^{comp} (cm) – **maximum pinch length** – the stable pinch length during maximum compression moment (final and maximum pinch length assuming cylindrical shape).
20) z_{p0}^{comp} (cm) – **initial pinch length** – the stable pinch length at the beginning of pinch phase of discharge (initial and minimum pinch length assuming cylindrical shape).
21) V_{pf}^{comp} (cm^3) – **final pinch volume** – the volume of stable plasma pinch at the maximum compression moment (final pinch volume assuming cylindrical shape).
22) V_{p0}^{comp} (cm^3) – **initial pinch volume** – the volume of stable plasma pinch at the beginning of pinch phase of discharge (initial pinch volume assuming cylindrical shape).

VI. Plasma pinch parameters – densities:

23) n_{pmaxD}^{comp} ($1/cm^3$) – **maximum pinch density of D** – the ion number density of deuterium during maximum compression moment (final and maximum deuterium density per discharge averaged and uniformed along pinch dimensions).
24) n_{p0D}^{comp} ($1/cm^3$) – **initial pinch density of D** – the ion number density of deuterium at the beginning of pinch phase of discharge (initial and minimum deuterium density per discharge averaged and uniformed along pinch dimensions).
25) n_{pmaxAr}^{comp} ($1/cm^3$) – **maximum pinch density of Ar** – the ion number density of argon during maximum compression moment (final and maximum argon density per discharge averaged and uniformed along pinch dimensions).
26) n_{p0Ar}^{comp} ($1/cm^3$) – **initial pinch density of Ar** – the ion number density of argon at the beginning of pinch phase of discharge (initial and minimum argon density per discharge averaged and uniformed along pinch dimensions).
27) n_{pmax}^{comp} ($1/cm^3$) – **total maximum pinch density** – the total ion number density of plasma during maximum compression moment (final and maximum plasma pinch density per discharge averaged and uniformed along pinch dimensions).
28) n_{p0}^{comp} ($1/cm^3$) – **total initial pinch density** – the total ion number density of plasma at the beginning of pinch phase of discharge (initial and minimum plasma pinch density averaged and uniformed along pinch dimensions).
29) N_{pfD}^{comp} (1/cm) – **final linear pinch density of D** – the linear ion number density of deuterium during maximum compression moment (final linear deuterium density averaged and uniformed along pinch dimensions, see equation (2.1.7)).
30) N_{p0D}^{comp} (1/cm) – **initial linear pinch density of D** – the linear ion number density of deuterium at the beginning of pinch phase of discharge (initial linear deuterium density averaged and uniformed along pinch dimensions, see equation (2.1.7)).
31) N_{pfAr}^{comp} (1/cm) – **final linear pinch density of Ar** – the linear ion number density of argon during maximum compression moment (final linear argon density averaged and uniformed along pinch dimensions, see equation (2.1.7)).
32) N_{p0Ar}^{comp} (1/cm) – **initial linear pinch density of Ar** – the linear ion number density of argon at the beginning of pinch phase of discharge (initial linear argon density averaged and uniformed along pinch dimensions, see equation (2.1.7)).

33) N_{pf}^{comp} (1/cm) – **total final linear pinch density** – the total linear ion number density of plasma during maximum compression moment (final linear plasma pinch density averaged and uniformed along pinch dimensions, see equation (2.1.7)).
34) N_{p0}^{comp} (1/cm) – **total initial linear pinch density** – the total linear ion number density at the beginning of pinch phase of discharge (initial linear plasma pinch density averaged and uniformed along pinch dimensions, see equation (2.1.7)).

VII. Plasma pinch parameters – temperatures:

35) T_{pmin}^{comp} (keV) – **minimum pinch temperature** – the plasma pinch ion temperature during maximum compression moment (final and minimum plasma pinch temperature averaged and uniformed along pinch dimensions).
36) T_{p0}^{comp} (keV) – **initial pinch temperature** – the plasma pinch ion temperature at the beginning of pinch phase of discharge (maximum and initial plasma pinch temperature averaged and uniformed along pinch dimensions).

VIII. Radiation yields and ohmic heating yield:

37) Y_{ohm}^{comp} (J/discharge) – **total ohmic heating yield** – the total yield of ohmic heating (Joule heat) per discharge.
38) Y_{brem}^{comp} (J/discharge) – **total X-ray bremsstrahlung yield** – the total yield of X-ray bremsstrahlung radiation per discharge.
39) Y_{rec}^{comp} (J/discharge) – **total X-ray recombination yield** – the total yield of X-ray recombination radiation per discharge.
40) Y_{line}^{comp} (J/discharge) – **total X-ray line yield** – the total yield of X-ray line radiation per discharge.
41) Y_{totrad}^{comp} (J/discharge) – **total X-ray yield** – the total yield of X-ray radiation per discharge ($Y_{totrad}^{comp} = Y_{brem}^{comp} + Y_{rec}^{comp} + Y_{line}^{comp}$).
42) Y_{eff}^{comp} (J/discharge) = $-Q$ – **effective total X-ray yield** – the difference between total X-ray radiation yield and total ohmic heating yield per discharge ($Y_{eff}^{comp} = -Q = Y_{totrad}^{comp} - Y_{ohm}^{comp} = Y_{brem}^{comp} + Y_{rec}^{comp} + Y_{line}^{comp} - Y_{ohm}^{comp}$).
43) Y_n^{comp} (n/discharge) – **total neutron yield** – the total yield of neutrons per discharge.

6.4. Simulation and fitting procedure in the 5-phase Lee model code

6.4.1. Single execution of the code (simulation) and simulated current trace

In order to execute the Lee model code single time the user needs to enter all 20 input parameters (described in subsection 6.3.1) and press “ctr+a” buttons. The initial values of model parameters need to be chosen by user himself or typically achieved values from previous experiments on different PF devices can be used. The computations during single execution last usually about 5-15 minutes on standard laptop computer. When the program ends the computations all output data will appear in columns starting from column A in the main worksheet of Excel (“Sheet1”). Each column represents one type of data (in reference to the beginning of entire discharge or beginning of radial phase) – see [RADPF 2019]. The graphs showing the time traces of selected data will appear automatically. In addition, the values of some important parameters will be also displayed in row 17.

In column A of the Sheet1 user will find the computed time steps (in microseconds) and in column B the computed values of simulated total discharge current (in kiloampers). Figure 6.4.1 shows the exemplary simulated trace of the total discharge current together with measured one. The simulated trace was generated using following 6 input parameters of the code: L_0 = 8.5 nH, R_0 = 3.1 mΩ, f_m = 0.1, f_c = 0.6, f_{mr} = 0.2 and f_{cr} = 0.5.

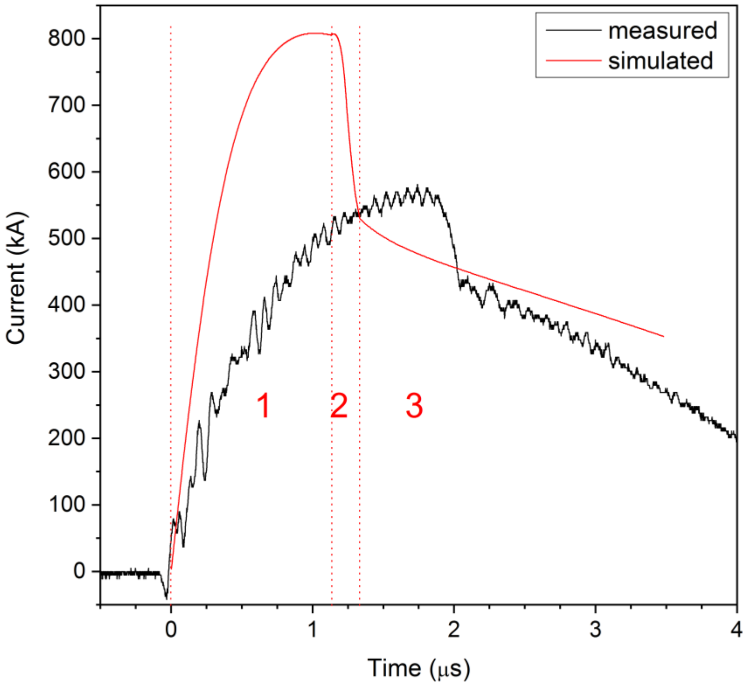

Figure 6.4.1. Exemplary measured (black curve) and simulated (red curve) total discharge current trace. The simulation was performed using: L_0 = 8.5 nH, R_0 = 3.1 mΩ, f_m = 0.1, f_c = 0.6, f_{mr} = 0.2 and f_{cr} = 0.5 input parameters. The numbers indicate parts of the discharge and refer to the computed trace (parts of computed trace). Part 1 (axial 1) is the axial phase. Part 2 (radial) is: the radial inward shock phase, the radial reflected shock phase and the pinch phase. Part 3 (axial 2) is the expanded column axial phase.

6.4.2. Theoretical phases of discharge vs experimental phases of discharge

In the 5-phase Lee model code the discharge is divided into 5 different phases (2 axial and 3 radial) as was presented in subsections from 6.2.1 to 6.2.5. On the other hand, the experimental discharge is usually divided into 3 phases in the Mather type plasma-focus devices as was presented in subsection 2.2.2. The theoretical phase I (axial) corresponds to the experimental phase I (breakdown and build-up) and phase II (run-down). The experimental phase I (breakdown and build-up) is actually not simulated in the Lee model code – properly generated plasma sheet-shock structure moving starting from the back wall of experimental chamber is always assumed (see figure 6.2.1). Still, in the experiments break-down and build-up of current sheet takes place very quickly and is only but a small fraction of entire run-down phase. Thus, the approximation of movement of very fast magnetic piston (supersonic velocities achived) starting from the back of experimental chamber wall is justified. The theoretical phase II (radial inward shock), III (radial reflected shock) and IV (pinch) correspond to the experimental phase III (radial compression and pinch). The Lee model code simulates a stable plasma pinch that relatively slowly compresses throughout entire pinch phase. Thus, only the quiet pinch experimental phase is actually simulated by the code (stable pinch in form of a column – instabilities neglected). Finally, the theoretical phase V corresponds to the last part of experimental phase III (late pinch phase or part of late pinch phase). Thus, three different groups of phases can be distinguished during theoretical discharges and in simulated current traces (parts of current traces) as well as they can be assigned to the experimental phases of discharge as was described. This division was marked in figure 6.4.1: part 1 – axial 1 (generation of plasma structure and run-down along anode), part 2 – radial (radial compression of plasma structure and plasma pinch generation), part 3 – axial 2 (expansion of plasma at the end of pinch phase).

6.4.3. Fitting procedure of current traces

The simulated current trace is used in the fitting procedure, during which it is adjusted to the measured current trace. The fitting procedure in the Lee model code is done manually by multiply execution of the code (multiply simulations). To start the fitting process, the user should paste I vs t data of measured trace of total discharge current anywhere in the "Sheet2" of Excel. Next, the user should display on the same graph both measured and computed current traces and observe whether they match in part 1 and 2 – see figure 6.4.1 (matching in part 3 is not important since it refers to the phases after plasma pinch generation). If the traces are not sufficiently well matched the fitting procedure continues. The user should now change the value of one or more input parameters of the code (see subsection 6.3.1), execute the code and compare the measured and computed current traces again. This procedure should be repeated until suffiecent match is achieved. The input parameters which are changed during the fitting procedure are called the fitting parameters – presented in next subsection.

6.4.4. Fitting parameters

There are 6 input parameters of the 5-phase Lee model code which are usually changed during fitting procedure – fitting parameters [Lee 2014], [Lee 2017]. These fitting parameters are the model parameters: f_m, f_c, f_{mr} and f_{cr} and two operation parameters: L_0 and R_0 (see subsections 6.3.1 and 6.3.2). First, it is advisable that the user tries to change only the values of f_m and f_c parameters (changing three significant numbers is usually enough) and observe if measured and computed trace are sufficiently well matched in part 1 (see figure 6.4.1). If it is not possible to match the traces in axial 1 part using only f_m and f_c fitting parameters then the user should start to change the values of L_0 and R_0 parameters and then again change the f_m and f_c parameters until sufficient match in axial 1 part is achieved. After determining the sufficient match of measured and computed current trace in axial 1 part and establishing the values of L_0, R_0, f_c and f_m fitting parameters the user should also change the values of f_{mr} and f_{cr} parameters referring only to the part 2 – radial (see figure 6.4.1). When also the f_{mr} and f_{cr} parameters are setteled and sufficient match of measured and computed (fitted) current trace in radial part is achieved then the entire fitting procedure is successful and all fitting parameters are established.

6.4.5. Examplary fitting procedure of simulated current trace

Figure 6.4.1 shows the simulated and measured current traces, which are not matched. As it is clearly seen, the initially used set of fitting parameters does not ensure the suffiecent match of current traces. However, if the 6 fitting parameters will be change to the: L_0^{comp} = 22 nH, R_0^{comp} = 10.8 mΩ, f_m = 0.155, f_c = 0.7, f_{mr} = 0.28 and f_{cr} = 0.64, the sufficient match is achived. Figure 6.4.2 shows the changes of the computed current trace after a successive adjustment of the fitting parameters. Each of the 6 computed traces corresponds to the change of single fitting parameter. The order of parameter changes was the following: L_0^{comp}, R_0^{comp}, f_m, f_c, f_{mr} and f_{cr}.

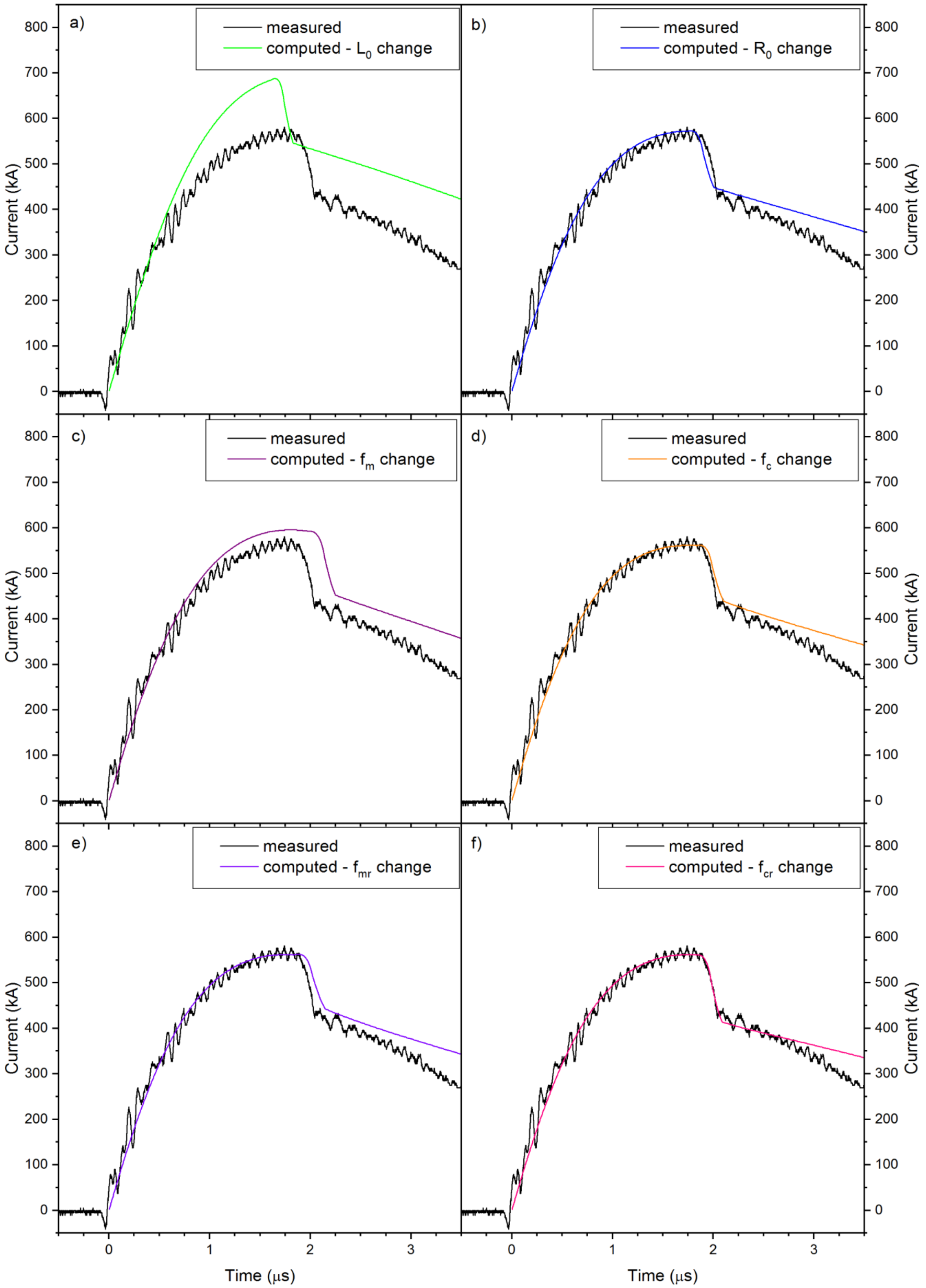

Figure 6.4.2. The measured discharge current trace is marked with black curve. The 6 computed current traces are marked with: green, blue, purple, orange, violet and pink trace. The green trace **a)**: L_0^{comp} = 22 nH, R_0^{comp} = 3.1 mΩ, f_m = 0.1, f_c = 0.6, f_{mr} = 0.2 and f_{cr} = 0.5. The blue trace **b)**: L_0^{comp} = 22 nH, R_0^{comp} = 10.8 mΩ, f_m = 0.1, f_c = 0.6, f_{mr} = 0.2 and f_{cr} = 0.5. The purple trace **c)**: L_0^{comp} = 22 nH, R_0^{comp} = 10.8 mΩ, f_m = 0.155, f_c = 0.6, f_{mr} = 0.2 and f_{cr} = 0.5. The orange trace **d)**: L_0^{comp} = 22 nH, R_0^{comp} = 10.8 mΩ, f_m = 0.155, f_c = 0.7, f_{mr} = 0.2 and f_{cr} = 0.5. The violet trace **e)**: L_0^{comp} = 22 nH, R_0^{comp} = 10.8 mΩ, f_m = 0.155, f_c = 0.7, f_{mr} = 0.28 and f_{cr} = 0.5. And the pink trace **f)**: L_0^{comp} = 22 nH, R_0^{comp} = 10.8 mΩ, f_m = 0.155, f_c = 0.7, f_{mr} = 0.28 and f_{cr} = 0.64.

Figure 6.4.2f shows the final step of fitting procedure, where the measured current trace is well matched with the computed one (in axial 1 part and radial part). The results indicate that effectively about 15.5% and 28% of the total mass of gas in front of moving structure was swept by the sheet-shock (became part of the structure) in the: axial 1 part and radial part, respectively. And, effectively about 70% and 64% of total discharge current was flowing through the current sheet structure in the: axial 1 part and radial part, respectively. The total inductance and resistance of the device were effectively equal to: 22 nH and 10.8 mΩ, respectively. In general, the higher total values of nominal inductance (L_0^{comp}) and resistance (R_0^{comp}) lead to smaller values of maximum currents and longer axial 1 part (see figure 6.4.1 and 6.4.2) – higher inductance and resistance in the system lead to smaller electric currents (assuming constant voltage power supply). The higher values of axial mass factor (f_m) lead to higher maximum currents and longer axial 1 part. This is due to the fact that, higher f_m values lead to increase of total mass (density) of working gas between electrodes, this results in slower movement of current sheet along electrodes and smaller values of plasma inductance in axial phase of discharge. The higher values of axial current factor (f_c) lead to smaller maximum currents and shorter axial 1 part. This is due to the fact that higher f_c values increase back electromotive force (EMF) causing increase in axial velocity of current sheet and increase inductance in axial phase which results ultimately in smaller maximum current. Similarly, the higher values of radial mass factor (f_{mr}) lead to higher pinch currents and longer radial part (see figure 6.4.1 and 6.4.2). While the higher values of radial current factor (f_{cr}) lead to smaller pinch currents and shorter radial part. The mechanism of f_{mr} and f_{cr} change in radial phase is analogous to the one for f_m and f_c in the axial 1 phase, but in radial phase the current sheet moves also in radial direction which also influences the inductance (see equation (6.2.21)).

Furthermore, it should be remembered that the presented computed currents in figure 6.4.2 describe discharges with smaller or optimum total mass/density of working gas or gases in the experimental chamber. However, if the experimental discharge will be performed in the higher than optimum total mass/density of working gas or gases then the current sheet will be unable to further sweep up mass as was explained in section 3.1. So, during the fitting procedure of this type of measured current trace with the computed current trace the increase of fitting parameters may not lead to the same changes as presented in figure 6.4.2. Finally, it should be remembered that the parameters achieved during the final step of the axial 1 part will influence the initial conditions in the radial part and thus entire radial part (indirect influence of axial fitting parameters on the radial phases) [Al-Hawat 2012], [Gautam 2017].

The fitting procedure in the Lee model code is currently performed manually by users. This means that a user after each execution of the code has to compare the measured and computed current traces simply using his own “naked eye”. The user himself assesses whether the current traces are sufficiently well matched, only by looking at both traces presented in the same graph. This usually gives proper results. Finally, the user should also determine the kintetic and electric output parameters of the discharge based on the measured and the computed traces (see subsections 5.3.2 and 6.3.3). If the computed current trace has similar character as the corresponding measured current trace and the computed parameters are within the error ranges of corresponding measured parameters (or at least close to them) the traces are assumed as sufficiently well matched. Otherwise, the entire fitting procedure should be performed again or the discharge should be marked as: “unable to match all the output parameters” (part of output parameters is well fitted), or even: “unable to be sufficiently well fitted” (most of output parameters is not sufficiently well fitted and characters of traces are significantly different) and discarded (cannot simulate).

6.4.6. Importance of current traces and fitting

The fitting procedure is based on the total discharge current because it is assumed to carry in its wave shape information on all processes occurring within the discharge, including the dynamics, energetics, thermodynamics and radiation (or at least the process that lead to change of mass sweep and current flow in moving sheet-shock structure). Thus, if the computed and measured total discharge current traces are sufficiently well matched then the computed current trace should present the realistic PF discharge in approximation. And this means that the entire computed discharge will be energy-, charge-, momentum- and mass-wise and the code will model approximately correct output data [Lee 2014], [Lee 2017]. In other words, the proper fitting of simulated current trace of discharge is a requirement in order to achieve realistic (approximately) and more precise data.

7. Performed discharges and acquired fitting parameters

A total number of 54 theoretical discharges was simulated using the 5-phase Lee model code – 12 in D_2, 21 in Ar and 21 in D_2+Ar mixtures. The total number of 501 experimental discharges was performed using the PF-24 device – 422 in D_2, 10 in Ar and 69 in D_2+Ar mixtures. From these 501 experimental discharges the total number of 123 was computed (simulated and fitted individually) using the 5-phase Lee mdoel code – 44 in D_2, 10 in Ar and 69 in D_2+Ar mixtures.

7.1. Theoretical discharges in D_2, Ar and D_2+Ar mixtures

Before carrying out series of experiments and corresponding computations, the theoretical discharges were performed using the 5-phase Lee model code (RADPFV5.013.9b version). For all theoretical discharges the following operation parameters (see section 6.3.1) were used to represent configuration of the PF-24 device (see subsection 5.1):

- $C_0 = 116.12$ µF, $U_0 = 17$ kV,
- $L_0^{mea} = 8.5$ nH, $R_0^{mea} = 3.1$ mΩ
- $b_0 = 3.1$ cm, $a_0 = 4.9$ cm, $z_0 = 17$ cm.

The following gas parameters were used to represent D_2 and Ar:

- $MW_1 = 4$, $A_1 = 1$, $DN_1 = 2$,
- $MW_2 = 40$, $A_2 = 18$, $DN_2 = 1$.

The following model parameters were chosen from previous plasma-focus experiments in the NX2 device:

- $f_m = 0.1$, $f_c = 0.7$,
- $f_{mr} = 0.2$, $f_{cr} = 0.9$.

Only the gas parameters: p_0, v_1 and v_2 were changed depending on the gas or gas mixture in which the theoretical discharges were carried out.

The fraction of D_2 was set as: $v_1 = 1$ and $v_2 = 0$ during 12 theoretical discharges in D_2, while the $v_1 = 0$ and $v_2 = 1$ was set during 21 theoretical discharges in Ar. For both discharges in pure D_2 and Ar, the initial pressure p_0 was changed between 0.5 mbar and 5.0 mbar.

The total initial pressure of the D_2+Ar mixture was kept at 3.0 mbar and $v_1 + v_2 = 1$, during 21 theoretical discharges in D_2+Ar gas mixtures. The percentage of Ar fraction (x) in the mixture was changed in the 1-95% range, where $x = 100\% \times v_2$.

The main aim of these theoretical simulations was to verify a possibility of plasma radiative compression phenomenon occurrence during discharges in the PF-24 device. Additional goal was to observe the dependence of output parameters on the gas pressure of D_2 and Ar and on Ar fraction in the Ar+D_2 mixture. Finally, the last goal was to compare the theoretical results with the results from coupled experiments-computations which were carried later on – comparison of changes in output plasma parameters, for discharges with constant and variable fitting parameters, including influence on radiative compression occurrence and strength.

7.2. Discharges in D_2 and acquired fitting parameters

A large number of experimental discharges (388) were carried out in the PF-24 device under variable initial D_2 pressure. Out of all 388 discharges 10 were selected as a representation – each for different initial D_2 pressure. The discharges were selected based on considerations concerning average total neutron emission – explained in subsection 8.7.2. The 10 discharges were simulated and fitted using 5-phase Lee model code – computed discharges. Below, in table 7.2.1 all the variable input parameters of the 5-phase Lee model code describing 10 discussed discharges are presented.

Table 7.2.1. The varable input parameters describing 10 discharges in D_2 and computed using the 5-phase Lee model code. The p_0, L_0^{comp}, R_0^{comp}, f_m, f_c, f_{mr} and f_{cr} stand for: the initial D_2 pressure, the computed nominal inductance, the computed nominal resistance, the axial mass factor, the axial current factor, the radial mass factor and the radial current factor, respectively.

O. n.	Discharge ID	p_0 (mbar)	L_0^{comp} (nH)	R_0^{comp} (mΩ)	f_m	f_c	f_{mr}	f_{cr}
1	17060101	2.16(±0.01)	19	7.5	0.053	0.7	0.45	0.9
2	17051108	2.25(±0.02)	19	9	0.13	0.7	0.35	0.9
3	17022304	2.36(±0.01)	25	10	0.08	0.7	0.35	0.9
4	17060806	2.50(±0.01)	19	9	0.07	0.7	0.35	0.9
5	17052903	2.73(±0.03)	19	10	0.1	0.7	0.35	0.9
6	17052303	3.00(±0.01)	17	8	0.14	0.7	0.35	0.9
7	17053004	3.32(±0.02)	19	9	0.14	0.7	0.35	0.9
8	17062707	3.72(±0.04)	19	9	0.11	0.7	0.35	0.9
9	17063013	4.45(±0.01)	21	6	0.14	0.7	0.35	0.8
10	17063019	4.71(±0.04)	19	10	0.135	0.7	0.41	0.9

As can be seen the L_0^{comp} and R_0^{comp} have higher values than the 8.5 nH and 3.1 mΩ. The average value of $<L_0^{comp}>$ and $<R_0^{comp}>$ is equal to: 19.6 nH and 8.8 mΩ, respectively. The f_m changes in the range between 0.053 and 0.14 ($<f_m> = 0.110$), while the f_c and f_{cr} remin almost constant at the level of: 0.7 and 0.9, respectively. The f_{mr} is equal to 0.35 except of the discharges in the lowest and highest pressure, where its value rises above 0.4 ($<f_{mr}> = 0.366$). Thus, the f_m and f_{mr} are next parameters, except L_0 and R_0, which were significantly different than during theoretical discharges in D_2 (especially f_{mr}). Moreover, it should be mentioned that all 10 discharges have been stated as sufficiently well fitted, despite the fact that in 2 discharges not all parameters have been sufficiently well fitted – see chapter 8 (most of parameters have been sufficiently well fitted and current traces have similar character).

Additionaly, the measured current traces and corresponding current derivative over time traces for discharges at 2.16(±0.01) mbar, 3.00(±0.01) mbar, and 4.71(±0.04) mbar (ID numbers: #17060101, #17052303 and #17063019, respectively) were already presented in section 3.1 in figure 3.1.3. As can be seen in table 7.2.1, for all three discharges L_0, R_0, f_c and f_{cr} fitting parameters were rather similar or the same while f_m and f_{mr} were in general different (typical behavior for PF dischares in single gas).

7.3. Discharges in D_2, Ar and D_2+Ar mixtures and acquired fitting parameters

In the main stage of investigation dedicated to this work experimental discharges in D_2, Ar and mixtures of D_2+Ar were performed in the PF-24 under approximately constant initial pressure. The initial total pressure p_0 for all discharges in D_2 and D_2+Ar was equal to 2.9(±0.2) mbar. While the initial total pressure p_0 for all discharges in Ar was equal to 1.2(±0.1) mbar. The total number of discharges carried under these conditions is: 34 in D_2, 10 in Ar and 69 in D_2+Ar. All the 113 discharges were performed in 5 experimental series (sessions) during different periods of time (weeks and months of difference). The values of Ar fraction (v_2) during experiments and computations in D_2+Ar mixtures were associated with values of D_2 fraction (v_1) with the following relation: $v_2 = 1 - v_1$. The percentage values of Ar fraction ($x = 100\% \times v_2$) were changed between 3% and 60% (with a change of step). Wherein, the discharges in D_2 and Ar under constant total pressure can be considered as discharges in $x = 0\%$ of Ar and $x = 100\%$ of Ar, respectively. Thus, in general in this subsection experimental and computed discharges in $(100\%\text{-}x)D_2\text{+}x\text{Ar}$ mixtures are presented. All the variable input parameters describing the 113 discharges are presented below in table 7.3.1.

Table 7.3.1. The variable input parameters describing 113 discharges in $(100\%\text{-}x)D_2\text{+}x\text{Ar}$ mixtures computed using the 5-phase Lee model code. The p_0, x, L_0^{comp}, R_0^{comp}, f_m, f_c, f_{mr} and f_{cr} stand for: the initial total gas or gas mixture pressure, the percentage of Ar fraction in the mixture, the computed nominal inductance, the computed nominal resistance, the axial mass factor, the axial current factor, the radial mass factor and the radial current factor, respectively.

O. n.	Series ID	Discharge ID	p_0 (mbar)	x (%)	L_0^{comp} (nH)	R_0^{comp} (mΩ)	f_m	f_c	f_{mr}	f_{cr}
1	I	17071001	3.00 (±0.01)	0	21	4.8	0.095	0.7	0.345	0.9
2		17071002	2.98 (±0.03)	0	20	6	0.115	0.7	0.3	0.9
3		17071003	2.98 (±0.03)	0	20	9	0.09	0.7	0.3	0.9
4		17071004	2.98 (±0.03)	0	20	6.5	0.105	0.7	0.3	0.9
5		17071005	2.98 (±0.03)	0	20	6	0.12	0.7	0.05	0.7
6		17071006	2.98 (±0.03)	0	20	10	0.09	0.7	0.18	0.9
7		17071007	2.98 (±0.03)	0	22	4.5	0.105	0.7	0.25	0.9
8		17071008	2.98 (±0.03)	0	20	11	0.095	0.7	0.13	0.9
9		17071009	2.98 (±0.03)	0	22	5.5	0.11	0.7	0.1	0.9
10		17071010	2.98 (±0.03)	0	23	7.5	0.09	0.7	0.19	0.9
11	II	17082201	3.00 (±0.01)	0	20	9.5	0.175	0.7	0.13	0.8
12		17082202	2.91 (±0.10)	0	20	12.5	0.145	0.7	0.45	0.72
13		17082203	2.81 (±0.01)	0	20	10.5	0.165	0.7	0.25	0.6
14		17082204	2.79 (±0.03)	0	22	15.5	0.125	0.7	0.45	0.77
15		17082205	2.79 (±0.03)	0	20	13	0.16	0.7	0.25	0.67
16		17082207	2.79 (±0.03)	0	21	13.5	0.14	0.7	0.4	0.71
17		17082209	2.79 (±0.03)	0	22	10.8	0.155	0.7	0.28	0.64
18		17082210	2.79 (±0.03)	0	19	11	0.19	0.7	0.3	0.62

19	III	17092801	2.91 (±0.01)	0	22	10	0.125	0.7	0.065	0.9
20		17092802	2.87 (±0.01)	0	20	9.4	0.115	0.7	0.6	0.82
21		17092803	2.87 (±0.01)	0	24	8	0.115	0.7	0.23	0.9
22		17092804	2.87 (±0.01)	0	23	8.5	0.125	0.7	0.27	0.9
23		17092805	2.87 (±0.01)	0	21	11	0.128	0.7	0.427	0.9
24		17092807	2.86 (±0.01)	0	22.5	14.5	0.105	0.7	0.1	0.7
25		17092808	2.86 (±0.01)	0	23	14	0.12	0.7	0.11	0.9
26		17092810	2.86 (±0.01)	0	20	9.7	0.135	0.7	0.4	0.9
27	IV	17100401	3.00 (±0.01)	0	27.5	3.5	0.09	0.7	0.12	0.9
28		17100402	2.98 (±0.01)	0	22	12.5	0.105	0.7	0.06	0.9
29		17100403	2.98 (±0.01)	0	24	6.5	0.1	0.7	0.27	0.9
30		17100404	2.98 (±0.01)	0	21	12.5	0.09	0.7	0.22	0.9
31		17100405	2.98 (±0.01)	0	21	13.5	0.108	0.7	0.05	0.9
32		17100406	2.98 (±0.01)	0	22	21	0.08	0.7	0.05	0.9
33		17100409	2.98 (±0.01)	0	20	8.3	0.13	0.7	0.42	0.9
34		17100410	2.98 (±0.01)	0	25	18	0.06	0.7	0.18	0.9
35	III	17092811	3.00 (±0.01)	3.0 (±0.4)	24	6	0.115	0.7	0.27	0.9
36		17092812	2.98 (±0.01)	3.0 (±0.4)	21	21	0.095	0.75	0.2	0.9
37		17092813	2.97 (±0.01)	3.0 (±0.4)	23	17	0.11	0.7	0.2	0.9
38		17092816	2.97 (±0.01)	3.0 (±0.4)	23	8.5	0.13	0.7	0.28	0.74
39		17092817	2.96 (±0.01)	3.0 (±0.4)	18	11	0.14	0.7	0.24	0.8
40		17092818	2.96 (±0.01)	3.0 (±0.4)	19	5.1	0.18	0.7	0.27	0.54
41		17092819	2.96 (±0.01)	3.0 (±0.4)	18	5.7	0.183	0.7	0.39	0.7
42		17092820	2.96 (±0.01)	3.0 (±0.4)	22	6	0.14	0.7	0.288	0.7
43	I	17071801	3.00 (±0.01)	5.0 (±0.4)	21	11.5	0.12	0.7	0.25	0.9
44		17071802	2.88 (±0.03)	5.0 (±1.1)	23	9.5	0.13	0.7	0.26	0.8
45		17071803	2.88 (±0.03)	5.0 (±1.1)	23	8	0.13	0.7	0.27	0.7
46		17071804	2.88 (±0.03)	5.0 (±1.1)	23	13.5	0.1	0.7	0.232	0.7
47		17071805	2.88 (±0.03)	5.0 (±1.1)	20	9	0.15	0.7	0.2	0.6
48		17071806	2.88 (±0.03)	5.0 (±1.1)	20	9.5	0.14	0.7	0.275	0.58
49		17071807	2.88 (±0.03)	5.0 (±1.1)	19	9	0.155	0.73	0.155	0.63
50		17071808	2.88 (±0.03)	5.0 (±1.1)	22	7.5	0.155	0.7	0.155	0.51
51		17071809	2.88 (±0.03)	5.0 (±1.1)	21	11.3	0.087	0.53	0.04	0.36
52	II	17083101	2.85 (±0.15)	10.0 (±5.3)	30	15.5	0.084	0.7	0.085	0.9
53		17083102	2.85 (±0.15)	10.0 (±5.3)	21	17	0.225	0.9	0.05	0.65
54		17083103	2.85 (±0.15)	10.0 (±5.3)	22	15.5	0.037	0.4	0.25	0.4
55		17083104	2.85 (±0.15)	10.0 (±5.3)	31	16	0.113	0.7	0.08	0.73
56		17083105	2.85 (±0.15)	10.0 (±5.3)	24	13.6	0.057	0.45	0.09	0.45
57		17083107	2.85 (±0.15)	10.0 (±5.3)	25	20.5	0.056	0.5	0.09	0.5
58		17083108	2.85 (±0.15)	10.0 (±5.3)	18	9.1	0.067	0.4	0.1	0.3
59		17083109	2.85 (±0.15)	10.0 (±5.3)	18	12.2	0.098	0.5	0.11	0.4
60		17083110	2.85 (±0.15)	10.0 (±5.3)	27	14.5	0.131	0.7	0.131	0.75

61	I	17071013	2.93 (±0.08)	15.0 (±2.8)	23	11.5	0.037	0.45	0.02	0.33
62		17071014	2.93 (±0.08)	15.0 (±2.8)	24	7	0.045	0.5	0.06	0.43
63		17071015	2.93 (±0.08)	15.0 (±2.8)	23	10.5	0.047	0.5	0.074	0.49
64		17071101	2.92 (±0.09)	15.0 (±3.1)	22	10.3	0.064	0.5	0.08	0.65
65		17071102	2.92 (±0.09)	15.0 (±3.1)	23	7.5	0.068	0.5	0.08	0.46
66		17071104	2.92 (±0.09)	15.0 (±3.1)	21	8	0.07	0.5	0.1	0.49
67		17071105	2.92 (±0.09)	15.0 (±3.1)	27	9	0.047	0.5	0.09	0.47
68		17071107	2.92 (±0.09)	15.0 (±3.1)	22	9.8	0.048	0.45	0.086	0.45
69		17071108	2.92 (±0.09)	15.0 (±3.1)	22	16.8	0.046	0.5	0.075	0.5
70		17071109	2.92 (±0.09)	15.0 (±3.1)	23	17	0.042	0.5	0.21	0.8
71		17071110	2.92 (±0.09)	15.0 (±3.1)	30	11.5	0.042	0.5	0.11	0.6
72	II	17090101	3.00 (±0.09)	22.0 (±3.0)	27	5.2	0.058	0.5	0.06	0.35
73		17090102	3.00 (±0.09)	22.0 (±3.0)	17	12.7	0.065	0.5	0.068	0.41
74		17090103	2.90 (±0.02)	22.0 (±0.7)	21	12.8	0.035	0.4	0.04	0.32
75		17090104	2.90 (±0.02)	22.0 (±0.7)	16	9.5	0.054	0.4	0.06	0.35
76		17090105	2.87 (±0.02)	22.0 (±0.7)	22	16.3	0.027	0.4	0.062	0.42
77		17090108	2.85 (±0.02)	22.0 (±0.7)	23	10	0.035	0.4	0.075	0.4
78		17090109	2.84 (±0.02)	22.0 (±0.7)	17	8.5	0.048	0.4	0.05	0.23
79		17090110	2.84 (±0.02)	22.0 (±0.7)	22	11.5	0.038	0.4	0.07	0.3
80	IV	17100413	2.98 (±0.01)	25.0 (±0.4)	21	14.5	0.06	0.7	0.078	0.7
81		17100414	2.98 (±0.01)	25.0 (±0.4)	21	16.5	0.048	0.7	0.112	0.8
82		17100416	2.98 (±0.01)	25.0 (±0.4)	20	16	0.03	0.5	0.072	0.5
83		17100417	2.98 (±0.01)	25.0 (±0.4)	24	8.2	0.072	0.7	0.12	0.7
84		17100420	2.97 (±0.01)	25.0 (±0.4)	19	7.5	0.078	0.7	0.135	0.6
85	I	17071111	2.93 (±0.08)	30.0 (±2.8)	21	12.5	0.067	0.7	0.08	0.63
86		17071112	2.93 (±0.08)	30.0 (±2.8)	21	6.2	0.043	0.4	0.045	0.31
87		17071113	2.93 (±0.08)	30.0 (±2.8)	22.5	9.6	0.031	0.4	0.03	0.3
88		17071114	2.93 (±0.08)	30.0 (±2.8)	21	9	0.045	0.4	0.052	0.4
89		17071116	2.93 (±0.08)	30.0 (±2.8)	23	15.5	0.025	0.4	0.025	0.38
90		17071118	2.93 (±0.08)	30.0 (±2.8)	23	9.5	0.072	0.6	0.08	0.52
91		17071119	2.93 (±0.08)	30.0 (±2.8)	23	12.7	0.03	0.4	0.04	0.5
92	I	17071202	2.89 (±0.12)	45.0 (±4.2)	22	16.5	0.035	0.5	0.04	0.55
93		17071204	2.89 (±0.12)	45.0 (±4.2)	18	17	0.028	0.4	0.01	0.4
94		17071205	2.89 (±0.12)	45.0 (±4.2)	21	9.3	0.025	0.35	0.035	0.35
95		17071206	2.89 (±0.12)	45.0 (±4.2)	21	15.5	0.0185	0.35	0.026	0.35
96		17071207	2.89 (±0.12)	45.0 (±4.2)	16	12.5	0.04	0.4	0.042	0.5
97	I	17071312	2.89 (±0.12)	60.0 (±4.2)	21	17	0.016	0.35	0.02	0.3
98		17071314	2.89 (±0.12)	60.0 (±4.2)	18	9	0.023	0.3	0.02	0.25
99		17071315	2.89 (±0.12)	60.0 (±4.2)	20	12.5	0.017	0.3	0.018	0.3
100		17071316	2.89 (±0.12)	60.0 (±4.2)	21.5	15	0.0175	0.35	0.04	0.5
101		17071317	2.89 (±0.12)	60.0 (±4.2)	24	20	0.01	0.3	0.03	0.45
102		17071318	2.89 (±0.12)	60.0 (±4.2)	20	12	0.021	0.35	0.025	0.3
103		17071319	2.89 (±0.12)	60.0 (±4.2)	21	8.7	0.019	0.3	0.023	0.26

104	V	17101814	1.20 (±0.01)	100	20	10.5	0.021	0.4	0.4	0.4
105		17101816	1.20 (±0.01)	100	18	10	0.045	0.6	0.45	0.45
106		17101817	1.18 (±0.01)	100	16	11.5	0.0193	0.4	0.45	0.35
107		17101818	1.16 (±0.01)	100	17	10	0.0163	0.4	0.4	0.3
108		17101820	1.12 (±0.01)	100	17	14.5	0.01	0.31	0.15	0.2
109		17102002	1.19 (±0.01)	100	17	11.5	0.0038	0.2	0.15	0.2
110		17102003	1.19 (±0.01)	100	21	2.9	0.094	0.7	0.12	0.65
111		17102007	1.19 (±0.01)	100	18	7.7	0.023	0.4	0.25	0.33
112		17102009	1.18 (±0.01)	100	17	12.2	0.017	0.4	0.2	0.35
113		17102016	1.13 (±0.01)	100	16	9.5	0.0163	0.35	0.2	0.3

Below, in table 7.3.2 the average values of the variable input parameters from the table 7.3.1 are presented (division into different series included). The total number of discharges used to calculate single average value is presented in the column marked with the N_{dis} symbol.

Table 7.3.2. The average values of variable input parameters describing 113 discharges in (100%-x)D_2+xAr mixtures and computed using the 5-phase Lee model code. The N_{dis}, $<p_0>$, $<x>$, $<L_0^{comp}>$, $<R_0^{comp}>$, $<f_m>$, $<f_c>$, $<f_{mr}>$ and $<f_{cr}>$ are: the number of discharges used to calculate average value, the average total initial pressure of gas or gas mixture, the average percentage of Ar fraction in the mixture, the average computed nominal inductance, the average computed nominal resistance, the average axial mass factor, the average axial current factor, the average radial mass factor and the average radial current factor.

Series ID	N_{dis}	$<p_0>$ (mbar)	$<x>$ (%)	$<f_m>$	$<f_c>$	$<f_{mr}>$	$<f_{cr}>$	$<L_0^{comp}>$ (nH)	$<R_0^{comp}>$ (mΩ)
I	10	2.98 (±0.03)	0	0.1	0.7	0.21	0.88	20.8	7.1
II	8	2.83 (±0.03)	0	0.16	0.7	0.31	0.69	20.5	12
III	8	2.87 (±0.01)	0	0.12	0.7	0.28	0.87	21.9	10.6
IV	8	2.98 (±0.01)	0	0.1	0.7	0.17	0.9	22.8	12
III	8	2.97 (±0.01)	3.0 (±0.4)	0.14	0.71	0.27	0.77	21	10
I	9	2.89 (±0.03)	5.0 (±1.0)	0.13	0.68	0.2	0.64	21.3	9.9
II	9	2.85 (±0.15)	10.0 (±5.3)	0.1	0.58	0.11	0.56	24	14.9
I	11	2.92 (±0.09)	15.0 (±3.0)	0.05	0.49	0.09	0.52	23.6	10.8
II	8	2.90 (±0.04)	22.0 (±1.3)	0.05	0.43	0.06	0.35	20.6	10.8
IV	5	2.98 (±0.01)	25.0 (±0.4)	0.06	0.66	0.1	0.66	21	12.5
I	7	2.93 (±0.08)	30.0 (±2.8)	0.04	0.47	0.05	0.43	22.1	10.7
I	5	2.89 (±0.12)	45.0 (±4.2)	0.03	0.4	0.03	0.43	19.6	14.2
I	7	2.89 (±0.12)	60.0 (±4.2)	0.02	0.32	0.03	0.34	20.8	13.5
V	10	1.17 (±0.01)	100	0.03	0.42	0.28	0.35	17.7	10

The average values of fitting parmeters from table 7.3.2 were also presented in figure 7.3.1.

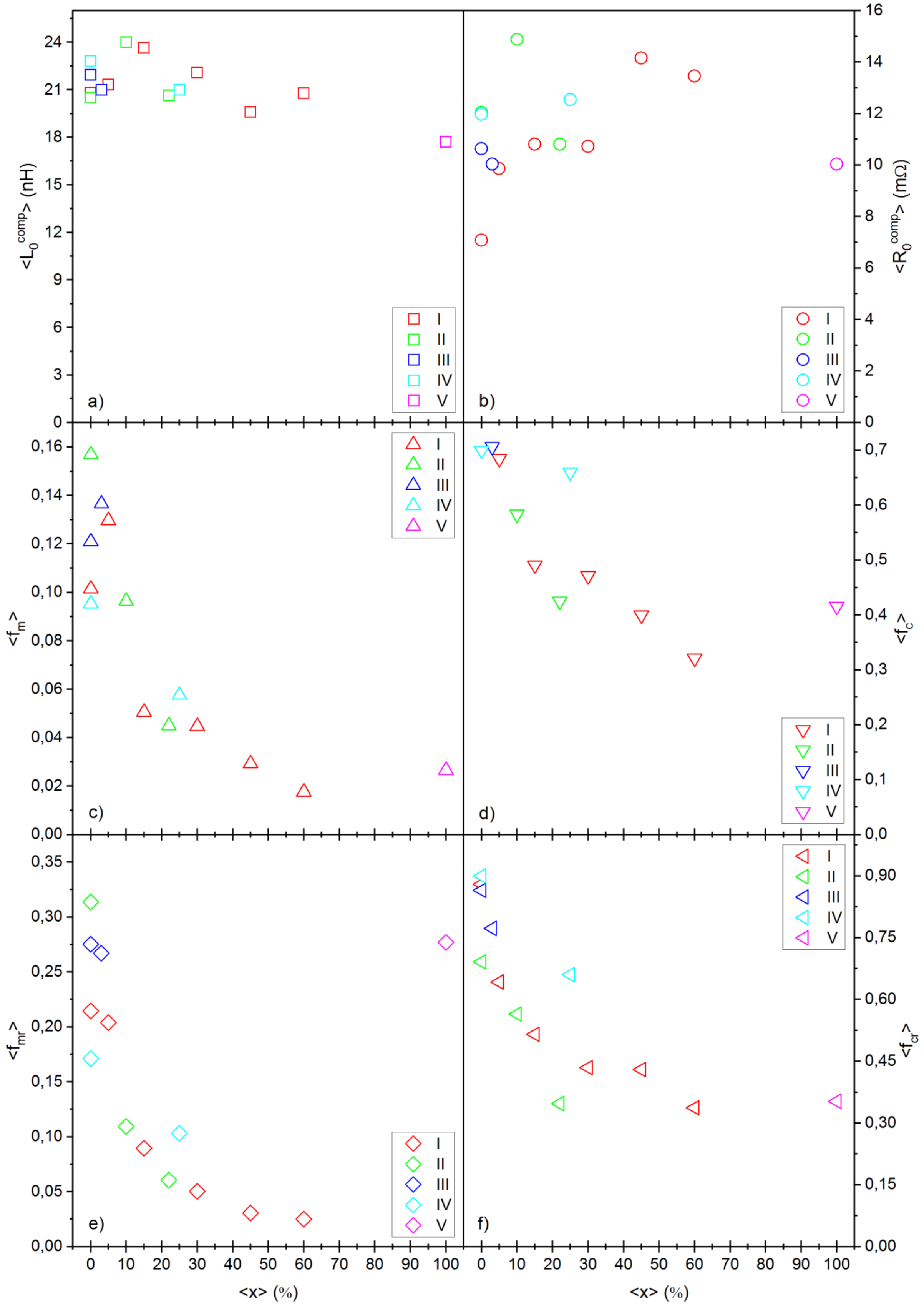

Figure 7.3.1. Determined (computed) average values of fitting parameters of the 5-phase Lee model code for 113 experimental discharges in (100%-x)D_2+xAr mixtures: **a)** $<L_0^{comp}>$ – nominal inductance, **b)** $<R_0^{comp}>$ – nominal resitance, **c)** $<f_m>$ – axial mass factor, **d)** $<f_c>$ – axial current factor, **e)** $<f_{mr}>$ – radial mass factor, **f)** $<f_{cr}>$ – radial current factor. Roman numerals mark given series of discharges.

The value of about 3.0 mbar was stated before as the optimum pressure in the PF-24 device for the total neutron emission (neutron-optimized device) – presented in detail in section 8.7.2 (see also article [Marciniak 2018]). Thus, discharges in D_2 and D_2+Ar mixtures (series from I to IV) under constant total pressure of 2.9(±0.2) mbar were performed. On the other hand, for discharges in Ar (series V) only for 1.2(±0.1) mbar of initial Ar pressure pinch effect was observed using registered electric traces (lower and higher initial pressures were tested). This is probably connected with not proper initial generation of plasma sheet during breakdown and current sheet build-up phase due to for example too small charging voltage (Pashen law) for the given PF-24 configuration of electrodes and isolator inside the experimental chamber. For different smaller PF devices operated with Ar good pinching was reported for example during discharges under 9-15 kV of charging voltage, shortest distance between cathode (oxygen-free copper) and anode (oxygen-free copper) equal to 4.3 cm in straight line, while Pyrex glass isolator of 4.5 cm in length and 0.5 cm thick was used and initial pressure varied in 0.27-1.33 mbar range (SABALAN2 PF device) [Piriaei 2015] or during discharges under 10-15 kV of charging voltage, smallest distance between cathode (copper) and anode (copper) equal to 3.08 cm in straight line, while Pyrex glass isolator of 4.8 cm in length was used and initial pressure varied in 0.67-2.66 mbar range (Amirkabir PF device) [Sharak 2013].

The reason for displaying the data in the five different series is that there were significant changes in values of some determined plasma parameters between discharges from the two different series, even under the theoretically same initial conditions – discharges in 0% of Ar. This will be shown in chapter 8 of this work. Differences between series of discharges can be already seen while looking at the $<f_m>$, $<f_{mr}>$, $<f_{cr}>$ and $<R_0^{comp}>$ parameters (see especially discharges in 0% of Ar in series I-IV) in table 7.3.2 and in figure 7.3.1. Moreover, determined model parameters, despite some differences between series, tend to decrease with increase of the Ar fraction in the mixture in 0-60% range (see figure 7.3.1) – less percentage of the mass of gas is being swept effectively by the current sheet (effective mass sweeping into plasma pinch does not increase with Ar for higher fractions) and less percentage of current effectively flows through the magnetic piston (effective currents driving the moving plasma structure decrease). For the discharges in 100% of Ar fraction some increase is stated for $<f_m>$ and $<f_c>$ parameters (figure 7.3.1c and 7.3.1d) in reference to 60% of Ar and for $<f_{mr}>$ parameter large increase in reference to 60% in stated (figure 7.3.1e). The decreae of values of model parameters with Ar fraction can be ascribed to the fact that the Ar ions have higher mass and are more easily left behind by the moving current sheet – separation of Ar and D fractions is possible [Commisso 1975], [Weingarten 2001]. Still, these are only conjectures and real reasons of decrease of model parameters are in general unknown. Furthermore, the $<R_0^{comp}>$ parameter appears to slightly increase with Ar fraction. The values of R_0^{comp} are spread around the average value of 11.1 mΩ (from all 113 discharges). On the other hand, the values of $<L_0^{comp}>$ parameter appear to decrees slightly with Ar fraction increase. The values of L_0^{comp} are spread around the average value of about 21.3 nH (from all 113 discharges).

It should be also mentioned that all 113 discharges in table 7.3.1 were stated as sufficiently well fitted – sufficient match of the measured and the computed current traces was achieved. Although, for 3 discharges in D_2+Ar mixtures (from 69) and for 9 discharges in Ar (from 10) worst match of some of the investigated electro-kinetic plasma parameters was stated (see chapter 8) – not all 5 electro-kinetic parameters have been well matched. During the discharges in 100% of Ar (series V) the pinching effect was in general “weak” (in fact weakest from all 113 discharges). This most probably resulted in worst match of measured and computed current traces. As was already mentioned in this section, this is probably the result of a not proper initial generation of the current sheet. Furthermore, in general the more Ar was added into the D_2+Ar mixture the weaker the pinching effect became during investigated discharges in the PF-24 – the smaller average total neutron yields per discharge were stated (see subsection 8.7.2) and the smaller minimum values of *dI/dt* and wider *dI/dt* jumps were observed. This appears to be mainly the result of a not optimum total mass/density value which was being swept by the moving magnetic piston (as was explained in section 3.1). In other words, taking into account that: the optimum initial pressure value of deuterium was stated as about 3 mbar, the corresponding optimum mass between electrodes was stated as about 0.4 mg, the 103 discharges presented in this work (discharges in D_2 and D_2+Ar) were performed under constant initial total pressure of about 2.9 mbar and the Ar fraction was systematicly increased while D_2 fraction was systematicly decreased simultaneously (Ar is about 10 times heavier than the D_2) means that the discharges in 3-60% of Ar fraction were performed in general under not optimum initial total mass/density in the experimental chamber. More precisely, the 34 discharges in 0% Ar were performed under optimum initial total mass/density, discharges in 3-5% of Ar were performed under relatively close to optimum initial total mass/density condition and discharges in 30-60% of Ar fraction (highest Ar fractions) were performed under initial total mass/density far from optimum (almost all discharges). The experiments have been designed this way in order to verify if some average total neutron yield increase and relatively strong radiative compression occurrence is possible under smaller fraction of Ar in almost optimimum mass conditions as well as under higher fraction of Ar in not-optimum mass conditions (for higher mass than optimum). Finally, since the L_0 and R_0 parameters fluctuated from discharge to discharge as well as model parameters fluctuate and decreased with time it was not certain that given discharge performed under given initial total mass/density of D_2+Ar mixture will be performed in optimum conditions for kinetic and magnetic energy transfer or not.

8. Analysis of the results

The main results of data analysis in this work are presented in form of graphs (sections from 8.1 to 8.7) and tables (sections from 8.8 to 8.10). The graphs show changes of different parameters and indicators describing discharge and plasma under initial gas pressure p_0 of D_2 and Ar as well as fraction of Ar (x) in (100%-x)D_2+xAr mixtures – parameters and indicators were described in section and subsections 5.2, 5.3.2 and 6.3.3. While the tables show summary (total ranges of changes) of all parameters and indicators for different groupes of theoretical and computed discharges in reference to plasma pinch compression investigation.

The full analysis of the coupled measured-computed discharges in D_2 is carried only for 44 discharges in total – 10 discharges under variable initial pressure of D_2 and 34 discharges under approximately constant initial pressure. The 10 discharges were selected from 388 based on the analysis of the total neutron emission – explained in details in subsection 8.7.2.

The analysis of the coupled measured-computed discharges in (100%-x)D_2+xAr mixtures (including 34 discharges in D_2 and 10 discharges in Ar) is based on parameters and indicators from individual discharges as well as on the average values of parameters and indicators calculated talking into account division into Ar fraction and series. Only the graphs containing average values of parameters and indicators are presented. If the parameters determined for some individual discharge differ significantly from the average values, this will be indicated in the text.

8.1. Kinetic parameters

In this subsection, changes of the compression times (t_c), the pinch times (t_p), the average axial velocities (v_z), the maximum axial velocities (v_{zmax}) and the maximum radial velocities (v_{rmax}) will be presented.

8.1.1. Kinetic parameters – times

Theoretical discharges

The computed theoretical: compression (t_c) and pinch (t_p) time for the discharges in: D_2 and Ar as a function of pressure (p_0) are shown in figure 8.1.1 and figure 8.1.2, respectively. The theoretical t_c and t_p times computed for Ar+D_2 mixtures as a function of Ar fraction (x) are shown in figure 8.1.3.

The increasing of the t_c and t_p with increasing p_0 of x is observed. The snow-plough and slug theories applied in the Lee model code assume that a very fast, thin and radially symmetrical current sheet moves along the anode in the axial and radial direction sweeping and ionizing working gas particles that become some of the sheet-shock structure. In general, the higher the total mass of the working gas or the gas mixture in front of magnetic piston, the slower the sheet-shock structure and hence the later the compression times and the pinch times. Argon ions have approximately 20 times bigger mass than deuterium ions, so the t_c and t_p times are higher in pure Ar than D_2 for the same p_0 because the larger mass is swept effectively during discharges in D_2 and Ar. The constant percentage of mass swept by the current sheet is assumed as well as the constant percentage of current flows through the magnetic piston – constant f_m, f_c, f_{mr} and f_{cr} parameters. The total mass sweeping by the current sheet continuously increases with increase of initial D_2 and Ar pressure and the maximum current flowing through magnetic piston increases but the current flowing through plasma pinch does not necessarily increase (see subsection 8.2.1).

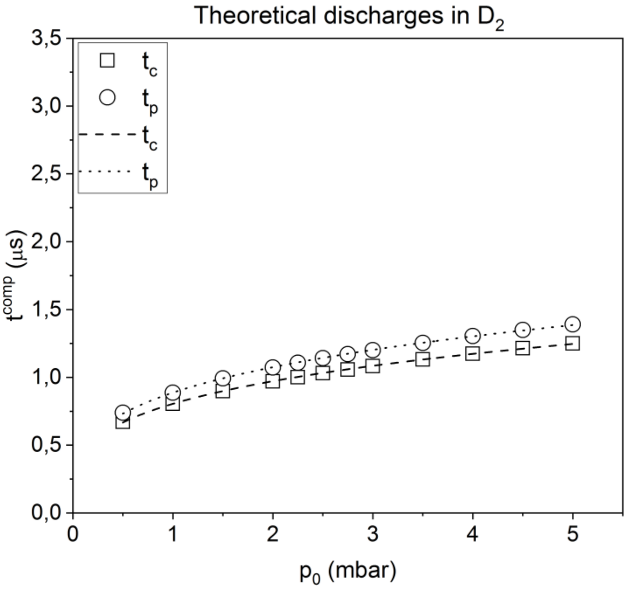

Figure 8.1.1. The computed theoretical compression time (t_c^{comp}) and pinch time (t_p^{comp}) versus initial D_2 pressure (p_0).

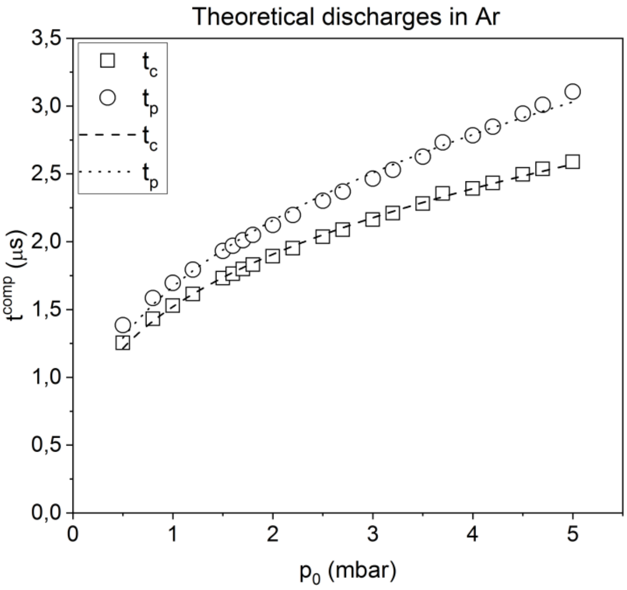

Figure 8.1.2. The computed theoretical compression time (t_c^{comp}) and pinch time (t_p^{comp}) versus initial Ar pressure (p_0).

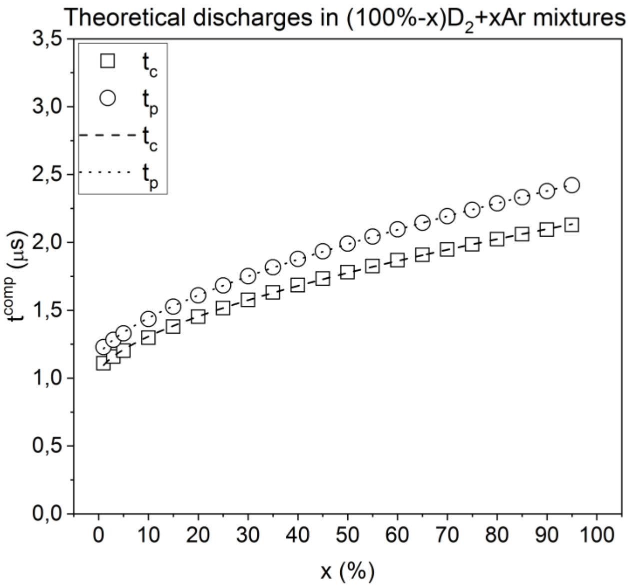

Figure 8.1.3. The computed theoretical compression time (t_c^{comp}) and pinch time (t_p^{comp}) versus Ar fraction (x) in $(100\%\text{-}x)D_2+x$Ar mixture.

The dependencies for t_c and t_p vs Ar fraction in $(100\%\text{-}x)D_2+x$Ar mixtures look similarly as in D_2 and Ar. The discharges in $(100\%\text{-}x)D_2+x$Ar mixtures were performed under constant total gas pressure (of 3.0 mbar). Since the fraction of D_2 decreased and the fraction of Ar increased simultaneously, the initial total mass of the gas mixture between and in front of electrondes increased (initial total density of gas or gas mixture increased). This occurs under assumed constant values of fitting parameters. Thus, total mass sweeping by the current sheet continuously increases with increase of Ar fraction and the maximum current flowing through magnetic piston increases but the current flowing through plasma pinch shows maximum (see subsection 8.2.1).

For the snow-plough and slug model the $t \sim p^n$ relation was stated [Mather 1971]. The compression and pinch times rise with the initial gas pressure as approximately $p_0^{0.3\text{-}0.4}$ for both D_2 and Ar (for all data damped least-squares method of fitting was used – Levenberg-Marquardt iteration algorithm). The power function applied to fit the computed theoretical t_c and t_p as a function of x in (100%-x)D_2+xAr mixtures gave the approximate relations $t_c \sim x^{0.6}$ and $t_p \sim x^{0.7}$ (fitting with shifted power function was used – see figure 8.1.3). This shows that the character of changes of theoretical discharge dynamics up to pinch phase is similar for D_2 and Ar as well as for (100%-x)D_2+xAr mixtures.

Experimental and computed discharges in deuterium

Figure 8.1.4 presents the measured (t_c^{mea}) and computed (t_c^{comp}) compression times and the measured (t_p^{mea}) and computed (t_p^{comp}) pinch times versus pressure p_0 for the discharges in D_2.

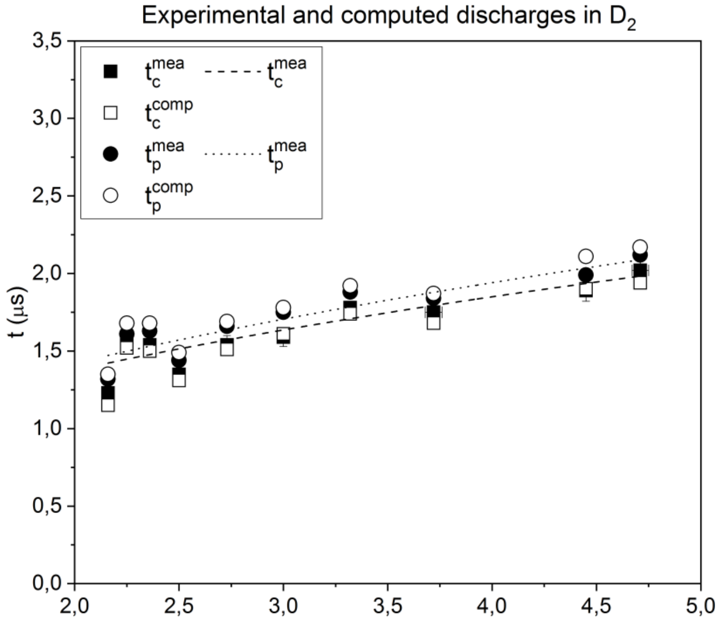

Figure 8.1.4. The measured (t_c^{mea}) and computed (t_c^{comp}) compression time and the measured (t_p^{mea}) and computed (t_p^{comp}) pinch time versus initial D_2 pressure (p_0).

The measured and computed compression and pinch times increase with increase of D_2 pressure (figure 8.1.4) similar as for the theoretical discharges. The reason for this behaviour is the same as for the theoretical discharges (despite not constant fitting parameter values) – increase of effective mass sweeping by the current sheets with increase of initial D_2 pressure as well as some increase of the maximum currents flowing through magnetic piston and the maximum pinch currents flowing through plasma column with increase of D_2 pressure (see subsection 8.2.1). The fluctuations of the t_c and t_p values occur and the increase is slightly stronger $\sim p_0^{0.4}$ than for the theoretical values (figure 8.1.1). Both t_c and t_p, measured and computed, are higher than the theoretical t_c and t_p for the same D_2 pressure – the presented parameters were determined on the basis of 10 measured and computed discharges with included changes in the: f_m, f_c, f_{mr}, f_{cr}, R_0^{comp} and L_0^{comp} parameters enabling different scenarios of discharge and accompanying effects taking place. The measured t_c and t_p are sufficiently well fitted with the computed t_c and t_p suggesting the credible consistence between experiments and computations. This means that the snow-plough and slug models are a good representation of discharge.

Experimental and computed discharges in deuterium-argon mixtures

Figure 8.1.5a presents the average measured ($<t_c^{mea}>$) and computed ($<t_c^{comp}>$) compression times and figure 8.1.5b presents the average measured ($<t_p^{mea}>$) and computed ($<t_p^{comp}>$) pinch times for the discharges in (100%-x)D_2+xAr mixtures.

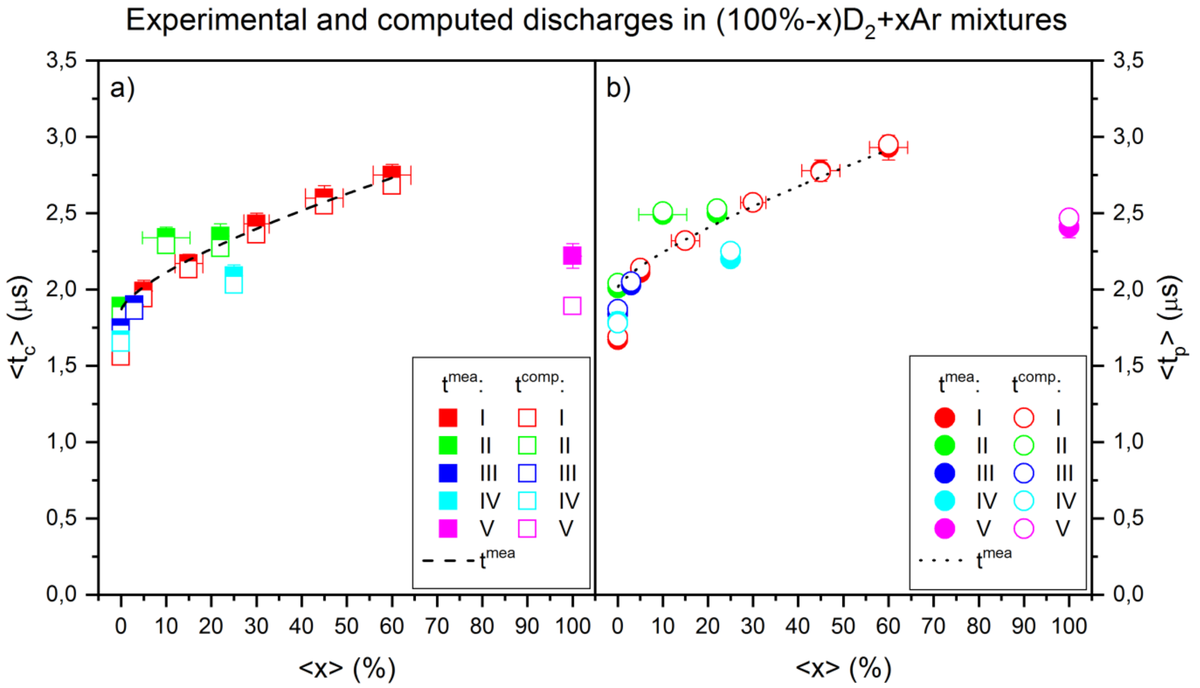

Figure 8.1.5. a) The average measured ($<t_c^{mea}>$) and computed ($<t_c^{comp}>$) compression time and **b)** the average measured ($<t_p^{mea}>$) and computed ($<t_c^{comp}>$) pinch time versus Ar fraction ($<x>$) in (100%-x)D_2+xAr mixture. Roman numerals mark given series of discharges.

Both compression and pinch times (measured and computed) presented in figure 8.1.5a and 8.1.5b (series from I to IV considered) increase with increase of Ar fraction similarly as for theoretical discharges (figure 8.1.3). However, the reason (explanation) for this increase is more complex than for the other discharges (including the theoretical discharges in (100%-x)D_2+xAr mixtures) since all model parameters of the 5-phase Lee model code for discharges in 0-60% of Ar show strong decreasing tendencies with increase of Ar fraction (see figure 7.3.1). The effective increase of total mass sweeping is in general not stated for the experimental and computed discharges in (100%-x)D_2+xAr mixtures as for theoretical discharges with Ar fraction increase (probably some type of maximum exists – not clear relation). And the maximum currents flowing through magnetic piston and maximum currents flowing through plasma pinch decrease with Ar fraction increase (despite the increase of the maximum discharge currents) – see subsection 8.2.1. Thus, the back electromotive force (Ampere's force) pushing the piston decreases with Ar fraction – this is to be the main reason for the increase of compression and pinch times.

The fitting of power functions to $<t_c^{mea}>$ and $<t_p^{mea}>$ without division into different series and omitting the 100% point gives $<t_c^{mea}> \sim <x>^{0.7}$ and $<t_p^{mea}> \sim <x>^{0.8}$ (shifted power functions were used – see figure 8.1.5) – smaller increase was stated for theoretical discharges (figure 8.1.3). The large fluctuations are observed between different series of discharges. It should be also mentioned that, the measured and computed $<t_c>$ and $<t_p>$ times in 100% of Ar are significantly shorter than in 60% of Ar. The discharges in 100% of Ar were performed at the initial pressure of about 1.2 mbar. According to the snow-plough and slug theory, when total mass of gas or gas mixture between electrodes is the same, the generated current sheets should move similarly. Assuming the constant values of fitting parameters the t_c and t_p are similar for both the theoretical discharge in 70%D_2+30%Ar mixture and in 1.2 mbar of Ar since the initial mass between the electrodes is equal to about: 1.6 mg and 1.4 mg, respectively. But this is not the case for the coupled measured-computed discharges – the significantly smaller $<t_c>$ and $<t_p>$ for 100% of Ar (series V) are stated than for 30% of Ar (series I). Also, the $<t_c>$ and $<t_p>$ for 0% (series I, III, IV), 10% (series II) and 25% (series IV) of Ar are not fitted as good as the rest of posints with the anticipated curve. This is not the case when fitting to only given series of discharges is made. This is the result in general of the different fitting parameters which were used for 0%, 10%, 25%, 30% and 100% of Ar – the different scaling of mass sweeping by the current sheets and different scaling of currents flow driving the magnetic pistons. The reason for the change of values of L_0^{comp} and R_0^{comp} parameters from discharge to discharge is believed to be a signicant spread of spark-gaps triggering times (jitter of the condenser bank of PF-24 significantly higher than 50 ns). The possible reasons for the changes of model parameter values and development of different type of discharge are numerous. The possible ones are believed to be: the fluctuations of copper impurities (or other type of impurities) penetrating the plasma structure, arcing, deformation of the cathode and anode rods with the number of discharges, not proper generation of current sheet, separation of Ar and D species (different for different series) as well as some other type of mechanism not included which influences the mass and current flow during axial and radial phase of discharge like stronger development of some kind of instabilities for dischares with higher Ar fraction.

The first three reasons are connected with each other. After all 113 discharges when the experimental chamber of the PF-24 was opened some deformation of the anode rod were stated (asymmetrc). Copper was sprayed all over the chamber as well as large pieces of copper (seen with "naked eye") were found.

The not proper generation of current sheet – may be connected with the Paschen law of break-down and ionization. The Paschen law states in general that break-down voltage has to be high enough for given configuration of electrodes and medium. Thus, perhaps too small charging voltage was used in the PF-24 device needed to generate proper discharge over the surface of isolator inside noble gas like Ar. For 100% of Ar fraction only for about 1.2 mbar of Ar some pinch effect was observed and registered on electric traces.

The separation of Ar and D species and the presence of different type of instabilities of different "strength" during axial and radial phases – seem also to be theoretically possible. According the previously published articles [Commisso 1975] [Weingarten 2001] the separation of species during z-pinch discharges is possible and should be expected. And the computations using the Lee model code assume always constant ratio of fractions during modeling of discharges in gas mixtures. Moreover, the existence of instabilities during run-down and run-in phases was stated during many previous experiments in different PF devices. These are to be mainly Rayleigh-Taylor MHD instabilities and are in general not simulated by the Lee model code. However, the influence of the Rayleigh-Taylor instabilities on mass and current flow during discharge is approximately included using model parameters – f_m, f_c, f_{mr} and f_{cr}. Furthmore, model parameters are also in general sensitive to the separation of D and Ar species since heavier ions like Ar are to be easier left behind and change of the total mass of moving magnetic piston is taken into account (majority of mass comes from Ar ions). Still, it should be emphasized that, model parameters give information only on the sum of all effects during axial and radial phases of discharge.

As was mentioned in above paragraphs, the effect of the increase of $<t_c>$ and $<t_p>$ times with the increase of Ar fraction during the experimental and computed discharges is not continuous and suitable proportional (unlike in figure 8.1.3). However, if only $<t_c>$ and $<t_p>$ values of single series are compared no large fluctuations of values (see figure 8.1.5) is observed. The explanation of this and determination of main reasons of large fluctuations due to changes of model parameters and occurrence of different scenarios of discharge is believed to be found on the basis of comparison of discharges in 0% of Ar (discharges D_2) between different series (from I to IV). The discharges in 0% of Ar fraction should be generated in each series for the same initial conditions. Thus, no significant difference in current sheet initial generation, separation of Ar and D species and development of instabilities is to be expected. Still, the $<t_c>$ and $<t_p>$ times are also significantly different from each other among the four investigated series (see figure 8.1.5). And not only the average values itself are different but the spread of single values is also significantly different – see figure 8.1.6.

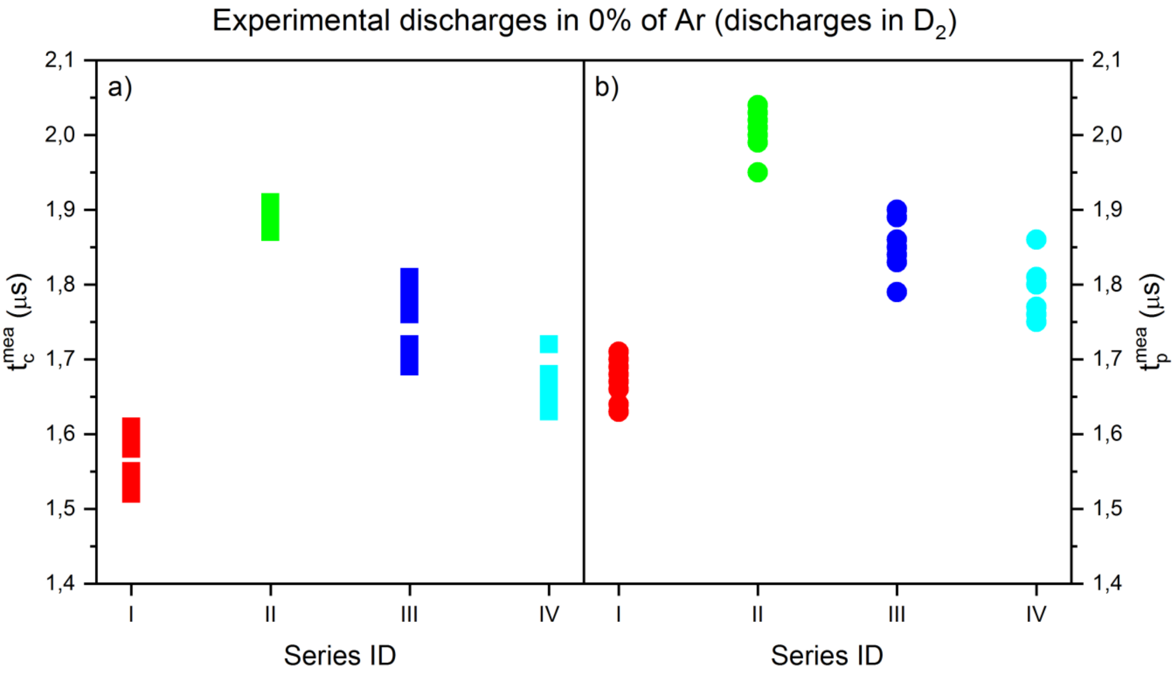

Figure 8.1.6. a) The measured (t_c^{mea}) compression time, **b)** the measured (t_p^{mea}) pinch time versus series ID for all single discharges in 0%Ar (discharges in D_2 in the four experimental series).

The discharges in 0% of Ar from four different series (figure 8.1.6) are characterized by: the 2.0 nH of maximum difference between $<L_0^{comp}>$ values, the 4.9 mΩ of maximum difference between $<R_0^{comp}>$ values, the 0.06 maximum difference between $<f_m>$ values, the 0 maximum difference between $<f_c>$, the 0.14 maximum difference between $<f_{mr}>$, the 0.21 maximum difference between $<f_{cr}>$, the 67 kA of maximum difference between $<I_{max}>$, the 320 ns of maximum difference between $<t_c>$ and the 340 ns of maximum difference between <t_p>. Based on all the above considerations and the fact that discharges from different series occur in the same initial D_2 pressure (and under the same charging voltage) the main reasons for the different behavior between series are anticipated as: the fluctuations of copper impurities (or other type of impurities) which penetrate into the plasma structure, arcing and deformation of the cathode and anode rods with the number of discharges. Also, changes in the theoretically static L_0^{comp} and R_0^{comp} may be the secondary probable cause. Furthermore, for the discharges in 100% of Ar (series V) the current sheet was probably not generated properly because of some unknown effect.

It should be also mention that the measured and computed values of <t_c> and <t_p> are sufficiently matched for all Ar fractions and series except for the series V – this indicates that the snow-plough and slug models are still a good representation of discharges. For the discharges in 100% of Ar (series V) the mismatch of measured and computed <t_c> parameters (see figure 8.1.1.5a) is connected with the fact that, almost all the discharges in 100% of Ar fraction are weakly pinched. So, the obtained results may not represent the conditions achieved during experiments as good as for the rest of investigated discharges. Still, for the <t_p> and for few other parameters (described in next two subsections) sufficient match of measured and computed values was achieved – the measured and computed traces have still rather similar character (similar shape). Thus the computed discharges in 100% of Ar were accepted for further analysis and as possible sufficient approximation of measured discharges.

8.1.2. Kinetic parameters – velocities

Theoretical discharges

Figure 8.1.7, figure 8.1.8 and figure 8.1.9 presents the computed theoretical average axial (v_z^{comp}) and maximum axial (v_{zmax}^{comp}) velocities, and the computed theoretical maximum radial velocities (v_{rmax}^{comp}) for the discharges in: D_2 and Ar and (100%-x)D_2+xAr mixtures.

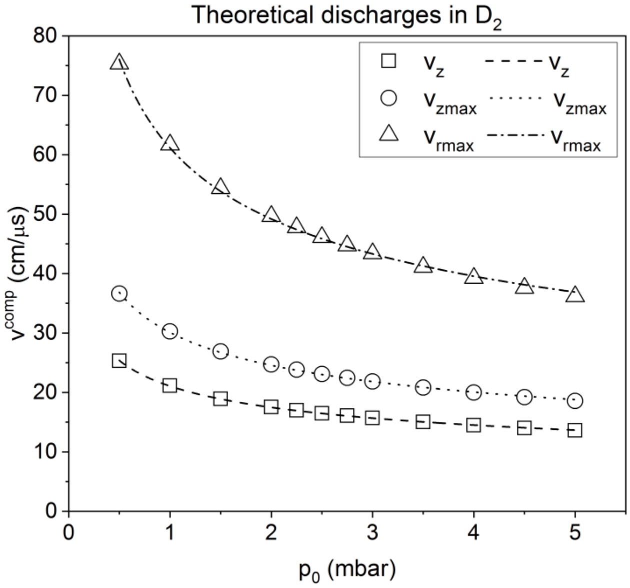

Figure 8.1.7. The computed theoretical average axial velocity (v_z^{comp}), maximum axial velocity (v_{zmax}^{comp}) and maximum radial velocity (v_{rmax}^{comp}) versus initial D_2 pressure (p_0).

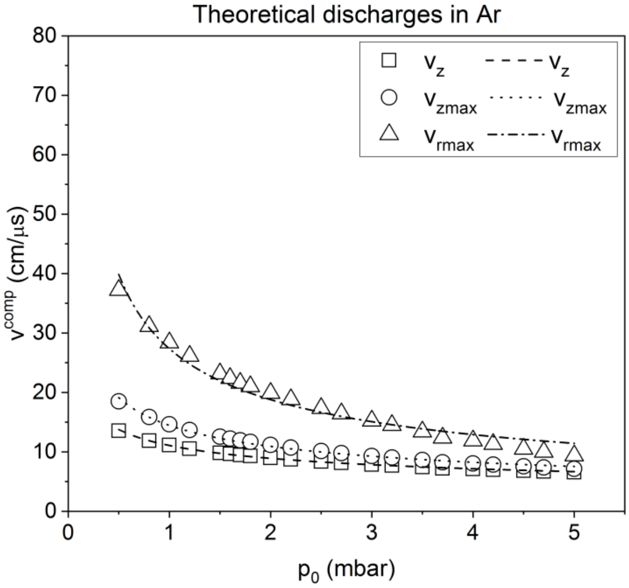

Figure 8.1.8. The computed theoretical average axial velocity (v_z^{comp}), maximum axial velocity (v_{zmax}^{comp}) and maximum radial velocity (v_{rmax}^{comp}) versus initial Ar pressure (p_0).

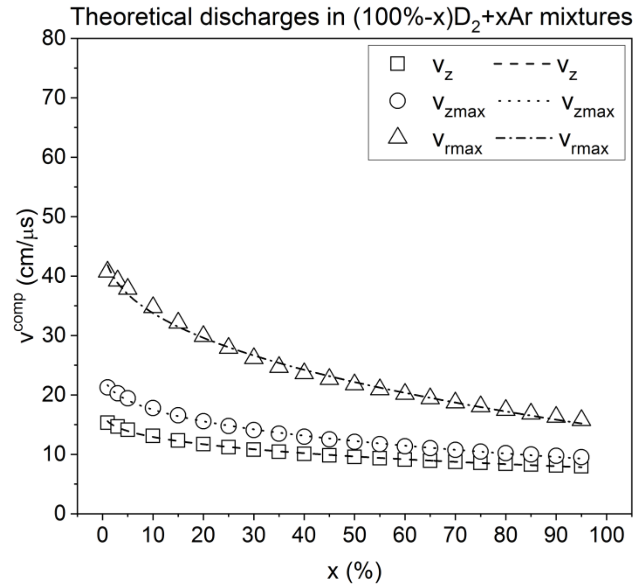

Figure 8.1.9. The computed theoretical average axial velocity (v_z^{comp}), maximum axial velocity (v_{zmax}^{comp}) and maximum radial velocity (v_{rmax}^{comp}) versus the Ar fraction (x) in (100%-x)D_2+xAr mixture.

The v_z^{comp}, v_{zmax}^{comp}, v_{rmax}^{comp} values decrease with the increase of total mass of gas or gas mixture between and in front of electrodes (initial gas or gas mixture density inside the experimental chamber), because the effective mass sweeping by current sheet increases. The power functions ($v \sim p^{-n}$) applied to fit the data in D_2 (figure 8.1.7) gave approximatly: $v_z \sim p_0^{-0.3}$, $v_{zmax} \sim p_0^{-0.3}$ and $v_{rmax} \sim p_0^{-0.3}$, while in Ar approximately: $v_z \sim p_0^{-0.3}$, $v_{zmax} \sim p_0^{-0.4}$ and $v_{rmax} \sim p_0^{-0.5}$ (figure 8.1.8) and in (100%-x)D_2+xAr mixtures approximately: $v_z \sim -x^{0.3}$, $v_{zmax} \sim -x^{0.3}$ and $v_{rmax} \sim -x^{0.4}$ was obtained using shifted power functions (figure 8.1.9). For all data damped least-squares method of fitting was used as in subsection 8.1.1. Wherein, for the highest initial pressures (masses) for discharges in Ar the v_{rmax} insignificantly changed resulting in worst matching of curvers (figure 8.1.8) – this effect was discussed in [Singh 2017].

Experimental and computed discharges in deuterium

Figure 8.1.10 presents the measured (v_z^{mea}) and computed (v_z^{comp}) average axial velocities, the computed maximum: axial (v_{zmax}^{comp}) and radial (v_{rmax}^{comp}) velocities for the discharges in D_2.

The dependencies of measured and computed velocities versus initial D_2 pressure have decreasing character: $v_z^{mea} \sim p_0^{-0.4}$, $v_{zmax}^{comp} \sim p_0^{-0.6}$ and $v_{rmax}^{comp} \sim p_0^{-0.3}$ (figure 8.1.10). The v_{rmax}^{comp} vs x data in figure 8.1.10 may represent different relation than the standard one from the slug model (lower quality of fitting). Still, the presence of large fluctuations for v_{rmax}^{comp} vs x data is to high to be sure. Moreover, the determined measured and computed values of velocities in figure 8.1.10 are smaller than the corresponding theoretical ones presented in figure 8.1.7. And the achieved measured and computed $<v_z>$ in figure 8.1.10 are in sufficient agreement suggesting achievement of the credible consistence between experiments and computations. This also suggests that the snow-plough model is still a good representation of discharge (at least in the run-down phase).

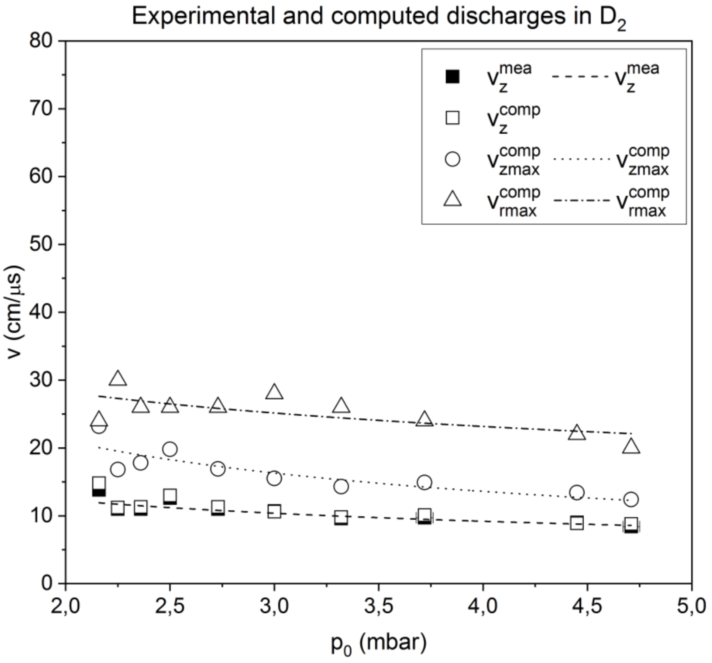

Figure 8.1.10. The measured (v_z^{mea}) and computed (v_z^{comp}) average axial velocity, the computed (v_{zmax}^{comp}) maximum axial velocity and computed (v_{rmax}^{comp}) maximum radial velocity versus initial D_2 pressure (p_0).

Experimental and computed discharges in deuterium-argon mixtures

Figure 8.1.11 presents the average measured ($<v_z^{mea}>$) and computed ($<v_z^{comp}>$) axial velocities (average both over the number of discharges and by the definition of v_z time), the computed average maximum: axial ($<v_{zmax}^{comp}>$) and radial ($<v_{rmax}^{comp}>$) velocities for the discharges in (100%-x)D_2+xAr mixtures.

The dependencies of measured and computed velocities versus Ar fraction have decreasing character (figure 8.1.10). When power functions are fitted (without division into different series and omitting point for 100% of Ar fraction) following approximate relations are achieved: $<v_z^{mea}> \sim -x^{0.4}$, $<v_{zmax}^{comp}> \sim -x^{0.6}$ and $<v_{rmax}^{comp}> \sim -x^{0.3}$. Wherein, the approximate $<v_{rmax}^{comp}> \sim -x^{0.3}$ relation was obtained using – orthogonal distance regression iteration algorithm – in comparison to the approximate $<v_z^{mea}> \sim -x^{0.4}$ and $<v_{zmax}^{mea}> \sim -x^{0.6}$ relations which were obtained as before using damped least-squares method (Levenberg-Marquardt iteration algorithm). The new fitting algorithm was used in order to obtain the same type of relation for all three types of data (this was impossible using damped least-squares method due to very large fluctuation of $<v_{rmax}^{comp}>$). The fitting for $<v_{rmax}^{comp}>$ values may suggest different dependency than the standard one from the slug model (still the fluctuations are too high to be sure). The decrease of velocities with Ar fraction is not fully continuous and not suitable proportional – suitable proportional decrease is observed only among single series of discharges for $<v_z^{mea}>$ vs x and $<v_{zmax}^{mea}>$ vs x relations. Moreover, the measured and computed $<v_z^{mea}>$ and $<v_{zmax}^{mea}>$ values in figure 8.1.11 are smaller than corresponding theoretical values in figure 8.1.7 (3.0 mbar of D_2), 8.1.8 (1.2 mbar of Ar) and 8.1.9 (3-60% of Ar). And sufficient matching of the measured and computed values of $<v_z>$ parameter was achieved, except for the discharges in 100% of Ar fraction.

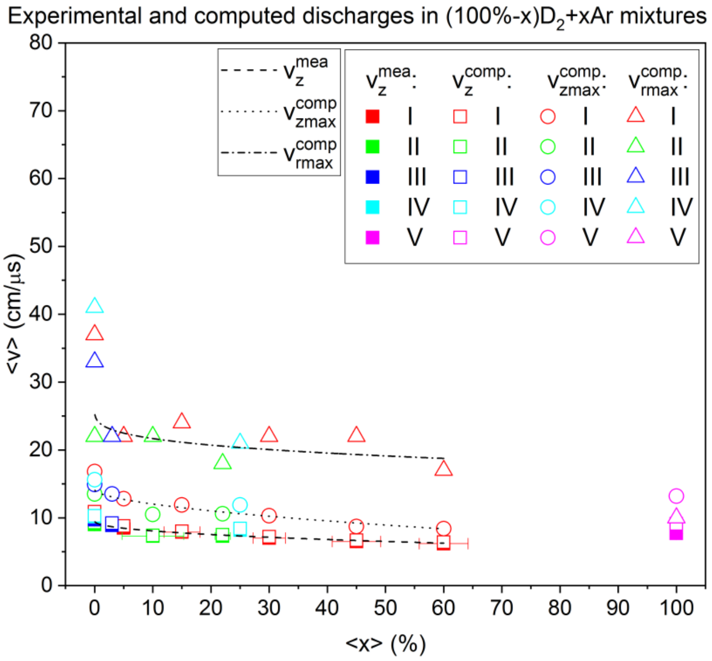

Figure 8.1.11. The average measured ($<v_z^{mea}>$) and computed ($<v_z^{comp}>$) axial velocity, the average computed maximum axial velocity ($<v_{zmax}^{comp}>$) and the average computed maximum radial velocity ($<v_{rmax}^{comp}>$) versus Ar fraction ($<x>$) in (100%-x)D_2+xAr mixtures. Roman numerals mark given series of discharges.

The measured and computed $<v_z>$ and computed $<v_{zmax}>$ for the discharges in 100% of Ar have higher values than in 30% of Ar fraction. And significant changes in the $<v_z>$ vs x and $<v_{zmax}>$ vs x relations are observed between different series of discharges – best seen for discharges in 0% of Ar fraction. The explanation is the same as given in subsection 8.1.1 for the $<t_c>$ and $<t_p>$ parameters – discharges in 0–60% of Ar and in 100% of Ar were performed under different initial total gas pressures and total masses (densities) as well as fluctuations of copper impurities (or other types of inpurities) inside plasma during different discharges, electric arcing, deformation of the anode rod with number of discharges appeard and plasma sheet was probably not generated properly for discharges in Ar.

The computed values of $<v_{rmax}>$ in figure 8.1.11 change significantly among and between different series of discharges – very large differences are stated for discharges in 0% of Ar fraction. The range of changes of $<v_{rmax}>$ in figure 8.1.11 and v_{rmax} in figure 8.1.7 (3.0 mbar D_2), figure 8.1.8 (1.2 mbar Ar) and figure 8.1.9 (3-60% of Ar) is similar. The computed value of $<v_{rmax}>$ for 100% of Ar fraction in figure 8.1.11 is smaller than the $<v_{rmax}>$ computed for all other Ar fractions.

8.2. Electric parameters

In this subsection, changes of the maximum currents (I_{max}), the maximum piston currents (I_{maxpis}), the pinch currents (I_p), the pinch plasma currents (I_{pp}) and the maximum voltages (U_{max}) will be presented.

8.2.1. Electric parameters – currents

Theoretical discharges

The computed theoretical maximum currents (I_{max}^{comp}), the computed theoretical maximum piston currents (I_{maxpis}^{comp}), the computed theoretical pinch currents (I_p^{comp}) and the computed theoretical pinch plasma currents (I_{pp}^{comp}) from the discharges in: D_2, Ar and $(100\%\text{-}x)D_2+x$Ar mixtures are presented in figure 8.2.1, figure 8.2.2 and figure 8.2.3, respectively.

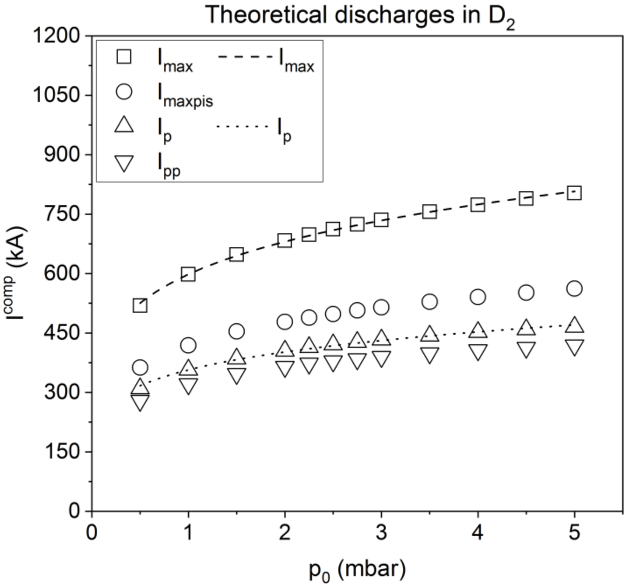

Figure 8.2.1. The computed theoretical maximum current (I_{max}^{comp}), maximum piston current (I_{maxpis}^{comp}), pinch current (I_p^{comp}) and pinch plasma current (I_{pp}^{comp}) versus initial D_2 pressure (p_0).

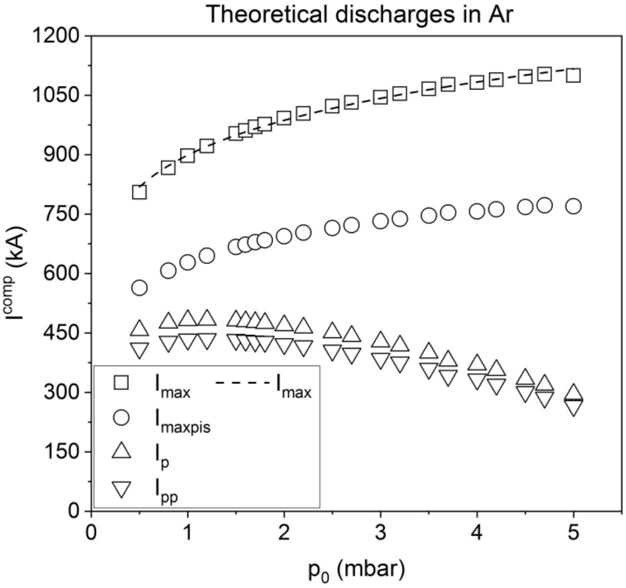

Figure 8.2.2. The computed theoretical maximum current (I_{max}^{comp}), maximum piston current (I_{maxpis}^{comp}), pinch current (I_p^{comp}) and pinch plasma current (I_{pp}^{comp}) versus initial Ar pressure (p_0).

The computed theoretical maximum currents (I_{max}^{comp}) and the computed theoretical maximum piston currents (I_{maxpis}^{comp}) in D_2 (figure 8.2.1), Ar (figure 8.2.2) and $(100\%\text{-}x)D_2+x$Ar (figure 8.2.3) increase following the power functions (changes of I_{max}^{comp} and I_{mapisx}^{comp} are described by the same type of relation – constant scalling parameter $I_{maxpis}^{comp} = I_{max}^{comp} f_c$): $I_{max}^{comp} \sim p_0^{0.2}$, $I_{max}^{comp} \sim p_0^{0.1}$ and $I_{max}^{comp} \sim x^{0.4}$, respectively (damped least-squares method of fitting was used). The reason for the increase of maximum current values (both total and flowing through magnetic piston) with the initial gas pressure or mixture is the decrease of plasma/tube inductances due to slower sheet-shock structure movement. The computed theoretical pinch currents (I_p^{comp}) and the computed theoretical pinch plasma currents (I_{pp}^{comp}) in D_2 (figure 8.2.1) also increase systematicly with initial D_2 pressure as approximately $\sim p_0^{0.2}$ (changes of I_p^{comp} and I_{pp}^{comp} are described by the same type of relation – constant scalling parameter $I_{pp}^{comp} = I_p^{comp} f_{cr}$). On the other hand, the relations of the pinch current and pinch plasma current versus the initial Ar pressure (figure 8.2.2) as well as pinch current and pinch plasma current versus Ar fraction (figure 8.2.3) show maximums. In D_2 when the range of initial pressure values would be increased up to about 12 mbar, the maximum of pinch currents and pinch plasma currents is also reached and similar dependency is obtained. This means that there is always some optimum initial pressure of gas and optimum fraction for given total pressure of gas mixture (optimal initial total mass and density) for which pinch current and plasma pinch current values are the highest. And this can result in most efficient transfer of kinetic and magnetic energy into plasma pinch. For the presented range of initial D_2 pressures in figure 8.2.1 pinch plasma currents change in the 279-419 kA range. The pinch plasma currents in Ar (figure 8.2.2) change in the 266-435 kA range with the mximum at 1.2 mbar. And for the presented range of Ar fractions (figure 8.2.3) pinch plasma current change only in the 392-435 kA range with the mximum at 35-40%.

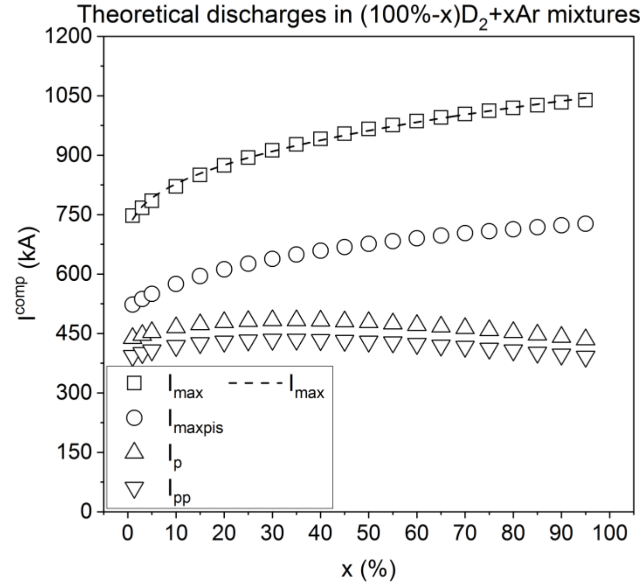

Figure 8.2.3. The computed theoretical maximum current (I_{max}^{comp}), maximum piston current (I_{maxpis}^{comp}), pinch current (I_p^{comp}) and pinch plasma current (I_{pp}^{comp}) versus Ar fraction (x) in $(100\%\text{-}x)D_2+x$Ar mixture.

Experimental and computed discharges in deuterium

The measured (I_{max}^{mea}) and computed (I_{max}^{comp}) maximum currents, the computed (I_{maxpis}^{comp}) maximum piston currents, the measured (I_p^{mea}) and computed (I_p^{comp}) pinch currents and the computed (I_{pp}^{comp}) pinch plasma currents from the coupled experimental-computed discharges in D_2 are presented in figure 8.2.4.

The measured and computed maximum currents in figure 8.2.4 appear to increase with initial D_2 pressure approximately as: $I_{max}^{mea} \sim p_0^{0.3}$ (the computed maximum piston currents appear to increase rather as $I_{maxpis}^{comp} \sim p_0^{0.2}$ with the similar quality of fitting). However, large fluctuations of I_{max} and I_{maxpis} are observed (higher than for the kinetic parameters except v_{rmax}) lowering the quality of fitting. The reason for the increase of maximum current values (both total and flowing through magnetic piston) with the initial gas or gas mixture pressure is the decrease of plasma/tube inductance due to slower sheet-shock structure movement. The determined I_{max} and I_{maxpis} values are smaller than the theoretical values (figure 8.2.1). Moreover, the measured and computed pinch currents also appear to increase slightly with increasing initial D_2 pressure approximately as: $I_p^{mea} \sim p_0^{0.2}$ (the computed pinch plasma currents appear to increase as $I_{pp}^{comp} \sim p_0^{0.1\text{-}0.2}$ with significantly better fitting quality – adjusted $R^2 \approx 0.60$). But the fluctuations of I_p^{mea} are even larger than for I_{max}^{mea} resulting in the worse fitting of the power function (figure 8.2.4). All the measured and computed maximum currents are in good agreement. While the measured and computed pinch currents are only in sufficient agreement except the values for discharge in 2.25 mbar and 4.45 mbar (larger errors). Still, this suggests credible consistence between experiments and computations for most of initial pressures. It is also worth to emphasize that the computed pinch plasma currents are spread in the range of 339-387 kA. This is a bit tigher range of changes than for the theoretical values in figure 8.2.1 but still at the similar level.

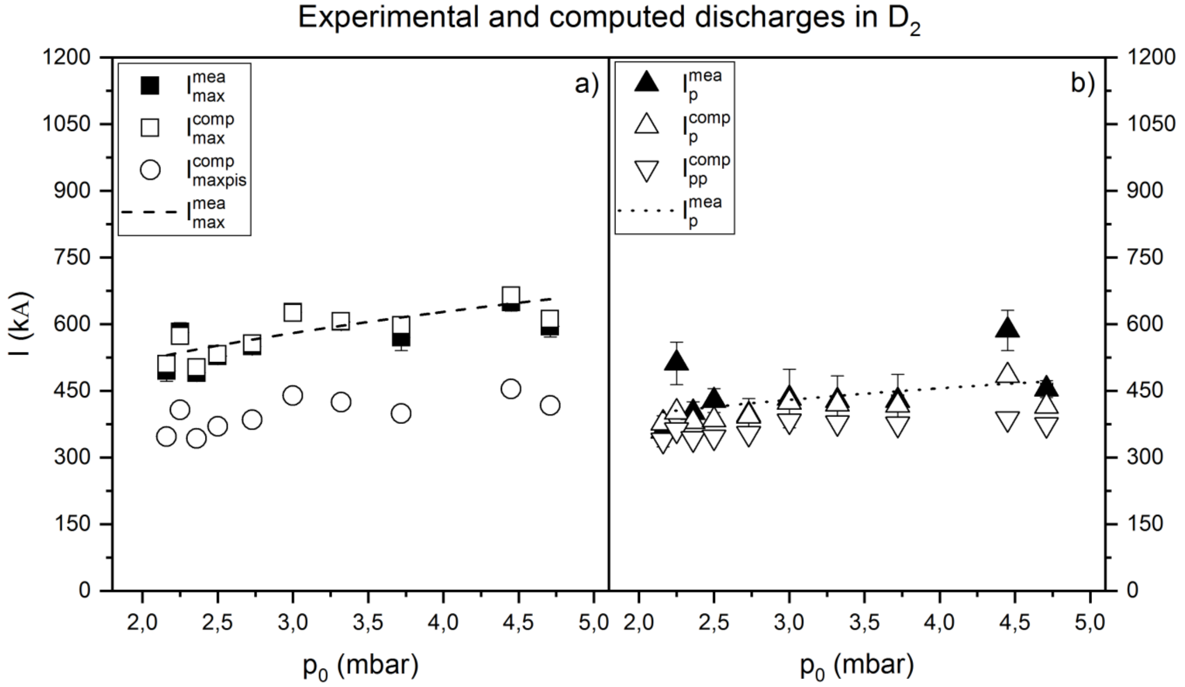

Figure 8.2.4. a) The measured (I_{max}^{mea}) and computed (I_{max}^{comp}) maximum current and the computed maximum piston current (I_{maxpis}^{mea}) versus initial D$_2$ pressure (p_0). **b)** The measured (I_p^{comp}) and computed (I_p^{comp}) pinch current and the computed pinch plasma current (I_{pp}^{comp}) versus initial D$_2$ pressure (p_0).

Experimental and computed discharges in deuterium-argon mixtures

Figure 8.2.5 presents the average measured ($<I_{max}^{mea}>$) and computed ($<I_{max}^{comp}>$) maximum currents, the average computed maximum piston currents ($<I_{maxpis}^{comp}>$), the average measured ($<I_p^{mea}>$) and computed ($<I_p^{comp}>$) pinch currents and the average computed pinch plasma currents ($<I_{pp}^{comp}>$) from the discharges in (100%-x)D$_2$+xAr mixtures.

The average measured and computed maximum current versus Ar fraction (figure 8.2.5a) appear to increase with increasing fraction as approximately: $<I_{max}^{mea}> \sim x^{0.6}$ (100% of Ar point omitted). However, the fitting of the power function is very poor due to large fluctuations. The fluctuations of $<I_{max}>$ are present even among points from the same series (unlike for measured $<t_c>$, $<t_p>$ and $<v_z>$). On the other hand, the computed maximum piston currents clearly decrease with the increase of the Ar fraction (figure 8.2.5a) which results in a slower movement of the sheet-shock structure, a decrease of plasma/tube inductance and higher maximum currents as well as longer $<t_c>$ and $<t_p>$ times. The fluctuations of $<I_{maxpis}^{comp}>$ values are also present even for the same series. Still, the decrease is clearly seen. Moreover, the range of changes of measured and computed

<I_{max}> values (figure 8.2.5a) is smaller than the theoretical in figure 8.2.1 (3.0 mbar D_2) and figure 8.2.3 (3-60% of Ar). The significantly smaller values of <I_{maxpis}^{comp}> are stated (figure 8.2.5a) for higher Ar fractions in comparison to theoretical values for the same range of fractions (figure 8.2.3). This is the result of a change of character of the <I_{maxpis}^{comp}> vs <x> dependency in figure 8.2.5a in comparison to the one presented in figure 8.2.3 – decrease of <I_{maxpis}^{comp}> with Ar fraction.

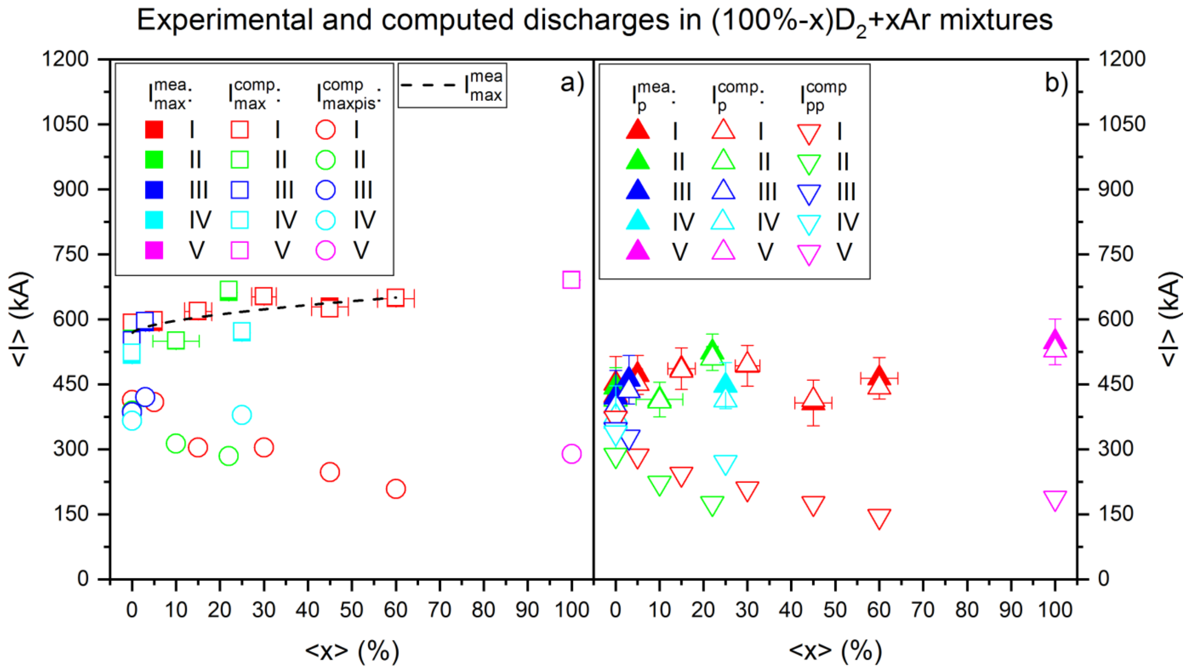

Figure 8.2.5. a) The average measured (<I_{max}^{mea}>) and computed (<I_{max}^{comp}>) maximum current and the average computed maximum piston current (<I_{maxpis}^{comp}>) versus <x> fraction of Ar in (100%-x)D_2+xAr mixture. **b)** The average measured (<I_p^{mea}>) and computed (<I_p^{comp}>) pinch current and the average computed pinch plasma current (<I_{pp}^{comp}>) versus <x> fraction of Ar in (100%-x)D_2+xAr mixture. Roman numerals indicate the series ID.

The average measured (<I_p^{mea}>) and computed (<I_p^{comp}>) pinch currents versus Ar fractions show no clear dependency (figure 8.2.5b) described by power functions. This may be sign of similar behaviour as for theoretical discharges (figure 8.2.3) or this may be due to very large fluctuations present even among the data from the same series. On the other hand, the computed pinch plasma current values (<I_{pp}^{comp}>) cleary show some type of decreasing dependency, regardless of the present fluctuations – they are significantly smaller than for <I_p> values. Moreover, there are no large fluctuations present when only <I_{pp}^{comp}> data from single series are considered. The range of changes of the measured and computed <I_p> values is far wider in D_2+Ar mixture (figure 8.2.1.5b) than the theoretical in 3.0 mbar D_2 (figure 8.2.1) and in 3-60% of Ar (figure 8.2.3). And the range of changes of the <I_{pp}^{comp}> (145-372) kA (figure 8.2.5b) – is also far wider than for the theoretical values in figure 8.2.1 (3.0 mbar D_2) and figure 8.2.3 (3-60% of Ar), wherein the <I_{pp}^{comp}> values in figure 8.2.5b are also smaller than the theoretical ones. This is the result of change of character of <I_{pp}^{comp}> vs <x> dependency in figure 8.2.5b in comparison to the one presented in figure 8.2.3.

The measured and computed <I_{max}> for 100% of Ar fraction are the highest despite the fact of carrying the discharges in about 1.2 mbar of initial pressure (although they are also significantly smaller than theoretical values in figure 8.2.2). Similarly, the measured and computed <I_p> for 100% of Ar fraction are the highest (and they are slightly higher than the theoretical value in figure 8.2.2). On the other hand, the <I_{maxpis}^{comp}> and <I_{pp}^{comp}> are not the highest (and they are far smaller than the theoretical values in figure 8.2.2). Taking into account single discharges in 100% of Ar fraction the minimum and maximum I_{pp}^{comp} is equal to: 97 kA (discharge #17101820) and 341 kA (discharge #17102003), respectively. While taking into account single discharges in 0-60% of Ar fractions the minimum and maximum I_{pp}^{comp} is equal to: 110 kA (discharge in 60% of Ar) and about 380 kA (discharges in 0-3% of Ar), respectively.

Furthermore, all the measured and computed <I_{max}> and <I_p> values are well matched (even for the discharges in 100% of Ar). Again, this suggests credible consistence between experiments and computations.

8.2.2. Electric parameters – maximum voltage

Theoretical discharges

The computed theoretical maximum voltages (U_{max}^{comp}) from the discharges in D_2, Ar and (100%-x)D_2+xAr mixtures are presented in: figure 8.2.6, figure 8.2.7 and figure 8.2.8, respectively.

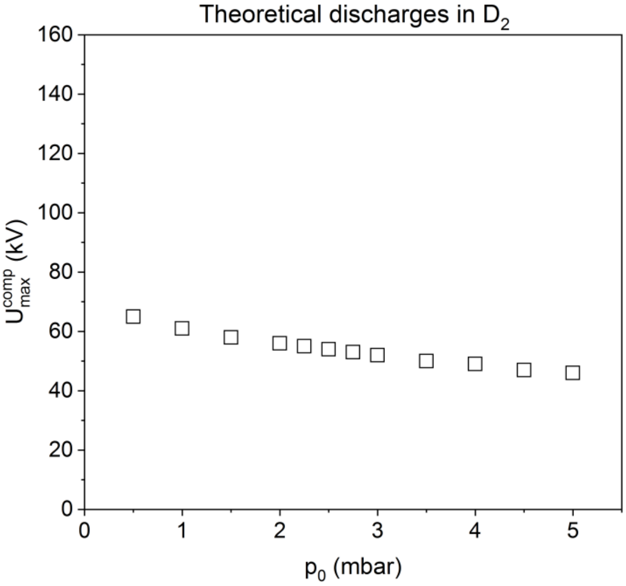

Figure 8.2.6. The computed theoretical maximum voltage (U_{max}^{comp}) versus initial D_2 pressure (p_0).

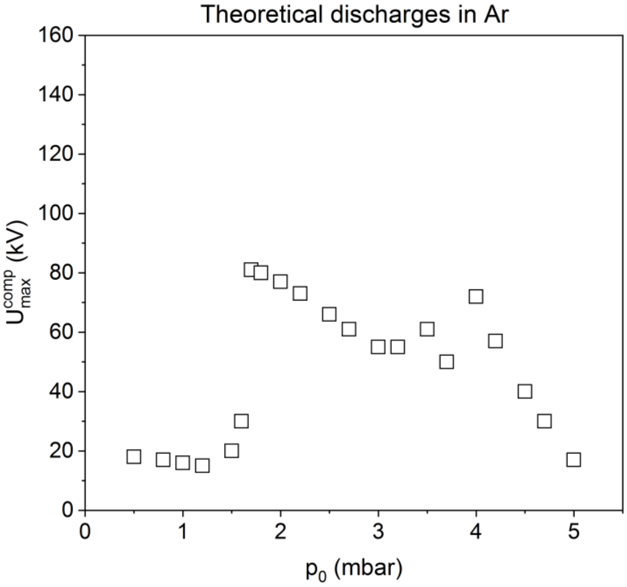

Figure 8.2.7. The computed theoretical maximum voltage (U_{max}^{comp}) versus initial Ar pressure (p_0).

The maximum induced voltages (U_{max}^{comp}) versus initial D_2 pressure (figure 8.2.6) decrease with increasing p_0. This is mainly due to the decrease of the radial piston velocity and the axial sheet-shock velocity with p_0 (see figure 8.1.7 and equation (6.2.24)).

The dependency of theoretical maximum induced voltage (U_{max}^{comp}) versus initial Ar pressure is presented in figure 8.2.7. It has three maximums (one global and two local). Up to 1.2 mbar of Ar the U_{max}^{comp} slightly decrease down to 15 kV (due to decrease of radial and axial velocities with p_0 – see equation (6.2.24)). Then at 1.5 mbar of Ar they rapidly increase up to 81 kV at 1.7 mbar. Then U_{max}^{comp} again start to decrease down to 55 kV at 3.0-3.2 mbar. From 3.2 mbar of Ar again increase and two local maximums appear at 3.5 mbar (61 kV) and 4.0 mbar (72 kV). Above 4.0 mbar of Ar decrease of U_{max}^{comp} values is observed. The rapid increasing character and the existence of the global maximum is connected mainly with the achievement of very high plasma compression – radiative compression which leads to significant increase in the velocity of compressing current sheet forming plasma column, significant decreases in radiuses of column and significant increase in lengths of column with p_0 (see equation (6.2.24)). While the local minimums appear to be connected with the changes inside plasma pinch as a result of achievement of significant opacity state resulting in changes in ohmic heating and total X-ray radiation emission which influence plasma parameters describing compression. Additionaly, this may be also connected with changes in plasma effective charges and SHRs which also influence plasma compression.

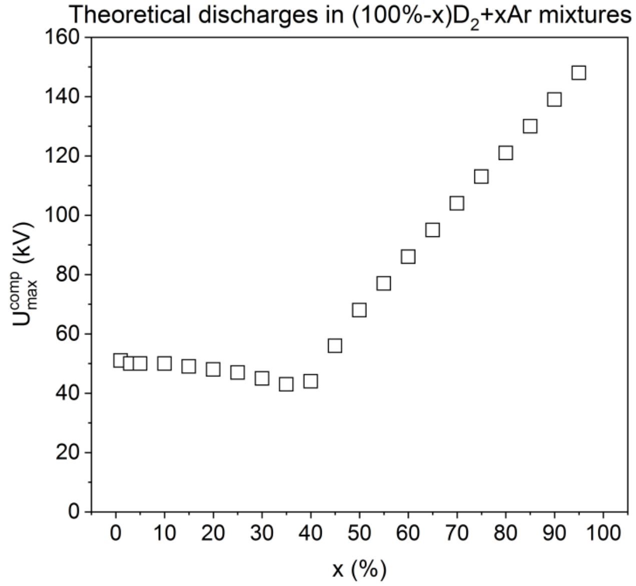

Figure 8.2.8. The computed theoretical maximum voltage (U_{max}^{comp}) versus Ar fraction (x) in (100%-x)D_2+xAr mixture.

The dependency of theoretical maximum voltage (U_{max}^{comp}) versus Ar fraction (figure 8.2.8) has completely different character than for pure gases (figure 8.2.6 and 8.2.7). In the range 43-51 kV at 1-35% of Ar fractions the maximum voltage values decrease – decreasing axial and radial velocities (equation (6.2.24)). Starting from 40% of Ar the voltages increase rapidly up to 148 kV at 95% of Ar. This increase is connected with plasma radiative compression phenomenon and achivement of significantly higher velocities of compression, smaller radiuses and bigger pinch lengths.

Computed discharges in deuterium

Figure 8.2.9 presents the computed maximum voltages (U_{max}^{comp}) from the discharges in D_2.

The computed maximum voltages (U_{max}^{comp}) seem to be approximately constant (or decrease slightly) with increase of initial D_2 pressure at the level of about 40 kV (figure 8.2.9) – axial and radial velocities change in relatively small range while pinch radiuses and lengths fluctuate at approximately constant level. Moreover, the U_{max}^{comp} values are a bit smaller than the theoretical (figure 8.2.6).

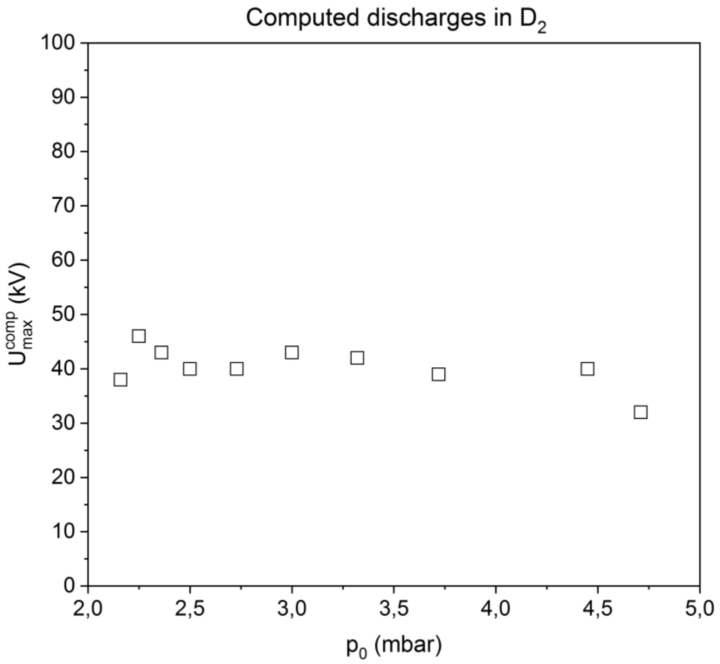

Figure 8.2.9. The computed maximum voltage (U_{max}^{comp}) versus initial D_2 pressure (p_0).

Computed discharges in deuterium-argon mixtures

Figure 8.2.10 presents the average computed maximum voltages ($<U_{max}^{comp}>$) from the discharges in (100%-x)D_2+xAr mixtures.

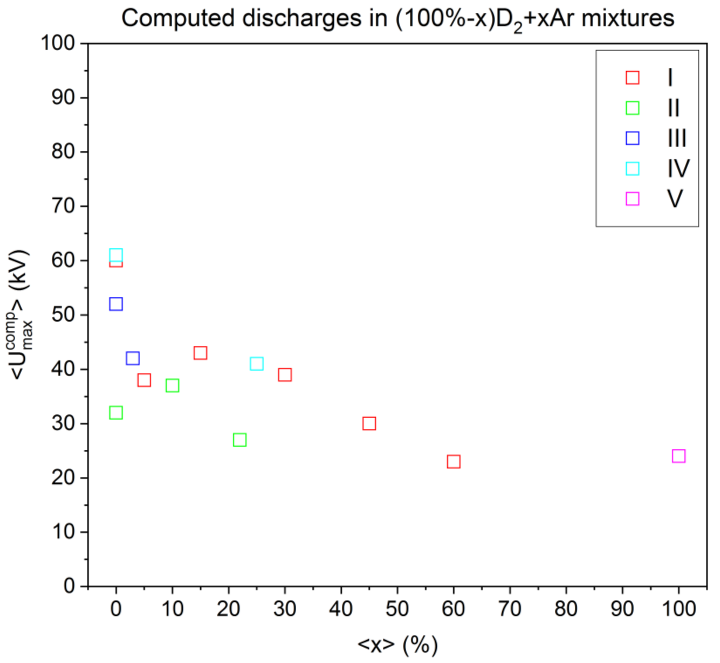

Figure 8.2.10. The average computed maximum voltage ($<U_{max}^{comp>}$) versus Ar fraction ($<x>$) in (100%-x)D_2+xAr mixture. Roman numerals indicates the series ID.

The computed maximum voltages (figure 8.2.10) decrease with Ar fraction down to 23 kV at 60% (axial and radial velocities decrease). Significant fluctuations of $<U_{max}^{comp}>$

are observed between different series as well as within given series of discharges and the dependency has completely different character than the theoretical (figure 8.2.8). For discharges in 100% of Ar (figure 8.2.10) slight increase of $<U_{max}^{comp}>$ is observed in reference to 60% of Ar. Moreover, the range of changes of $<U_{max}^{comp}>$ is wider than the theoretical from figure 8.2.6 (3.0 mbar D_2) and 8.2.8 (3-40% of Ar fraction) up to 40% of Ar fraction. And the average values in figure 8.2.10 for 3-60% of Ar are a bit smaller than the corresponding theoretical in figure 8.2.8. The existence of large voltage spikes due to higher plasma compression for 40-60% of Ar in figure 8.2.10 was not stated. In fact, the highest U_{max}^{comp} value from single discharge at 60% of Ar fraction is equal to 30 kV only. On the other hand, for discharges in 100% of Ar fraction the $<U_{max}^{comp}>$ value is bigger than the theoretical from figure 8.2.7 (1.2 mbar of Ar). The single U_{max}^{comp} values for 100% of Ar fraction are also relatively small – in the 6-41 kV range (the 6 kV was stated for discharge #17101817 and the 41 kV for discharge #17102007).

8.3. Radiative compression indicators

In this subsection, changes of the minimum reduced P-B currents ($I_{P\text{-}Breduced}(t_1)$), the corresponding P-B currents ($I_{P\text{-}B}(t_1)$), the corresponding pinch plasma currents ($I_{pp}(t_1)$), the pinch lifetimes (t_{pl}), the radiative compression lifetimes (t_{rcl}) and the characteristic radiation depletion times (t_Q) will be presented.

8.3.1. Radiative compression indicators – currents

Theoretical discharges

The computed theoretical P-B currents ($I_{P\text{-}B}^{comp}(t_1)$), the computed theoretical minimum reduced P-B currents ($I_{P\text{-}Breduced}^{comp}(t_1)$) and the computed theoretical pinch plasma currents ($I_{pp}^{comp}(t_1)$), determined at the same time (t_1), from the discharges in D_2, Ar and (100%-x)D_2+xAr mixtures are presented in figure 8.3.1, figure 8.3.2 and figure 8.3.3, respectively.

The determined computed theoretical P-B currents ($I_{P\text{-}B}^{comp}(t_1)$) for discharges in D_2 (figure 8.3.1) are constant at the level of 1455 kA. This level can be decreased insignificantly when total X-ray emission is taken into account – the minimum reduced P-B currents ($I_{P\text{-}Breduced}^{comp}(t_1)$) slowly decrease with initial D_2 pressure because of increase in total X-ray emission power (due to small increase in ion number density and decrease in ion temperature – see equations from (2.1.19) to (2.1.21)). Then the smallest minimum reduced P-B current, achieved for the highest investigated initial pressure value (5.0 mbar), is equal to 1277 kA. Still, this value is about 3.3 times higher than the corresponding current flowing through plasma pinch – $I_{pp}^{comp}(t_1) = 382$ kA. This state indicates that no radiative compression should be possible during investigated discharges in all initial D_2 pressures according to the $I_{P\text{-}B}^{comp}(t_1)$, $I_{P\text{-}Breduced}^{comp}(t_1)$ and $I_{pp}^{comp}(t_1)$.

The determined computed theoretical P-B currents ($I_{P\text{-}B}^{comp}(t_1)$) in Ar (figure 8.3.2) slowly increase from 768 kA at 0.50 mbar up to 824 kA at 3.50 mbar. Above 3.50 mbar P-B currents increase faster and faster due to the significant increase of plasma opacity (see equation (2.1.13) and (6.2.39)). This increase causes P-B currents to reach quickly very high values as 3075 kA and far more. On the other hand, the computed theoretical minimum reduced P-B currents ($I_{P\text{-}Breduced}^{comp}(t_1)$) are always significantly decreased in the entire investigated range of initial Ar pressures due to mainly high X-ray line radiation emission (because of relatively high Z and Z_{eff} numbers and increase in n_p and z_p and decrease in T_p with Ar pressure – see equation (2.1.19)) – the minimum reduced P-B currents decrease with initial Ar pressure up to about 4.2 mbar of Ar and above 4.2 mbar the values increase relatively slowly (figure 8.3.2) due to plasma opacity effect influence and decrease in X-ray line emission power (which decreases due to decrease of T_p and z_p and decrease of significance of Z and Z_{eff} parameters – see equation (6.2.37)). This results in far smaller minimum reduced P-B currents ($I_{P\text{-}Breduced}^{comp}(t_1)$) than pinch plasma currents ($I_{pp}^{comp}(t_1)$) – the minimum reduced P-B currents are in the 13-67 kA range while the pinch plasma currents are in the 266-389 kA range. For example, the smallest minimum reduced P-B current equal to 13 kA is achieved at 4.2 mbar of Ar while corresponding pinch plasma current equals 320 kA (which is about 25 times higher value). This state indicates the possibility of radiative compression occurrence during investigated discharges in the entire range of initial Ar pressures according to $I_{P\text{-}Breduced}^{comp}(t_1)$ and $I_{pp}^{comp}(t_1)$.

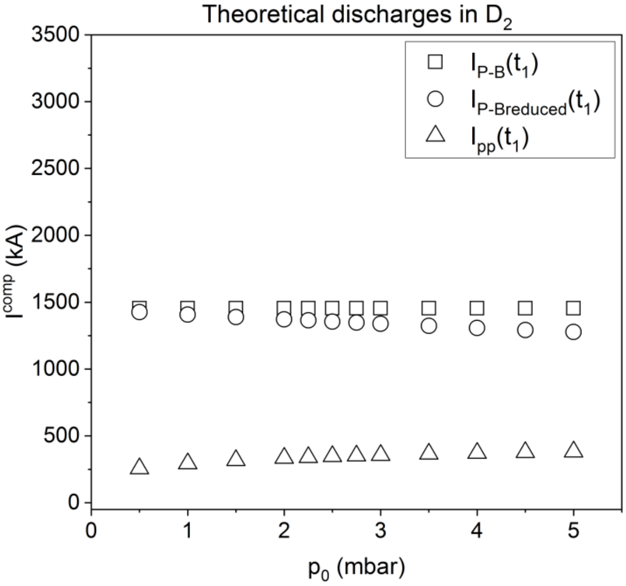

Figure 8.3.1. The computed theoretical P-B current at t_1 time ($I_{P\text{-}B}^{comp}(t_1)$), the computed theoretical reduced P-B current at t_1 time ($I_{P\text{-}Breduced}^{comp}(t_1)$) and the computed theoretical pinch plasma current at t_1 time ($I_{pp}^{comp}(t_1)$) versus initial D_2 pressure (p_0).

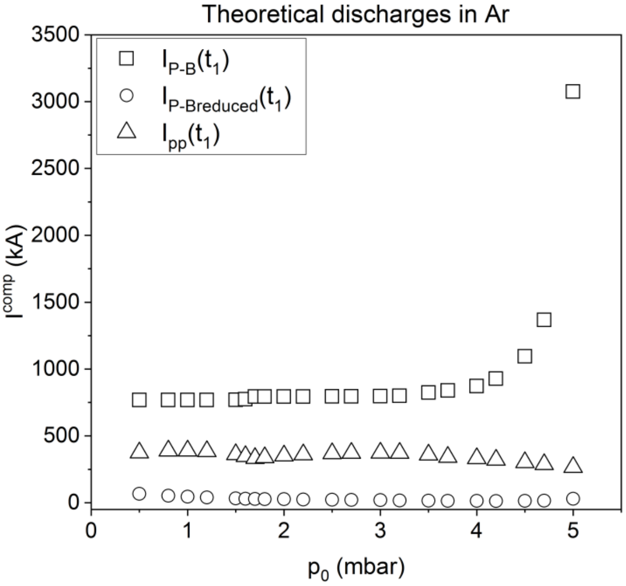

Figure 8.3.2. The computed theoretical P-B current at t_1 time ($I_{P\text{-}B}^{comp}(t_1)$), the computed theoretical reduced P-B current at t_1 time ($I_{P\text{-}Breduced}^{comp}(t_1)$) and the computed theoretical pinch plasma current at t_1 time ($I_{pp}^{comp}(t_1)$) versus initial Ar pressure (p_0).

The determined computed theoretical P-B currents ($I_{P\text{-}B}^{comp}(t_1)$) in (100%-$x$)$D_2$+$x$Ar mixtures (figure 8.3.3) decrease with Ar fraction from 1349 kA at 1% down to 799 kA at 95% – this is caused by the increase in the total atomic numbers – see equation (2.1.21)). All of these values are bigger than the corresponding pinch plasma currents ($I_{pp}^{comp}(t_1)$) which are in the 360-393 kA range. The minimum reduced P-B currents ($I_{P\text{-}Breduced}^{comp}(t_1)$) also decrease with Ar fraction from 1035 kA at 1% of Ar down to 19 kA at 95% of Ar – this appears to be mainly due to increase in the total atomic numbers and total effective charges of plasma with increase of Ar fraction as well as due to decrease in ion pinch temperatures and increase in pinch densities and lengths resulting in mainly higher X-ray line emission (equation (2.1.19)). From 3% of Ar fraction the minimum reduced P-B currents become smaller than the corresponding pinch plasma currents indicating possibility of plasma radiative compression phenomenon occurrence during discharges in 3-95% mixtures.

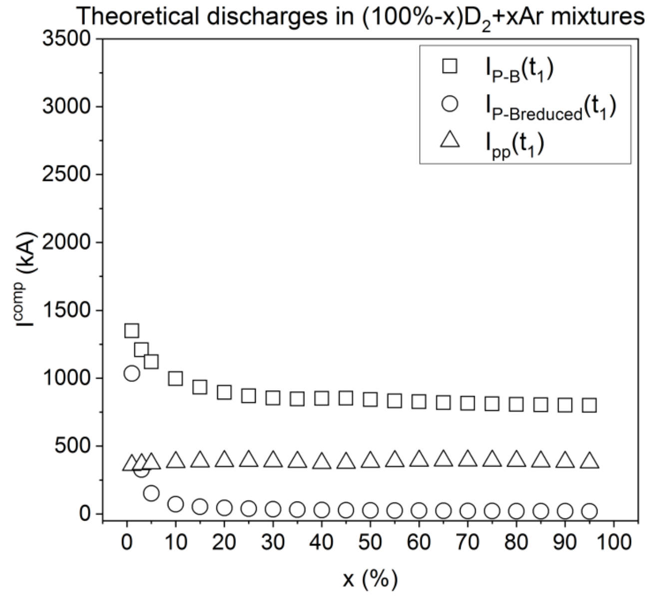

Figure 8.3.3. The computed theoretical P-B current at t_1 time ($I_{P\text{-}B}^{comp}(t_1)$), the computed theoretical reduced P-B current at t_1 time ($I_{P\text{-}Breduced}^{comp}(t_1)$) and the computed theoretical pinch plasma current at t_1 time ($I_{pp}^{comp}(t_1)$) versus Ar fraction (x) in (100%-x)D_2+xAr mixture.

Computed discharges in deuterium

Figure 8.3.4 presents the computed P-B currents ($I_{P\text{-}B}^{comp}(t_1)$), the computed minimum reduced P-B currents ($I_{P\text{-}Breduced}^{comp}(t_1)$) and the computed pinch plasma currents ($I_{pp}^{comp}(t_1)$), determined at the same time (t_1), from the discharges in D_2.

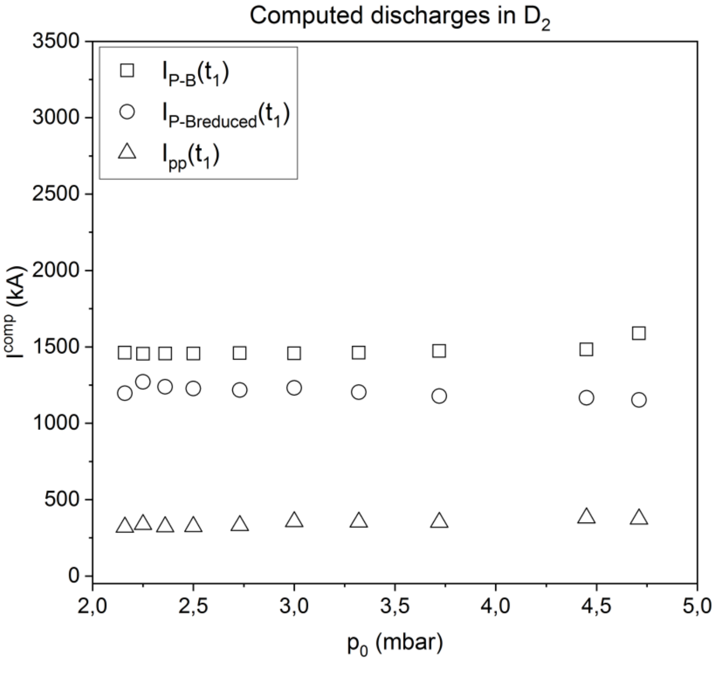

Figure 8.3.4. The computed P-B current at t_1 time ($I_{P\text{-}B}^{comp}(t_1)$), the computed reduced P-B current at t_1 time ($I_{P\text{-}Breduced}^{comp}(t_1)$) and the computed pinch plasma current at t_1 time ($I_{pp}^{comp}(t_1)$) versus initial D_2 pressure (p_0).

The computed pinch plasma currents ($I_{pp}^{comp}(t_1)$) in D_2 (figure 8.3.4) are significantly smaller than the corresponding P-B currents ($I_{P\text{-}B}^{comp}(t_1)$) and the minimum reduced P-B currents ($I_{P\text{-}Breduced}^{comp}(t_1)$) – same situation as for the theoretical discharges in D_2 (figure 8.3.1). The computed pinch plasma currents are in the 320-381 kA range, while the P-B currents are approximately constant at the level of 1455-1590 kA. The minimum reduced P-B currents decrease slightly from 1271 kA down to 1153 kA (higher thereotical values were anticipated – figure 8.3.1). The presented state in figure 8.3.4 indicates no possibility of the radiative compression phenomenon occurrence for all initial D_2 pressures.

Computed discharges in deuterium-argon mixtures

Figure 8.3.5 presents the average computed P-B currents ($<I_{P\text{-}B}^{comp}(t_1)>$), the average computed minimum reduced P-B currents ($<I_{P\text{-}Breduced}^{comp}(t_1)>$) and the average computed pinch plasma currents ($<I_{pp}^{comp}(t_1)>$), determined at the time (t_1), from the computed discharges in (100%-x)D_2+xAr mixtures.

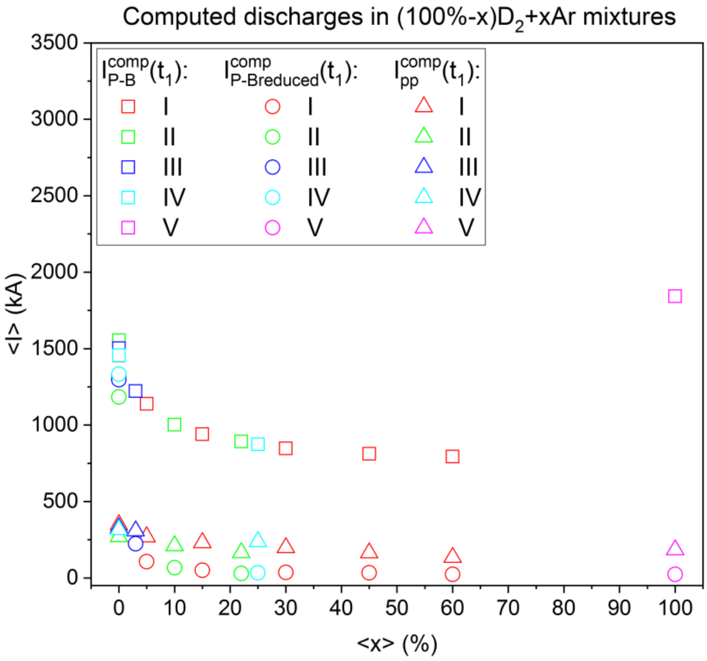

Figure 8.3.5. The average computed P-B current at t_1 time ($<I_{P\text{-}B}^{comp}(t_1)>$), the average computed reduced P-B current at t_1 time ($<I_{P\text{-}Breduced}^{comp}(t_1)>$) and the average computed ($<I_{pp}^{comp}(t_1)>$) pinch plasma current at t_1 time versus Ar fraction ($<x>$) in (100%-x)D_2+xAr mixture. Roman numerals mark given series of discharges.

The average computed pinch plasma currents ($<I_{pp}^{comp}(t_1)>$) for discharges in (100%-x)D_2+xAr mixtures (figure 8.3.5) decrease with Ar fraction increase up to 60% unlike the theoretical discharges in (100%-x)D_2+xAr mixtures (figure 8.3.3). At 100% of Ar slight increase is stated. The range of changes of $<I_{pp}^{comp}(t_1)>$ is equal to 135-348 kA. The smallest $I_{pp}^{comp}(t_1)$ value from single discharge is equal to 97 kA (discharge #17101820 in 100% of Ar) and highest is equal to 380 kA (discharge #17071007 in 0% of Ar and #17092811 in 3% of Ar). The 135-348 kA range is wider than the theoretical range in figure 8.3.1 (3.0 mbar of D_2), figure 8.3.2 (1.2 mbar of Ar) and figure 8.3.3 (3-60% of Ar) and the computed values are smaller.

The average P-B currents ($<I_{P-B}^{comp}(t_1)>$) for discharges in (100%-x)D_2+xAr mixtures (figure 8.3.5) decrease with Ar fraction (similarly as for the theoretical values in (100%-x)D_2+xAr mixtures in figure 8.3.3) except for the discharges in 100% of Ar. The $<I_{P-B}^{comp}(t_1)>$ values decrease from 1456-1555 kA (series I-IV) at 0% down to 794 kA at 60% – due to increase in total atomic numbers of plasma (equation (2.1.21)). For the discharges in 100% of Ar fraction the computed average P-B current at t_1 is significantly higher due to high plasma opacity effect included through f_0 factor (equation (2.1.13)). Moreover, there are three individual discharges for which $I_{P-B}^{comp}(t_1)$ values differ very significantly from average value computed at t_1 moment – because of this fact they were not included into calculation of average values. The IDs of these discharges are: #17083103 (10% of Ar fraction), #17101817 (100% of Ar fraction) and #17101818 (100% of Ar fraction). The $I_{P-B}^{comp}(t_1)$ for the discharge #17083103, #17101817 and #17101818 is approximately equal to: 1.9×10^4 kA, 2.0×10^8 kA and 5.3×10^5 kA, respectively. Such extremely high values of the P-B currents are caused by the correction for plasma opacity effect which strongly develops. Furthermore, single $I_{P-B}^{comp}(t_1)$ values for 100% of Ar fraction are relatively widely spread around corresponding average value – the smallest value is equal to 768 kA (discharge #17102003) while the highest value is equal to 2.0×10^8 kA (discharges #17101817).

The average computed minimum reduced P-B currents ($<I_{P-Breduced}^{comp}(t_1)>$) for discharges in (100%-x)D_2+xAr mixtures (figure 8.3.5) decrease with increasing Ar fraction (similarly as the theoretical values in (100%-x)D_2+xAr mixtures in figure 8.3.3). This includes also $<I_{P-Breduced}^{comp}(t_1)>$ for 100% of Ar fraction. The $<I_{P-Breduced}^{comp}(t_1)>$ value for 100% of Ar fraction is the smallest one taking into accont all investigated fractions, despite the fact of corresponding $<I_{P-B}^{comp}(t_1)>$ value being the highest one of all fractions (result of highest total X-ray line emission power proportional among others to Z and Z_{eff} – see equation (2.1.19)). The averaged computed minimum reduced P-B currents for 0% of Ar fraction are at the level of 1184-1333 kA (series I-IV). These values are higher than the corresponding average computed pinch plasma currents ($<I_{pp}^{comp}(t_1)>$). For the 3% of Ar fraction $<I_{P-Breduced}^{comp}(t_1)>$ value decreases down to 224 kA because of strong increase in total X-ray emission power. The 224 kA value is about 1.4 times smaller than the corresponding computed average pinch plasma current value – plasma radiative compression occurrence possible. Moreover, the smallest $<I_{P-Breduced}^{comp}(t_1)>$ from all investigated Ar fractions, achieved at 100% of Ar, is equal to 23 kA. The 23 kA is 8 times smaller value than the corresponding $<I_{pp}^{comp}(t_1)>$ value. Thus, in the range of 3-60% of Ar and at 100% of Ar radiative compression should be possible according to $I_{P-Breduced}^{comp}(t_1)$ and $I_{pp}^{comp}(t_1)$ indicators – this is the same situation as for the theoretical discharges in (100%-x)D_2+xAr mixtures in figure 8.3.3 (3-60% of Ar) and in Ar in figure 8.3.2 (1.2 mbar of Ar). And this situation is valid for almost all single investigated discharges except for the three discharges – one in 10% of Ar and two in 100% of Ar. The three discharges are the ones already mentioned in this subsection: #17083103, #17101817 and #17101818. For discharge #17083103, #17101817 and #17101818 the $I_{P-Breduced}^{comp}(t_1)$ is equal to: 382 kA, 1.4×10^6 kA and 4.1×10^3 kA, respectively. While the corresponding $I_{pp}(t_1)$ values are only equal to: 175 kA, 169 kA and 165 kA.

8.3.2. Radiative compression indicators – times

Theoretical discharges

The computed theoretical pinch lifetimes (t_{pl}^{comp}), the computed theoretical radiative compression lifetimes (t_{rcl}^{comp}) and the computed theoretical characteristic radiation depletion times (t_Q^{comp}) from the discharges in D_2, Ar and (100%-x)D_2+xAr mixtures are presented in figure 8.3.6, figure 8.3.7 and figure 8.3.8, respectively.

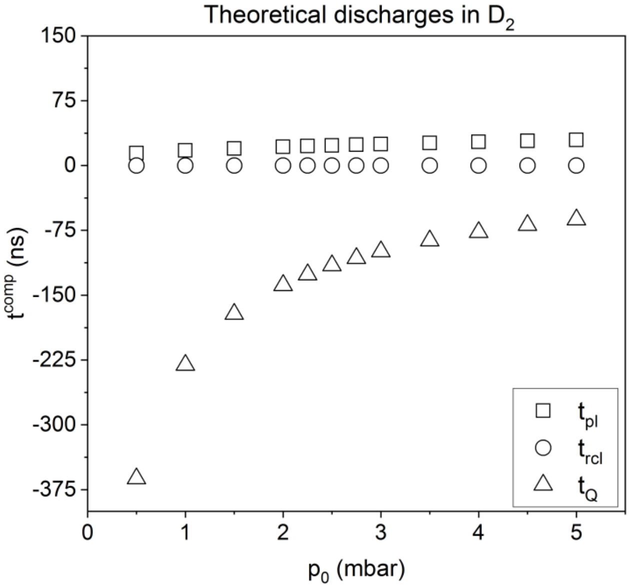

Figure 8.3.6. The computed theoretical pinch lifetime (t_{pl}^{comp}), the computed theoretical radiative compression lifetime (t_{rcl}^{comp}) and the computed theoretical characteristic radiation depletion time (t_Q^{comp}) versus initial D_2 pressure (p_0).

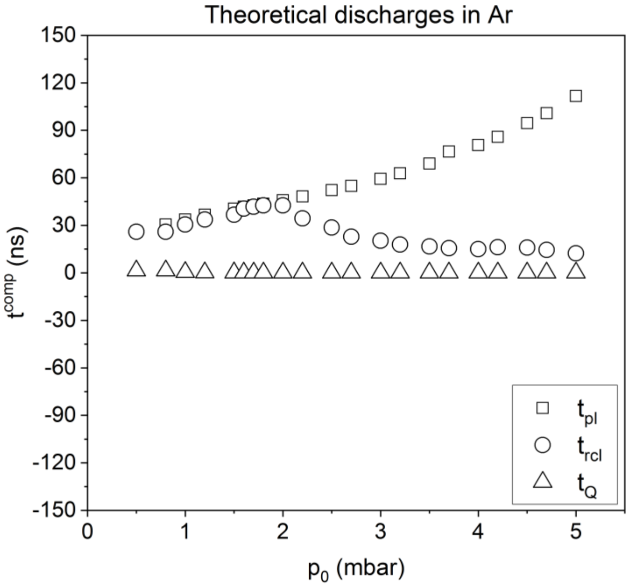

Figure 8.3.7. The computed theoretical pinch lifetime (t_{pl}^{comp}), the computed theoretical radiative compression lifetime (t_{rcl}^{comp}) and the computed theoretical characteristic radiation depletion time (t_Q^{comp}) versus initial Ar pressure (p_0).

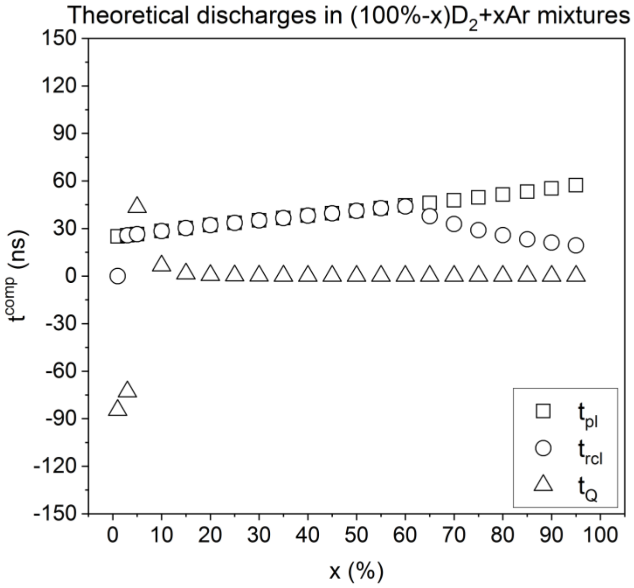

Figure 8.3.8. The computed theoretical pinch lifetime (t_{pl}^{comp}), the computed theoretical radiative compression lifetime (t_{rcl}^{comp}) and the computed theoretical characteristic radiation depletion time (t_Q^{comp}) versus Ar fraction (x) in (100%-x)D_2+xAr mixture.

The computed theoretical radiative compression lifetimes (t_{rcl}^{comp}) for discharges in D_2 (figure 8.3.6) are always equal to zero while the computed theoretical pinch lifetimes (t_{pl}^{comp})

slightly increase with initial D_2 pressure resulting in maximum duration of 30 ns at 5.0 mbar. The t_{rcl}^{comp} being always equal to zero is the result of the minimum reduced P-B currents being smaller than the corresponding pinch plasma currents during entire pinch phase of discharge – the situation from figure 8.3.6 upholds during the entire discharge (not only during t_1 time). Moreover, the computed theoretical characteristic times of radiation depletion (t_Q^{comp}) are always negative regardless of the initial D_2 pressures. This means that more power is to be generated through the plasma heating than loss due to the total X-ray radiation emission – fast and significant radiative cooling of plasma is to be impossible during pinch phase of discharges for all investigated initial D_2 pressures according to the t_{pl}^{comp}, t_{rcl}^{comp} and t_Q^{comp} indicators.

The computed theoretical pinch lifetimes (t_{pl}^{comp}) in Ar (figure 8.3.7) increse with Ar pressure increase achieving 112 ns at 5.0 mbar of Ar. The computed theoretical radiative compression (t_{rcl}^{comp}) lasts almost as long as the entire pinch phase of the investigated discharges for Ar pressures up to 1.8 mbar. Above 1.8 mbar the t_{rcl}^{comp} and t_{pl}^{comp} diverge. This is caused by the plasma opacity which decreases the t_{rcl}^{comp} through influencing the minimum reduced P-B currents. The influence of opacity takes visible effects on the t_{rcl}^{comp} starting from 1.8 mbar and starting from about 4.0-4.2 mbar its influence becomes very high causing a small change in the character of dependency in figure 8.3.7. Moreover, the computed theoretical characteristic times of radiation depletion (t_Q^{comp}) are always positive and decrease with Ar always achiving smaller values than the t_{pl}^{comp} and t_{rcl}^{comp}. Thus, the plasma radiative compression is possible during discharges in all investigated initial pressures of Ar according to the t_{pl}^{comp}, t_{rcl}^{comp} and t_Q^{comp} indicators.

The computed theoretical pinch lifetimes (t_{pl}^{comp}) for discharges in $(100\%\text{-}x)D_2+x$Ar mixtures (figure 8.3.8) increase with Ar fraction achieving 57 ns at 95%. The computed theoretical radiative compression lifetime (t_{rcl}^{comp}) at 1% of Ar is equal to 0 ns – no radiative compression is to be present according to the t_{rcl}^{comp}. From 3% of Ar the t_{rcl}^{comp} become nonzero and follow the changes of t_{pl}^{comp} up to 60% of Ar. From 65% of Ar t_{rcl}^{comp} become smaller than the t_{pl}^{comp} and continue to decrease with Ar fraction despite the increase of t_{pl}^{comp}. This is the effect of plasma opacity influencing significantly t_{rcl}^{comp} from 65% of Ar fraction. The computed theoretical characteristic time of radiation depletion (t_Q^{comp}) in the 1-3% range of Ar fraction has negative values indicating no radiative compression occurrence because of total power of plasma ohmic heating exceeding total emission power of X-ray radiation (slow cooling of plasma column). At 5% positive value of t_Q^{comp} at the level of 43 ns is obtained. However, the 43 ns is still bigger than the value of corresponding t_{pl}^{comp} and t_{rcl}^{comp} which are equal to 26 ns. This indicates also no possibility of radiative compression occurrence up to 5% of Ar. Starting from 10% of Ar fraction t_Q^{comp} become smaller than the t_{pl}^{comp} and t_{rcl}^{comp} (the power of total emission of X-ray radiation exceeds the total power of ohmic heating) and decrease further with Ar achieving about 0.0003 ns time at 95% of Ar (about 190000 times smaller value than the corresponding t_{pl}^{comp} and about 63333 times smaller value than the corresponding t_{rcl}^{comp}). Thus, radiative compression should be possible starting from 10% of Ar fraction according to the t_{pl}^{comp} and t_Q^{comp} as well as t_{rcl}^{comp}.

Computed discharges in deuterium

Figure 8.3.9 presents the computed pinch lifetimes (t_{pl}^{comp}), the computed radiative compression lifetimes (t_{rcl}^{comp}) and the computed characteristic radiation depletion times (t_Q^{comp}) from the discharges in D_2.

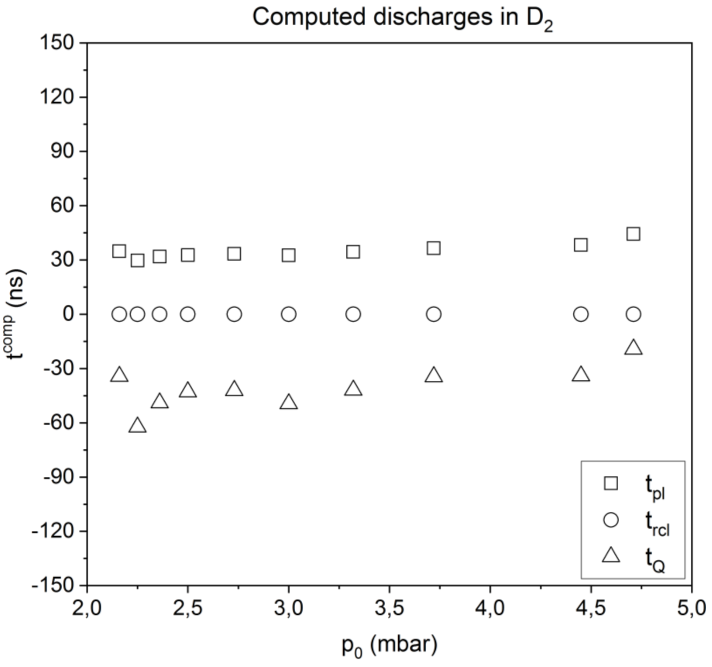

Figure 8.3.9. The computed pinch lifetime (t_{pl}^{comp}), the computed radiative compression lifetime (t_{rcl}^{comp}) and computed characteristic radiation depletion time (t_{Q}^{comp}) versus initial D_2 pressure (p_0).

The plasma pinch lifetimes (t_{pl}^{comp}) for computed discharges in D_2 (figure 8.3.9) slightly increase with D_2 pressure (similar as for theoretical discharges in D_2 in figure 8.3.6) varying between 30 ns and 44 ns (higher values than the anticipated theoretical ones in figure 8.3.6). The computed radiative compression lifetimes (t_{rcl}^{comp}) in D_2 (figure 8.3.9) are always equal to zero since $I_{P\text{-}Breduceed}^{comp}(t)$ are always bigger than $I_{pp}^{comp}(t)$ (the same as for the theoretical discharges in D_2 in figure 8.3.6) – the situation from figure 8.3.4 upholds during entire discharge. Moreover, the computed characteristic times of radiation depletion (t_{Q}^{comp}) in D_2 (figure 8.3.4) are always negative indicating that the total power of ohmic heating is always bigger than the total power of X-ray radiation emission (the same as for the theoretical discharges in D_2 in figure 8.3.6). The t_{Q}^{comp} values increase with initial D_2 pressure (also similar as for theoretical discharges in D_2 in figure 8.3.6). Thus, all the determined time indicators prevent the occurrence of plasma radiative compression phenomenon for computed discharges in D_2 in all investigated initial pressures.

Computed discharges in deuterium-argon mixtures

Figure 8.3.10 presents the average computed pinch lifetimes ($<t_{pl}^{comp}>$), the average computed radiative compression lifetimes ($<t_{rcl}^{comp}>$) and the average computed characteristic radiation depletion times ($<t_{Q}^{comp}>$) from the discharges in $(100\%\text{-}x)D_2\text{+}x\text{Ar}$ mixtures.

The average computed pinch lifetimes ($<t_{pl}^{comp}>$) in $(100\%\text{-}x)D_2\text{+}x\text{Ar}$ mixtures (figure 8.3.10) for discharges in 0-60% of Ar fraction do not show any clear relation (taking into account all data series). However, when taking into account only data from series I, III and IV seperatly some increase of $<t_{pl}^{comp}>$ is identified. The $<t_{pl}^{comp}>$ values in the 0-60% od Ar change between 24 ns and 39 ns – a bit smaller range of changes than for the theoretical discharges in figure 8.3.6 (3.0 mbar of D_2) and figure 8.3.8 (3-60% of Ar). The shortest t_{pl}^{comp} during single discharge in 0-60% of Ar is equal to 15 ns (discharges in 0% of Ar) and longest is equal to 57 ns (discharge in 10% of Ar). For the discharges in 100% of Ar fraction the $<t_{pl}^{comp}>$ is prolonged up to 66 ns. The shortest t_{pl}^{comp} during single discharge in 100%

of Ar is equal to 29 ns (discharges #17102003) and longest computed pinch lifetime is equal to 91 ns (discharge #17101817). The 66 ns is longer time than the predicted one from the theoretical discharges in figure 8.3.7 (1.2 mbar of Ar).

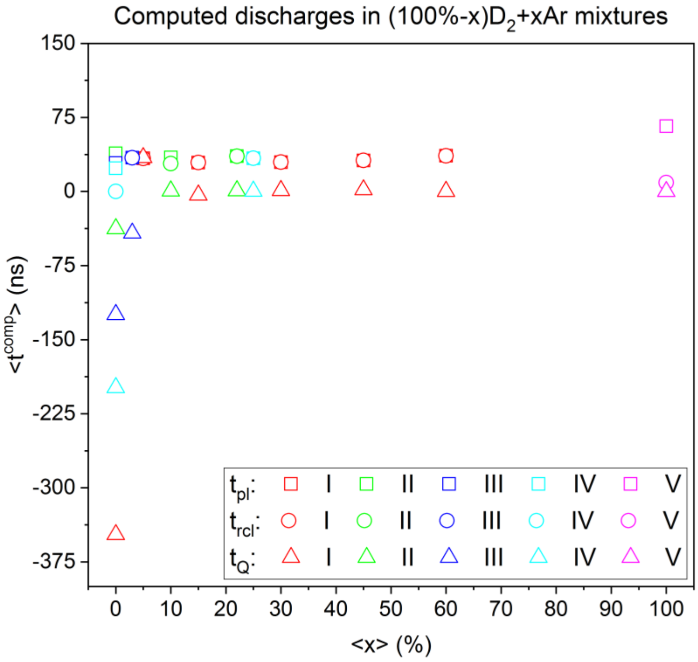

Figure 8.3.10. The average computed pinch lifetime ($<t_{pl}^{comp}>$), the average computed radiative compression lifetime ($<t_{rcl}^{comp}>$) and the average computed characteristic radiation depletion time ($<t_Q^{comp}>$) versus Ar fraction ($<x>$) in (100%-x)D$_2$+xAr mixture. Roman numerals indicates the series ID.

The average computed radiative compression lifetimes ($<t_{rcl}^{comp}>$) for discharges in (100%-x)D$_2$+xAr mixtures (figure 8.3.10) for 0% of Ar fraction are always equal to 0 ns, all series included – again no radiatvie compression is to be possible during discharges in D$_2$. But for the discharges in 3-60% of Ar the $<t_{rcl}^{comp}>$ are almost the same as the $<t_{pl}^{comp}>$ (the same situation as for the theoretical discharges in (100%-x)D$_2$+xAr mixtures in figure 8.3.8). In fact, in the 3-60% range of Ar fractions only for one discharge the computed radiative compression lifetime is significantly shorter than the computed pinch lifetime and the computed characteristic depletion time (t_Q^{comp}). This discharge is #17083103 and was carried in 10% of Ar fraction – t_{rcl}^{comp} = 0 ns, t_{pl}^{comp} = 57 ns and t_Q^{comp} = 0.3 ns. The plasma behaviour during discharge #17083103 is the results of instant transition into the high opacity state. For the discharges in 100% of Ar fraction the $<t_{rcl}^{comp}>$ is smaller than the $<t_{pl}^{comp}>$ (7.3 times smaller) and higher than $<t_Q^{comp}>$ (about 300 times higher) – for the theoretical discharge in 1.2 mbar of Ar in figure 8.3.7 $t_{pl}^{comp} \approx t_{rcl}^{comp}$ and $t_{rcl}^{comp} > t_Q^{comp}$. However, for the 2 single discharges in 100% of Ar fraction the t_{rcl}^{comp} is equal to 0 ns. The two computed discharges in which no radiative compression is to be expected are the: #17101817 and #17101818. During these two discharges plasma enters instantly very high opacity state. On the other hand, the longest t_{rcl}^{comp} from single discharges in 100% of Ar faction was equal to 29 ns – discharge #17102003. For the discharge #17102003 $t_{rcl}^{comp} = t_{pl}^{comp}$ and $t_{rcl}^{comp} > t_Q^{comp}$.

The average computed characteristic times of radiation depletion ($<t_Q^{comp}>$) for discharges in (100%-x)D$_2$+xAr mixtures (figure 8.3.10) are always negative for 0% of Ar (the same situation as for the theoretical discharges in (100%-x)D$_2$+xAr mixtures in figure 8.3.6 and as for the computed discharges in D_2 in figure 8.3.9). The differences between $\langle t_Q^{comp} \rangle$ values for different series of discharges are high – especially for 0% of Ar fraction (figure 8.3.10). For the discharges in the 3-15% of Ar range some of the discharges has negative values of t_Q^{comp}. For the discharges in 3% of Ar fraction all t_Q^{comp} values are negative (the same as for the theoretical discharges in (100%-x)D_2+xAr mixtures in figure 8.3.8). For the discharges in 5% of Ar, 3 t_Q^{comp} values are negative and 5 t_Q^{comp} values are positive but bigger than the corresponding t_{pl}^{comp} and t_{rcl}^{comp} values (or at the similar level). For the discharges in 10% of Ar fraction, 1 t_Q^{comp} value is negative and 2 t_Q^{comp} values are positive but bigger than the corresponding t_{pl}^{comp} and t_{rcl}^{comp} values. And for the discharges in 15% of Ar fraction, only 1 t_Q^{comp} value is still negative. For the investigated discharges in the 22-60% of Ar fraction range all t_Q^{comp} values are positive and smaller than the corresponding t_{pl}^{comp} and t_{rcl}^{comp} values. And for 100% of Ar fraction almost all t_Q^{comp} values, except for two discharges, are positive and smaller than corresponding t_{pl}^{comp} and t_{rcl}^{comp} values. Thus, the increase of Ar fraction increases the probability that the performed discharge in the PF-24 device will have positive value of characteristic radiation depletion time as well as that this time will be smaller than the corresponding pinch lifetime and radiative compression lifetime (due to increase of total X-ray emission power with Ar fraction caused mainly by the increase in Z and Z_{eff}). For the discharges in the 22%, 25%, 30%, 45%, 60% and 100% of Ar fraction the $\langle \tau_Q^{comp} \rangle$ is equal to about: 0.81 ns, 0.35 ns, 1.05 ns, 1.79 ns, 0.14 ns and 0.03 ns, respectively. The fluctuations of $\langle \tau_Q^{comp} \rangle$ values are the result of many different possible scenarios of discharge which may occur in the PF-24 device. Still, the smallest t_Q^{comp} values on average are achieved during investigated discharges in 100% of Ar fraction. The $\langle \tau_Q^{comp} \rangle$ for 100% of Ar fraction is about 2200 times smaller than the corresponding $\langle t_{pl}^{comp} \rangle$ and about 300 times smaller than the corresponding $\langle t_{rcl}^{comp} \rangle$ – smaller ratios are anticipated for the theoretical discharge in 1.2 mbar of Ar in figure 8.3.7. Summarizing, for the some of the investigated discharges in the 5-60% and 100% of Ar fraction radiative compression is possible according to the t_{rcl}^{comp}, t_Q^{comp} and t_{pl}^{comp} indicators – from the theoretical predictions in Ar in figure 8.3.7 (1.2 mbar of Ar) and in (100%-x)D_2+xAr mixtures in 8.3.8 (1-60% of Ar) in the entire 10-100% range radiative compression was to be expected. On the other hand, for all the investigated computed discharges in 0% and 3% of Ar fraction no radiative compression should be expected – from the theoretical discharges in D_2 in figure 8.3.6 (3.0 mbar of D_2) and in (100%-x)D_2+xAr mixtures in figure 8.3.8 (1-5% of Ar) up to 5% of Ar fraction no radiative compression phenomenon was to be expected.

It is also worth to quote again the example of discharges: #17083103 (10% of Ar), #17101817 (100% of Ar) and #17101818 (100% of Ar). For these discharge $t_{rcl}^{comp} = 0$ ns. While the $t_Q^{comp} \approx 0.3$ ns, 0.0006 ns and 0.0008 ns. And $t_{pl}^{comp} = 57$ ns, 91 ns, 80 ns. This shows, from one side, that the t_Q^{comp} is always smaller than t_{pl}^{comp} but also not smaller than t_{rcl}^{comp} which is always equal to zero because $I_{P\text{-}Breduced}^{comp}(t)$ is always bigger than $I_{pp}^{comp}(t)$. In this situation no radiative compression should be expected because the basic condition is not fulfilled. Yet, some weak radiative compression phenomenon can be stated for the two discharges in 100% of Ar. Moreover, in all investigated computed discharges in 5-60% of Ar fraction and in half of computed discharges in 100% of Ar only weak radiative compression phenomenon is present (significantly changing only some of the parameters describing plasma pinch) despite the $I_{P\text{-}Breduced}^{comp}(t_1) \ll I_{pp}^{comp}(t_1)$ as well as positive $t_Q^{comp} \ll t_{pl}^{comp}$ and $t_Q^{comp} \ll t_{rcl}^{comp}$ for some discharges. This will be shown in the next subsections.

8.4. Plasma pinch parameters – dimensions

In this subsection, changes of the initial pinch radius (r_{p0}), the minimum pinch radius (r_{pmin}), the initial pinch length (z_{p0}), the maximum pinch length (z_{pmax}), the initial pinch volume (V_{p0}) and final pinch volume (V_{pf}) will be presented.

8.4.1. Plasma pinch parameters – radiuses

Theoretical discharges

The computed theoretical initial pinch radiuses (r_{p0}^{comp}) and the computed theoretical minimum pinch radiuses (r_{pmin}^{comp}) from the discharges in D_2, Ar and (100%-x)D_2+xAr mixtures are presented in figure 8.4.1, figure 8.4.2 and figure 8.4.3, respectively.

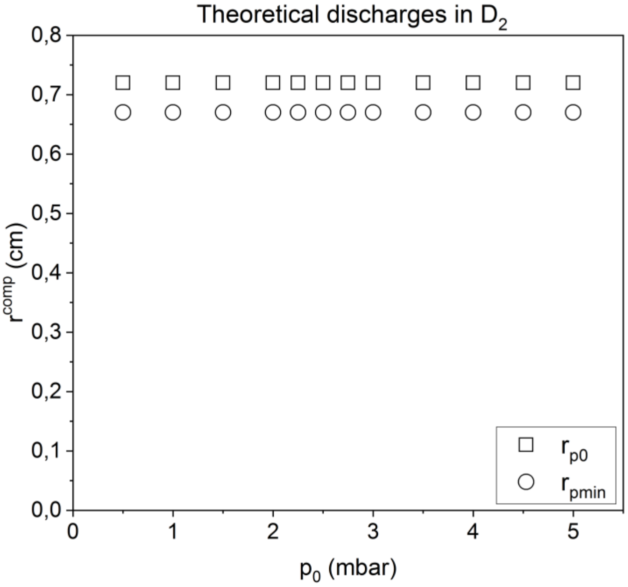

Figure 8.4.1. The computed theoretical initial pinch radius (r_{p0}^{comp}) and the computed theoretical minimum pinch radius (r_{pmin}^{comp}) versus initial D_2 pressure (p_0).

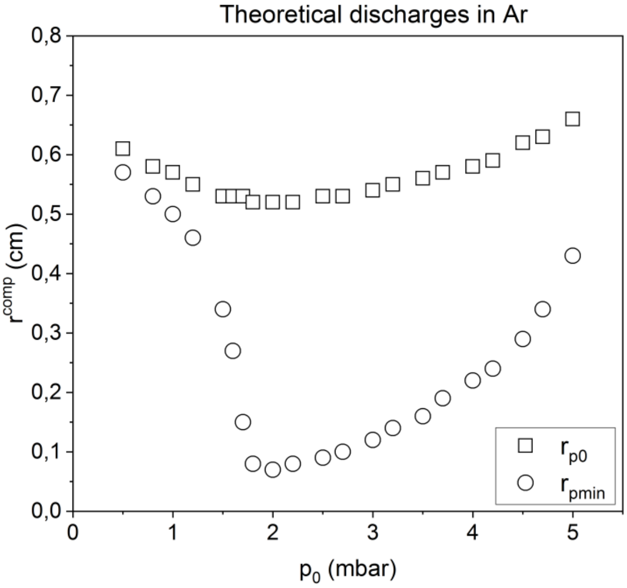

Figure 8.4.2. The computed theoretical initial pinch radius (r_{p0}^{comp}) and the computed theoretical minimum pinch radius (r_{pmin}^{comp}) versus initial Ar pressure (p_0).

The computed theoretical initial (r_{p0}^{comp}) and minimum (r_{pmin}^{comp}) pinch radiuses for discharges in D_2 (figure 8.4.1) are constant – pinch radius is always equal to 0.67 cm while the initial pinch radius is alwys equal to 0.72 cm. Thus, the total change in the pinch radius during pinch phase of discharge is equal to 0.05 cm. So, the changes in the plasma dynamics, ohmic heating and in the total power of X-ray emission have almost no influence on the changes of pinch radius during theoretical discharges in D_2. Thus, no radiative compression is stated for theoretical discharges in D_2 according to the r_{pmin}^{comp} and r_{p0}^{comp} - r_{pmin}^{comp}. Moreover, the plasma compressibility is constant during discharges is pure D_2 (constant SHRs).

The computed theoretical minimum plasma pinch radiuses (r_{pmin}^{comp}) for discharges in Ar (figure 8.4.2) slowly decrease up to 1.2 mbar. Above 1.2 mbar of Ar r_{pmin}^{comp} continue to decrease more rapidly achieving 0.07 cm at 2.0 mbar – smallest theoretical pinch radius for discharges in Ar. The dependency of r_{p0}^{comp} vs p_0 exhibits similar behaviour.

The computed theoretical initial pinch radius (r_{p0}^{comp}) at 2.0 mbar of Ar is equal to 0.52 cm. Thus, the highest total change of pinch radius during pinch phase of discharge (r_{p0}^{comp} - r_{pmin}^{comp}) for 2.0 mbar of Ar is equal to 0.45 cm (about 7.4 times decrease in radius). Above 2.0 mbar of Ar r_{pmin}^{comp} increase and r_{p0}^{comp} - r_{pmin}^{comp} decrease. All r_{pmin}^{comp} (achived for all initial Ar pressures) are smaller than for theoretical discharges in D_2 (smaller values than 0.67 cm) and starting from 1.00 mbar of initial Ar pressure the r_{p0}^{comp} - r_{pmin}^{comp} are smaller than 0.05 cm achived for theoretical discharges in D_2. The behaviour of r_{p0}^{comp} and r_{pmin}^{comp} is connected with both changes in plasma compressibility (due to changes in SHRs) and total X-ray radiation emission. The changes of r_{p0}^{comp} are dominated by changes in plasma compressibility due to changes in SHRs (confirmed with computations with total X-ray radiation emission equal to 0) – radiative compression has no time to develop at the beginning of pinch phase of discharge. While the significant decrease in r_{pmin}^{comp} values and increase in r_{p0}^{comp} - r_{pmin}^{comp} values is triggerd by radiation losses (mainly X-ray line radiation connected with high Z and Z_{eff} numbers and increase in n_p and z_p and decrease in T_p with Ar pressure – see equation (2.1.19)) – this is the radiative compression phenomenon taking place. The increase in r_{pmin}^{comp} and decrease in r_{p0}^{comp} - r_{pmin}^{comp} values above 2.0 mbar is caused by the plasma opacity effect (see subsection 6.2.12) and the following decrease in the total X-ray line emission power (equation (6.2.37)). Moreover, as was shown for the theoretical discharges in D_2 the changes in plasma dynamics have practically no influence on pinch radiuses when model parameters are constant – the same for theoretical discharges in Ar. So, for theoretical discharges in 1.00-5.00 mbar of initial Ar pressure some radiative compression can be stated according to the theoretical r_{pmin}^{comp} and r_{p0}^{comp} - r_{pmin}^{comp} (current and time indicators stated entire 0.50-5.00 mbar range).

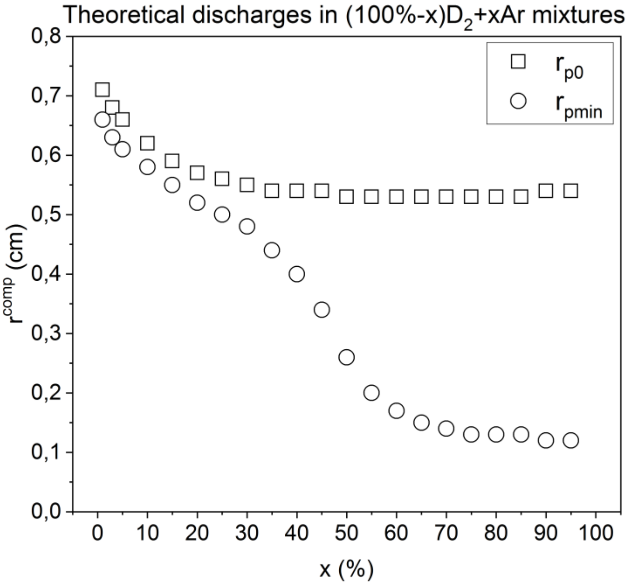

Figure 8.4.3. The computed theoretical initial pinch radius (r_{p0}^{comp}) and the computed theoretical minimum pinch radius (r_{pmin}^{comp}) versus Ar fraction (x) in (100%-x)D_2+xAr mixture.

The computed theoretical minimum pinch radiuses (r_{pmin}^{comp}) for discharges in (100%-x)D_2+xAr mixtures (figure 8.4.3) decrease with Ar fraction, wherein up to about 30% of Ar fraction the r_{pmin}^{comp} decrease relatively slowly. Up to 30% of Ar fraction also the computed theoretical initial pinch radiuses (r_{p0}^{comp}) decrease similarly as the r_{pmin}^{comp} – similar difference between the r_{p0}^{comp} and r_{pmin}^{comp} (0.04-0.07 cm). For the theoretical discharges in 25% and 30% of Ar fraction the r_{p0}^{comp} - r_{pmin}^{comp} is equal to: 0.06 cm and 0.07 cm, respectively. From about 35% of Ar fraction the r_{p0}^{comp} stop to decrease (approximately constant values) and the r_{pmin}^{comp} start to decrease more rapidly (effect of high X-ray line emission power) up to 60-65% of Ar. And from about 65% of Ar fraction the r_{pmin}^{comp} decrease only insignificantly (effect of high plasma opacity and slowing down total emission of X-ray line radiation). The smallest value of the r_{pmin}^{comp} is achieved at the 90-95% of Ar and is equal to 0.12 cm while the corresponding r_{p0}^{comp} has 0.54 cm. This situation results in 0.42 cm of total change in plasma pinch radius during pinch phase of discharge (4.5 times decrease in radius). The decrease of r_{p0}^{comp} is mainly connected with changes in the plasma compressibility due to changes in the SHRs of ionized gas mixtures (confirmed with computations with total X-ray radiation emission equal to 0) – radiative compression has no time to develop. While the significant decrease in r_{pmin}^{comp} and increase in r_{p0}^{comp} - r_{pmin}^{comp} values is driven mostly by X-ray line radiation losses – changes in r_{pmin}^{comp} and r_{p0}^{comp} - r_{pmin}^{comp} follow changes of total X-ray line yield. Also, the model parameters are constant so no changes of pinch radiuses caused by changes in plasma dynamics are to be expected. Summarizing, for the theoretical discharges in 25-95% range of Ar fractions in $(100\%\text{-}x)D_2+x\text{Ar}$ mixtures some radiative compression can be stated according to the theoretical r_{pmin}^{comp} and r_{p0}^{comp} - r_{pmin}^{comp} (current and time indicators stated 10-95% range). Moreover, it should be emphasized that the determined theoretical dependencies of r_{p0}^{comp} and r_{pmin}^{comp} for D_2, Ar and $(100\%\text{-}x)D_2+x\text{Ar}$ mixtures in figure 8.4.1, 8.4.2 and 8.4.3 have in general different characters (characteristic shapes).

Computed discharges in deuterium

The computed initial pinch radiuses (r_{p0}^{comp}) and the computed minimum pinch radiuses (r_{min}^{comp}) from the discharges in D_2 are presented in figure 8.4.4.

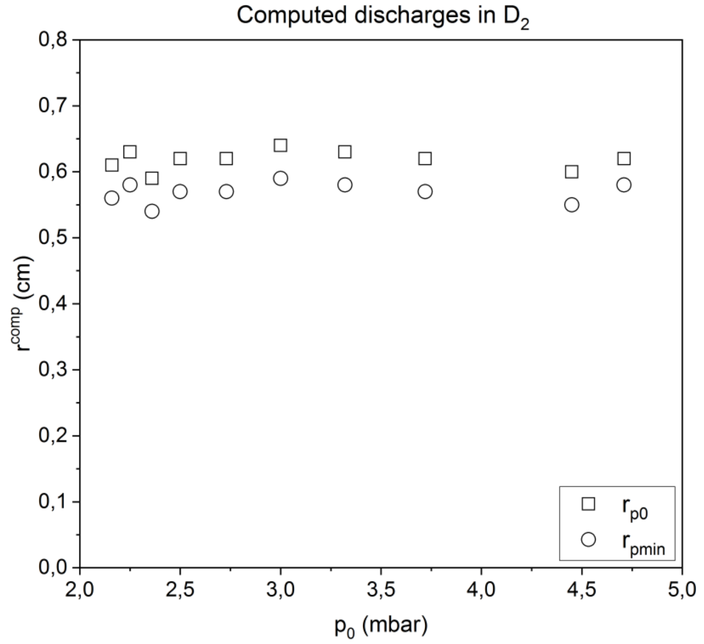

Figure 8.4.4. The computed initial pinch radius (r_{p0}^{comp}) and the computed minimum pinch radius (r_{pmin}^{comp}) versus initial D_2 pressure (p_0).

The computed initial (r_{p0}^{comp}) and minimum (r_{pmin}^{comp}) pinch radiuses for discharges in D_2 (figure 8.4.4) are approximately constant (similar as for the theoretical discharges in D_2

in figure 8.4.1). Some fluctuations of values are present due to different scenario of discharge accounted through changes of the fitting parameters – changes in the dynamic of discharges have some relatively small influence on the total changes of plasma pinch radius during computed discharges in D_2. The determined computed r_{p0}^{comp} and r_{pmin}^{comp} are equal to: 0.59-0.64 cm and 0.54-0.59 cm, respectively (smaller values than the theoretically predicted in D_2 in figure 8.4.1). The highest difference between r_{p0}^{comp} and r_{pmin}^{comp} for all investigated discharges (initial pressures of D_2) is equal to 0.05 cm – the same value as for the theoretical discharges in D_2 in figure 8.4.1. So, no radiative compression can be stated for computed discharges in D_2 according to the r_{pmin}^{comp} and r_{p0}^{comp} - r_{pmin}^{comp}.

Computed discharges in deuterium-argon mixtures

The average computed initial pinch radius ($<r_{p0}^{comp}>$) and the average computed minimum pinch radius ($<r_{pmin}^{comp}>$) for the discharges in $(100\%\text{-}x)D_2\text{+}x\text{Ar}$ mixtures are presented in figure 8.4.5.

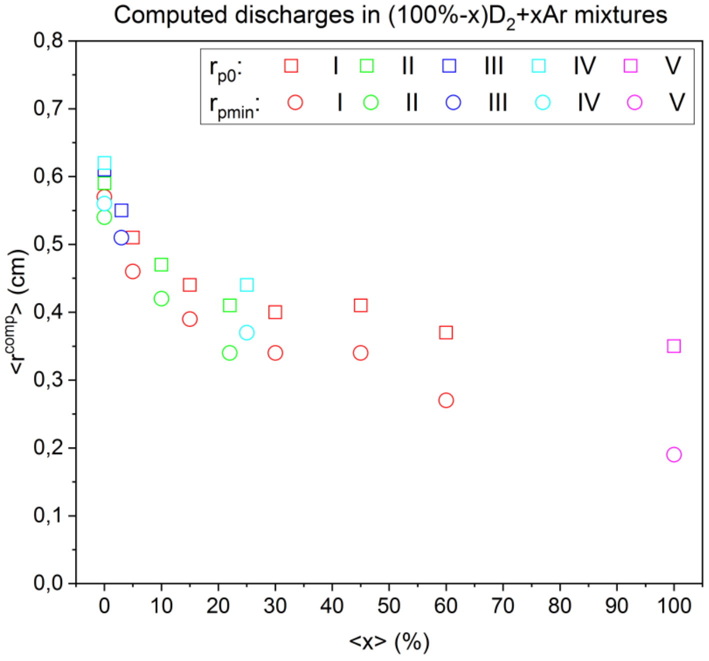

Figure 8.4.5. The average computed initial pinch radius ($<r_{p0}^{comp}>$) and the average computed minimum pinch radius ($<r_{pmin}^{comp}>$) versus Ar fraction ($<x>$) in $(100\%\text{-}x)D_2\text{+}x\text{Ar}$ mixture. Roman numerals mark given series of discharges.

Both average computed initial ($<r_{p0}^{comp}>$) and minimum ($<r_{pmin}^{comp}>$) pinch radiuses in $(100\%\text{-}x)D_2\text{+}x\text{Ar}$ mixtures (figure 8.4.5) decrease with Ar fraction. At the 30% of Ar some bending points maybe present for both $<r_{pmin}^{comp}>$ vs $<x>$ and $<r_{p0}^{comp}>$ vs $<x>$ dependencies (change of character of decrease). The $<r_{p0}^{comp}>$ and $<r_{pmin}^{comp}>$ for the discharges in $(100\%\text{-}x)D_2\text{+}x\text{Ar}$ mixtures are the smallest for 100% of Ar (despite smaller total initial pressure of gas mixture – 1.2 mbar). Moreover, the dependencies based on the computed discharges in figure 8.4.5 are different from the ones based on the theoretical discharges in figure 8.4.3 – presence of the bending points is not certain (not certain change of character of decrease) for the $<r_{pmin}^{comp}>$ vs $<x>$ and for the $<r_{p0}^{comp}>$ vs $<x>$ dependencies in figure 8.4.5, $<r_{p0}^{comp}>$ appear the decrease up 100% of Ar fraction as well as the decrease of $<r_{p0}^{comp}>$ with $<x>$ is relatively large and the decrease of $<r_{pmin}^{comp}>$ with $<x>$ is relatively small in comparison to the theoretical values in figure 8.4.1 (3.0 mbar of D_2), 8.4.2

(1.2 mbar of Ar) and 8.4.3 (3-60% of Ar fraction). For comparison, the $<r_{p0}^{comp}>$ in figure 8.4.5 achived for 60% and 100% is equal to: 0.37 cm and 0.35 cm, respectively. And the theoretical $<r_{p0}^{comp}>$ in figure 8.4.3 (60% of Ar) and 8.4.2 (1.2 mbar of Ar) achived for 60% and 100% is equal to: 0.53 cm and 0.55 cm, respectively. On the other hand, the $<r_{pmin}^{comp}>$ in figure 8.4.5 achived for 60% and 100% is equal to: 0.27 cm and 0.19 cm, respectively. And the theoretical $<r_{pmin}^{comp}>$ in figure 8.4.3 (60% of Ar) and 8.4.2 (1.2 mbar of Ar) achived for 60% and 100% is equal to: 0.17 cm and 0.46 cm, respectively. So, the maximum difference between $<r_{p0}^{comp}>$ and $<r_{pmin}^{comp}>$ for $(100\%\text{-}x)D_2+x$Ar mixtures (achived for 100% of Ar) in figure 8.4.5 is only equal to 0.16 cm. While the maximum difference between theoretical $<r_{p0}^{comp}>$ and $<r_{pmin}^{comp}>$ for $(100\%\text{-}x)D_2+x$Ar mixtures (achived for 90-95% of Ar) in figure 8.4.3 is equal to 0.42 cm and the maximum difference for 0-60% range of Ar is equal to 0.36 cm (at 60% of Ar). The significant differences between computed and theoretical discharges come mainly from the changes of fitting parameters and some unclear effects which lead to decrease of model parameter values with Ar fraction. This all causes changes in global plasma/discharge dynamics and decrease in the total X-ray emission power. The decrease of $<r_{p0}^{comp}>$ is due to changes in plasma dynamics and plasma compressibility (changes in SHRs) and not X-ray radiation emission power and radiative compression. Since, the r_{p0}^{comp} values in general are not so sensible to the total X-ray emission power (radiative compression only starts to develop at the beginning of pinch phase of discharge), the smallest $<r_{p0}^{comp}>$ achived for the computed discharges (0.35 cm) is significantly smaller than the smallest $<r_{p0}^{comp}>$ achived for the theoretical discharges (0.53 cm) while the average total X-ray line yield (and entire X-ray emission power) was actually smaller during computed discharges than during the theoretical discharges in $(100\%\text{-}x)D_2+x$Ar mixtures (as will be shown in subsection 8.7.1) – result confirmed also with computations with X-ray radiation emission set to 0. Moreover, the decrease of $<r_{pmin}^{comp}>$ values with Ar fraction is also mainly caused by changes in plasma dynamics and plasma compressibility – result determined with computations with X-ray radiation emission set to 0. Still, increase in $<r_{p0}^{comp}>$ - $<r_{pmin}^{comp}>$ with Ar fraction to higher values (than achived for discharges in 0% of Ar) is caused by X-ray radiation emission and radiative compression – the same as for the theoretical discharges in $(100\%\text{-}x)D_2+x$Ar mixtures (figure 8.4.3). And this increase is the highest for discharges in 100% of Ar.

The 0.16 cm of total change of the average plasma pinch radius (achived at 100% of Ar fraction) during computed discharges is considered as moderate – it is almost three times higher than the 0.06 cm. The 0.06 cm is the maximum change in the plasma pinch radius from all investigated discharges in 0% of Ar fraction (a bit higher value than for the theoretical and computed discharges under variable D_2 pressures – 0.05 cm). On the other hand, the maximum difference between $<r_{p0}^{comp}>$ and $<r_{pmin}^{comp}>$, when 0-60% Ar fractions are only considered, is achived at 60% and is equal to 0.10 cm. The 0.10 cm of total change in pinch radius is considered as small – not significantly bigger than 0.06 cm. The highest total changes of the average plasma pinch radius equal to 0.10 cm and 0.16 cm correspond to: 1.4 times decrease and 1.8 times decrease in radius, respectively. Still, the 0.10 cm and 0.16 cm are only average values. The maximum difference between r_{p0}^{comp} and r_{pmin}^{comp} from single discharges, when 0-60% of Ar fractions are only considered, is equal to 0.12 cm (discharges in 60% of Ar) – small or moderate change. While the maximum difference between r_{p0}^{comp} and r_{pmin}^{comp} for all computed discharges in 0-30% range is smaller or equal to 0.07 cm – only for 45%, 60% and 100% the changes were bigger than 0.07 cm. And the r_{p0}^{comp} - r_{pmin}^{comp} higher than 0.06 cm is achived for seleted discharges in 15-60% of Ar and for 100%. The highest difference between r_{p0}^{comp} and r_{pmin}^{comp} from single discharges, when 100% of Ar fraction is considered, is equal to 0.25 cm – high change.

Furthermore, the smallest r_{pmin}^{comp} achived for computed discharges in 0% of Ar is equal to 0.52 cm. The r_{pmin}^{comp} values smaller than 0.52 cm are achived for selected discharges in 3-60% and in 100% of Ar fraction.

The discharges in 100% of Ar fraction have relatively wide spread of r_{p0}^{comp} and r_{pmin}^{comp} values. The smallest and highest difference between r_{p0}^{comp} and r_{pmin}^{comp}, for discharges in 100% of Ar, is equal to: 0.06-0.07 cm and 0.24-0.25 cm, respectively. The 0.06 cm is achieved for discharge #17101817 and 0.07 cm is achieved for discharge #17102003. For the discharge #17101817 r_{p0}^{comp} = 0.34 cm and r_{pmin}^{comp} = 0.28 cm. And for the discharge #17102003 r_{p0}^{comp} = 0.43 cm and r_{pmin}^{comp} = 0.36 cm. On the other hand, the 0.24 cm is achieved for discharge #17102007 and #17102016 and 0.25 cm is achieved for discharge #17102009. For the discharge #17102007 and #17102016 r_{p0}^{comp} = 0.35 cm and r_{pmin}^{comp} = 0.11 cm. And for the discharge #17102009 r_{p0}^{comp} = 0.36 cm and r_{pmin}^{comp} = 0.11 cm. From the presented values in this paragraph the 0.43 cm is the highest initial pinch radius from all investigated computed discharges in 100% of Ar and the 0.11 cm is the smallest minimum (final) plasma pinch radius from all investigated computed discharges in 100% of Ar (as well as from discharges in all Ar fractions).

The above considerations concerning plasma pinch radiuses for the computed discharges in (100%-x)D_2+xAr mixtures indicate that some plasma radiative compression phenomenon occurs for selected discharges in 15-60% range of Ar fractions and in 100% according to the r_{pmin}^{comp} and r_{p0}^{comp} - r_{pmin}^{comp}.

8.4.2. Plasma pinch parameters – lengths

Theoretical discharges

The computed theoretical initial pinch length (z_{p0}^{comp}) and the computed theoretical maximum pinch length (z_{pmax}^{comp}) from the discharges in D_2, Ar and (100%-x)D_2+xAr mixtures are presented in: figure 8.4.6, figure 8.4.7 and figure 8.4.8, respectively.

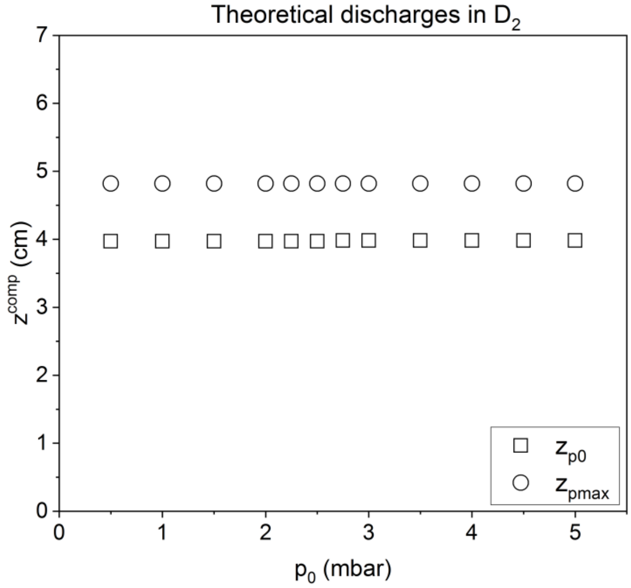

Figure 8.4.6. The computed theoretical initial pinch length (z_{p0}^{comp}) and the computed theoretical maximum pinch length (z_{pmax}^{comp}) versus initial D_2 pressure (p_0).

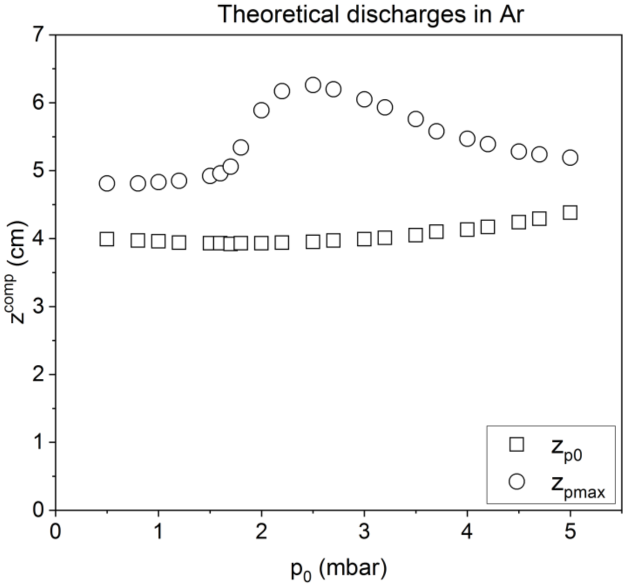

Figure 8.4.7. The computed theoretical initial pinch length (z_{p0}^{comp}) and the computed theoretical maximum pinch length (z_{pmax}^{comp}) versus initial Ar pressure (p_0).

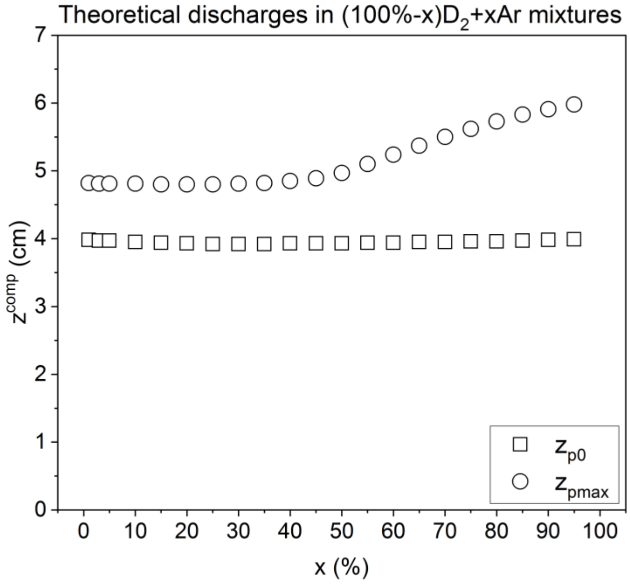

Figure 8.4.8. The computed theoretical initial pinch length (z_{p0}^{comp}) and the computed theoretical maximum pinch length (z_{pmax}^{comp}) versus Ar fraction (x) in (100%-x)D_2+xAr mixture.

The computed theoretical initial (z_{p0}^{comp}) and maximum (z_{pmax}^{comp}) pinch lengths for discharges in D_2 (figure 8.4.6) are approximately constant – z_{p0}^{comp} = 3.97-3.98 cm and z_{pmax}^{comp} = 4.82 cm. Thus, the difference between z_{pmax}^{comp} and z_{p0}^{comp} is approximately constant and equal to 0.84-0.85 cm. This is the same situation as for the theoretical pinch radiuses in D_2 in figure 8.4.1. So, the changes in plasma dynamics and in the total power of X-ray emission have almost no infuelnce on the changes in the initial and maximum (final) plasma pinch length during theoretical discharges in D_2. Thus, no radiative compression can be stated for theoretical discharges in D_2 according to the z_{pmax}^{comp} and z_{pmax}^{comp} - z_{p0}^{comp}.

The dependency of computed theoretical maximum pinch length (z_{pmax}^{comp}) versus initial Ar pressure (figure 8.4.7) shows maximum. This is in general opposite behaviour in comparison to the dependency describing changes of the minimum pinch radiuses with initial Ar pressures (figure 8.4.2). The maximum of 6.26 cm is achieved at 2.5 mbar of Ar (figure 8.4.7). The corresponding computed theoretical initial pinch length (z_{p0}^{comp}) is equal to 3.95 cm. And this gives 2.31 cm of total change in plasma pinch length during pinch phase of discharge (1.6 times increase in length). The 2.31 cm achived for the 2.5 mbar of initial Ar pressure is also the highest total change of pinch length for theoretical discharges in Ar. The dependency of z_{pmax}^{comp} vs p_0 for Ar (figure 8.4.7), opposite to the r_{pmin}^{comp} vs p_0 for Ar (figure 8.4.2), is caused by the fact that internal plasma pressure values first decrease due to high emission of X-ray radiation (radiative compression). Because of this external magnetic pressure forces can pinch the plasma column to smaller radius. And significant decrese in radius again increases the internal plasma pressure which pushes faster plasma in the axial direction. In other words the plasma pinch length is dependent mainly on the current flowing through plasma pinch, plasma pinch radius as well as on the specific heat ratio of not fully ionised Ar plasma (see equation 6.2.12). Because of this connection between pinch radius and length the significant increase in pinch length maybe another sign of the plasma radiative compression phenomenon occurrence. Moreover, the computed theoretical initial pinch lengths in figure 8.4.7 increase insignificantly at higher initial Ar pressures – connected with changes in plasma compressibility. Summarizing, for initial Ar pressures in 1.0-4.7 mbar range radiative compression can be stated according to the z_{pmax}^{comp} and z_{pmax}^{comp} - z_{p0}^{comp} (higher values in comparison to all the theoretical discharges in D_2).

The computed theoretical maximum pinch lengths (z_{pmax}^{comp}) for discharges in (100%-x)D_2+xAr mixtures (figure 8.4.8) are approximately constant up to about 35-40% of Ar. Above 40% of Ar fraction the z_{pmax}^{comp} increase. This behaviour is in general opposite in comparison to the dependency describing changes of the computed theoretical minimum pinch radiuses with initial Ar fractions (figure 8.4.3). And the explanation of changes is analogic as in the above paragraph refering to the theoretical discharges in Ar. Moreover, the computed theoretical initial pinch lengths (z_{p0}^{comp}) for discharges in (100%-x)D_2+xAr mixtures (figure 8.4.8) are approximately constant. The maximum difference between z_{pmax}^{comp} and z_{p0}^{comp} achived at 95% of Ar is equal to 1.99 cm (1.5 times increase in length). While, z_{pmax}^{comp} = 5.98 cm and z_{p0}^{comp} = 3.99 cm at 95% of Ar. The 5.98 cm is the highest achived computed maximum pinch length during theoretical discharges in (100%-x)D_2+xAr mixtures. According to the determined values of z_{pmax}^{comp} and z_{pmax}^{comp} - z_{p0}^{comp} in 40-95% range of Ar fraction in (100%-x)D_2+xAr mixtures radiative compression is stated (higher values in comparison to theoretical discharges in D_2). Moreover, it is worth to mention that the determined theoretical dependencies of z_{p0}^{comp} and z_{pmax}^{comp} for D_2, Ar and (100%-x)D_2+xAr mixtures in figure 8.4.6, 8.4.7 and 8.4.8 have in general different character (characteristic shapes).

Computed discharges in deuterium

Figure 8.4.9 presents the computed initial pinch lengths (z_{p0}^{comp}) and the computed maximum pinch lengths (z_{pmax}^{comp}) from the computed discharges in D_2.

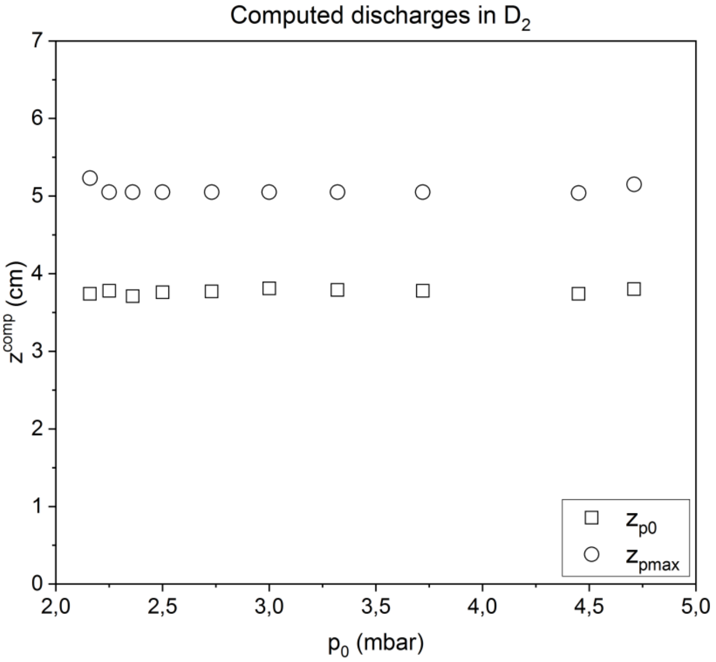

Figure 8.4.9. The computed initial pinch length (z_{p0}^{comp}) and the computed maximum pinch length (z_{pmax}^{comp}) versus initial D_2 pressure (p_0).

The computed initial (z_{p0}^{comp}) and maximum (z_{pmax}^{comp}) pinch lengths in D_2 (figure 8.4.9) are approximately constant (similar as for the theoretical discharges in D_2 in figure 8.4.6). So, the differences between z_{pmax}^{comp} and z_{p0}^{comp} are approximately constant and equal to 1.24-1.49 cm. While, the determined z_{p0}^{comp} and z_{pmax}^{comp} are equal to: 3.71-3.81 cm and 5.04-5.23 cm, respectively. Moreover, the computed initial pinch lengths in figure 8.4.9 are smaller than the theoretical values in D_2 in figure 8.4.6. On the other hand, the computed maximum pinch lengths in figure 8.4.9 are bigger than the theoretical values in figure 8.4.6. Thus, bigger total change in computed plasma pinch lengths during pinch phase of discharge is achived than anticipated theoretically. Still, again no radiative compression can be stated for computed discharges in D_2 according to the z_{pmax}^{comp} and z_{pmax}^{comp} - z_{p0}^{comp}.

Computed discharges in deuterium-argon mixtures

Figure 8.4.10 presents the average computed initial pinch lengths ($<z_{p0}^{comp}>$) and the average computed maximum pinch lengths ($<z_{pmax}^{comp}>$) from the computed discharges in (100%-x)D_2+xAr mixtures.

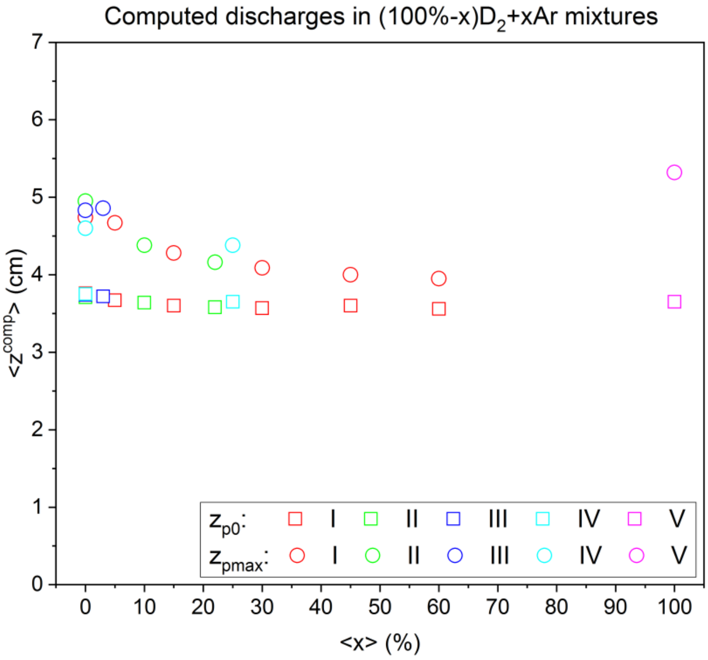

Figure 8.4.10. The average computed initial pinch length ($<z_{p0}^{comp}>$) and the average computed maximum pinch length ($<z_{pmax}^{comp}>$) versus Ar fraction ($<x>$) in (100%-x)D_2+xAr mixture. Roman numerals mark given series of discharges.

The computed average initial pinch lengths ($<z_{p0}^{comp}>$) for discharges in (100%-x)D_2+xAr mixtures (figure 8.4.10) are approximately constant at the level of 3.56-3.76 cm. This is similar as for the theoretical discharges in (100%-x)D_2+xAr mixtures in figure 8.4.8, although, smaller $<z_{p0}^{comp}>$ values are achived for the computed discharges in figure 8.4.10 than for the theoretical discharges in figure 8.4.6 (3.0 mbar of D_2), figure 8.4.7 (1.2 mbar of Ar) and 8.4.8 (3-60% of Ar). The average computed maximum pinch lengths ($<z_{pmax}^{comp}>$) decrease with Ar fraction except for the discharges in 100% of Ar. This is completely different relation than the excepted one from theoretical discharges in figure 8.4.8. So, it appears that the forces of internal plasma pressure were not strong enough to cause increase in pinch lengths for discharges in 0-60% fraction of Ar despite some decrese in the computed minimum plasma pinch radiuses (see figure 8.4.10). This confirmes also the previous statements about the lack of a strong radiative compression phenomenon during discharges in 0-60% of Ar fraction and changes in the plasma/discharge dynamics and compressibility as the main cause of decrease of $<r_{p0}^{comp}>$ and also $<r_{pmin}^{comp}>$

(see subsection 8.4.1 and figure 8.4.5). For the 100% of Ar fraction $<z_{pmax}^{comp}>$ is the highest and equal to 5.32 cm. The 5.32 cm in 100% of Ar is higher than the theoretically anticipated z_{pmax}^{comp} for 1.2 mbar of Ar (figure 8.4.7). On the other hand, the 5.32 cm in 100% of Ar is also smaller than the highest z_{pmax}^{comp} for theoretical discharges in 1-95% of Ar, achieved at 95% of Ar (figure 8.4.8). Corresponding $<z_{p0}^{comp}>$ for 100% of Ar fraction is equal to 3.65 cm. This results in 1.67 cm of total change of average plasma pinch length (about 1.5 times increase in length) – the highest value from all investigated Ar fractions. The 1.67 cm value is higher than the anticipated theoretical one for 1.2 mbar of Ar equal to 0.91 cm. On the other hand, this value is smaller than the theoretical one for discharge in 95% of Ar fraction under 3.0 mbar of total pressure (figure 8.4.8) – 1.99 cm. For the 0-60% range of Ar fractions, the highest total change of average plasma pinch length is achived for 0% (series II) – 1.24 cm, while the smallest total change of average plasma pinch length is achived for 60% – 0.39 cm. The 1.24 cm is the same value as for the computed discharge in 3.0 mbar of D_2 (figure 8.4.9) but also higher than the theoretical anticipated one in 3.0 mbar of D_2 in figure 8.4.6 – 0.84 cm. And the 0.39 cm for 60% of Ar is smaller total change than the theoretical one in 60% of Ar in figure 8.4.8 – 1.30 cm.

For single discharges in 0-60% range of Ar fractions the highest total change of plasma pinch length during pinch phase of discharge is also achived for discharges in 0% of Ar. For the discharge #17092802 the difference is as high as 1.71 cm (highest total change not considering discharges in 100% of Ar) (series III) while for the discharge #17100405, also in 0% of Ar, it is only equal to 0.48 cm (smallest total change in 0% of Ar) (series IV) – wide spread of z_{pmax}^{comp} values is stated. On the other hand, the smallest total change of plasma pinch length during pinch phase of discharge for computed discharges in 0-60% range of Ar is equal to 0.24 cm – discharge #17071204 in 45% of Ar. For single discharges in 100% of Ar the spread of z_{pmax}^{comp} is very wide – the highest total change of pinch length is equal to 2.29 cm (discharge #17102007) while the smallest is equal to 0.81 cm (discharge #17102003). So, for all computed dischares in 3-60% range of Ar fractions no significant total change of plasma pinch length was stated in comparison to discharges in 0% of Ar. For some of the computed discharges in 100% of Ar fraction the total change of pinch length is stated as significant while for the other part the change is insignificant (in comparison to discharges in 0%). Moreover, the smallest z_{p0}^{comp} from single discharge is equal to 3.52 cm (discharges in 22% and 30% of Ar) while the highest z_{pmax}^{comp} from single discharge is equal to 5.92 cm (discharge #17102007 in 100% of Ar). Summarizing, only for selected discharges in 100% of Ar fractions in $(100\%\text{-}x)D_2+x\text{Ar}$ mixtures radiative compression occurs according to the z_{pmax}^{comp} and z_{pmax}^{comp} - z_{p0}^{comp} (higher values than for computed discharges in D_2).

8.4.3. Plasma pinch parameters – volumes

Theoretical discharges

The initial computed theoretical pinch volume (V_{p0}^{comp}) and the computed theoretical final pinch volume (V_{pf}^{comp}) from the discharges in D_2, Ar and $(100\%\text{-}x)D_2+x\text{Ar}$ mixtures are presented in figure 8.4.11, figure 8.4.12 and figure 8.4.13, respectively.

The computed theoretical initial (V_{p0}^{comp}) and final (V_{pf}^{comp}) plasma pinch volumes in D_2 (figure 8.4.11) are approximately constant due to almost constant computed theoretical plasma pinch radiuses (figure 8.4.1) and plasma pinch lengths (figure 8.4.6) in D_2. Thus, the ratios of V_{p0}^{comp} to V_{pf}^{comp} are approximately constant. The total volumes of generated plasma pinches (columns) during pinch phase of discharge in D_2 always increase – always $V_{pf}^{comp} > V_{p0}^{comp}$. This is the result of domination of total increase in length over total decrease in radius. So, no radiative compression can be stated for theoretical discharges in D_2 according to the V_{pf}^{comp} and V_{p0}^{comp} - V_{pf}^{comp} (or V_{p0}^{comp} / V_{pf}^{comp}).

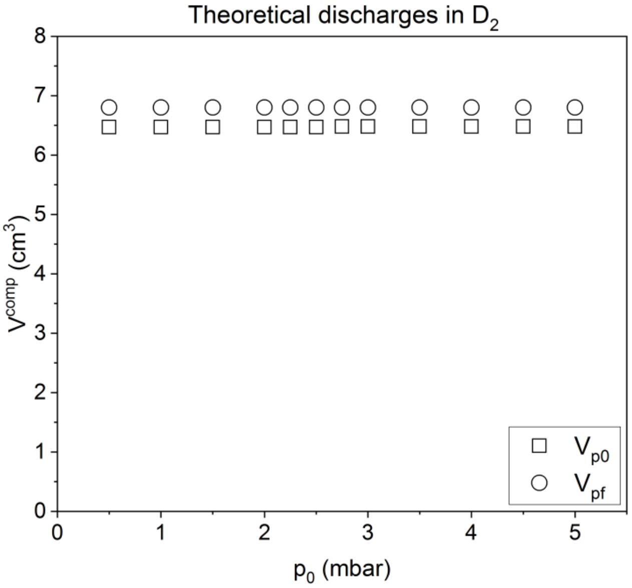

Figure 8.4.11. The computed theoretical initial pinch volume (V_{p0}^{comp}) and the computed theoretical final pinch volume (V_{pf}^{comp}) versus initial D_2 pressure (p_0).

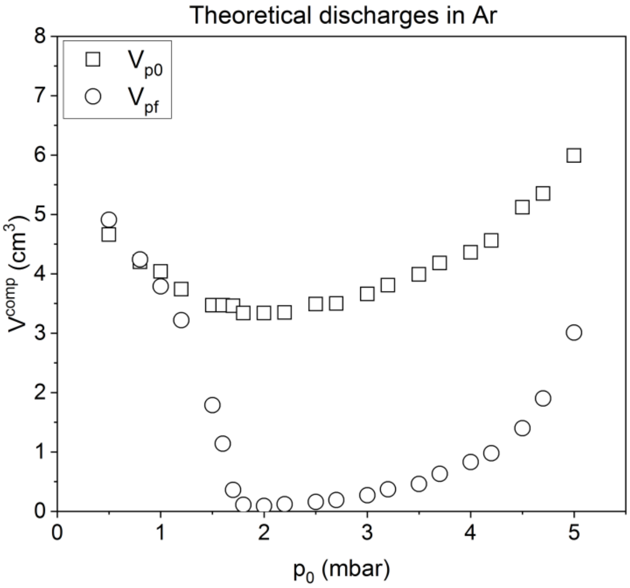

Figure 8.4.12. The computed theoretical initial pinch volume (V_{p0}^{comp}) and the computed theoretical final pinch volume (V_{pf}^{comp}) versus initial Ar pressure (p_0).

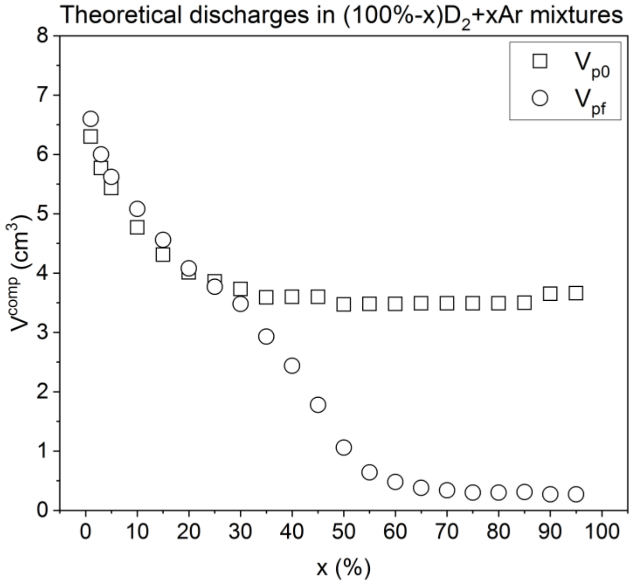

Figure 8.4.13. The computed theoretical initial pinch volume (V_{p0}^{comp}) and the computed theoretical final pinch volume (V_{pf}^{comp}) versus Ar fraction (x) in (100%-x)D_2+xAr mixture.

The dependencies of computed theoretical initial (V_{p0}^{comp}) and final (V_{pf}^{comp}) plasma pinch volumes versus initial Ar pressures (figure 8.4.12) show minima. These minima are achived during discharges in 2.0 mbar of initial Ar pressure. The ratios of V_{p0}^{comp} to V_{pf}^{comp} increase slowly up to 1.2 mbar of Ar. Between about 1.2 mbar and 2.0 mbar the increase is faster. Above 2.0 mbar the total ratios of V_{p0}^{comp} to V_{pf}^{comp} decrease. It should be also mentioned that for the discharges in 0.5-0.8 mbar of initial Ar pressure $V_{pf}^{comp} > V_{p0}^{comp}$ (expansion of the total volume of plasma column) but above 0.8 mbar of Ar $V_{pf}^{comp} < V_{p0}^{comp}$ is always stated (compression of the total volume of plasma column). At 2.0 mbar of initial Ar pressure about 37 times decrease in total pinch volume is stated. The compression of the total volume of plasma column during pinch phase of discharge may be another evidence for plasma radiative compression phenomenon occurrence – for the theoretical discharges in D_2 V_{pf}^{comp} is always bigger than V_{p0}^{comp} (see figure 8.4.11). Moreover, the theoretical dependencies presented in figure 8.4.12 are similar to the theoretical dependencies describing changes of $<r_{p0}^{comp}>$ and $<r_{pmin}^{comp}>$ in Ar (figure 8.4.2). Thus, the changes of total volume during theoretical discharges in Ar are dominated by the total changes of pinch radius during pinch phase of discharge. Summarizing, for the theoretical discharges in 1.0-5.0 mbar of initial Ar pressures the radiative compression can be stated according to the V_{pf}^{comp} and V_{p0}^{comp} / V_{pf}^{comp} (or V_{p0}^{comp} - V_{pf}^{comp}).

The determined computed theoretical initial (V_{p0}^{comp}) and final (V_{pf}^{comp}) plasma pinch volumes for discharges in $(100\%\text{-}x)D_2+x$Ar mixtures (figure 8.4.13) decrease similarly with Ar fraction up to about 30%. Above 30% of Ar fraction the V_{p0}^{comp} become approximately constant but the V_{pf}^{comp} decrease further up to about 60-65% of Ar fraction resulting in significant increase of ratios of V_{p0}^{comp} to V_{pf}^{comp}. Above 65% of Ar fraction the decrease of V_{pf}^{comp} becomes insignificant. Up to 20% of Ar fraction the $V_{pf}^{comp} > V_{p0}^{comp}$ (expansion of the total volume of plasma column) but above 20% of Ar fraction $V_{pf}^{comp} < V_{p0}^{comp}$ (compression of the total volume of plasma column). The highest ratio of V_{p0}^{comp} to V_{pf}^{comp} is achived at 90% of Ar fraction – about 14 time decrease in total volume of plasma column during pinch phase of discharge. Moreover, the theoretical dependencies in figure 8.4.13 are similar to the theoretical dependencies describing changes of theoretical $<r_{p0}^{comp}>$ and $<r_{pmin}^{comp}>$ in $(100\%\text{-}x)D_2+x$Ar mixtures in figure 8.4.3. Thus, for the theoretical discharges in $(100\%\text{-}x)D_2+x$Ar mixtures the changes in total volumes of plasma columns are dominated by the total changes in the radii of the plasma column (especially the total changes of V_{pf}^{comp} are dominated by the total changes of r_{pmin}^{comp}). Summarizing, for the theoretical discharges in 25-95% range of Ar fractions in $(100\%\text{-}x)D_2+x$Ar mixtures the radiative compression is stated according to the V_{pf}^{comp} and V_{p0}^{comp} / V_{pf}^{comp} (or V_{p0}^{comp} - V_{pf}^{comp}).

Computed discharges in deuterium

Figure 8.4.14 presents the computed initial pinch volume (V_{p0}^{comp}) and the computed final pinch volume (V_{pf}^{comp}) from the discharges in D_2.

The determined computed initial (V_{p0}^{comp}) and final (V_{pf}^{comp}) plasma pinch volumes in D_2 (figure 8.4.14) are approximately constant. This is a similar behaviour as for the theoretical discharges in D_2 (figure 8.4.11). This behaviour is caused by approximately constant values of the computed pinch radii (figure 8.4.14) and the computd pinch lengths (figure 8.4.9) in D_2 (the same as for the theoretical discharges in D_2). Moreover, the V_{pf}^{comp} are always bigger than the V_{p0}^{comp} – domination of the total increase in pinch length over the total decrease in pinch radius (the same as for the theoretical discharges in figure 8.4.11). On the other hand, the computed V_{pf}^{comp} and V_{p0}^{comp} in D_2 (figure 8.4.14) are smaller than the theoretical V_{pf}^{comp} and V_{p0}^{comp} in D_2 (figure 8.4.11). Still, no radiative compression can be stated for the computed discharges in D_2 according to the V_{pf}^{comp} and V_{p0}^{comp} - V_{pf}^{comp} (or V_{p0}^{comp} / V_{pf}^{comp}).

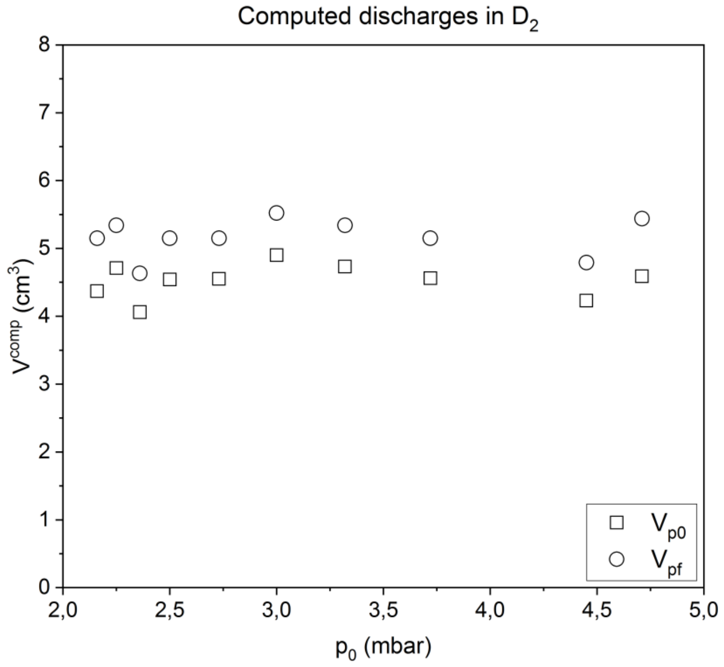

Figure 8.4.14. The computed initial pinch volume (V_{p0}^{comp}) and the computed final pinch volume (V_{pf}^{comp}) versus initial D_2 pressure (p_0).

Computed discharges in deuterium-argon mixtures

Figure 8.4.15 presents the average computed initial pinch volume ($<V_{p0}^{comp}>$) and the average computed final pinch volume ($<V_{pf}^{comp}>$) from the discharges in (100%-x)D_2+xAr mixtures.

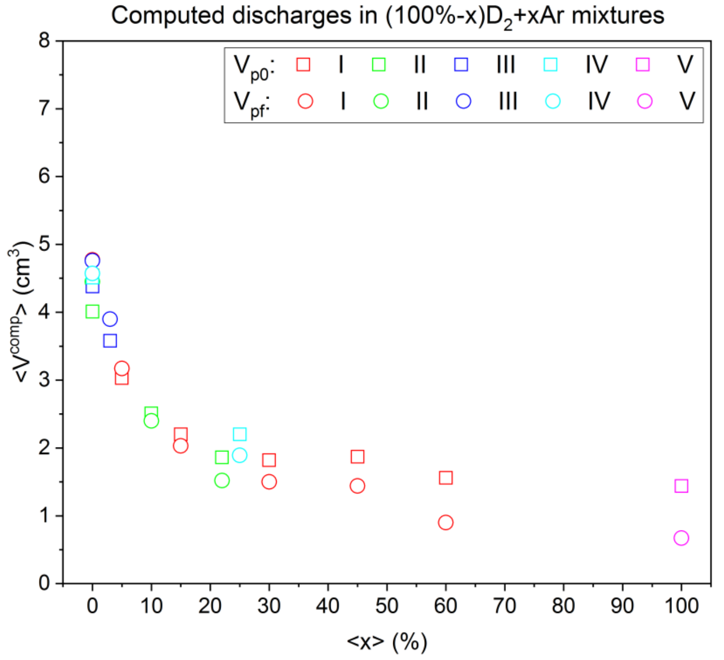

Figure 8.4.15. The average computed initial pinch volume ($<V_{p0}^{comp}>$) and the average computed final pinch volume ($<V_{pf}^{comp}>$) versus Ar fraction ($<x>$) in (100%-x)D_2+xAr mixture. Roman numerals indicates the series ID.

The computed average initial ($<V_{p0}^{comp}>$) and final ($<V_{pf}^{comp}>$) plasma pinch volumes in (100%-x)D_2+xAr mixtures (figure 8.4.15) decrease with Ar fraction. However, the decrease is different from the anticipated one in figure 8.4.13 – bending points cannot be clearly located, $<V_{p0}^{comp}>$ appear to decrease up to 100% of Ar fraction and the decrease of $<V_{p0}^{comp}>$ with $<x>$ is relatively large in comparison to the theoretical values in figure 8.4.13. The situation presented in figure 8.4.15 is similar as for the computed average plasma pinch radii in (100%-x)D_2+xAr mixtures in figure 8.4.5. Thus, the total changes of the average plasma pinch volumes during computed discharges in (100%-x)D_2+xAr mixtures are dominated by the total changes in the average plasma column radius. The decrease of $<V_{p0}^{comp}>$ and $<V_{pf}^{comp}>$ with Ar fraction is mainly caused by the changes in plasma dynamics and compressibility as was explained in subsection 8.4.1. Moreover, up to 5% of Ar fraction $<V_{pf}^{comp}>$ are bigger than the corresponding $<V_{p0}^{comp}>$ (up to 20% was anticipated from the theoretical discharges in (100%-x)D_2+xAr mixtures in figure 8.4.13). Above 5% of Ar fraction $<V_{pf}^{comp}>$ become smaller than the corresponding $<V_{p0}^{comp}>$. And the maximum ratio of $<V_{p0}^{comp}>$ to $<V_{pf}^{comp}>$ is determined for 100% of Ar fraction – about 2.1 times total decrease in average plasma column volume. And when 0-60% Ar fractions are only considered, the highest relative decrease in average plasma column volume, achieved for 60% of Ar fraction, is equal to 1.7 times. The 2.1 times of relative total decrease in pinch volume is small in comparison to 37 times total decrease for the theoretical discharges in 3.0 mbar of initial Ar pressure (figure 8.4.12) or 14 times total decrease for the theoretical discharges in 95% of Ar fraction for 3.0 mbar of initial pressure of the mixture (figure 8.4.13). Although, the 2.1 is also bigger value than the anticipated theoretical one (1.2 times) for discharge in 1.2 mbar of initial Ar pressure (figure 8.4.12).

For the single discharges in 0-60% range of Ar fractions maximum total decrease of plasma column volume is equal only to 2.0 times (discharges in 60% of Ar). Single discharges for which $V_{pf}^{comp} < V_{p0}^{comp}$ are present in 0-60% range of Ar and in 100% of Ar. So, also for some of the discharges in 0% of Ar V_{pf}^{comp} values were smaller than V_{p0}^{comp} – changes in the dynamic of discharge can cause some relatively small decrease in the total plasma column volume during pinch phase of discharge. The selected discharges for which changes of total pinch volume are higher than for all computed discharges in 0% of Ar take place only in 0-60% of Ar and in 100% of Ar. On the other hand, the discharges for which $V_{pf}^{comp} > V_{p0}^{comp}$ are present only in 0-10% range of Ar. For 100% of Ar fraction the maximum total decrease of plasma column volume is equal to about 6.8 times (discharge #17102009) and the smallest total decrease is equal only to 1.1 times (discharge #17101817). Summarizing, for some of the single discharges in 30-60% range of Ar fractions and in 100% of Ar fraction radiative compression is stated according to the V_{pf}^{comp} and V_{p0}^{comp} / V_{pf}^{comp} (or V_{p0}^{comp} - V_{pf}^{comp}) – higher (positive) values than for all computed discharges in D_2.

8.5. Plasma pinch parameters – densities

In this subsection, changes of the total initial (volumetric) pinch density (n_{p0}^{comp}), the initial (volumetric) pinch density of D (n_{p0D}^{comp}), the initial (volumetric) pinch density of Ar (n_{p0Ar}^{comp}), the maximum total (volumetric) pinch density (n_{pmax}^{comp}), the maximum (volumetric) pinch density of D (n_{pmaxD}^{comp}), the maximum (volumetric) pinch density of Ar (n_{pmaxAr}^{comp}), the total initial linear pinch density (N_{p0}^{comp}), the initial linear pinch density of D (N_{p0D}^{comp}), the initial linear pinch density of Ar (N_{p0Ar}^{comp}), the total final linear pinch density (N_{pf}^{comp}), the final linear pinch density of D (N_{pfD}^{comp}) and the final linear pinch density of Ar (N_{pfAr}^{comp}) will be presented.

8.5.1. Plasma pinch parameters – volumetric densities

Theoretical discharges

The computed theoretical total initial pinch densities (n_{p0}^{comp}) and the computed theoretical total maximum pinch densities (n_{pmax}^{comp}) from the discharges in D_2 and Ar are presented in figure 8.5.1 and figure 8.5.2, respectively. For the theoretical discharges in D_2, the total initial pinch densities are equal to the initial pinch densities of D ($n_{p0}^{comp} = n_{p0D}^{comp}$), the total maximum pinch densities are equal to the maximum pinch densities of D ($n_{pmax}^{comp} = n_{pmaxD}^{comp}$) and both initial and maximum pinch densities of Ar are equal to 0 ($n_{p0Ar}^{comp} = n_{pmaxAr}^{comp} = 0$). And for the theoretical discharges in Ar, the total initial pinch densities are equal to the initial pinch densities of Ar ($n_{p0}^{comp} = n_{p0Ar}^{comp}$), the total maximum pinch densities are equal to the maximum pinch densities of Ar ($n_{pmax}^{comp} = n_{pmaxAr}^{comp}$) and both initial and maximum pinch densities of D are equal to 0 ($n_{p0D}^{comp} = n_{pmaxD}^{comp} = 0$). Moreover, the computed theoretical initial pinch densities of D (n_{p0D}^{comp}), the computed theoretical initial pinch densities of Ar (n_{p0Ar}^{comp}), the computed theoretical total initial pinch densities (n_{p0}^{comp}), the computed theoretical maximum pinch densities of D (n_{pmaxD}^{comp}), the computed theoretical maximum pinch densities of Ar (n_{pmaxAr}^{comp}) and the computed theoretical total maximum pinch densities (n_{pmax}^{comp}) for discharges in (100%-x)D_2+xAr mixutures were presented in figure 8.5.1.3.

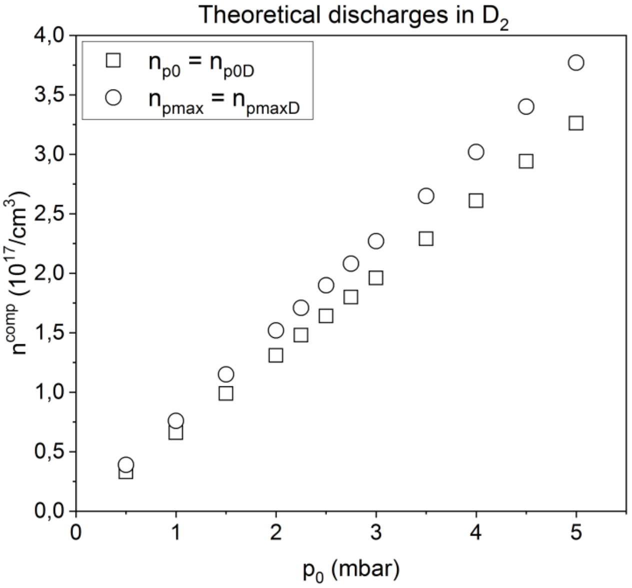

Figure 8.5.1. The computed theoretical total initial pinch density (n_{p0}^{comp}) and the computed theoretical total maximum (final) pinch density (n_{pmax}^{comp}) versus initial D_2 pressure (p_0).

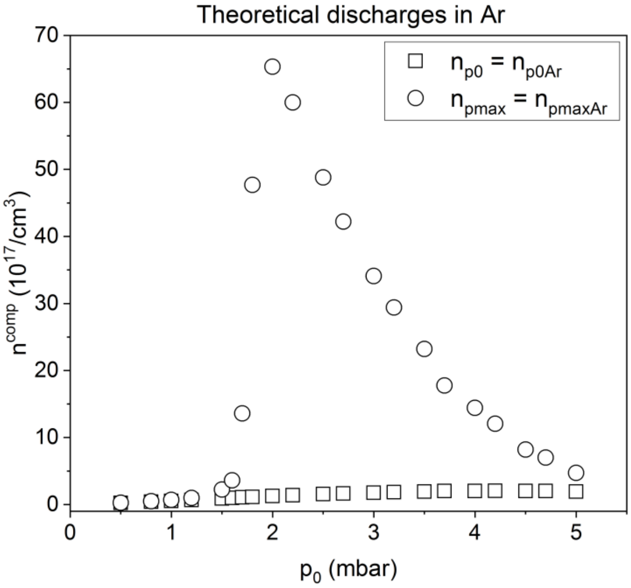

Figure 8.5.2. The computed theoretical total initial pinch density (n_{p0}^{comp}) and the computed theoretical total maximum (final) pinch density (n_{pmax}^{comp}) versus initial Ar pressure (p_0).

The computed theoretical total initial (n_{p0}^{comp}) and maximum (n_{pmax}^{comp}) plasma densities for discharges in D_2 (figure 8.5.1) increase linearly with initial pressure due to constant pinch radii (figure 8.4.1) and linearly increasing n_0 values (total ambient number density in equation (6.2.34)). The increase is relatively small in comparison to increase in plasma density predicted for the radiative compression during previous studies – few orders of magnitude. The highest achieved value of n_{p0}^{comp} is equal to $3.26 \times 10^{17}/\mathrm{cm}^3$ (at 5.0 mbar of initial D_2 pressure) while the highest achieved value of n_{pmax}^{comp} is equal to $3.77 \times 10^{17}/\mathrm{cm}^3$

(also at 5.0 mbar of initial D_2 pressure). Thus, the increase in deuterium ion number density during pinch phase of discharge (difference between n_{pmax}^{comp} and n_{p0}^{comp}) is equal to $0.51 \times 10^{17}/\mathrm{cm}^3$ at 5.0 mbar of D_2. This is the highest theoretical increase from all investigated initial D_2 pressures, since the differences between final plasma density and initial plasma density during discharge become bigger with the initial D_2 pressure increase (figure 8.5.1). So, no radiative compression is stated for the theoretical discharges in D_2 according to the n_{pmax}^{comp} and n_{pmax}^{comp} - n_{p0}^{comp}.

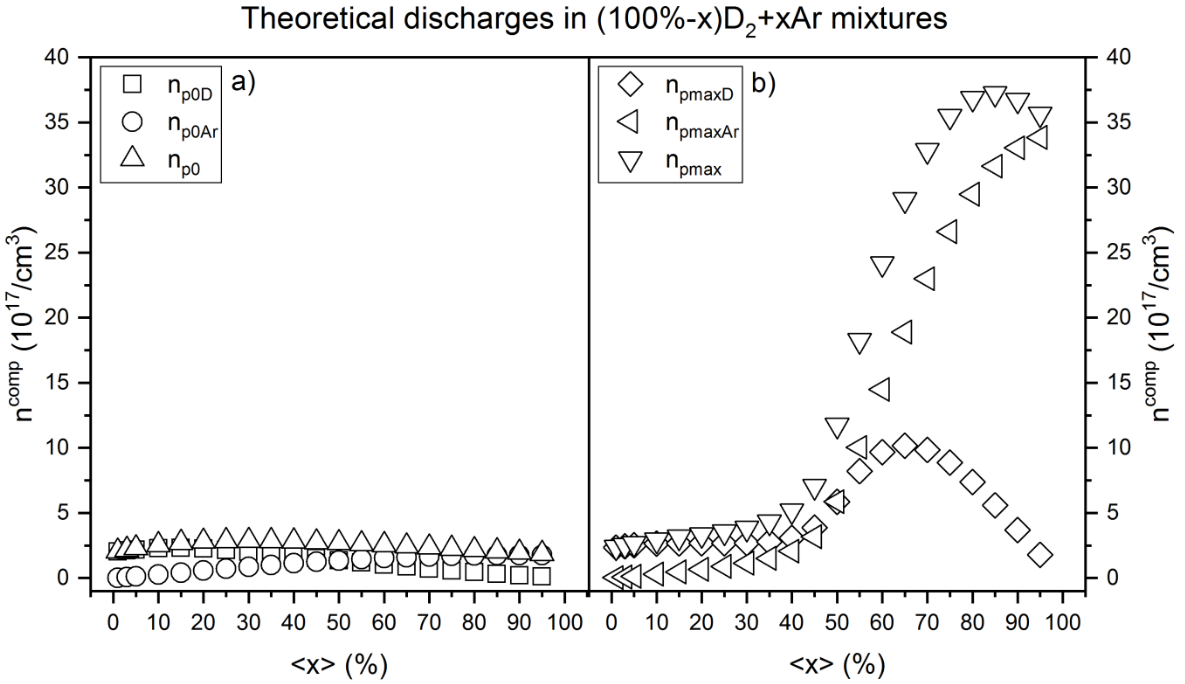

Figure 8.5.3. a) The computed theoretical initial pinch density of D (n_{p0D}^{comp}), the computed theoretical initial pinch density of Ar (n_{p0Ar}^{comp}) and the computed theoretical total initial pinch density (n_{p0}^{comp}) versus Ar fraction (x) in (100%-x)D_2+xAr mixture. **b)** The computed theoretical maximum (final) pinch density of D (n_{pmaxD}^{comp}), the computed theoretical maximum (final) pinch density of Ar (n_{pmaxAr}^{comp}) and the computed theoretical total maximum (final) pinch density (n_{pmax}^{comp}) versus Ar fraction (x) in (100%-x)D_2+xAr mixture.

The computed theoretical total initial (n_{p0}^{comp}) and maximum (n_{pmax}^{comp}) plasma densities, for discharges in (100%-x)D_2+xAr mixtures, are the sum of densities coming from D and Ar ions: $n_{p0}^{comp} = n_{p0D}^{comp} + n_{p0Ar}^{comp}$ and $n_{pmax}^{comp} = n_{pmaxD}^{comp} + n_{pmaxAr}^{comp}$ (see subsection 6.2.10 and equation (6.2.34)). The n_{p0}^{comp} vs x dependency (figure 8.5.3a) shows maximum at 30% of Ar – $2.86 \times 10^{17}/\mathrm{cm}^3$ – connected with changes in plasma compressibility. The n_{p0D}^{comp} slightly increase up to 15% of Ar and above 15% constantly decrease, while n_{p0Ar}^{comp} constantly increase with Ar fraction in 1-95% range of Ar. Both n_{p0D}^{comp} vs x and n_{p0Ar}^{comp} vs x dependencies cross at 50% of Ar. The n_{pmax}^{comp} increase relatively slowly up to about 40% of Ar fraction (figure 8.5.3b). Starting from 30% of Ar fraction the n_{pmax}^{comp} become higher than the n_{pmax}^{comp} for all theoretical discharges in D_2. Above 40% of Ar fraction the increase of n_{pmax}^{comp} becomes more rapid and last up to about 85% of Ar – mostly connected with the increase in total X-ray line emission power and radiative compression occurrence. Above 85% of Ar fraction the n_{pmax}^{comp} start to decrease – connected with the plasma opacity and the slowing down increase of total X-ray line emission power. At 85% of Ar the highest n_{pmax}^{comp} is stated equal to $37.21 \times 10^{17}/\mathrm{cm}^3$, while the corresponding

$n_{p0}{}^{comp}$ value is equal to 2.06 × 10^{17}/cm^3, corresponding $n_{pmaxD}{}^{comp}$ = 5.58 × 10^{17}/cm^3 and corresponding $n_{pmaxAr}{}^{comp}$ = 31.63 × 10^{17}/cm^3. The $n_{pmaxD}{}^{comp}$ and $n_{pmaxAr}{}^{comp}$ also increase relatively slowly up to about 40% of Ar fraction ($n_{pmaxD}{}^{comp} > n_{pmaxAr}{}^{comp}$). Above 40% the increase becomes more rapid for both $n_{pmaxD}{}^{comp}$ and $n_{pmaxAr}{}^{comp}$ ($n_{pmaxD}{}^{comp} = n_{pmaxAr}{}^{comp}$ at 50% of Ar fraction), wherein $n_{pmaxD}{}^{comp}$ reach maximum at 65% of Ar while $n_{pmaxAr}{}^{comp}$ increase up to 95% of Ar (from about 85% the increase of $n_{pmaxAr}{}^{comp}$ slows down slightly). At 65% of Ar $n_{pmaxD}{}^{comp}$ = 10.17 × 10^{17}/cm^3 (higher value than 3.77 × 10^{17}/cm^3 for theoretical discharges in D_2) while $n_{p0D}{}^{comp}$ = 0.85 × 10^{17}/cm^3. And at 95% of Ar $n_{pmaxAr}{}^{comp}$ = 33.85 × 10^{17}/cm^3 (smaller value than 65.34 × 10^{17}/cm^3 for theoretical discharges in Ar) while $n_{p0Ar}{}^{comp}$ = 1.77 × 10^{17}/cm^3. So, the maximum increase in deuterium ion number density for the theoretical discharges in (100%-x)D_2+xAr mixtures equals: 9.32 × 10^{17}/cm^3 (about 12 times increase) – large increase in comparison to theoretical discharges in D_2 (figure 8.5.1). The maximum increase in argon ion number density for the theoretical discharges in (100%-x)D_2+xAr mixtures equals: 32.09 × 10^{17}/cm^3 (about 19 times increase) – smaller increase than for theoretical discharges in Ar (figure 8.5.2). And the maximum increase in total ion number density for the theoretical discharges in (100%-x)D_2+xAr mixtures equals: 35.15 × 10^{17}/cm^3 (about 18 times increase). The $n_{pmax}{}^{comp}$ - $n_{p0}{}^{comp}$ = 35.15 × 10^{17}/cm^3 is large increase in comparison to 0.51 × 10^{17}/cm^3 value achived for the theoretical discharges in D_2 (figure 8.5.1) but smaller than 64.09 × 10^{17}/cm^3 achived for theoretical discharges in Ar (figure 8.5.2). Starting from 20% of Ar fraction $n_{pmax}{}^{comp}$ - $n_{p0}{}^{comp}$ values for discharges in (100%-x)D_2+xAr mixtures become higher than the highest difference for theoretical discharges in D_2 in figure 8.5.1. Similarly, the highest $n_{pmax}{}^{comp}$ = 37.21 × 10^{17}/cm^3 is large in comparison to 3.77 × 10^{17}/cm^3 value achived for the theoretical discharges in D_2 (figure 8.5.1) but smaller than 65.34 × 10^{17}/cm^3 for theoretical discharges in Ar (figure 8.5.2). Summarizing, for the theoretical discharges in 30-95% range of Ar fractions the radiative compression can be stated according to the $n_{pmax}{}^{comp}$ and $n_{pmax}{}^{comp}$ - $n_{p0}{}^{comp}$ (higher values than for all theoretical discharges in D_2). Moreover, the theoretical dependencies describing changes of $n_{p0}{}^{comp}$ and $n_{pmax}{}^{comp}$ for (100%-x)D_2+xAr mixtures presented in figure 8.5.3 are different from the ones in Ar (in figure 8.5.2) and completely different from the ones in D_2 (in figure 8.5.1).

Computed discharges in deuterium

Figure 8.5.4 presents the computed total initial pinch density ($n_{p0}{}^{comp}$) and the computed total maximum pinch density ($n_{pmax}{}^{comp}$) from the discharges in D_2. For the theoretical discharges in D_2 the total initial pinch densities are equal to the initial pinch densities of D ($n_{p0}{}^{comp} = n_{p0D}{}^{comp}$), the total maximum pinch densities are equal to the maximum pinch densities of D ($n_{pmax}{}^{comp} = n_{pmaxD}{}^{comp}$) and both initial and maximum pinch densities of Ar are equal to 0 ($n_{p0Ar}{}^{comp} = n_{pmaxAr}{}^{comp} = 0$).

The computed total initial ($n_{p0}{}^{comp}$) and maximum ($n_{pmax}{}^{comp}$) plasma pinch densities (figure 8.5.4) increase with initial D_2 pressure – connected with increase in initial total ambient number density (n_0) of deuterium and some increase in f_m model parameter values (higher mass sweeping above 3.0 mbar – see table 7.2.1). In the 2.0-2.5 mbar range of initial D_2 pressures there are some bigger fluctuations present which suggest that at the beginning the increase is rather slow or the values are approximately constant. In general, the characters of the dependencies in figure 8.5.4 are different from the theoretical ones in figure 8.5.1. The highest achieved value of $n_{p0}{}^{comp}$ is equal to 8.47 × 10^{17}/cm^3 (at 4.71 mbar of initial D_2 pressure) and highest achived $n_{pmax}{}^{comp}$ is equal to 9.90 × 10^{17}/cm^3 (also at 4.71 mbar of initial D_2 pressure). Both values are bigger than the corresponding theoretical in figure 8.5.1.

In fact, all n_{p0}^{comp} and n_{pmax}^{comp} values in figure 8.5.4 are bigger than corresponding theoretical ones in figure 8.5.1. Also, the increase in total pinch density during discharge in 4.71 mbar of initial D_2 pressure – $1.43 \times 10^{17}/cm^3$ – is higher than the highest theoretically anticipated $0.51 \times 10^{17}/cm^3$ (figure 8.5.1). Still, the $n_{pmax}^{comp} - n_{p0}^{comp} = 1.43 \times 10^{17}/cm^3$ and the $n_{pmax}^{comp} = 9.90 \times 10^{17}/cm^3$ are relatively small in comparison to maximum values predicted for theoretical discharges in Ar (figure 8.5.2) and in (100%-x)D_2+xAr mixtures (figure 8.5.3). So, no radiative compression can be stated for the computed discharges in D_2 according to the n_{pmax}^{comp} and $n_{pmax}^{comp} - n_{p0}^{comp}$.

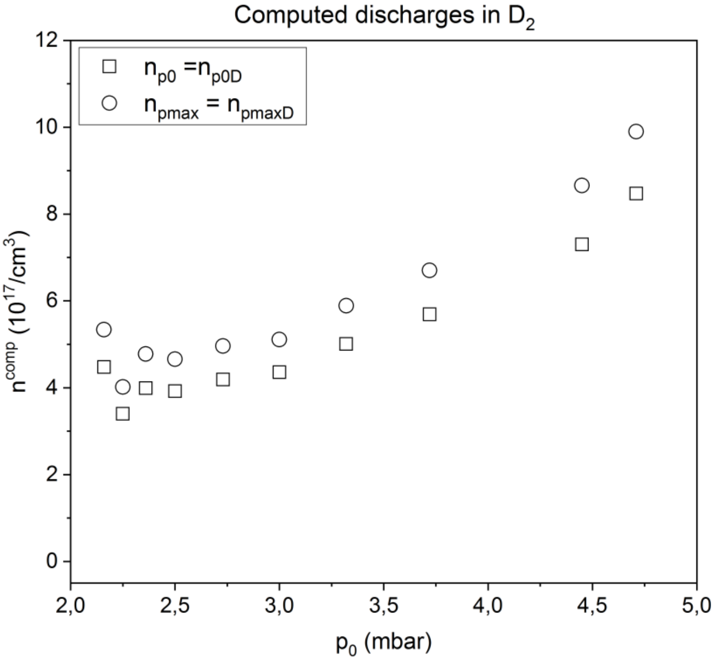

Figure 8.5.4. The computed total initial pinch density (n_{p0}^{comp}) and the computed total maximum (final) pinch density (n_{pmax}^{comp}) versus initial D_2 pressure (p_0).

Computed discharges in deuterium-argon mixtures

Figure 8.5.5 presents: the average computed total initial pinch density ($<n_{p0}^{comp}>$), the average computed initial pinch density of D ($<n_{p0D}^{comp}>$), the average computed initial pinch density of Ar ($<n_{p0Ar}^{comp}>$), the average computed total maximum pinch density ($<n_{pmax}^{comp}>$), the average computed maximum pinch density of D ($<n_{pmaxD}^{comp}>$) and the average computed maximum pinch density of Ar ($<n_{pmaxAr}^{comp}>$) from the discharges in (100%-x)D_2+xAr mixtures. Wherein, $<n_{p0}^{comp}> = <n_{p0D}^{comp}> + <n_{p0Ar}^{comp}>$ and $<n_{pmax}^{comp}> = <n_{pmaxD}^{comp}> + <n_{pmaxAr}^{comp}>$ (see subsection 6.2.10 and equation (6.2.34)).

The average total initial ($<n_{p0}^{comp}>$) and maximum ($<n_{pmax}^{comp}>$) plasma densities in (100%-x)D_2+xAr mixtures (figure 8.5.5) decrease with Ar fraction up to 45%. Fluctuations of $<n_{p0}^{comp}>$ and $<n_{pmax}^{comp}>$ are present, especially for 0% of Ar fraction – for the series II and III taken into account independently some increase of $<n_{p0}^{comp}>$ and $<n_{pmax}^{comp}>$ with Ar fraction can be stated. The decrese of $<n_{p0}^{comp}>$ and $<n_{pmax}^{comp}>$ up to 45% of Ar fraction in figure 8.5.5 was not anticipated for the theoretical discharges in (100%-x)D_2+xAr mixtures in figure 8.5.3. At about 60% of Ar fraction, the $<n_{pmax}^{comp}>$ value increases a little bit in comparison to the value at 45% of Ar fraction (figure 8.5.5b). The $<n_{pmax}^{comp}>$ at 45% is equal to $1.08 \times 10^{17}/cm^3$ and at 60% is equal to $1.21 \times 10^{17}/cm^3$. These values are far smaller than the theoretically ancitipated

$7.03 \times 10^{17}/\mathrm{cm}^3$ at 45% and $24.14 \times 10^{17}/\mathrm{cm}^3$ at 60% – no significant increase in the average total ion number density above 40% of Ar fraction is stated, except for the discharges in 100% of Ar. Both $<n_{p0D}^{comp}>$ and $<n_{pmaxD}^{comp}>$ decrease with Ar fraction similarly to $<n_{p0}^{comp}>$ and $<n_{pmax}^{comp}>$ (similar values). On the other hand, $<n_{p0Ar}^{comp}>$ and $<n_{pmaxAr}^{comp}>$ slowly increase with Ar (insignificantly) ($<n_{pmaxD}^{comp}>> <n_{pmaxAr}^{comp}>$). The $<n_{p0D}^{comp}> \approx <n_{p0Ar}^{comp}>$ and $<n_{pmaxD}^{comp}> \approx <n_{pmaxAr}^{comp}>$ at 45% of Ar (ion number density of D is a little bit higher). For the discharges in 100% of Ar fraction both $<n_{p0}^{comp}> = <n_{p0Ar}^{comp}>$ and $<n_{pmax}^{comp}> = <n_{pmaxAr}^{comp}>$ are significantly increased in comparison to values at 45% and 60%. In fact, the $<n_{pmax}^{comp}>$ value at 100% is the highest of all Ar fractions – result of the highest average X-ray line emission power. This value is equal to $10.43 \times 10^{17}/\mathrm{cm}^3$ which is almost twice higher than the highest $<n_{pmax}^{comp}>$ at 0% of Ar. On the other hand, $10.43 \times 10^{17}/\mathrm{cm}^3$ is only little bit higher value than the $9.90 \times 10^{17}/\mathrm{cm}^3$ achived for computed discharge in 4.71 mbar of initial D_2 pressure (figure 8.5.4) or $9.75 \times 10^{17}/\mathrm{cm}^3$ for single discharge in 0% of Ar. The $10.43 \times 10^{17}/\mathrm{cm}^3$ is also smaller than the highest n_{pmax}^{comp} for theoretical discharges in Ar (figure 8.5.2) and for theoretical discharges in $(100\%\text{-}x)D_2+x$Ar mixtures (figure 8.5.3). On the other hand, it is significantly higher than the theoretically predicted value for 1.2 mbar of initial Ar pressure (figure 8.5.2). Moreover, the increase in the average total plasma pinch density ($<n_{pmax}^{comp}>$ - $<n_{p0}^{comp}>$) during pinch phase of discharge at 45%, 60% and 100% of Ar is equal to: $0.35 \times 10^{17}/\mathrm{cm}^3$, $0.59 \times 10^{17}/\mathrm{cm}^3$, and $8.15 \times 10^{17}/\mathrm{cm}^3$, respectively. The increase in the average plasma pinch density of D ($<n_{pmaxD}^{comp}>$ - $<n_{p0D}^{comp}>$) at 45% and 60% of Ar is equal to: $0.20 \times 10^{17}/\mathrm{cm}^3$ and $0.23 \times 10^{17}/\mathrm{cm}^3$, respectively. And the increase in the average plasma pinch density of Ar ($<n_{pmaxAr}^{comp}>$ - $<n_{p0Ar}^{comp}>$) at 45% and 60% of Ar is equal to: $0.16 \times 10^{17}/\mathrm{cm}^3$ and $0.35\times10^{17}/\mathrm{cm}^3$, respectively. All of these values are relatively small except the $8.15\times10^{17}/\mathrm{cm}^3$ at 100% of Ar fraction. The $<n_{pmax}^{comp}>$ - $<n_{p0}^{comp}>$ = $8.15\times10^{17}/\mathrm{cm}^3$ is large in comparison to the maximum computed increase for discharges in D_2 – $1.48 \times 10^{17}/\mathrm{cm}^3$ is the maximum increase in total plasma pinch density taking into account all investigated single computed discharges in 0% of Ar. Moreover, all changes in the average total plasma pinch densities for discharges in 3-60% of Ar are smaller than the values achived for discharges in 0% of Ar.

When single discharges are taken into account the situation looks similar. The highest achived n_{pmax}^{comp} for discharges in 0-60% of Ar range is equal to $9.75 \times 10^{17}/\mathrm{cm}^3$ – discharge in 0% of Ar. And the maximum increase in total plasma pinch density (n_{pmax}^{comp} - n_{p0}^{comp}) for discharges in 0-60% of Ar range is equal to $1.62 \times 10^{17}/\mathrm{cm}^3$ – discharge in 25% of Ar. The $1.62 \times 10^{17}/\mathrm{cm}^3$ value is only a little bit higher than the highest increase of $1.48\times10^{17}/\mathrm{cm}^3$ for single discharges in 0% of Ar. For the discharges in 100% of Ar fraction the smallest and highest n_{pmax}^{comp} values are equal to: $0.93 \times 10^{17}/\mathrm{cm}^3$ (discharge #17102003) and $19.76 \times 10^{17}/\mathrm{cm}^3$ (discharge #17102007), respectively. Moreover, the smallest and highest increase in the computed total plasma pinch density for 100% of Ar fraction is equal to: $0.27 \times 10^{17}/\mathrm{cm}^3$ (discharge #17102003) and $17.70 \times 10^{17}/\mathrm{cm}^3$ (discharge #17102007), respectively. Summarizing, only for part of single computed discharges in 100% of Ar fractions the radiative compression can be stated according to the n_{pmax}^{comp} and n_{pmax}^{comp} - n_{p0}^{comp} (higher values than for all computed discharges in D_2).

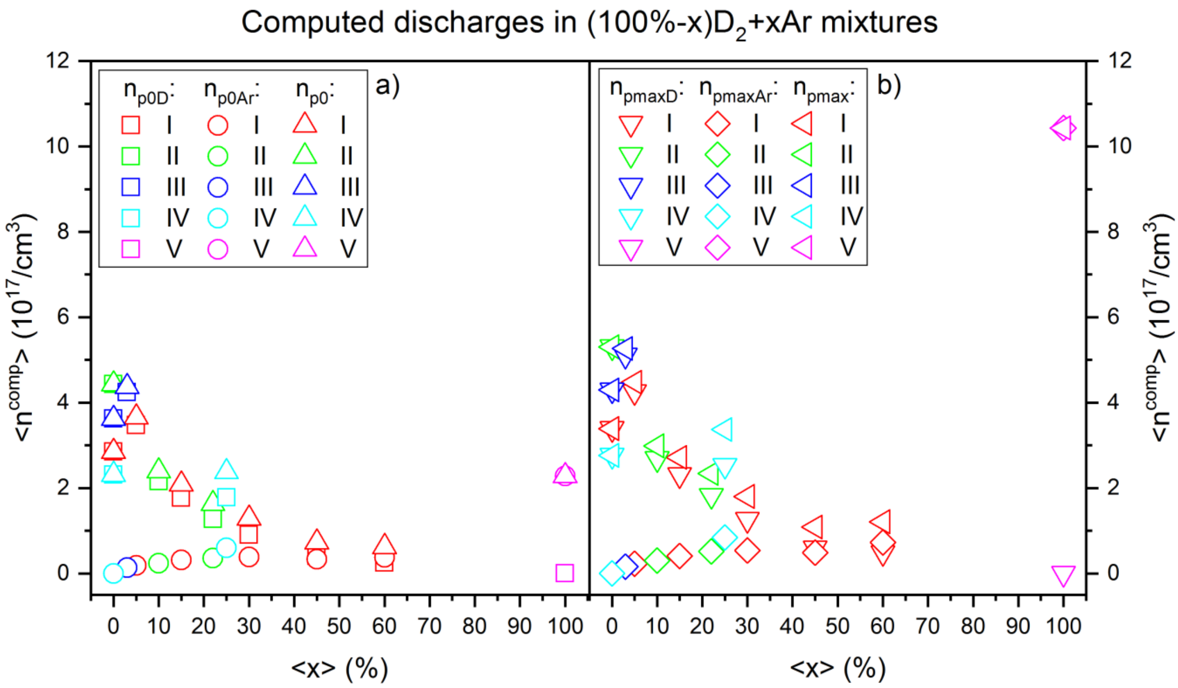

Figure 8.5.5. a) The average computed initial pinch density of D ($<n_{p0D}{}^{comp}>$), the average computed initial pinch density of Ar ($<n_{p0Ar}{}^{comp}>$) and the average computed total initial pinch density ($<n_{p0}{}^{comp}>$) versus Ar fraction ($<x>$) in (100%-x)D_2+xAr mixture. **b)** The average computed maximum (final) pinch density of D ($<n_{pmaxD}{}^{comp}>$), the average computed maximum (final) pinch density of Ar ($<n_{pmaxAr}{}^{comp}>$) and the average computed total maximum (final) pinch density ($<n_{pmax}{}^{comp}>$) versus Ar fraction ($<x>$) in (100%-x)D_2+xAr mixture. Roman numerals indicate the series ID.

8.5.2. Plasma pinch parameters – linear densities

Theoretical discharges

The computed theoretical total initial linear pinch densities ($N_{p0}{}^{comp}$) and the computed theoretical total final linear pinch densities ($N_{pf}{}^{comp}$) from the theoretical discharges in D_2 and Ar are presented in: figure 8.5.6 and figure 8.5.7, respectively. For the theoretical discharges in D_2, the total initial linear pinch densities are equal to the initial linear pinch densities of D ($N_{p0}{}^{comp} = N_{p0D}{}^{comp}$), the total final linear pinch densities are equal to the final linear pinch densities of D ($N_{pf}{}^{comp} = N_{pfD}{}^{comp}$) and both initial and maximum linear pinch densities of Ar are equal to 0 ($N_{p0Ar}{}^{comp} = N_{pfAr}{}^{comp} = 0$). And for the theoretical discharges in Ar, the total initial linear pinch densities are equal to the initial linear pinch densities of Ar ($N_{p0}{}^{comp} = N_{p0Ar}{}^{comp}$), the total final linear pinch densities are equal to the final linear pinch densities of Ar ($N_{pf}{}^{comp} = N_{pfAr}{}^{comp}$) and both initial and final linear pinch densities of D are equal to 0 ($N_{p0D}{}^{comp} = N_{pfD}{}^{comp} = 0$). Moreover, the computed theoretical initial linear pinch densities of D ($N_{p0D}{}^{comp}$), the computed theoretical initial linear pinch densities of Ar ($N_{p0Ar}{}^{comp}$), the computed theoretical total initial linear pinch densities ($N_{p0}{}^{comp}$), the computed theoretical final linear pinch densities of D ($N_{pfD}{}^{comp}$), the computed theoretical final linear pinch densities of Ar ($N_{pfAr}{}^{comp}$) and the computed theoretical total final linear pinch densities ($N_{pf}{}^{comp}$) for discharges in (100%-x)D_2+xAr mixutures were presented in figure 8.5.8.

The computed theoretical total initial ($N_{p0}{}^{comp}$) and final ($N_{pf}{}^{comp}$) linear plasma densities constantly increase with initial D_2 pressure (figure 8.5.6). This increase is linear since the linear plasma densities are calculated based on the plasma pinch radiuses (figure 8.4.1) and the volumetric plasma densities (figure 8.5.1) – the pinch radiuses are constant and the plasma volumetric densities increase linearly. Moreover, the corresponding N_{p0}^{comp} and N_{pf}^{comp} are equal – the plasma linear densitiy is constant during theoretical discharges in D_2 during pinch phase of discharge.

The computed total initial (N_{p0}^{comp}) and final (N_{pf}^{comp}) linear plasma densities increase with initial Ar pressure (figure 8.5.7). The approximately linear behaviour of N_{p0}^{comp} and N_{pf}^{comp} comes from the fact that the computed theoretical pinch radiuses (figure 8.4.2) and the computed theoretical volumetric densities (figure 8.5.2) have opposite dependencies – decrease in pinch radius under constant discharge conditions causes proportional increase in volumetric plasma density during pinch phase of discharge (see equation 6.2.34). The corresponding N_{p0}^{comp} and N_{pf}^{comp} values are similar and their increase (figure 8.5.7) with initial Ar pressure is slower than for theoretical discharges in D_2 (figure 8.5.6).

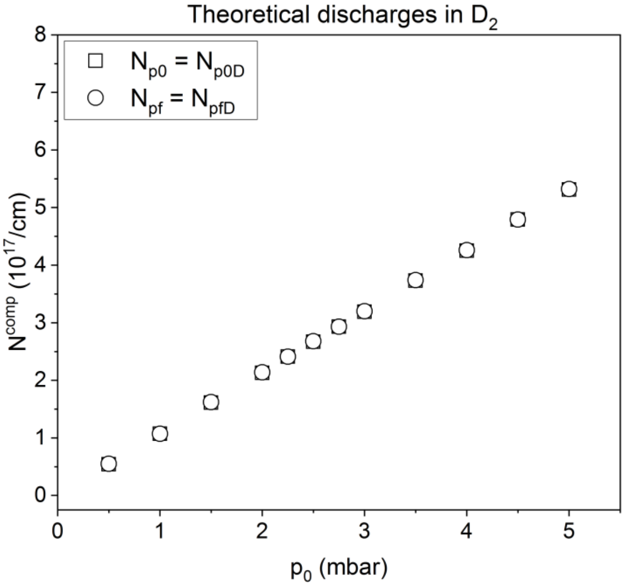

Figure 8.5.6. The computed theoretical total initial linear pinch density (N_{p0}^{comp}) and the computed theoretical total final linear pinch density (N_{pf}^{comp}) versus initial D_2 pressure (p_0).

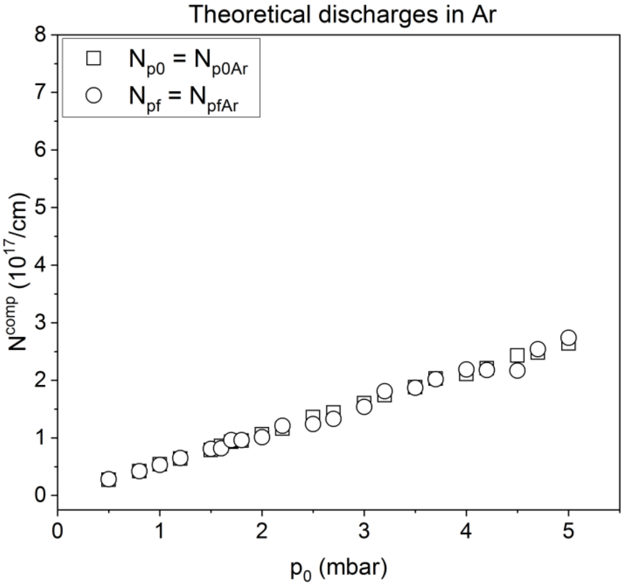

Figure 8.5.7. The computed theoretical total initial linear pinch density (N_{p0}^{comp}) and the computed total final linear pinch density (N_{pf}^{comp}) versus initial Ar pressure (p_0).

The computed theoretical total initial (N_{p0}^{comp}) and maximum (N_{pmax}^{comp}) linear plasma densities, for discharges in (100%-x)D_2+xAr mixtures, are the sum of densities coming from D and Ar ions: $N_{p0}^{comp} = N_{p0D}^{comp} + N_{p0Ar}^{comp}$ and $N_{pf}^{comp} = N_{pfD}^{comp} + N_{pfAr}^{comp}$ (similar as for volumetric densities in subsection 8.5.1). The N_{p0}^{comp} and N_{pf}^{comp} for discharges in (100%-x)D_2+xAr mixtures (figure 8.5.3) decrease with initial Ar fraction. The decrease has approximately linear character. The N_{p0D}^{comp} and N_{pfD}^{comp} decrease with Ar fraction and N_{p0Ar}^{comp} and N_{p0Ar}^{comp} increase with Ar fraction. The $N_{p0D}^{comp} = N_{p0Ar}^{comp}$ and $N_{pfD}^{comp} = N_{pfAr}^{comp}$ at 50% of Ar. The approximately linear character comes from the dependency between the computed theoretical pinch radiuses in (100%-x)D_2+xAr mixtures (figure 8.4.3) and computed theoretical volumetric pinch densities (figure 8.5.3) as was explained for theoretical discharges in Ar. The decrease (instead of increase) appears to be caused by the changes in the total specific heat ratios of ionized gases. In general, the SHRs are constant during discharges in D_2 and at the beginning of dicharges in Ar SHRs are not very different, while during discharges in gas mixtures they are dependent on the gas mixture composition (volumetric fraction of Ar and D_2 – see equation (6.2.26) and (6.2.28)) from the beginning of discharge making significant changes in the plasma compressibility. This shows in general that the composition of gas mixture has strong influence on linear plasma densities and plasma compressibility. Moreover, the range of changes of N_{p0}^{comp} and N_{pf}^{comp} in figure 8.5.8 is smaller in comparison to theoretical discharges in D_2 (figure 8.5.6) and Ar (figure 8.5.7). And the corresponding N_{p0}^{comp} and N_{pf}^{comp} have similar values during discharge.

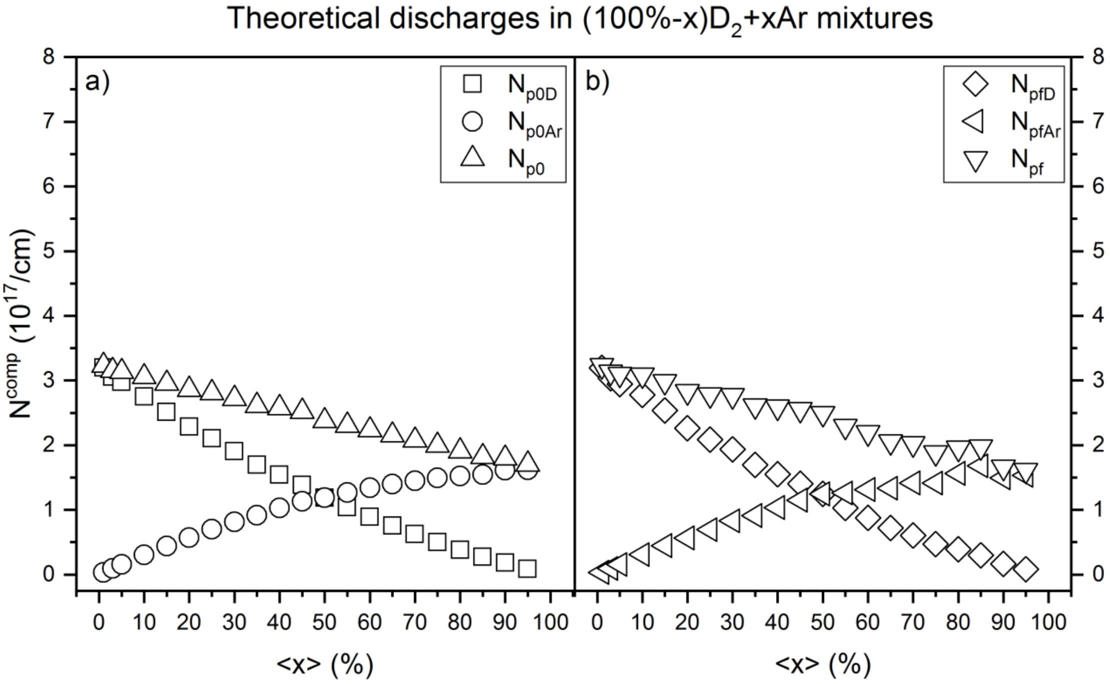

Figure 8.5.8. a) The computed theoretical initial linear pinch density of D (N_{p0D}^{comp}), the computed theoretical initial linear pinch density of Ar (N_{p0Ar}^{comp}) and the computed theoretical total initial linear pinch density (N_{p0}^{comp}) versus Ar fraction (x) in (100%-x)D_2+xAr mixture. **b)** The computed theoretical final linear pinch density of D (N_{pfD}^{comp}), the computed theoretical final linear pinch density of Ar (N_{pfAr}^{comp}) and the computed theoretical total final linear pinch density (N_{pf}^{comp}) versus Ar fraction (x) in (100%-x)D_2+xAr mixture.

Computed discharges in deuterium

Figure 8.5.9 presents the computed total initial linear pinch density (N_{p0}^{comp}) and the computed total final linear pinch density (N_{pf}^{comp}) from the discharges in D_2. For the theoretical discharges in D_2 the total initial linear pinch densities are equal to the initial linear pinch densities of D ($N_{p0}^{comp} = N_{p0D}^{comp}$), the total final linear pinch densities are equal to the final linear pinch densities of D ($N_{pf}^{comp} = N_{pfD}^{comp}$) and both initial and maximum linear pinch densities of Ar are equal to 0 ($N_{p0Ar}^{comp} = N_{pfAr}^{comp} = 0$).

The computed total initial (N_{p0}^{comp}) and final (N_{pf}^{comp}) linear plasma densities increase with initial D_2 pressure (figure 8.5.9). The increase is approximately linear and some large fluctuations of values appear to be present for discharge in 2.15 mbar and 4.71 mbar of D_2. Moreover, the determined N_{p0}^{comp} and N_{pf}^{comp} in figure 8.5.9 are higher than the corresponding computed theoretical values in D_2 in figure 8.5.6. And corresponding N_{p0}^{comp} and N_{pf}^{comp} have similar values (only small changes during pinch phase of discharge).

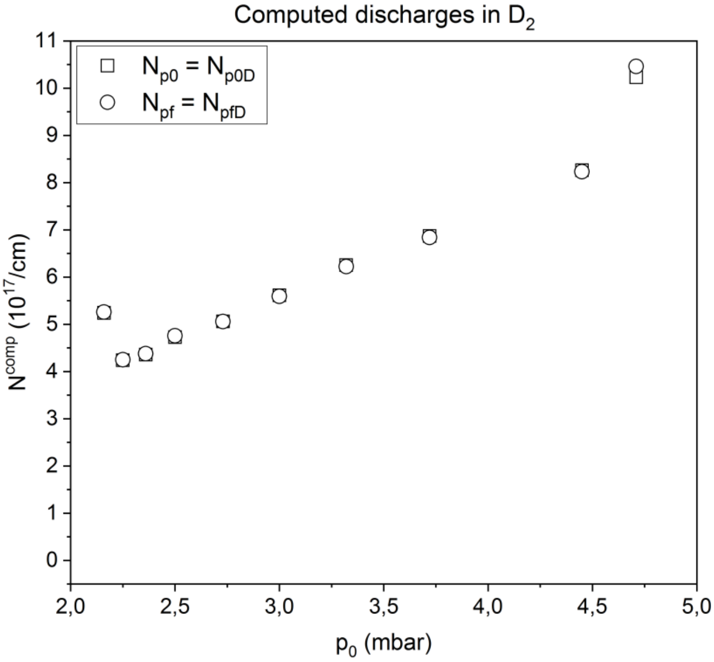

Figure 8.5.9. The computed total initial linear pinch density (N_{p0}^{comp}) and the computed total final linear pinch density (N_{pf}^{comp}) versus initial D_2 pressure (p_0).

Computed discharges in deuterium-argon mixtures

Figure 8.5.10 presents: the average computed total initial linear pinch density ($<N_{p0}^{comp}>$), the average computed initial linear pinch density of D ($<N_{p0D}^{comp}>$), the average computed initial linear pinch density of Ar ($<N_{p0Ar}^{comp}>$), the average computed total final linear pinch density ($<N_{pf}^{comp}>$), the average computed final linear pinch density of D ($<N_{pfD}^{comp}>$) and the average computed final linear pinch density of Ar ($<N_{pfAr}^{comp}>$) from the discharges in (100%-x)D_2+xAr mixtures. Wherein, $<N_{p0}^{comp}> = <N_{p0D}^{comp}> + <N_{p0Ar}^{comp}>$ and $<N_{pf}^{comp}> = <N_{pfD}^{comp}> + <N_{pfAr}^{comp}>$ (as for volumetric densities in subsection 8.5.1).

The average computed total initial ($<N_{p0}^{comp}>$) and final ($<N_{pf}^{comp}>$) linear plasma densities for discharges in (100%-x)D_2+xAr mixtures decrease with Ar fraction up to 60% (figure 8.5.10). The $<N_{p0D}^{comp}>$ and $<N_{pfD}^{comp}>$ decrease with Ar fraction (following closely $<N_{p0}^{comp}>$ and $<N_{pf}^{comp}>$) while $<N_{p0Ar}^{comp}>$ and $<N_{pfAr}^{comp}>$ increase insignificantly (almost constant values). The decrease of $<N_{p0}^{comp}>$ and $<N_{pf}^{comp}>$ in figure 8.5.10 is not linear and large fluctuations of values are present between different series of discharges (especially for 0% of Ar). The non-linear character of the dependencies in figure 8.5.10 appears to be the outcome of the decrease in values of model parameters and following changes in the dynamics of discharge. The increase of $<N_{p0}^{comp}>$ and $<N_{pf}^{comp}>$ for 100% of Ar fraction is connected with different total initial gas pressure of mixture (1.2 mbar of Ar) as well as changes in the fitting parameters. Moreover, the $<N_{p0}^{comp}>$ and $<N_{pf}^{comp}>$ in figure 8.5.10 have still similar values during discharge (as for the theoretical discharges in figure 8.5.8).

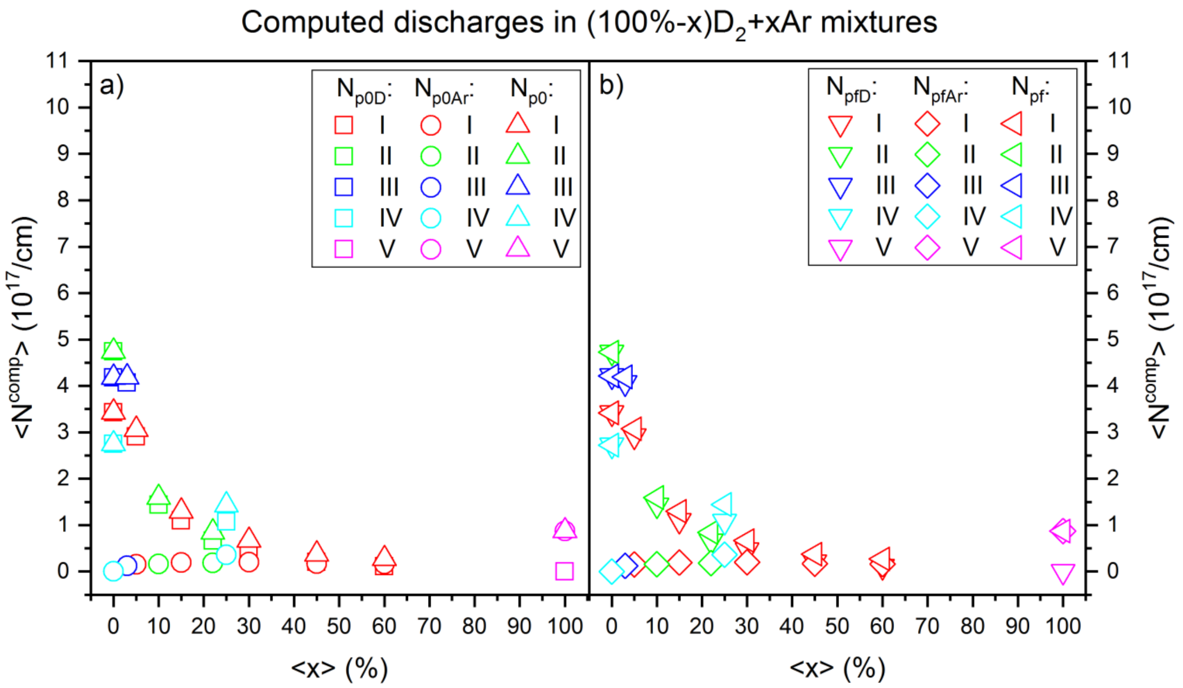

Figure 8.5.10. a) The average computed initial linear pinch density of D ($<N_{p0D}{}^{comp}>$), the average computed initial linear pinch density of Ar ($<N_{p0Ar}{}^{comp}>$) and the average computed total initial linear pinch density ($<N_{p0}{}^{comp}>$) versus Ar fraction ($<x>$) in (100%-x)D$_2$+xAr mixture. **b)** The average computed final linear pinch density of D ($<N_{pfD}{}^{comp}>$), the average computed final linear pinch density of Ar ($<N_{pfAr}{}^{comp}>$) and the average computed total final linear pinch density ($<N_{pf}{}^{comp}>$) versus Ar fraction ($<x>$) in (100%-x)D$_2$+xAr mixture. Roman numerals mark given series of discharges.

8.6. Plasma pinch parameters – temperatures

In this subsection, changes of the initial (maximum) pinch temperature (T_{p0}) and the minimum (final) pinch temperature (T_{pmin}) will be presented.

Theoretical discharges

The computed theoretical initial pinch temperature ($T_{p0}{}^{comp}$) and the computed theoretical minimum pinch temperature ($T_{pmin}{}^{comp}$) from the discharges in D$_2$, Ar and (100%-x)D$_2$+xAr mixtures are presented in: figure 8.6.1, figure 8.6.2 and figure 8.6.3, respectively.

The computed theoretical initial ($T_{p0}{}^{comp}$) and minimum ($T_{pmin}{}^{comp}$) plasma pinch temperatures decrease with initial D$_2$ pressure (figure 8.6.1). The main reason of this state is decrease of radial velocities of shock wave (see equation (6.2.30) and (6.2.31)) which behave similarly as piston/sheet velocities (figure 8.1.7) – shock heating decreasing with p_0. The corresponding $T_{pmin}{}^{comp}$ are always smaller than the $T_{p0}{}^{comp}$ – cooling of plasma column during pinch phase of discharge, mainly because of decrease of pinch plasma currents during pinch phase of discharge (equation (6.2.33)). The differences between the corresponding $T_{pmin}{}^{comp}$ and $T_{p0}{}^{comp}$ become smaller with the increase of initial D$_2$ pressure – the decrease of plasma temperature during pinch phase of discharge becomes slower. The highest and smallest difference between $T_{p0}{}^{comp}$ and $T_{pmin}{}^{comp}$ is equal to: 0.37 keV (at 0.5 mbar of D$_2$) and 0.08 keV (at 5.0 mbar of D$_2$), respectively. While the maximum ratio of T_{p0}^{comp} to T_{pmin}^{comp} is equal to about 1.2 – approximately 1.2 times decrease in plasma pinch temperature during pinch phase of discharge.

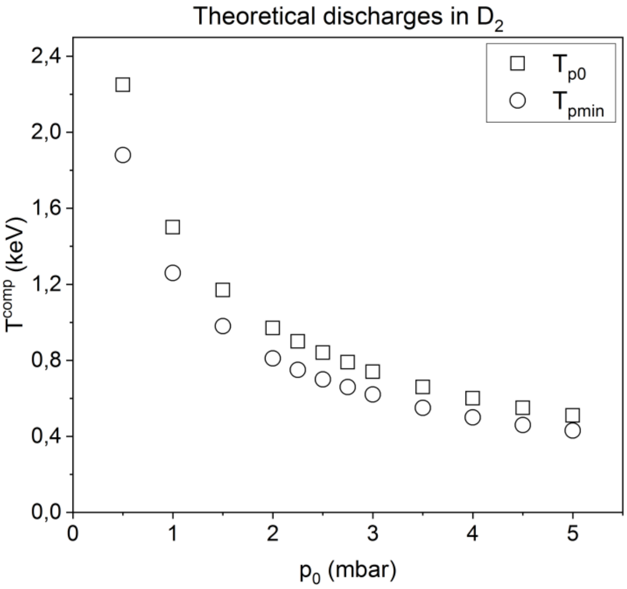

Figure 8.6.1. The computed theoretical initial (maximum) pinch temperature (T_{p0}^{comp}) and the computed theoretical minimum (final) pinch temperature (T_{pmin}^{comp}) versus initial D_2 pressure (p_0).

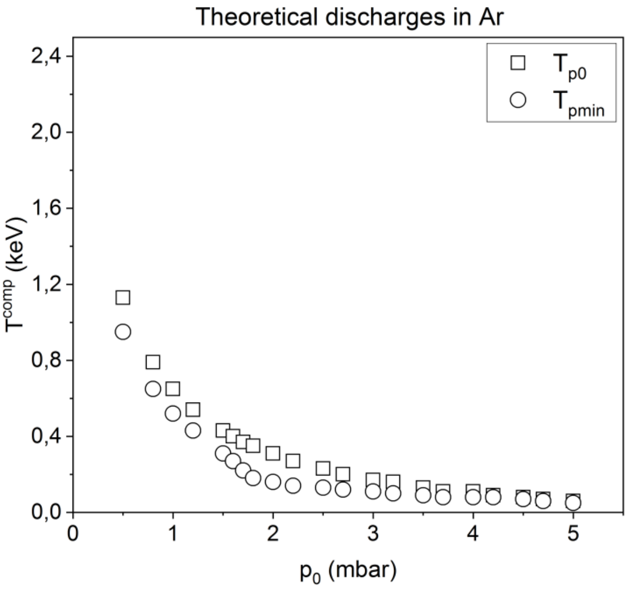

Figure 8.6.2. The computed theoretical initial (maximum) pinch temperature (T_{p0}^{comp}) and the computed theoretical minimum (final) pinch temperature (T_{pmin}^{comp}) versus initial Ar pressure (p_0).

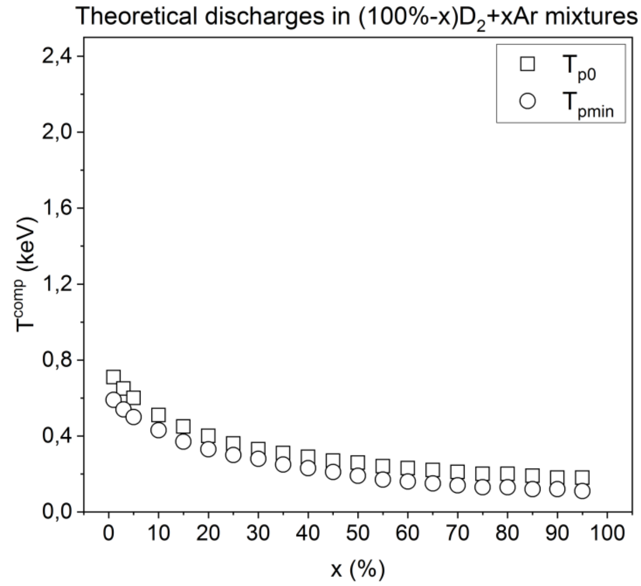

Figure 8.6.3. The computed theoretical initial (maximum) pinch temperature (T_{p0}^{comp}) and the computed theoretical minimum (final) pinch temperature (T_{pmin}^{comp}) versus Ar fraction (x) in (100%-x)D_2+xAr mixture.

The computed theoretical initial (T_{p0}^{comp}) and minimum (T_{pmin}^{comp}) plasma pinch temperatures decrease with initial Ar pressure (figure 8.6.2). The reasons are the same as for theoretical discharges in D_2 (figure 8.6.1) – similar behaviour. The T_{pmin}^{comp} values in figure 8.6.2 decrease fast up to 1.80 mbar of Ar and above 1.80 mbar of Ar the decrease is slower – at 1.8 mbar of Ar there is a bending point and character of T_{pmin}^{comp} decrease changes while the character of decrese of T_{p0}^{comp} is approximately unchanged. The corresponding T_{pmin}^{comp} are always smaller than the T_{p0}^{comp} – cooling of plasma column during pinch phase of discharge (decrease of currents flowing through plasma column during pinch phase of discharge). The differences between corresponding T_{p0}^{comp} and T_{pmin}^{comp} decrease with Ar fraction up to 1.2 mbar, above 1.2 mbar the differences increase up to 1.8 mbar and above 1.8 mbar again the differences decrease. The biggest absolute difference between corresponding T_{pmin}^{comp} and T_{p0}^{comp} is equal to 0.18 keV (at 0.5 mbar of Ar) and the smallest difference is equal to 0.01 keV (at 5.0 mbar of Ar) – smaller absolute changes than for theoretical discharges in D_2 (figure 8.6.1). The maximum relative decrease of temperature during pinch phase of discharge (ratio of T_{p0}^{comp} to T_{pmin}^{comp}) is equal to about 1.9 times (higher value than 1.2 time relative decrease for the theoretical discharges in D_2). Moreover, the T_{pmin}^{comp} and T_{p0}^{comp} in figure 8.6.2 are smaller than the corresponding values achived for the theoretical discharges in D_2 in figure 8.6.1 – axial and radial shock wave velocities are higher for theoretical discharges in D_2 for the same initial pressure values (similar as for piston velocities for theoretical discharges in Ar presented in figure 8.1.8 and in D_2 in figure 8.1.7).

The computed theoretical initial (T_{p0}^{comp}) and minimum (T_{pmin}^{comp}) plasma temperatures for discharges in $(100\%\text{-}x)D_2\text{+}x\text{Ar}$ mixutres (figure 8.6.3) decrease with Ar fraction (similar as for the theoretical discharges in D_2 and Ar – figure 8.6.1 and 8.6.2). No clearly seen bending point is located in the presented dependency of T_{pmin}^{comp} vs x in figure 8.6.3 unlike in the dependency for theoretical discharges in Ar in figure 8.6.2. Moreover, the absolute differences between corresponding T_{p0}^{comp} and T_{pmin}^{comp} decrease up to 30% of Ar fraction. And above 30% of Ar the differences slightly increase (almost constant difference). The biggest absolute difference between corresponding T_{p0}^{comp} and T_{pmin}^{comp} in figure 8.6.3 is equal to 0.12 keV (at 1% of Ar fraction) and the smallest difference is equal to 0.05 keV (at 30% of Ar fraction). The 0.12 keV is smaller value than the highest absolute decrease for the theoretical discharges in D_2 (figure 8.6.1) and in Ar (figure 8.6.2). And the 0.05 keV value is smaller than the smallest absolute change for the theoretical discharges in D_2 (figure 8.6.1) but also bigger than the smallest absolute change for the theoretical discharges in Ar (figure 8.6.2). On the other hand, the relative decrease (ratio of T_{p0}^{comp} to T_{pmin}^{comp}) in the plasma pinch temperature for the theoretical discharges in $(100\%\text{-}x)D_2\text{+}x\text{Ar}$ mixtures is about 1.6 times. The 1.6 times is higher value than for the theoretical discharges in D_2 but smaller than for the theoretical discharges in Ar. Moreover, the T_{p0}^{comp} and T_{pmin}^{comp} values are smaller than for theoretical discharges in Ar (figure 8.6.2) probably because of significant changes in the SHRs from the beginning of radial phases of discharge (shock nad piston velocities are similar for both theoretical discharges in Ar and $(100\%\text{-}x)D_2\text{+}x\text{Ar}$ mixtures).

Computed discharges in deuterium

Figure 8.6.4 presents the computed initial (maximum) pinch temperature (T_{p0}^{comp}) and the computed minimum (final) pinch temperature (T_{pmin}^{comp}) from the discharges in D_2.

The computed initial (T_{p0}^{comp}) and minimum (T_{pmin}^{comp}) plasma pinch temperatures relatively slowly decrease with initial D_2 pressure (figure 8.6.4). It is unclear whether the corresponding T_{p0}^{comp} and T_{pmin}^{comp} decrease with initial D_2 pressure similarly as for the theoretical discharges in D_2 (figure 8.6.1) – different character of dependency is possible (shock and piston velocities fluctuate). Moreover, the corresponding T_{pmin}^{comp} values are always smaller than the T_{p0}^{comp} – cooling of plasma column during pinch phase of discharge. The highest and smallest absolute difference between T_{p0}^{comp} and T_{pmin}^{comp}

is equal to: 0.07 keV and 0.03 keV, respectively. The 0.07 keV is achived at 2.25 mbar of D_2 and 0.03 keV is achived at 4.45 mbar and 4.71 mbar of D_2. The biggest relative decrease of plasma pinch temperature is equal to 1.2 times. The T_{pmin}^{comp} and T_{p0}^{comp} values in figure 8.6.4 are much smaller than the corresponding theoretical in D_2 in figure 8.6.1. The maximum absolute difference of 0.07 keV between corresponding T_{pmin}^{comp} and T_{p0}^{comp} is smaller than the theoretical one in figure 8.6.1 (0.37 keV). While the highest relative decrease of 1.2 times is at the similar level as for the theoretical discharges in D_2.

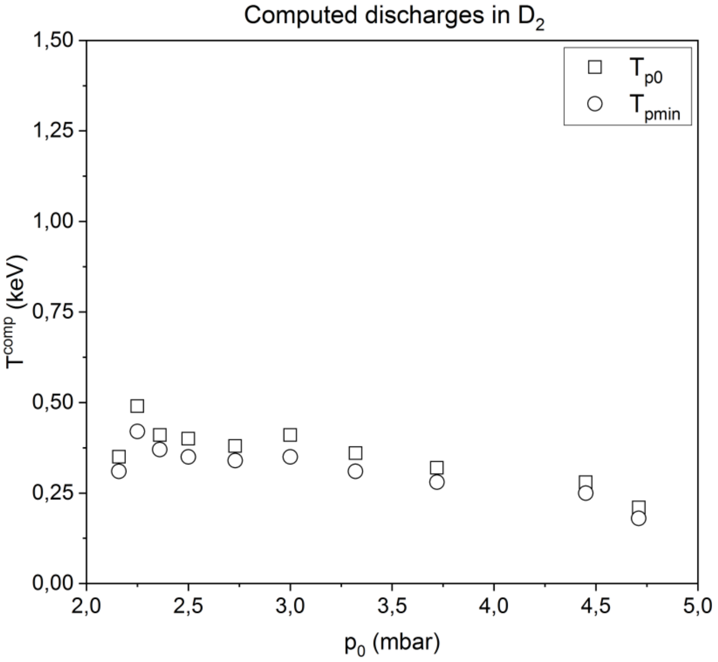

Figure 8.6.4. The computed initial (maximum) pinch temperature (T_{p0}^{comp}) and the computed minimum (final) pinch temperature (T_{pmin}^{comp}) versus initial D_2 pressure (p_0).

Computed discharges in deuterium-argon mixtures

Figure 8.6.5 presents the average computed initial pinch temperature ($<T_{p0}^{comp}>$) and the average computed minimum pinch temperature ($<T_{pmin}^{comp}>$) from the discharges in (100%-x)D_2+xAr mixtures under $<x>$ fraction of Ar.

Both average computed initial ($<T_{p0}^{comp}>$) and minimum ($<T_{pmin}^{comp}>$) pinch temperatures for discharges in (100%-x)D_2+xAr mixtures appear to decrease with Ar fraction (figure 8.6.5) following mainly changes of radial shock velocities and $<v_{rmax}^{comp}>$ (figure 8.1.11). Large fluctuations of values are present between and within series of discharges (especially for 0% of Ar fraction). The absolute differences between corresponding $<T_{p0}^{comp}>$ and $<T_{pmin}^{comp}>$ in figure 8.6.5 appear to decrease with Ar fraction. The biggest absolute difference between corresponding $<T_{p0}^{comp}>$ and $<T_{pmin}^{comp}>$ in figure 8.6.5 is equal to 0.13 keV and the smallest difference is equal to 0.01 keV – range of changes between corresponding $<T_{p0}^{comp}>$ and $<T_{pmin}^{comp}>$ is similar as for the theoretical discharges in figure 8.6.1 (3.0 mbar of D_2), 8.6.2 (1.2 mbar of Ar) and 8.6.3 (3-60% of Ar). The 0.13 keV value was achived for discharges in 0% of Ar fraction and the 0.01 keV value was achived for discharges in 22%, 60% and 100% of Ar fraction. On the other hand, the maximum ratio of $<T_{p0}^{comp}>$ to $<T_{pmin}^{comp}>$ is equal only to 1.1 times – this is smaller than the 1.4 times decrease anticipated theoretically for discharges in 0-60% of Ar and for discharge in 1.2 mbar of Ar. Moreover, the absolute range of changes of $<T_{p0}^{comp}>$ and $<T_{pmin}^{comp}>$ is wider than the theoretically anticipated in figure 8.6.1 (3.0 mbar of D_2), figure 8.6.2 (1.2 mbar of Ar) and figure 8.6.3 (3-60% of Ar). The highest and smallest $<T_{p0}^{comp}>$ is equal to: 1.04 keV (discharge in 0% of Ar) and 0.14 keV (discharges in 100% of Ar), respectivly. While the highest and smallest $<T_{pmin}^{comp}>$ value is equal to: 0.91 keV (discharges in 0% of Ar) and 0.13 keV (discharges in 100% of Ar), respectivly.

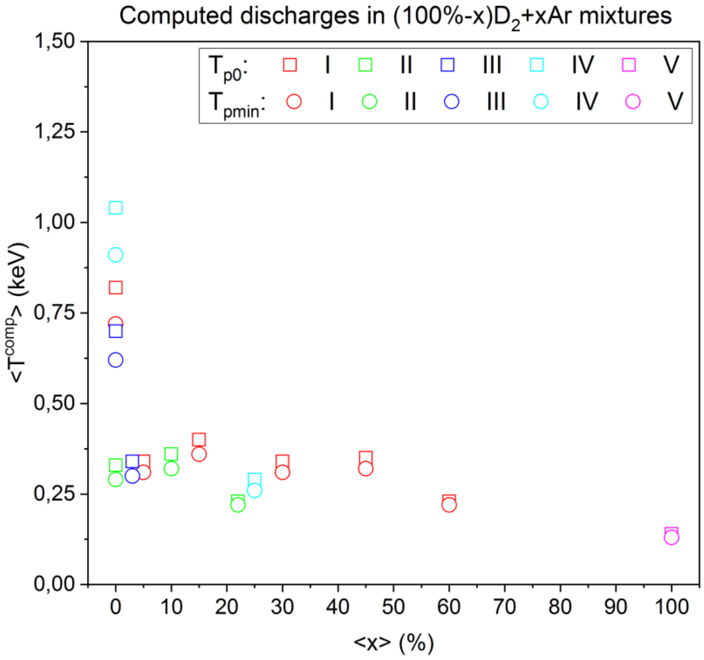

Figure 8.6.5. The average computed initial (maximum) pinch temperature ($<T_{p0}^{comp}>$) and the average computed minimum (final) pinch temperature ($<T_{pmin}^{comp}>$) versus Ar fraction ($<x>$) in $(100\%-x)D_2+x$Ar mixture. Roman numerals mark given series of discharges.

For the single computed discharges in $(100\%-x)D_2+x$Ar mixtures (figure 8.6.5) the range of changes of T_{p0}^{comp} - T_{pmin}^{comp} is equal to about: 0.01-0.24 keV. The 0.24 keV value is achived for discharges in 0% of Ar fraction and the 0.01 keV value (or smaller) is achived for selected discharges in 10%, 22%, 60% and 100% of Ar fraction. The maximum ratio of T_{p0}^{comp} to T_{pmin}^{comp} is equal to 1.2 times. The highest and smallest T_{p0}^{comp} is equal to: 2.03 keV (discharge in 0% of Ar) and 0.06 keV (discharges in 100% of Ar), respectively. While the highest and smallest T_{pmin}^{comp} is equal to: 1.76 keV (discharges in 0% of Ar) and 0.06 keV (discharges in 100% of Ar), respectively. For the 100% of Ar fraction T_{p0}^{comp} and T_{pmin}^{comp} values are in the range of: 0.06-0.64 keV and 0.06-0.56 keV, respectively. The 0.06 keV values correspond to the following discharges: #17101817, #17101818 and #17101820. And the 0.56 keV and 0.64 keV values corresponds to discharge #17102003. The biggest absolute difference between corresponding T_{p0}^{comp} and T_{pmin}^{comp} for 100% of Ar fraction is equal to 0.08 keV – discharge #17102003. While the smallest absolute difference (less than 0.01 keV) corresponds to the discharges: #17101814, #17101816, #17101817, #17101818, #17101820 and #17102002.

8.7. Radiation yields and ohmic heating yield

In this subsection, changes of the total ohmic heating yields (Y_{ohm}), the total (soft) X-ray bremsstrahlung yields (Y_{brem}), the total (soft) X-ray recombination yields (Y_{rec}), the total (soft) X-ray line yields (Y_{line}), the total (soft) X-ray yields (Y_{totrad}), the effective total (soft) X-ray yields (Y_{eff}) and the total (D-D fusion) neutron yields (Y_n) per discharge will be presented.

8.7.1. Radiation yields and ohmic heating yield – X-ray yields and ohmic heating yield

Theoretical discharges

The computed theoretical total ohmic heating yields (Y_{ohm}^{comp}), total X-ray bremsstrahlung yields (Y_{brem}^{comp}), total X-ray recombination yields (Y_{rec}^{comp}), total X-ray line yields (Y_{line}^{comp}), total X-ray yields (Y_{totrad}^{comp}) and effective total X-ray yields (Y_{eff}^{comp}) from the discharges in D_2, Ar and (100%-x)D_2+xAr mixtures are presented in: figure 8.7.1a, figure 8.7.2a and figure 8.7.3a, respectively. Additionaly, the percentages of: Y_{ohm}^{comp}, Y_{brem}^{comp}, Y_{rec}^{comp}, Y_{line}^{comp} and Y_{totrad}^{comp} in relation to the sum of all basic components (Y_{ohm}^{comp} + Y_{brem}^{comp} + Y_{rec}^{comp} + Y_{line}^{comp}) are presented in figures 8.7.1b, figure 8.7.2b and figure 8.7.3b.

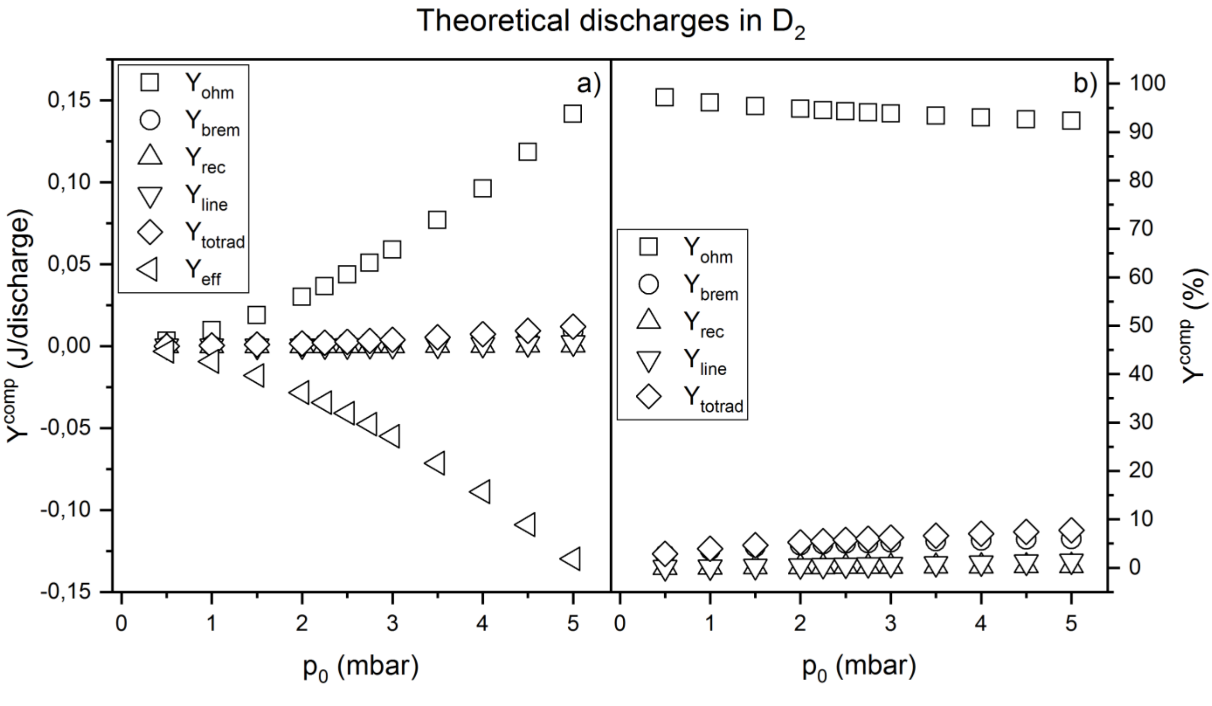

Figure 8.7.1. a) The computed theoretical total ohmic heating yield (Y_{ohm}^{comp}), total X-ray bremsstrahlung yield (Y_{brem}^{comp}), total X-ray recombination yield (Y_{rec}^{comp}), total X-ray line yield (Y_{line}^{comp}), total X-ray yield ($Y_{totrad}^{comp} = Y_{brem}^{comp} + Y_{rec}^{comp} + Y_{line}^{comp}$) and effective total X-ray yield ($Y_{eff}^{comp} = Y_{totrad}^{comp} - Y_{ohm}^{comp}$) versus initial D_2 pressure (p_0). **b)** Percentage of Y_{ohm}^{comp}, Y_{brem}^{comp}, Y_{rec}^{comp}, Y_{line}^{comp} and Y_{totrad}^{comp} in reference to $Y_{ohm}^{comp} + Y_{brem}^{comp} + Y_{rec}^{comp} + Y_{line}^{comp}$ sum versus initial D_2 pressure (p_0).

The dependencies of Y_{ohm}^{comp}, Y_{brem}^{comp}, Y_{rec}^{comp} and Y_{line}^{comp} versus initial D_2 pressure in figure 8.7.1a have continuously increasing character. The slowest increase is found for Y_{rec}^{comp} values, then for Y_{line}^{comp} values, then for Y_{brem}^{comp} values and then for Y_{ohm}^{comp} values. All achived Y_{brem}^{comp}, Y_{rec}^{comp} and Y_{line}^{comp} values are significantly smaller than the corresponding Y_{ohm}^{comp} values. This results in Y_{totrad}^{comp} values far smaller than the corresponding Y_{ohm}^{comp} values ($Y_{totrad}^{comp} = Y_{brem}^{comp} + Y_{rec}^{comp} + Y_{line}^{comp}$). And this leads to continuous decrease of Y_{eff}^{comp} values ($Y_{eff}^{comp} = Y_{totrad}^{comp} - Y_{ohm}^{comp}$) with initial D_2 pressure, reproducuing reverse character in comparison to the Y_{ohm}^{comp} values ($Y_{eff}^{comp} = -Q$ from equation 6.2.11 – slower plasma pinch compression). Moreover, the achieved Y_{line}^{comp} values (figure 8.7.1a) are relatively small and insignificant in comparison to theoretical discharges in Ar (figure 8.7.2a) and theoretical discharges in (100%-x)D_2+xAr mixtures (figure 8.7.3a) – maximally only about 0.002 J/discharge was achived at 5.0 mbar of initial D_2 pressure. Thus, the absolute Y_{line}^{comp} values are stated as too small (about 0.14 J/discharge is achived at 5.0 mbar) to alter the behaviour of plasma pinch compression significantly during pinch phase of discharge (this applies also to total bremsstrahlung and recombination yields). This is also confirmed with calculated percentages of Y_{ohm}^{comp}, Y_{brem}^{comp}, Y_{rec}^{comp}, Y_{line}^{comp} and Y_{totrad}^{comp} values. The percentrages of Y_{brem}^{comp}, Y_{rec}^{comp}, Y_{line}^{comp} and Y_{totrad}^{comp} values slowly increase with initial D_2 pressure achiving about 7.7% for the Y_{totrad}^{comp} at 5.0 mbar while the percentages of Y_{ohm}^{comp} slowly decrease with initial D_2 pressure achiving about 92.3% at 5.0 mbar. Moreover, the above presented results of simulations may suggest that if the pressure is to be increased above 5.0 mbar Y_{line}^{comp} and Y_{totrad}^{comp} would increase further achiving very large values at some point and enabling plasma radiative compression phenomenon occurrence during discharges in pure D_2. Unfortunately, this is not true. Theoretical simulations for higher pressures show that at some point plasma opacity becomes significant for discharges in D_2 and the P-B currents values and reduced P-B current values are largely increased, times of radiative compression duration are still equal to 0 and characteristic times of radiation depletion are always negative. Also, the PF discharges for far higher initial D_2 pressures than optimum will result in short-ciruit like discharges and lack of plasma pinching.

The dependencies of Y_{ohm}^{comp}, Y_{brem}^{comp}, Y_{rec}^{comp} and Y_{line}^{comp} versus initial Ar pressure show maxima (figure 8.7.2a). The lowest values are achived for Y_{brem}^{comp} parameter – maximum at 1.70 mbar of Ar equal to 4.3 J/discharge. The higher corresponding values than for Y_{brem}^{comp} parameter are achived for Y_{rec}^{comp} parameter – maximum also at 1.70 mbar of Ar equal to 109 J/discharge. The higher corresponding values than for Y_{brem}^{comp} and Y_{rec}^{comp} parameters are achived for Y_{ohm}^{comp} parameter – maximum at 2.50 mbar of Ar equal to 322 J/discharge. And the higher values than for Y_{brem}^{comp}, Y_{rec}^{comp} and Y_{ohm}^{comp} parameters are achived for Y_{line}^{comp} parameter – maximum at 2.20 mbar of Ar equal to 1702 J/discharge. The described situation results in significantly higher Y_{totrad}^{comp} values than corresponding Y_{ohm}^{comp} for all investigated theoretical discharges in Ar (Y_{totrad}^{comp} = 1752 J/discharge at 2.20 mbar of Ar – highest value). While the highest contribiution to Y_{totrad}^{comp} values always comes from Y_{line}^{comp} values (see figure 8.7.2). The smallest percentage of Y_{line}^{comp} equal to about 68% is stated at 0.50 mbar of Ar while the highest percentage equal to about 90% is stated at 1.80 mbar of Ar (see figure 8.7.2b) and the corresponding percentage Y_{ohm}^{comp} for 0.50 mbar and 1.80 mbar is equal to about: 11% and 4%, respectively. The resultant Y_{eff}^{comp} vs p_0 dependency has maximum at 2.00 mbar of Ar equal to 1535 J/discharge (Q from equation (6.2.11) is the smallest – fastest pinch compression) and follows approximately changes of Y_{line}^{comp} vs p_0 and Y_{totrad}^{comp} vs p_0 (biggest influence). The ratios of Y_{ohm}^{comp}, Y_{brem}^{comp}, Y_{rec}^{comp}, Y_{line}^{comp} and Y_{totrad}^{comp} to $Y_{ohm}^{comp} + Y_{brem}^{comp} + Y_{rec}^{comp} + Y_{line}^{comp}$ sum (percentage dependencies of parameters) are not constant with initial Ar pressure (figure 8.7.2b). More precisely, the percentage of Y_{line}^{comp} increase up to 1.80 mbar of Ar (about 90% at 1.80 mbar) and percentage of Y_{totrad}^{comp} increase up to 1.70 mbar of Ar (about 98% at 1.70 mbar), wherein at 0.50 mbar smallest percentage $Y_{line}^{comp} \approx 68\%$ is stated. Above 1.70-1.80 mbar of Ar Y_{line}^{comp} and Y_{totrad}^{comp} decrease up to about 2.70 mbar, wherein at 2.0 mbar Y_{line}^{comp} is about 87% and Y_{totrad}^{comp} is about 90%. Above 2.70 mbar of Ar percentages of Y_{line}^{comp} and Y_{totrad}^{comp} increase up to 4.20 mbar of Ar and then again decrease up to 5.00 mbar (relatively small changes), wherein at 2.70 mbar of initial Ar pressure smallest percentage equal to about 83% is stated for Y_{totrad}^{comp}. On the other hand, the percentage Y_{ohm}^{comp} values continuously decrease in 0.50-1.70 mbar range, wherein the smallest Y_{ohm}^{comp} is equal to 2% at 1.70 mbar. Above 1.70 mbar the percentage Y_{ohm}^{comp} values increase up to 3.0 mbar ($Y_{ohm}^{comp} \approx 17\%$). Above 3.00 mbar the percentage Y_{ohm}^{comp} values again decrease (relatively small change) up to 4.20 mbar ($Y_{ohm}^{comp} \approx 16\%$) and above 4.20 mbar the percentage Y_{ohm}^{comp} values again increase (also relatively small change) up to 5.00 mbar ($Y_{ohm}^{comp} \approx 19\%$). Finally, the percentages of Y_{rec}^{comp} and Y_{brem}^{comp} decrease in entire 0.50-.500 mbar range ($Y_{rec}^{comp} \approx 18.9\text{-}0.3\%$ and $Y_{brem}^{comp} \approx 2.41\text{-}0.01\%$), wherein Y_{rec}^{comp} and Y_{brem}^{comp} decrease relatively fast up to about 2.00 mbar of Ar ($Y_{rec}^{comp} \approx 3\%$ and $Y_{brem}^{comp} \approx 0.1\%$) and above 2.00 mbar slower decrease is stated.

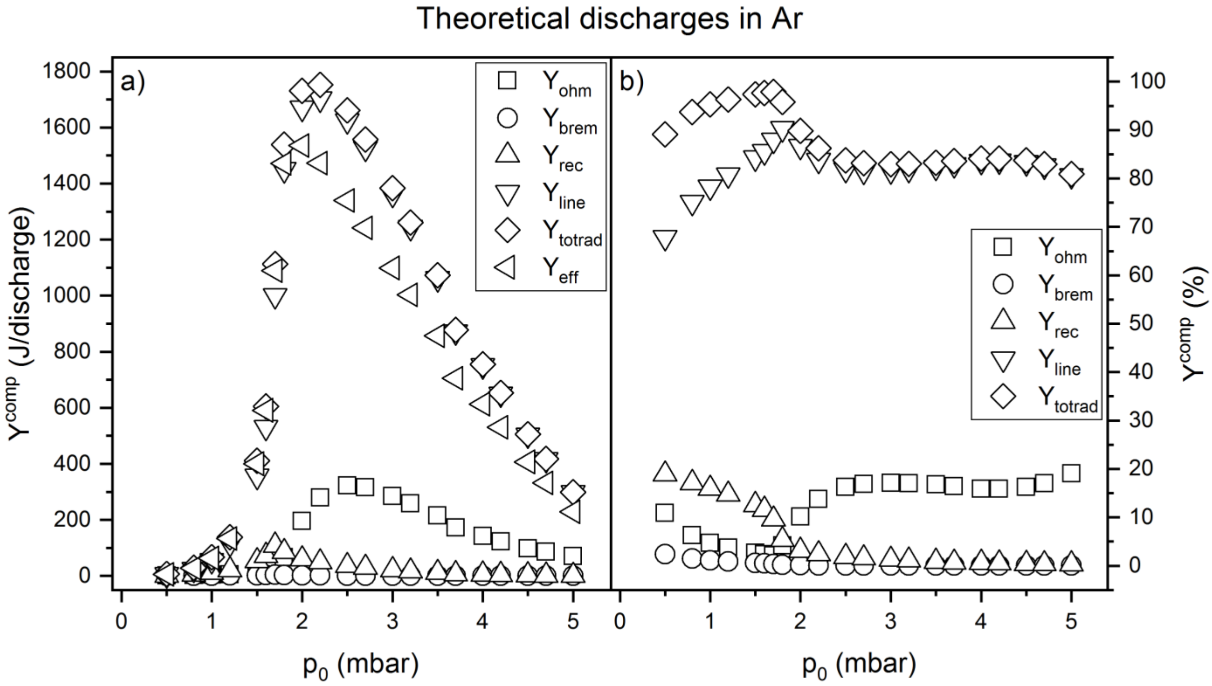

Figure 8.7.2. a) The computed theoretical total ohmic heating yield (Y_{ohm}^{comp}), total X-ray bremsstrahlung yield (Y_{brem}^{comp}), total X-ray recombination yield (Y_{rec}^{comp}), total X-ray line yield (Y_{line}^{comp}), total X-ray yield ($Y_{totrad}^{comp} = Y_{brem}^{comp} + Y_{rec}^{comp} + Y_{line}^{comp}$) and effective total X-ray yield ($Y_{eff}^{comp} = Y_{totrad}^{comp} - Y_{ohm}^{comp}$) versus initial Ar pressure (p_0). **b)** percentage of Y_{ohm}^{comp}, Y_{brem}^{comp}, Y_{rec}^{comp}, Y_{line}^{comp} and Y_{totrad}^{comp} in reference to $Y_{ohm}^{comp} + Y_{brem}^{comp} + Y_{rec}^{comp} + Y_{line}^{comp}$ sum versus initial Ar pressure (p_0).

The values presented in above paragraph show that the highest influence on the effective total X-ray radiation emission (Y_{eff}^{comp}) during theoretical discharges in Ar (figure 8.7.2) always comes from the total X-ray line emission (Y_{line}^{comp}). The secondary influence comes from the total X-ray recombination emission (Y_{rec}^{comp}) in 0.50-1.80 mbar range and from the total ohmic heating (Y_{ohm}^{comp}) in 2.00-5.00 mbar range (figure 8.7.2). The Y_{line}^{comp} up to 1.0-1.6 mbar of Ar do not exceed the 116-530 J/discharge value – this explains why the computed theoretical minimum radiuses (figure 8.4.2) and the computed theoretical maximum densities (figure 8.5.2) do not change significantly below 1.0-1.6 mbar despite the fact of achievement of the small computed theoretical reduced P-B currents in comparison to the computed theoretical pinch currents (figure 8.3.7) and the small computed theoretical characteristic times of radiation depletion in comparison to computed theoretical pinch lifetimes (figure 8.3.7) as well as the computed theoretical radiative compression lifetimes as long as computed theoretical pinch lifetimes (figure 8.3.7) – apparently the absolute Y_{line}^{comp} values were too low to alter significantly plasma compression. The decrease of Y_{line}^{comp} values above 2.2 mbar of Ar is caused by plasma opacity effect and change from volumetric to surface emission. The presented depency of Y_{line}^{comp} vs p_0 in figure 8.7.2 is to be the main cause of the occuring changes in the plasma compression during pinch phase of discharges – other computed parameters tend to follow mainly Y_{line}^{comp} versus p_0 also showing maximums or minimums (U_{max}^{comp} vs p_0 – figure 8.2.7, r_{pmin}^{comp} vs p_0 – figure 8.4.2, z_{pmax}^{comp} vs p_0 – figure 8.4.7, V_{pf}^{comp} vs p_0 – figure 8.4.12 and n_{pmax}^{comp} vs p_0 – figure 8.5.2). Moreover, this dependency is completely different than the one presented for theoretical discharges in D_2 (figure 8.7.1), where the highest value of total yield of X-ray line radiation is equal to about 0.002 J/discharge (851000 times smaller value than the 1702 J/discharge) and no possibility of radiative compression was stated mainly due to too low atomic Z number of D_2 (see equation (2.1.19)).

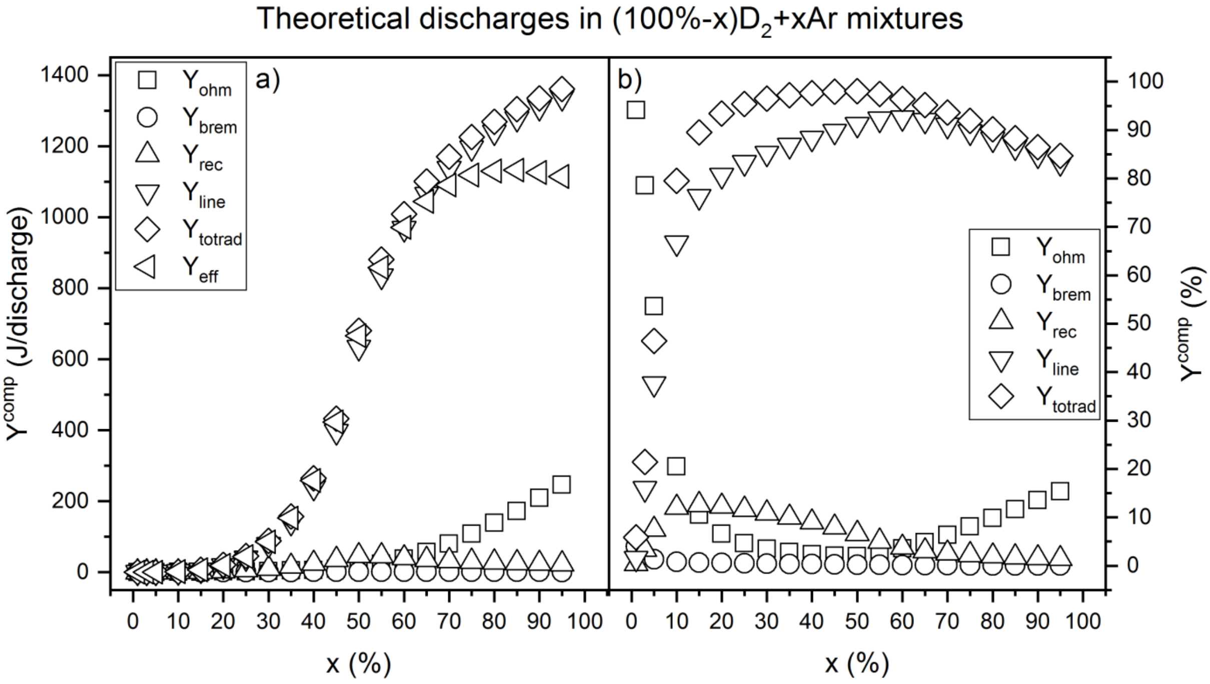

Figure 8.7.3. a) The computed theoretical total ohmic heating yield (Y_{ohm}^{comp}), total X-ray bremsstrahlung yield (Y_{brem}^{comp}), total X-ray recombination yield (Y_{rec}^{comp}), total X-ray line yield (Y_{line}^{comp}), total X-ray yield ($Y_{totrad}^{comp} = Y_{brem}^{comp} + Y_{rec}^{comp} + Y_{line}^{comp}$) and effective total X-ray yield ($Y_{eff}^{comp} = Y_{totrad}^{comp} - Y_{ohm}^{comp}$) versus Ar fraction ($x$) in (100%-$x$)$D_2$+$x$Ar mixture. **b)** percentage of Y_{ohm}^{comp}, Y_{brem}^{comp}, Y_{rec}^{comp}, Y_{line}^{comp} and Y_{totrad}^{comp} in reference to $Y_{ohm}^{comp} + Y_{brem}^{comp} + Y_{rec}^{comp} + Y_{line}^{comp}$ sum versus Ar fraction (x) in (100%-x)D_2+xAr mixture.

The presented dependencies in figure 8.7.2a can be in general explained using equation: (2.1.19), (2.1.20), (2.1.21), (2.1.22) and (6.2.37). When initial Ar pressure is increased initial pinch ion number densities (n_{p0}^{comp} – see figure 8.5.2) increase and initial pinch ion temperatures decrease (T_{p0}^{comp} – see figure 8.6.2) this can lead to increase in Y_{line}^{comp} and Y_{rec}^{comp}. Increase in Y_{brem}^{comp} values is stated when increase in n_{p0}^{comp} has higher influence than decrease in T_{p0}^{comp}. And the possible increase in Z_{eff}^{comp} can also lead to increase in Y_{line}^{comp}, Y_{rec}^{comp} and Y_{brem}^{comp} values. For initial Ar pressures approaching to 2.0 mbar increase in Y_{line}^{comp} is high enough to cause significant decrease in minimum plasma pinch radius (r_{pmin}^{comp} – see figure 8.4.2) leading to significant increase in the maximum pinch length (z_{pmax}^{comp} – see figure 8.4.7) and in maximum pinch ion number densities (n_{pmax}^{comp} – see figure 8.5.2). And increase in n_{pmax}^{comp} and z_{pmax}^{comp} can lead to further increase in Y_{line}^{comp}, Y_{rec}^{comp} and Y_{brem}^{comp} during pinch phase of discharge – feedback type of relation. Also, when pinch ion temperature is decreased, pinch radius is decreased, pinch length is increased and/or effective charge of plasma is increased this can lead to increase in Y_{ohm}^{comp} values. Above about 2.0 mbar of initial Ar pressure plasma opacity effect takes places and becomes stronger with further increase of initial Ar pressure. The appearance of strong opacity effect is connected with transformation of equation (2.1.19) describing emission power of X-ray line radiation to equation (6.2.37). The equation (6.2.37) is strongly dependent on plasma ion temperature – decrease of T_p^{comp} values leads to decrease of Y_{line}^{comp} values and increase in atomic number and effective charge results in smaller increase in Y_{line}^{comp} values. So, Y_{line}^{comp} values can be significantly decreased above 2.0 mbar of initial Ar pressure. And significant decrease in Y_{line}^{comp} leads to smaller z_{pmax}^{comp} and n_{pmax}^{comp} values which can also further decrease Y_{line}^{comp}, Y_{rec}^{comp} and Y_{brem}^{comp} values. Moreover, the increase in pinch radiuses and decrease in pinch lengths and effective plasma charges can also lead to decrease in Y_{ohm}^{comp} values (equation (2.1.22)). And for higher initial pressures than 1.20 mbar currents flowing through plasma pinch (I_{pp}^{comp} – see figure 8.2.2) decrease which may also lead to decrease of Y_{ohm}^{comp} values for higher initial Ar pressures.

The computed theoretical Y_{ohm}^{comp}, Y_{line}^{comp} and Y_{totrad}^{comp} for discharges in (100%-x)D_2+xAr mixtures increase continuously with Ar fraction while the Y_{brem}^{comp}, Y_{rec}^{comp} and Y_{eff}^{comp} show maxima, wherein the Y_{brem}^{comp} and Y_{rec}^{comp} show maxima at 50% of Ar and Y_{eff}^{comp} shows maximum at 85% of Ar (see figure 8.7.3a). The Y_{ohm}^{comp} values increase from 0.08 J/discharge at 1% of Ar to 246 J/discharge at 95% of Ar. For the discharges in Ar fractions up to 5% Y_{ohm}^{comp} values are higher than Y_{totrad}^{comp} values (figure 8.7.3b). Starting from about 10% of Ar Y_{totrad}^{comp} values exceed Y_{ohm}^{comp} values. This happens mainly because of significant increase in Y_{line}^{comp} with Ar fraction due to higher Z and Z_{eff} number (see equation (2.1.19)). The characters of increase of Y_{line}^{comp} and Y_{totrad}^{comp} change with Ar fraction. Up to about 30% of Ar the increase is relatively slow and Y_{line}^{comp} values do not exceed 100 J/discharge. At 50% of Ar fraction bending point is present (the increase starts to slows down due to plasma opacity) and Y_{line}^{comp} of 633 J/discharge is achived. At 85% of Ar the increase of Y_{line}^{comp} values further slows down (Y_{line}^{comp} = 1305 J/discharge at 85% of Ar). And at 95% highest Y_{line}^{comp} is achived – 1337 J/discharge. The Y_{totrad}^{comp} values almost exactly follow Y_{line}^{comp} values. The Y_{eff}^{comp} values also follow changes of Y_{line}^{comp} but only up to about 65% of Ar fraction. Starting from 65% of Ar fraction the Y_{line}^{comp} increase faster and Y_{eff}^{comp} increase slower. At 85% of Ar fraction maximum of Y_{eff}^{comp} = 1132 J/discharge is achived while Y_{line}^{comp} further increase. This discrepancy between Y_{line}^{comp} and Y_{eff}^{comp} for higher fractions is caused by increase in Y_{ohm}^{comp} – above 60% of Ar fraction percentage of Y_{ohm}^{comp} increases while percentages of Y_{line}^{comp} and Y_{totrad}^{comp} decrease (figure 8.7.3b). In general, percentages of Y_{ohm}^{comp} decrease from 94% at 1% of Ar down to 2% at 50% of Ar and then increase up to 15% at 95% of Ar. On the other hand, percentage Y_{line}^{comp} increase from 2% at 1% of Ar up to 93% at 60% of Ar and then decrease down to 83% at 95% of Ar. And percentage Y_{totrad}^{comp} increase from 6% at 1% of Ar up to 98% at 50% of Ar and then decrease down to 85% at 95% of Ar. Moreover, the Y_{brem}^{comp} values are always the smallest – maximum value at 50% of Ar equals 1.6 J/discharge. The Y_{rec}^{comp} values follow changes of Y_{brem}^{comp} but achived Y_{rec}^{comp} values are higher than Y_{brem}^{comp} – maximum value of Y_{rec}^{comp} at 50% of Ar equals 46 J/discharge. The Y_{rec}^{comp} values are higher than Y_{ohm}^{comp} values in 15-60% range of Ar fractions. The percenge Y_{brem}^{comp} continuously decrease with Ar fraction from 4% at 1%

of Ar down to 0.05% at 95% of Ar. And percenge Y_{rec}^{comp} first increase from 0.4% at 1% of Ar up to 13% at 15% of Ar and then decrease down to 1% at 95% of Ar.

The presented changes of Y_{line}^{comp} in figure 8.7.3 are completely different from the theoretical in D_2 (figure 8.7.1) and also different from theoretical in Ar (figure 8.7.2) – characteristic shape is again obtained this time for theoretical discharges in (100%-x)D_2+xAr mixtures. Changes of other parameters describing plasma pinch behaviour presented in: figure 8.2.8 (U_{max}^{comp} vs x), figure 8.4.3 (r_{pmin}^{comp} vs x), figure 8.4.8 (z_{pmax}^{comp} vs x), figure 8.4.13 (V_{pf}^{comp} vs x) and figure 8.5.3 (n_{pmax}^{comp} vs x) tend to follow this characteristic shape in similar or reversed way. For example the dependency of computed theoretical maximum plasma density versus Ar fraction (figure 8.5.3) has similar shape as the one presented in figure 8.7.3 – maximum stated at 2.0 mbar. And the dependency of the computed theoretical minimum plasma pinch radius versus Ar fraction (figure 8.4.3) also follows mainly the behavior of the total yield of X-ray line radiation but in reversed way – minimum stated at 2.0 mbar. In other words, the changes of the maximum pinch density and minimum pinch radius can be explained on the basis of changes of the total X-ray line radiation (similar as for theoretical discharges in Ar).

The presented dependencies in figure 8.7.3a for theoretical discharges in (100%-x)D_2+xAr mixtures can also be in general explained similarly as for theoretical discharges in Ar using equation: (2.1.19), (2.1.20), (2.1.21), (2.1.22) and (6.2.37), wherein this time the main cause of increase of Y_{line}^{comp} and Y_{totrad}^{comp} values is increase in total atomic number Z and total effective atomic charge number Z_{eff} which continuously increase with Ar fraction. Except the increase of Z and Z_{eff} other changes of plasma parameters which can lead to increase of Y_{line}^{comp} values are: decrease of T_p, increase of n_p and increase of z_p (for low plasma opacity state).

Computed discharges in deuterium

Figure 8.7.4a presents the computed total ohmic heating yields (Y_{ohm}^{comp}), total X-ray bremsstrahlung yields (Y_{brem}^{comp}), total X-ray recombination yields (Y_{rec}^{comp}), total X-ray line yields (Y_{line}^{comp}), total X-ray yields (Y_{totrad}^{comp}) and effective total X-ray yields (Y_{eff}^{comp}) from the discharges in D_2. Additionaly, the percentages of: Y_{ohm}^{comp}, Y_{brem}^{comp}, Y_{rec}^{comp}, Y_{line}^{comp} and Y_{totrad}^{comp} in relation to the sum of all basic components ($Y_{ohm}^{comp} + Y_{brem}^{comp} + Y_{rec}^{comp} + Y_{line}^{comp}$) are presented in figures 8.7.4b.

The presented computed dependencies of Y_{ohm}^{comp}, Y_{brem}^{comp}, Y_{rec}^{comp}, Y_{line}^{comp}, Y_{totrad}^{comp} and Y_{eff}^{comp} versus initial D_2 pressure (figure 8.7.4) have similar characters to the theoretical ones in figure 8.7.1, wherein fluctuations of values are present and higher values were in general obtained than for the theoretical parameters. The hghest computed Y_{ohm}^{comp}, Y_{brem}^{comp}, Y_{line}^{comp}, Y_{rec}^{comp} and Y_{totrad}^{comp} value achived at about 4.71 mbar of D_2 is equal to about: 0.9 J/discharge, 0.03 J/discharge, 0.03 J/discharge, 0.006 J/discharge and 0.07 J/discharge, respectively. The percentage of Y_{ohm}^{comp} values are always higher than 90% and percentage of Y_{totrad}^{comp} values are not bigger than about 8% (8% if achived for discharge in about 4.5 mbar of D_2). Again the highest contribution to Y_{totrad}^{comp} comes from the Y_{brem}^{comp} and the Y_{totrad}^{comp} values are still lower than the corresponding Y_{ohm}^{comp} values. This situation results in always negative Y_{eff}^{comp} values – no significant alteration of plasma pinch compression due to radiation emission is to be possible during pinch lifetime.

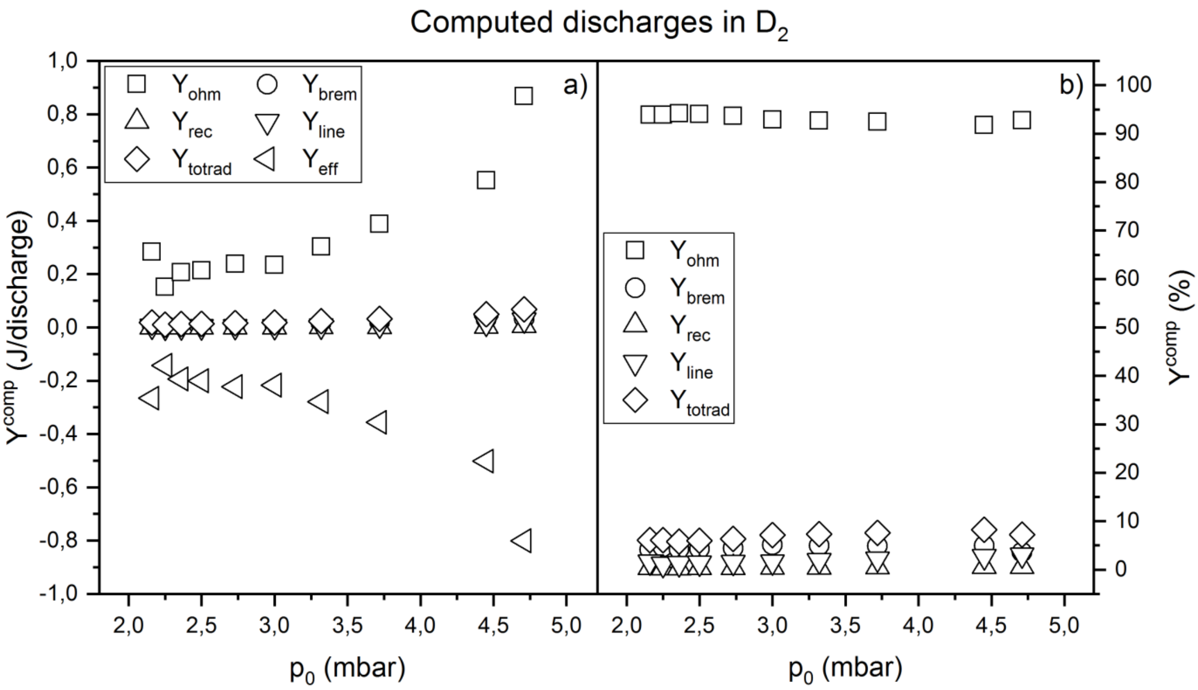

Figure 8.7.4. a) The computed total ohmic heating yield (Y_{ohm}^{comp}), total X-ray bremsstrahlung yield (Y_{brem}^{comp}), total X-ray recombination yield (Y_{rec}^{comp}), total X-ray line yield (Y_{line}^{comp}), total X-ray yield ($Y_{totrad}^{comp} = Y_{brem}^{comp} + Y_{rec}^{comp} + Y_{line}^{comp}$) and effective total X-ray yield ($Y_{eff}^{comp} = Y_{totrad}^{comp} - Y_{ohm}^{comp}$) versus initial D_2 pressure (p_0). **b)** percentage of Y_{ohm}^{comp}, Y_{brem}^{comp}, Y_{rec}^{comp}, Y_{line}^{comp} and Y_{totrad}^{comp} in reference to $Y_{ohm}^{comp} + Y_{brem}^{comp} + Y_{rec}^{comp} + Y_{line}^{comp}$ sum versus initial D_2 pressure (p_0).

Computed discharges in deuterium-argon mixtures

Figure 8.7.5a presents the average computed total ohmic heating yields ($<Y_{ohm}^{comp}>$), total X-ray bremsstrahlung yields ($<Y_{brem}^{comp}>$), total X-ray recombination yields ($<Y_{rec}^{comp}>$), total X-ray line yields ($<Y_{line}^{comp}>$), total X-ray yields ($<Y_{totrad}^{comp}>$) and effective total X-ray yields ($<Y_{eff}^{comp}>$) from the discharges in $(100\%\text{-}x)D_2+x\text{Ar}$ mixtures. Additionaly, the percentages of: $<Y_{ohm}^{comp}>$, $<Y_{brem}^{comp}>$, $<Y_{rec}^{comp}>$, $<Y_{line}^{comp}>$ and $<Y_{totrad}^{comp}>$ in relation to the sum of all basic components ($<Y_{ohm}^{comp}> + <Y_{brem}^{comp}> + <Y_{rec}^{comp}> + <Y_{line}^{comp}>$) are presented in figures 8.7.5b.

The $<Y_{ohm}^{comp}>$ values increase with Ar fraction, wherein up to 60% of Ar the $<Y_{ohm}^{comp}>$ values do not exceed 3 J/discharge while for 100% of Ar $<Y_{ohm}^{comp}>$ = 89 J/discharge. The percentage $<Y_{ohm}^{comp}>$ decrease with Ar fraction from 94-95 % level (all series) at 0% of Ar down to 8% at 25% of Ar. Above 25% some small increase of $<Y_{ohm}^{comp}>$ can be stated up to 16% at 45% of Ar and then again decrease down to 11% at 60% of Ar. At 100% of $<Y_{ohm}^{comp}>$ value is again significantly higher and equal to 32%. The $<Y_{line}^{comp}>$ and $<Y_{totrad}^{comp}>$ values increase with Ar fraction achiving at 60% of Ar: 19 J/discharge and 21 J/discharge, respectively. At 100% of Ar fraction $<Y_{line}^{comp}>$ = 181 J/discharge and $<Y_{totrad}^{comp}>$ = 183 J/discharge. The percentages of $<Y_{line}^{comp}>$ and $<Y_{totrad}^{comp}>$ values in general present revesersed situation as percentages of $<Y_{ohm}^{comp}>$ – increase up to 25% where $<Y_{line}^{comp}>$ = 82% and $<Y_{totrad}^{comp}>$ = 92%, then decrease of $<Y_{line}^{comp}>$ down to 74% and $<Y_{totrad}^{comp}>$ down to 84% at 45% of Ar, then increase up to $<Y_{line}^{comp}>$ = 82% and $<Y_{totrad}^{comp}>$ = 89% at 60% of Ar and then at 100% decrease down to $<Y_{line}^{comp}>$ = 66% and $<Y_{totrad}^{comp}>$ = 68%. The $<Y_{brem}^{comp}>$ and $<Y_{rec}^{comp}>$ values are always the smallest except for discharges in 0% and 25% of Ar fractions. For 0% of Ar fraction $<Y_{brem}^{comp}>$

values are higher than corresponding $<Y_{line}^{comp}>$ and $<Y_{rec}^{comp}>$, wherein $<Y_{rec}^{comp}>$ is smaller than $<Y_{line}^{comp}>$. And for 25% of Ar fraction $<Y_{rec}^{comp}>$ is a little bit higher than the corresponding $<Y_{ohm}^{comp}>$ value. The $<Y_{brem}^{comp}> = 0.09$ J/discharge and $<Y_{rec}^{comp}> = 2.2$ J/discharge achived at 25% of Ar fraction are the highest values except for 100% of Ar fraction. For 100% of Ar fraction $<Y_{brem}^{comp}> = 0.11$ J/discharge and $<Y_{rec}^{comp}> = 2.3$ J/discharge. Similarly, percentage of $<Y_{brem}^{comp}>$ and $<Y_{rec}^{comp}>$ values are always the smallest except for discharges in 25% of Ar. For 25% of Ar fraction percentage of $<Y_{rec}^{comp}> = 9\%$ is higher than the corresponding $<Y_{ohm}^{comp}>$, although the highest percentage $<Y_{rec}^{comp}> = 10\%$ is stated at 30% of Ar. Also, percentage of $<Y_{brem}^{comp}>$ is always smaller than percentage of $<Y_{rec}^{comp}>$ except for 0% of Ar fraction – for 0% of Ar $<Y_{brem}^{comp}> = 3\text{-}5\%$ (the highest values). The above described relations result in $<Y_{eff}^{comp}>$ following mainly changes of $<Y_{line}^{comp}>$ and $<Y_{totrad}^{comp}>$ except for discharges in 100% of Ar fraction (figure 8.7.5a). For 100% of Ar fraction $<Y_{eff}^{comp}>$ value is far smaller than the corresponding $<Y_{line}^{comp}>$ and $<Y_{totrad}^{comp}>$. This is the result of significant increase in $<Y_{ohm}^{comp}>$ for 100% of Ar. Nevertheless, for 100% of Ar percentage $<Y_{line}^{comp}>$ and $<Y_{totrad}^{comp}>$ are equal to: 66% and 68%, respectively, while corresponding $<Y_{ohm}^{comp}> = 32\%$ only. Moreover, at 10% of Ar fraction $<Y_{line}^{comp}>$ and $<Y_{totrad}^{comp}>$ values exceed corresponding $<Y_{ohm}^{comp}>$ value.

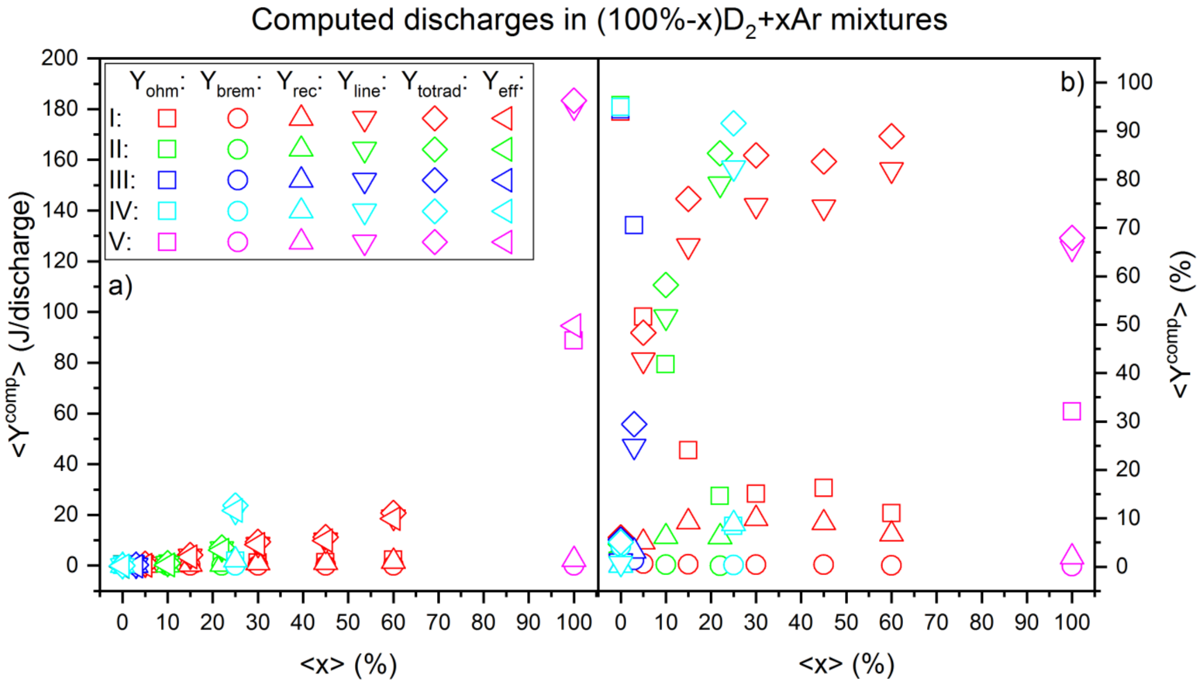

Figure 8.7.5. a) The average computed total ohmic heating yield ($<Y_{ohm}^{comp}>$), total X-ray bremsstrahlung yield ($<Y_{brem}^{comp}>$), total X-ray recombination yield ($<Y_{rec}^{comp}>$), total X-ray line yield ($<Y_{line}^{comp}>$), total X-ray yield ($<Y_{totrad}^{comp}> = <Y_{brem}^{comp}> + <Y_{rec}^{comp}> + <Y_{line}^{comp}>$) and effective total X-ray yield ($<Y_{eff}^{comp}> = <Y_{totrad}^{comp}> - <Y_{ohm}^{comp}>$) versus Ar fraction ($x$) in $(100\%\text{-}x)D_2+x$Ar mixture. **b)** percentage of $<Y_{ohm}^{comp}>$, $<Y_{brem}^{comp}>$, $<Y_{rec}^{comp}>$, $<Y_{line}^{comp}>$ and $<Y_{totrad}^{comp}>$ in reference to $<Y_{ohm}^{comp}> + <Y_{brem}^{comp}> + <Y_{rec}^{comp}> + <Y_{line}^{comp}>$ sum versus Ar fraction (x) in $(100\%\text{-}x)D_2+x$Ar mixture.

The computed dependencies presented in figure 8.7.5a and described in the above paragraph are in general different than the theoretical ones presented in figure 8.7.3a. Small fluctuations of values appear to be present as well as one higher fluctuation at 25% (series IV). The Y_{line}^{comp} values in the 0-60% range of Ar fractions do not exceed

50 J/discharge (all single discharges included) and are relatively tightly spread in reference to the corresponding average $<Y_{line}>$ values. On the other hand, the Y_{line}^{comp} values for the 100% of Ar fraction are relatively widely spread in reference to the $<Y_{line}^{comp}>$ value equal to 181 J/discharge – from 41 J/discharge up to 348 J/discharge (all single discharges included). Thus, the highest achieved Y_{line}^{comp} value from single discharge as well as the $<Y_{line}^{comp}>$ for 100% of Ar in figure 8.7.5a are significantly smaller than the highest theoretically achived Y_{line}^{comp} value for discharges in Ar (figure 8.7.2a) and in (100%-x)D_2+xAr mixtures (figure 8.7.3a). The increase of $<Y_{line}^{comp}>$ values with Ar fraction is belived to be mainly caused by increase in total atomic Z number (see equation (2.1.19)). Also, the possible increase in the average total effective ion charge numbers ($<Z_{eff}^{comp}>$) and the decrease in the average ion plasma temperatures ($<T_{p0}^{comp}>$ – see figure 8.6.5) with Ar fraction may increase $<Y_{line}^{comp}>$ values. On the other hand, the $<Y_{line}^{comp}>$ were significantly smaller than the Y_{line}^{comp} values for theoretical discharges in Ar (figure 8.7.2a) and (100%-x)D_2+xAr mixtures (8.7.3a). The main cause of this is to be decrease of values of model parameters with Ar fraction resulting in the decrease of the average initial pinch radiuses ($<r_{p0}^{comp}>$ – see figure 8.4.5) and in decrease of the average total pinch ion charge numbers (n_{p0}^{comp} – see figure 8.5.5). The decreasing $<r_{p0}^{comp}>$ and $<n_{p0}^{comp}>$ with Ar fraction (0-60%) resulted in smaller total $<Y_{line}^{comp}>$ and lack of strong radiative compression, which resulted also in decrease of $<z_{pmax}^{comp}>$ and $<n_{pmax}^{comp}>$ values with Ar fraction and this again leads to smaller $<Y_{line}^{comp}>$ – feedback type of relation. The relatively small Y_{line}^{comp} values are to be the main reason why the strong plasma radiative compression phenomenon was not stated for the computed discharges in 0-60% of Ar fraction and only for some of the discharges in 100% of Ar fraction. For the computed discharges in 100% of Ar fraction the atomic Z numbers were the highest and average ion temperatures were the lowest (see figure 8.6.5). Also, the $<f_{mr}>$ model parameter values for 100% of Ar were not decreased as for the other Ar fractions (see table 7.3.2 and figure 7.3.1) – significantly higher mass sweeping in radial phase for some of the discharges. And this resulted in increase in $<n_{p0}^{comp}>$ value in reference to 30-60% of Ar (figure 8.5.5) and in some small increase of $<z_{p0}^{comp}>$ values (figure 8.4.10). And the increase in $<n_{p0}^{comp}>$ and $<z_{p0}^{comp}>$ values for 100% of Ar enabled achievment of higher $<Y_{line}^{comp}>$ values and faster development of radiative compression resulting in the highest $<n_{pmax}^{comp}>$ and $<z_{pmax}^{comp}>$ values. On the other hand, the discharges in 100% of Ar fraction are also characterized by smallest averaged initial ($<r_{p0}^{comp}>$ – figure 8.4.5) and minimum ($<r_{pmin}^{comp}>$ – figure 8.4.5) pinch radiuses (smaller pinch radiuses in general lead to smaller X-ray emission and higher ohmic heating) and relatively high average percentage of ohmic heating power ($<Y_{ohm}^{comp}>$ – figure 8.7.5b). The percentages of Y_{ohm}^{comp} values for single discharges in 100% of Ar are in 7-43% range, while to absolute values are in 3-161 J/discharge range. When Y_{ohm}^{comp} are combined with Y_{line}^{comp} the achived Y_{eff}^{comp} values for single discharges in 100% of Ar are in 20-192 J/discharge range.

8.7.2. Radiation yields and ohmic heating yield – total neutron yield

Theoretical discharges

The computed theoretical total neutron yields (Y_n^{comp}) from the discharges in D_2 and (100%-x)D_2+xAr mixtures are presented in: figure 8.7.6 and figure 8.7.7, respectively. The computed theoretical total neutron yields for discharges in Ar are always equal to zero – too low temperatures of plasma and kinetic energies of Ar ions in comparison to columb repulsion (barier) energies of not fully ionized Ar ions.

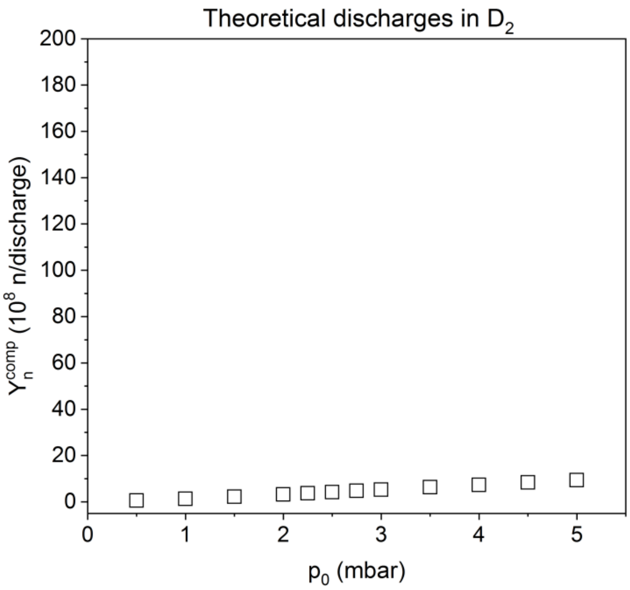

Figure 8.7.6. The computed theoretical total neutron yield (Y_n^{comp}) versus initial D_2 pressure (p_0).

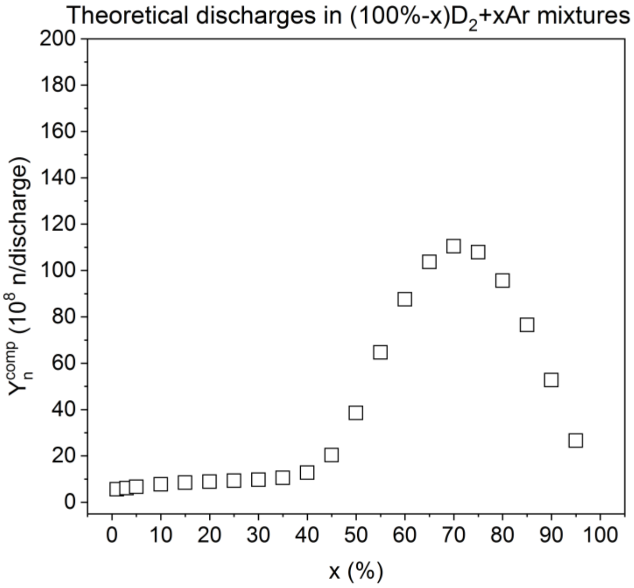

Figure 8.7.7. The computed theoretical total neutron yield (Y_n^{comp}) versus Ar fraction (x) in (100%-x)D_2+xAr mixture.

The computed theoretical total neutron yields (Y_n^{comp}) increase linearly with initial D_2 pressure (figure 8.7.6). Having in mind the phenomenological beam-target based neutron emission equation (6.2.41) incorporated into the 5-phase Lee model code, the increase can be caused by: the increase of pinch plasma currents – I_{pp}^{comp} (figure 8.2.1) and the increase in maximum plasma pinch ion densities of D – n_{pmaxD}^{comp} (figure 8.5.1) with initial D_2 pressure. The increase of n_{pmaxD}^{comp} values with initial D_2 pressure is to be the main cause of the increase (highest contribution) – n_{pmaxD}^{comp} values also increase linearly with p_0. Moreover, the highest Y_n^{comp} in figure 8.7.1 equals 9.34 × 10^8 n/discharge.

The computed theoretical total neutron yields (Y_n^{comp}) for discharges in (100%-x)D_2+xAr mixtures (figure 8.7.7) increase relatively slow with initial Ar fraction up to about 40% of Ar. Based on the beam-target based neutron emission equation (6.2.41) this increase can be caused by: the decrease of minimum pinch radiuses – r_{pmin}^{comp} (figure 8.4.3) and the increase of maximum plasma pinch ion densities of D – n_{pmaxD}^{comp} (figure 8.5.3b) with Ar fraction increase. The increase of n_{pmaxD}^{comp} values with initial Ar fraction is to be the main cause (highest contribution). From about 40% of Ar fraction Y_n^{comp} values increase more rapidly. This increase is connected with the stronger radiative compression phenomenon taking place due to significant increase mainly in the total yield of X-ray line radiation (figure 8.7.3) which causes further: decrease of the minimum pinch radiuses – r_{pmin}^{comp} (figure 8.4.3), increase of the maximum pinch lengths – z_{pmax}^{comp} (figure 8.4.8) and increase of the maximum plasma pinch ion densities of D – n_{pmaxD}^{comp} (figure 8.5.3b) with Ar fraction increase. Again the increase of n_{pmaxD}^{comp} values with initial Ar fraction is to be main cause of increase (highest contribution) – Y_n^{comp} follow mainly changes of n_{pmaxD}^{comp} (see figure 8.5.3b). At 70% of Ar fraction the highest value of Y_n^{comp} is achvied equal to 1.10×10^{10}n/discharge (at 65% of Ar highest n_{pmaxD}^{comp} value was obtained – figure 8.5.3b). Above 70% of Ar fraction the Y_n^{comp} values decrease rapidly. This decrease is connected with the plasma opacity effect taking place and slowing down total emission of X-ray line radiation – Y_{line}^{comp} (figure 8.7.3), resulting in weaker radiative compression phenomenon. And the weaker radiative compression occurrence is connected with:

stop of the decrease of minimum pinch radiuses – r_{pmin}^{comp} (figure 8.4.3) and slowing down of increase and further decrease of the maximum plasma pinch ion densities of D – n_{pmaxD}^{comp} (figure 8.5.3b) with Ar fraction increase. Moreover, the decrease of Y_n^{comp} values above 70% of Ar happens while the maximum voltages – U_{max}^{comp} (figure 8.2.8) and the maximum pinch lengths – z_{pmax}^{comp} (figure 8.4.8) further increase with Ar fraction.

Experimental and computed discharges in deuterium

Figure 8.7.8 presents the average measured total neutron yields ($<Y_n^{mea}>$) and the measured maximum neutron yields (Y_{nmax}^{mea}) from the discharges in D_2.

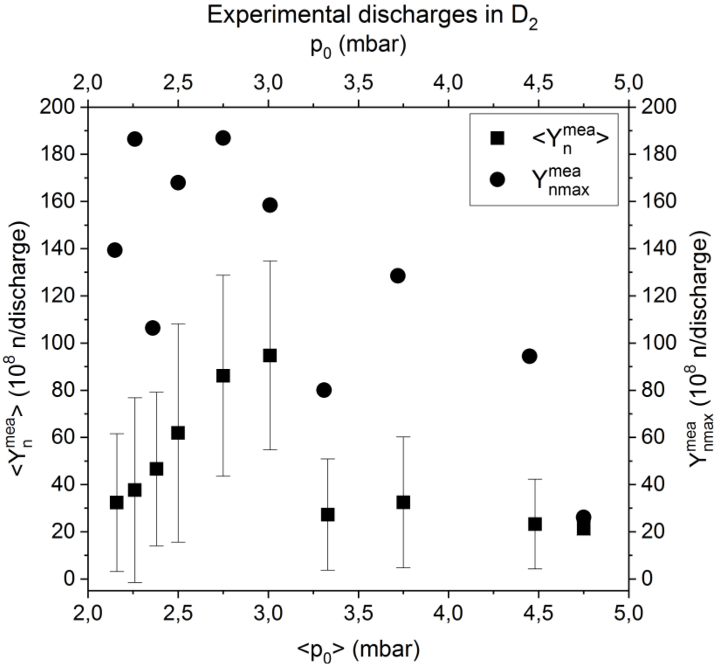

Figure 8.7.8. The average measured total neutron yield ($<Y_n^{mea}>$) versus average initial D_2 pressure ($<p_0>$) and the maximum measured total neutron yield (Y_{nmax}^{mea}) versus initial D_2 pressure (p_0).

The average measured total neutron yields ($<Y_n^{mea}>$) in D_2 (figure 8.7.8) were determined based on the 388 experimental discharges in total. The presented $<Y_n^{mea}>$ values increase constinusly with initial D_2 pressure up to 3.0 mbar. Thus, the 3.0 mbar has been stated as the optimum initial D_2 pressure with $<Y_n^{mea}> = 9.5(\pm0.2) \times 10^9$ n/discharge. Because of this fact, all experimental and computed discharges in $(100\%\text{-}x)D_2\text{+}x\text{Ar}$ mixtures were carried out under total pressure of about 2.9 mbar. At about 3.33 mbar of D_2 sudden drop of $<Y_n^{mea}>$ takes place – discontinuity of the $<Y_n^{mea}>$ versus $<p_0>$ dependency for higher initial D_2 pressures. The behaviour presented in figure 8.7.8 is completely different than the theoretically predicted one in figure 8.7.6. The large error bars presented in figure 8.7.8 are standard deviations ±σ (while the counter errors have the size of points or smaller) – the spread of Y_n^{mea} was relatively large except for the discharges in about 4.75 mbar of initial D_2 pressure.

The maximum measured total neutron yields (Y_{nmax}^{mea}) were determined for each investigated initial D_2 pressure (figure 8.7.8). The dependency of Y_{nmax}^{mea} versus p_0 differs from the dependency of $<Y_n^{mea}>$ versus $<p_0>$ – maximum is set between about 2.26-2.75 mbar of D_2 and large fluctuations of values are present. The highest value of Y_{nmax}^{mea} so far achived during experimental discharges in the PF-24 device under 17 kV of charging voltage and 16.8 kJ of energy storage is equal to $1.9(\pm0.1) \times 10^{10}$ n/discharge.

Based on the average measured total neutron yields ($<Y_n^{mea}>$) for discharges in D_2 (figure 8.7.8), 10 single discharges were selected (see also subsection 7.2) in order to best represent each of the 10 average values. For this purpose, from each of the 10 groups of discharges corresponding approximately to given p_0 pressure of D_2 single discharge was choosen for which: Y_n^{mea} / $<Y_n^{mea}>$ = 100(±10)%, where Y_n^{mea} is the closest value to given $<Y_n^{mea}>$ value but not bigger than $<Y_n^{mea}> + 0.1 \times <Y_n^{mea}>$ and not smaller than $<Y_n^{mea}> - 0.1 \times <Y_n^{mea}>$. The 10 Y_n^{mea} (10 selected discharges) which best represent given $<Y_n^{mea}>$ are presented in figure 8.7.9. Each of the 10 discharges was also computed using the 5-phase Lee model code and computed values of Y_n^{comp} were presented also in figure 8.7.9. Furthermore, measured and computed parameters and indicators presented in previous subsections of chapter 8 in figures: 8.1.4, 8.1.10, 8.2.4, 8.2.9, 8.3.4, 8.3.9, 8.4.4, 8.4.9, 8.4.14, 8.5.4, 8.5.9, 8.6.4 and 8.7.4 correspond to these 10 coupled measured-computed discharges in D_2 (as was presented in section 7.2) – discharges with plasma parameters for which typical values of Y_n^{mea} were obtained for given initial D_2 pressure.

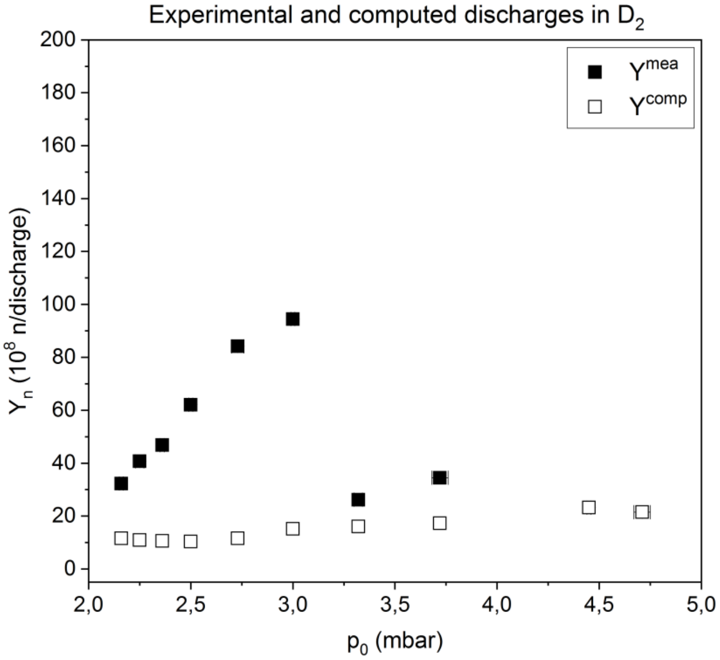

Figure 8.7.9. The measured (Y_n^{mea}) and computed (Y_n^{comp}) total neutron yield versus initial D_2 pressure (p_0).

The sudden drop between Y_n^{mea} values corresponding to 3.00(±0.01) mbar and 3.32(±0.02) mbar of initial D_2 pressures is also seen in figure 8.7.9. However, this drop is in general not connected with any discontinuity of changes of parameters presented in figures (experimental and computed parameters): 8.1.4, 8.1.10, 8.2.4, as well as in figures (computed parameters): 8.2.9, 8.4.4, 8.4.9, 8.4.14, 8.5.4, 8.5.9, 8.6.4 and 8.7.4. Thus, it appears that this drop may by caused by the change in the character of neutron production and/or it may be connected with higher compression due to shift of the plasma column structure into the hole at the center of the anode (the hole was becoming bigger with the number of discharges enabling at least half of the plasma column to enter after about 1500 discharges in total) for most of discharges for lower initial D_2 pressures than 3.0 mbar. The effect of the change of anode shape with the number of discharges and entrence of plasma column into the hole at the end of anode was in general not accounted during the computations using the Lee model code. The most of determined Y_n^{mea}

in figure 8.7.9 do not match the computed Y_n^{comp} – for eight discharges between about 2.16 mbar and 3.72 mbar of initial D_2 pressures the smallest and highest difference between Y_n^{mea} and Y_n^{comp} value is equal to: 1.0×10^9 n/discharge and 8.0×10^9 n/discharge, respectively. And when differences between Y_n^{mea} and Y_n^{comp} values are recalculated into relative errors the range of changes is equal to about 38-85% of the measured value. On the other hand, the two discharges for initial D_2 pressures corresponding to about 4.45 mbar and 4.71 mbar have: relative errors smaller than 5% of the measured value, the maximum difference between Y_n^{mea} and Y_n^{comp} value equal to 0.1×10^8 n/discharge and Y_n^{comp} within the error range of neutron counter. Thus, the two Y_n^{comp} are very well matched. Furthmore, the important fact to notice is that for the two discharges for which very well match of Y_n^{mea} and Y_n^{comp} values is stated have the smallest Y_n^{mea} from all determined – the highest Y_n^{mea} value for the these two discharges is equal to 2.3×10^9 n/discharge. This is connected with the fact that the 5-phase Lee model code appears to compute properly only the Y_n^{comp} for discharges with lower values of Y_n^{mea} (at least for the discharges in the PF-24 device) – smaller Y_n^{mea} than about 2.6×10^9 n/discharge are usually accuretly reproduced. As a proof, for the 73% of all computed discharges in D_2, which have $Y_n^{mea} < 2.6 \times 10^9$ n/discharge, Y_n^{mea} values were very well reproduced – relative errors between Y_n^{mea} and Y_n^{comp} below 6%. Wherein, it should be mentioned that all investiagated discharges in D_2 with Y_n^{mea} values smaller than 2.6×10^9 n/discharge were achieved only in 37% of cases for initial D_2 pressures below and equal to 3.0 mbar and in 80% of cases for initial D_2 pressures above 3.0 mbar (see figure 8.7.8 and figure 8.7.9).

Experimental and computed discharges in deuterium-argon mixtures

Figure 8.7.10 presents the average measured ($<Y_n^{mea}>$) and computed ($<Y_n^{comp}>$) total neutron yields from the experimental and computed discharges in $(100\%\text{-}x)D_2+x\text{Ar}$ mixtures.

The average measured total neutron yields ($<Y_n^{mea}>$) for discharges in $(100\%\text{-}x)D_2+x\text{Ar}$ mixtures decrease with Ar fraction (figure 8.7.10). This is completely different behaviour than theoretically anticipated one in figure 8.7.7. Fluctuations of $<Y_n^{mea}>$ values between different series of discharges occure. For example, the $<Y_n^{mea}>$ for 0% of Ar fraction in series II has smaller value than the $<Y_n^{mea}>$ for 3% of Ar fraction in series III. Thus, some increase in the average measured total neutron yields can be observed when Ar fraction is increased from 0% to 3% and when only data from series II and III are taken into account. On the other hand, when $<Y_n^{mea}>$ from single series are only considered continous decrease is observed for all four series of discharges (series V presented in previous subsections are discharges in Ar for which total neutron yield values are always equal to zero – not shown). The changes of $<Y_n^{mea}>$ values between different series of discharges are best seen for 0% of Ar fraction (8.7.10a). For discharges in 0% of Ar fraction, not only the average measured total neutron yields significantly differ from each other (figure 8.7.10a) but also values from single discharges for given series have different spread (while similar number of discharges was performed during each series – about 8-9 discharges) – see figure 8.7.11.

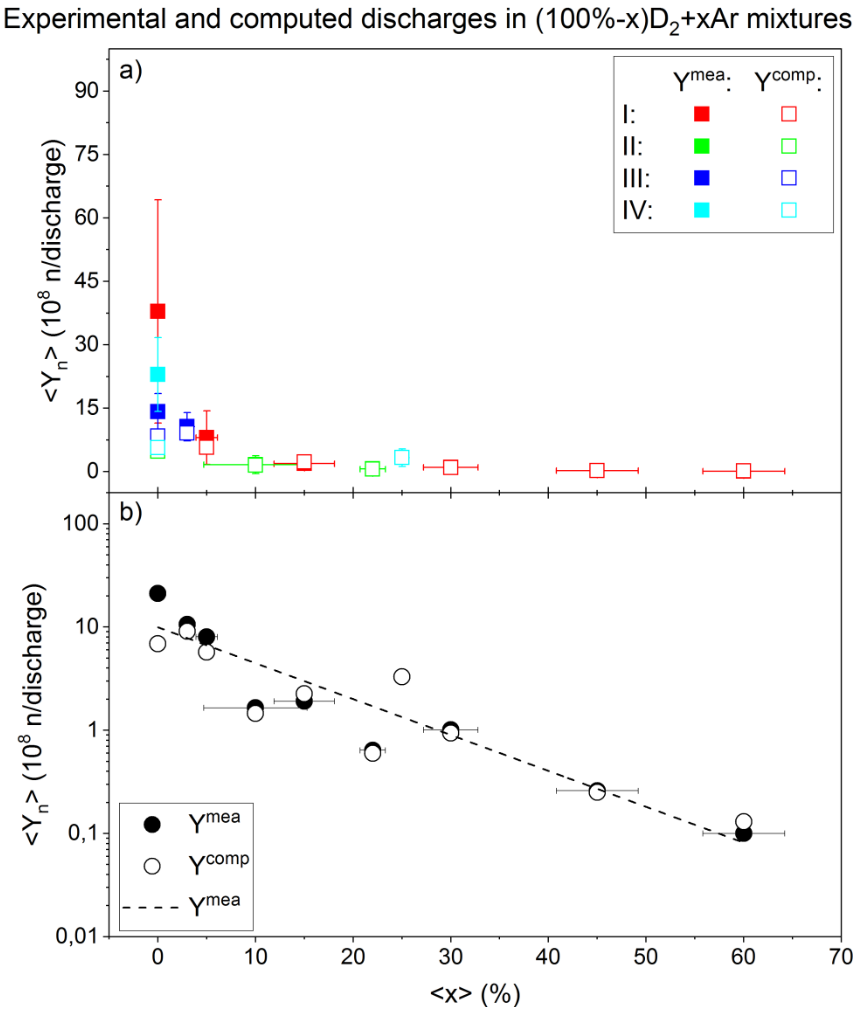

Figure 8.7.10. a) The average measured (<Y_n^{mea}>) and computed (<Y_n^{comp}>) total neutron yield versus Ar fraction (<x>) in (100%-x)D_2+xAr mixture (Roman numerals mark given series of discharges). **b)** the average measured (<Y_n^{mea}>) and computed (<Y_n^{comp}>) total neutron yield versus Ar fraction (<x>) in (100%-x)D_2+xAr mixture (without division into the different series).

The smallest and highest difference between <Y_n^{mea}> from two different series equals: 8.7 × 10^8 n/discharge (series II and III) and 32.4 × 10^8 n/discharge (series I and II), respectivly. The smallest and highest relative error between <Y_n^{mea}> from two different series equals about: 38% (series III and IV) and 86% (series I and II), respectivly. The smallest and highest Y_n^{mea} value from single discharges for series I equals: 15.8 × 10^8 n/discharge and 93.5 × 10^8 n/discharge, respectively. The smallest and highest Y_n^{mea} value from single discharges for series II equals about: 3.3 × 10^8 n/discharge and 8.8 × 10^8 n/discharge, respectively. The smallest and highest Y_n^{mea} value from single discharges for series III equals about: 7.8 × 10^8 n/discharge and 18.5 × 10^8 n/discharge, respectively. And the smallest and highest Y_n^{mea} value from single discharges for series IV equals about: 16.7 × 10^8 n/discharge and 43.8 × 10^8 n/discharge, respectively. Moreover, not only the <Y_n^{mea}> from different series are significantly different, also some of the other parameters describing discharge and plasma were significantly different between series of discharges – see for example time parameters in figure 8.1.5 (<t_c^{mea}> vs x and <t_p^{mea}> vs x). In fact, an interesting observation can be made while comparing <t_c^{mea}>, <t_p^{mea}> and <Y_n^{mea}> parameters for given series of 0% fraction – the highest <Y_n^{mea}> values are obtained for the smallest <t_c^{mea}> and <t_p^{mea}> values (series I). In other words, the fastest moving magnetic pistons on average produced plasma pinches which emited the highest total neutron yields on average (see figure 8.1.6 and figure 8.7.11). The main reasons for changes of neutron emission and plasma dynamics between series of discharges in 0% of Ar, are believed to be: fluctuations of copper impurities (or different impurities) which penetrate into the plasma structure, arcing and deformation of the cathode and anode rods with the number of discharges. Also, the changes in the L_0^{comp} and R_0^{comp} may be the secondary probable cause.

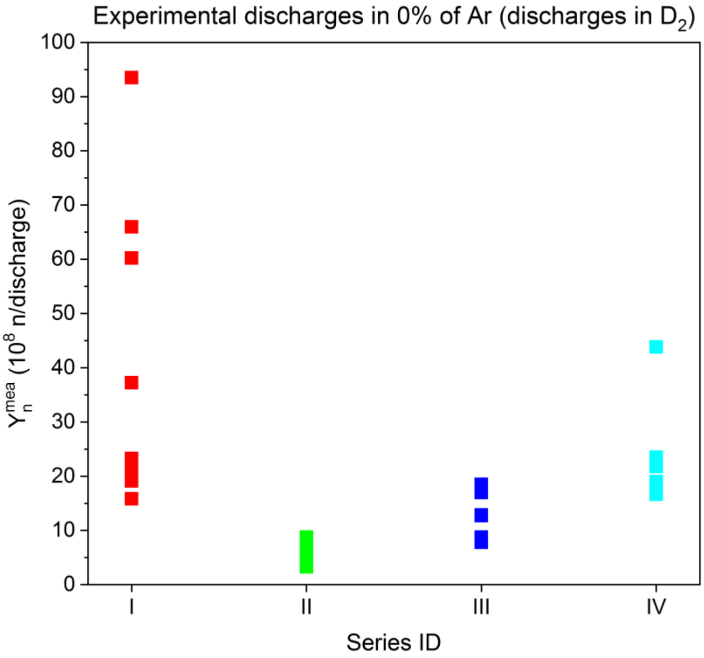

Figure 8.7.11. The measured (Y_n^{mea}) total neutron yield versus series ID for all single discharges in 0%Ar (discharges in D_2 in four experimental series).

The average measured ($<Y_n^{mea}>$) and computed ($<Y_n^{comp}>$) total neutron yields in figure 8.7.10 are relatively well matched, except maybe for the discharges in 0% of Ar. When the division into series is omitted (figure 8.7.10b) the absolute difference between $<Y_n^{mea}>$ and $<Y_n^{comp}>$ for 0% of Ar fraction is equal to about: 14.3 × 10^8 n/discharge. And the corresponding relative error is equal to about 67% of measured value. While, the highest difference between $<Y_n^{mea}>$ and $<Y_n^{comp}>$ for other Ar fractions is equal to 2.5×10^8 n/discharge with corresponding relative error equal to 29% of measured value (for discharges in 5% of Ar). And the highest relative error for other Ar fractions (3-60%) is equal to 31% of measured value while corresponding difference between $<Y_n^{mea}>$ and $<Y_n^{comp}>$ is equal to 0.03 × 10^8 n/discharge (discharges in 60% of Ar).

Despite the different behavior of the PF-24 device during different series of discharges, when $<Y_n^{comp}>$ are calculated without taking into account division into different series the scaling law can be obtained – see the fitted line in logarithmic scale (or exponent in line scale) in figure 8.7.10b. The equation describing the curve (scaling law) can be presented as: $<Y_n> = 2.3\times10^8\times exp(-0.079\times<x>)$. And the determination coefficient R^2 (adj. R-square) for the fitted exponential (or line) function is as high as 0.93 (least-squares method of fitting was used).

8.8. Summary and comparison of radiative compression indicators and plasma pinch parameters for discharges in D_2

The tables below list the highest and smallest values of indicators and parameters describing plasma pinch compression. Table 8.8.1 contains the results for the 12 theoretical discharges in 0.50-5.00 mbar of initial D_2 pressure and for the 44 computed discharges – 10 at initial D_2 pressure in the range 2.16(±0.01) mbar to 4.71(±0.04) mbar and 34 in the approximately constant initial D_2 pressure of 2.9(±0.1) mbar.

Table 8.8.1. Summary of the highest and smallest values of parameters and indicators (see subsection 6.3.3) describing plasma pinch compression for the 12 theoretical discharges in 0.50-5.00 mbar of initial D_2 pressure and for the 44 computed discharges in about 2.16-4.71 mbar of initial D_2 pressure including 34 discharges in constant pressure of about 2.9 mbar.

D_2 Indicator/parameter			**Theoretical**	**Computed**	Unit
			Pressure (mbar)		
			0.50-5.00	2.16-4.71	
U_{max}^{comp}	maximum voltage	highest	65	91	kV
		smallest	46	25	
$I_{pp}(t_1)^{comp}$	pinch plasma current at t_1	highest	383	380	kA
		smallest	256	249	
$I_{P\text{-}B}(t_1)^{comp}$	P-B current at t_1	highest	1455	1816	kA
		smallest	1455	1455	
$I_{P\text{-}Breduced}(t_1)^{comp}$	reduced P-B current at t_1	highest	1426	1423	kA
		smallest	1277	1119	
t_{pl}^{comp}	pinch lifetime	highest	30	46	ns
		smallest	14	15	
t_{rcl}^{comp}	radiative compression lifetime	highest	0	0	ns
		smallest	0	0	
t_Q^{comp}	characteristic radiation depletion time	highest	all negative	all negative	ns
		smallest (positive)	all negative	all negative	
r_{p0}^{comp}	**initial pinch radius**	**highest**	**0.72**	**0.64**	**cm**
		smallest	**0.72**	**0.57**	
r_{pmin}^{comp}	**minimum pinch radius**	**highest**	**0.67**	**0.59**	**cm**
		smallest	**0.67**	**0.52**	
$r_{p0}^{comp} - r_{pmin}^{comp}$	**change of pinch radius**	**highest**	**0.05**	**0.06**	**cm**
		smallest	**0.05**	**0.04**	
z_{p0}^{comp}	initial pinch length	highest	3.98	3.81	cm
		smallest	3.97	3.68	
z_{pmax}^{comp}	maximum pinch length	highest	4.82	5.45	cm
		smallest	4.82	4.22	
$z_{pmax}^{comp} - z_{p0}^{comp}$	change of pinch length	highest	0.85	1.71	cm
		smallest	0.84	0.48	
V_{p0}^{comp}	initial pinch volume	highest	6.48	4.9	cm^3
		smallest	6.47	3.76	

V_{pf}^{comp}	final pinch volume	highest	6.8	5.52	cm^3
		smallest	6.8	4.01	
V_{p0}^{comp} - V_{pf}^{comp}	change of pinch volume	highest	all negative	0.36	cm^3
		smallest	all negative	negative	
n_{p0}^{comp}	**initial total pinch density**	**highest**	**3.26**	**8.47**	**10^{17} cm^{-3}**
		smallest	**0.33**	**0.68**	
n_{pmax}^{comp}	**maximum total pinch density**	**highest**	**3.77**	**9.9**	**10^{17} cm^{-3}**
		smallest	**0.39**	**0.83**	
n_{pmax}^{comp} - n_{p0}^{comp}	**change of total pinch density**	**highest**	**0.51**	**1.48**	**10^{17} cm^{-3}**
		smallest	**0.06**	**0.13**	
N_{p0}^{comp}	initial total linear pinch density	highest	5.31	10.23	10^{17} cm^{-1}
		smallest	0.54	0.79	
N_{pf}^{comp}	final total linear pinch density	highest	5.32	10.46	10^{17} cm^{-1}
		smallest	0.55	0.83	
$\|N_{pf}^{comp}$ - $N_{p0}^{comp}\|$	change of total linear pinch density	highest	0.01	0.23	10^{17} cm^{-1}
		smallest	< 0.01	< 0.01	
T_{p0}^{comp}	**initial pinch temperature**	**highest**	**2.25**	**2.03**	**keV**
		smallest	**0.51**	**0.19**	
T_{pmin}^{comp}	minimum pinch temperature	highest	1.88	1.76	keV
		smallest	0.43	0.18	
T_{p0}^{comp} - T_{pmin}^{comp}	change of pinch temperature	highest	0.37	0.27	keV
		smallest	0.08	0.02	
Y_{ohm}^{comp}	total ohmic heating yield	highest	0.1416	0.89	J/discharge
		smallest	0.0033	0.0062	
Y_{brem}^{comp}	total X-ray bremsstrahlung yield	highest	0.00914	0.03353	J/discharge
		smallest	0.000095	0.00024	
Y_{rec}^{comp}	total X-ray recombination yield	highest	0.000629	0.005514	J/discharge
		smallest	0.000001	0.000004	
Y_{line}^{comp}	**total X-ray line yield**	**highest**	**0.0021**	**0.0262**	**J/discharge**
		smallest	**0.000002**	**0.000007**	
Y_{totrad}^{comp}	total X-ray yield	highest	0.011876	0.06763	J/discharge
		smallest	0.000099	0.00025	
Y_{eff}^{comp}	effective total X-ray yield	highest	all negative	all negative	J/discharge
		smallest	all negative	all negative	
Y_{n}^{comp}	total neutron yield	highest	9.34	21.5	×10^8 n/discharge
		smallest	0.5	0.77	

The results of the 44 computed discharges do not differ significantly from the results based on the 12 theoretical discharges (table 8.8.1) considering occurrence of plasma radiative compression phenomenon. Most importantly, Y_{line}^{comp} are always relatively small for both theoretical and computed discharges – up to 0.03 J/discharge. This is followed by too high $I_{P\text{-}B}(t_1)^{comp}$ (minimum 1455 kA) and the $I_{P\text{-}Breduced}(t_1)^{comp}$ (minimum 1119 kA) in comparison to $I_{pp}(t_1)^{comp}$ (maximum 383 kA). The negative t_Q^{comp} suggests always higher computed total power of ohmic heating than the computed total power of X-ray radiation emission (confirmed with Y_{eff}^{comp} parameter), and the t_{rcl}^{comp} always equal to zero (computed

$I_{P\text{-}Breduced}(t)^{comp}$ always bigger than corresponding $I_{pp}(t)^{comp}$ during entire pinch phase of discharge). This resulted in: the $U_{max}{}^{comp}$ up to 91 kV, the longest $t_{pl}{}^{comp}$ of 46 ns, the smallest $r_{pmin}{}^{comp}$ of 0.52 cm, the highest $z_{pmax}{}^{comp}$ of 5.45 cm, the smallest $V_{pf}{}^{comp}$ of 4.01 cm^3 and the highest $n_{pmax}{}^{comp}$ at the level of 9.9×10^{17} $1/cm^3$. Also, no significant changes of presented parameters during pinch phase of discharge were stated for different initial pressures. The highest $r_{p0}{}^{comp}$ - $r_{pmin}{}^{comp}$ was equal to 0.06 cm. The highest $z_{pmax}{}^{comp}$ - $z_{p0}{}^{comp}$ was equal to 1.71 cm. Mostly expansion in total volume of plasma columns was stated but some compression is also possible with highest difference up to 0.36 cm^3. And the highest $n_{pmax}{}^{comp}$ - $n_{p0}{}^{comp}$ was only equal 1.48×10^{17} $1/cm^3$. Summarizing, the plasma radiative compression phenomenon was not stated for even one theoretical or computed discharge in D_2 – no significant decrease in plasma pinch radius and increase in ion number density stated.

8.9. Summary and comparison of radiative compression indicators and plasma pinch parameters for discharges in Ar

The tables below list the highest and smallest values of the indicators and parameters describing plasma pinch compression in Ar. Table 8.9.1 contains the results of 21 theoretical discharges in 0.50–5.00 mbar of initial Ar pressure and the results of 10 computed discharges in 1.2(±0.1) mbar of initial Ar pressure.

The parameters and indicators are compared for two pressure ranges, taking into account the analysis of the results discussed in the chapters 8.1-8.7 the results of 9 theoretical discharges in the 0.50-1.60 mbar and 4.50-5.00 mbar of initial Ar pressure (Ar pressure range I) differ from the results in the 1.70-4.20 mbar of initial Ar pressure (Ar pressure range II) considering the appearance and strength of the plasma radiative compression phenomenon – see table 8.9.1. For the 9 investigated theoretical discharges in the pressure **range I** the $Y_{line}{}^{comp}$ are in the range of 5-530 J/discharge – far higher values than in D_2 (table 8.8.1). This is followed by the relatively big $I_{P\text{-}B}(t_1)^{comp}$ (minimum 768 kA) and the relatively small $I_{P\text{-}Breduced}(t_1)^{comp}$ (maximum 67 kA) in comparison to the $I_{pp}(t_1)^{comp}$ (minimum 266 kA). Also, the achived $t_Q{}^{comp}$ (minimum 0.0002 ns and maximum 1.4 ns) are always positive and small or very small in comparison to $t_{pl}{}^{comp}$ (minimum 26 ns) and $t_{rcl}{}^{comp}$ (minimum 7 ns). This results in the highest $U_{max}{}^{comp}$ equal to 40 kV – smaller values than the highest $U_{max}{}^{comp}$ for discharges in D_2. The smallest $r_{pmin}{}^{comp}$ (0.27 cm) is smaller than the smallest $r_{pmin}{}^{comp}$ for discharges in D_2. While the highest $r_{pmin}{}^{comp}$ (0.57 cm) is higher than the smallest $r_{pmin}{}^{comp}$ for discharges in D_2. All the $z_{pmax}{}^{comp}$ (minimum 4.81 cm and maximum 5.28 cm) are smaller than the highest $z_{pmax}{}^{comp}$ for discharges in D_2. The smallest $V_{pf}{}^{comp}$ (1.14 cm^3) is smaller in comparison to smallest $V_{pf}{}^{comp}$ for discharges in D_2. While the highest $V_{pf}{}^{comp}$ (4.91 cm^3) is higher than the smallest $V_{pf}{}^{comp}$ for discharges in D_2. All the $n_{pmax}{}^{comp}$ (maximum 8.2×10^{17} $1/cm^3$ and minimum 0.27×10^{17} $1/cm^3$) are smaller than the highest $n_{pmax}{}^{comp}$ for discharges in D_2. Moreover, the highest $r_{p0}{}^{comp}$ - $r_{pmin}{}^{comp}$ (0.33 cm) is higher than the highest $r_{p0}{}^{comp}$ - $r_{pmin}{}^{comp}$ for discharges in D_2. While the smallest $r_{p0}{}^{comp}$ - $r_{pmin}{}^{comp}$ (0.04 cm) is equal to the smallest $r_{p0}{}^{comp}$ - $r_{pmin}{}^{comp}$ for the discharges in D_2. All the $z_{pmax}{}^{comp}$ - $z_{p0}{}^{comp}$ (maximum 1.04 cm and minimum 0.81 cm) are smaller than the highest $z_{pmax}{}^{comp}$ - $z_{p0}{}^{comp}$ for discharges in D_2. The highest $V_{p0}{}^{comp}$ - $V_{pf}{}^{comp}$ (3.73 cm^3) is positive and higher in comparison to the highest positive $V_{p0}{}^{comp}$ - $V_{pf}{}^{comp}$ for D_2. While the smallest $V_{p0}{}^{comp}$ - $V_{pf}{}^{comp}$ are negative. And all the $n_{pmax}{}^{comp}$ - $n_{p0}{}^{comp}$ (maximum 6.19×10^{17} $1/cm^3$ and minimum 0.04×10^{17} $1/cm^3$) are smaller than the highest $n_{pmax}{}^{comp}$ - $n_{p0}{}^{comp}$ for discharges in D_2.

Summarizing, based mainly on the determined r_{pmin}^{comp}, n_{pmax}^{comp}, r_{p0}^{comp} - r_{pmin}^{comp} and n_{pmax}^{comp} - n_{p0}^{comp}, only the relatively weak or non-existent plasma radiative compression phenomenon is stated for the theoretical discharges in the PF-24 operated with the 0.50-1.60 mbar and the 4.50-5.00 mbar of initial Ar pressures **range I**.

Table 8.9.1. Summary of the highest and smallest values of parameters and indicators (see subsection 6.3.3) describing plasma pinch compression for the 21 theoretical discharges in 0.5-5.0 mbar of initial Ar pressure and for the 10 computed discharges in 1.2 mbar of initial Ar pressure. The theoretical discharges are divided into two pressure ranges and computed discharges are divided into two groups. **Group I**: #17101817, #17101818, #17101820, #17102002, #17102003; **group II**: #17101814, #17101816, #17102007, #17102009, #17102016.

Ar Indicator/parameter			**Theoretical**		**Computed**		Unit
			Pressure (mbar)				
			0.5-1.6 & 4.5-5.0	1.7-4.2	1.2		
			range I	**range II**	**group I**	**group II**	
U_{max}^{comp}	maximum voltage	highest	40	81	25	41	kV
		smallest	15	50	6	23	
$I_{pp}(t_1)^{comp}$	pinch plasma current at t_1	highest	389	373	341	216	kA
		smallest	266	320	97	170	
$I_{P\text{-}B}(t_1)^{comp}$	P-B current at t_1	highest	3075	928	2.0×10^{8}	2605	kA
		smallest	768	794	768	823	
$I_{P\text{-}Breduced}(t_1)^{comp}$	reduced P-B current at t_1	highest	67	28	1.4×10^{6}	28	kA
		smallest	14	13	10	12	
t_{pl}^{comp}	pinch lifetime	highest	112	86	91	70	ns
		smallest	26	43	29	58	
t_{rcl}^{comp}	radiative compression lifetime	highest	42	43	29	12	ns
		smallest	7	15	0	5	
t_{Q}^{comp}	characteristic radiation depletion time	highest	1.376	0.008	0.324	0.0008	ns
		smallest (positive)	0.0002	0.0002	0.0006	0.0007	
$\mathbf{r_{p0}^{comp}}$	**initial pinch radius**	**highest**	**0.66**	**0.59**	**0.43**	**0.37**	**cm**
		smallest	**0.53**	**0.52**	**0.31**	**0.35**	
$\mathbf{r_{pmin}^{comp}}$	**minimum pinch radius**	**highest**	**0.57**	**0.24**	**0.36**	**0.19**	**cm**
		smallest	**0.27**	**0.07**	**0.14**	**0.11**	
$\mathbf{r_{p0}^{comp} - r_{pmin}^{comp}}$	**change of pinch radius**	**highest**	**0.33**	**0.45**	**0.19**	**0.25**	**cm**
		smallest	**0.04**	**0.35**	**0.06**	**0.18**	
z_{p0}^{comp}	initial pinch length	highest	4.38	4.17	3.68	3.7	cm
		smallest	3.93	3.92	3.6	3.63	
z_{pmax}^{comp}	maximum pinch length	highest	5.28	6.26	5.19	5.92	cm
		smallest	4.81	5.06	4.48	5.5	
z_{pmax}^{comp} - z_{p0}^{comp}	change of pinch length	highest	1.04	2.31	1.51	2.29	cm
		smallest	0.81	1.14	0.81	1.82	
V_{p0}^{comp}	initial pinch volume	highest	5.99	4.56	2.13	1.59	cm^3
		smallest	3.47	3.34	1.09	1.4	
V_{pf}^{comp}	final pinch volume	highest	4.91	0.98	1.82	0.63	cm^3
		smallest	1.14	0.09	0.31	0.22	
V_{p0}^{comp} - V_{pf}^{comp}	change of pinch volume	highest	3.73	3.58	0.93	1.27	cm^3
		smallest	negative	3.1	0.06	0.94	
$\mathbf{n_{p0}^{comp}}$	**initial total pinch density**	**highest**	**2.01**	**2.02**	**3.87**	**3.38**	$\mathbf{10^{17}\ cm^{-3}}$
		smallest	**0.23**	**1.05**	**0.66**	**1.54**	

n_{pmax}^{comp}	**maximum total pinch density**	**highest**	**8.2**	**65**	**7.8**	**19.8**	**10^{17} cm^{-3}**
		smallest	**0.27**	**12**	**0.9**	**12.4**	
n_{pmax}^{comp} - n_{p0}^{comp}	**change of total pinch density**	**highest**	**6.19**	**64**	**6.32**	**17.7**	**10^{17} cm^{-3}**
		smallest	**0.04**	**10**	**0.27**	**9.2**	
N_{p0}^{comp}	initial total linear pinch density	highest	2.64	2.21	1.41	1.45	10^{17} cm^{-1}
		smallest	0.27	0.93	0.38	0.59	
N_{pf}^{comp}	final total linear pinch density	highest	2.74	2.19	1.43	1.43	10^{17} cm^{-1}
		smallest	0.28	0.96	0.38	0.63	
$\|N_{pf}^{comp} - N_{p0}^{comp}\|$	change of total linear pinch density	highest	0.26	0.12	0.03	0.04	10^{17} cm^{-1}
		smallest	< 0.01	0.01	< 0.01	0.02	
T_{p0}^{comp}	**initial pinch temperature**	**highest**	**1.13**	**0.37**	**0.64**	**0.11**	**keV**
		smallest	**0.06**	**0.09**	**0.06**	**0.08**	
T_{pmin}^{comp}	minimum pinch temperature	highest	0.95	0.22	0.56	0.1	keV
		smallest	0.05	0.08	0.06	0.08	
T_{p0}^{comp} - T_{pmin}^{comp}	change of pinch temperature	highest	0.18	0.17	0.08	0.02	keV
		smallest	0.01	0.01	< 0.01	< 0.01	
Y_{ohm}^{comp}	total ohmic heating yield	highest	98	322	71	161	J/discharge
		smallest	0.8	24	3.5	98	
Y_{brem}^{comp}	total X-ray bremsstrahlung yield	highest	3.09	4.26	0.616	0.128	J/discharge
		smallest	0.03	0.13	0.007	0.05	
Y_{rec}^{comp}	total X-ray recombination yield	highest	72	109	8.4	3.9	J/discharge
		smallest	1.2	4.1	0.3	1.5	
Y_{line}^{comp}	**total X-ray line yield**	**highest**	**530**	**1701**	**108**	**348**	**J/discharge**
		smallest	**4.9**	**649**	**41**	**221**	
Y_{totrad}^{comp}	total X-ray yield	highest	605	1752	108	353	J/discharge
		smallest	6.5	653	50	223	
Y_{eff}^{comp}	effective total X-ray yield	highest	591	1535	47	192	J/discharge
		smallest	5.9	530	20	124	
Y_{n}^{comp}	total neutron yield	highest	-	-	-	-	$\times 10^{8}$ n/discharge
		smallest	-	-	-	-	

On the other hand, for the 12 investigated theoretical discharges in the 1.70-4.20 mbar of initial Ar pressure (**range II**) (table 8.9.1) the Y_{line}^{comp} are in the range of 649-1702 J/discharge – far higher than in D_2 (table 8.8.1) and higher than for the theoretical discharges in 0.50-1.60 mbar and 4.50-5.00 mbar of initial Ar pressures range I (table 8.9.1). This is followed by the relatively big $I_{P\text{-}B}(t_1)^{comp}$ (minimum 794 kA) and the relatively small $I_{P\text{-}Breduced}(t_1)^{comp}$ (maximum 28 kA) in comparison to the $I_{pp}(t_1)^{comp}$ (minimum 320 kA). The achived t_Q^{comp} (minimum 0.0002 ns and maximum 0.008 ns) are always positive and very small in comparison to t_{pl}^{comp} (minimum 43 ns) and t_{rcl}^{comp} (minimum 15 ns). This results in the highest U_{max}^{comp} equal to 81 kV – a little bit smaller value than the highest U_{max}^{comp} for discharges in D_2 but also higher value than the highest U_{max}^{comp} for theoretical discharges in the Ar pressure range I. All the r_{pmin}^{comp} (minimum 0.07 cm and maximum 0.24 cm) are smaller than the smallest r_{pmin}^{comp} for discharges in D_2. And also the smallest r_{pmin}^{comp} (0.07 cm) is smaller than the smallest r_{pmin}^{comp} for theoretical discharges in the Ar pressure range I. The highest z_{pmax}^{comp} (6.26 cm) is higher than the highest z_{pmax}^{comp} in D_2 and in the Ar pressure range I. While the smallest

z_{pmax}^{comp} (5.06 cm) is smaller than the highest z_{pmax}^{comp} in D_2 but higher than the smallest z_{pmax}^{comp} for theoretical discharges in the Ar pressure range I. All the V_{pf}^{comp} (minimum 0.09 cm^3 and maximum 0.98 cm^3) are smaller than the smallest V_{pf}^{comp} in D_2 and in the Ar pressure range I. All the n_{pmax}^{comp} (maximum 65×10^{17} 1/cm^3 and minimum 12×10^{17} 1/cm^3) are higher than the highest n_{pmax}^{comp} for discharges in D_2 and in the Ar pressure range I. Moreover, all the r_{p0}^{comp} - r_{pmin}^{comp} (maximum 0.45 cm and minimum 0.35 cm), the highest r_{p0}^{comp} - r_{pmin}^{comp} (0.45 cm), the highest z_{pmax}^{comp} - z_{p0}^{comp} (2.31 cm), are higher than the highest values for discharges in D_2 and in the Ar pressure range I. While the smallest z_{pmax}^{comp} - z_{p0}^{comp} (1.14 cm) is smaller than the smallest z_{pmax}^{comp} - z_{p0}^{comp} for discharges in D_2 but higher than the smallest z_{pmax}^{comp} - z_{p0}^{comp} in the Ar pressure range I. All the V_{p0}^{comp} - V_{pf}^{comp} (maximum 3.58 cm^3 and minimum 3.10 cm^3) are positive and higher in comparison to the highest values for discharges in D_2. And also the smallest V_{p0}^{comp} - V_{pf}^{comp} is higher than the smallest positive V_{p0}^{comp} - V_{pf}^{comp} in Ar pressure range I. All the n_{pmax}^{comp} - n_{p0}^{comp} (maximum 64×10^{17} 1/cm^3 and minimum 10×10^{17} 1/cm^3) are far higher than the highest n_{pmax}^{comp} - n_{p0}^{comp} for discharges in D_2 and higher than for initial Ar pressure range I.

Summarizing, based mainly on the determined r_{pmin}^{comp}, n_{pmax}^{comp}, r_{p0}^{comp} - r_{pmin}^{comp} and n_{pmax}^{comp} - n_{p0}^{comp}, relativly strong plasma radiative compression phenomenon is stated for the theoretical discharges in the PF-24 operated with the 1.70-4.20 mbar of initial Ar pressures **range II**.

The results of investigation of the computed discharges in about 1.20 mbar of initial Ar pressure are divated into two groups considering occurrence of strong plasma radiative compression phenomenon (table 8.9.1). For the **group I** the Y_{line}^{comp} are in the range of 41-108 J/discharge – far higher values in comparison to the discharges in D_2 (table 8.8.1). This is followed by the big $I_{P-B}(t_1)^{comp}$ (minimum 768 kA) and the small $I_{P-Breduced}(t_1)^{comp}$ (maximum 46 kA) in comparison to the $I_{pp}(t_1)^{comp}$ (minimum 97 kA) for 3 of 5 discharges. While for the 2 discharges of 5 extremely high values of $I_{P-B}(t_1)^{comp}$ and $I_{P-Breduced}(t_1)^{comp}$ are stated – far higher than the corresponding $I_{pp}(t_1)^{comp}$ (maximum 341 kA). The achived t_Q^{comp} (maximum 0.3 ns) are positive and very small in comparison to t_{pl}^{comp} (minimum 29 ns) and t_{rcl}^{comp} (minimum 6 ns) for 3 of 5 discharges. While for the 2 discharges of 5 the t_{rcl}^{comp} are equal to 0 ns – discharges with very high level of $I_{P-B}(t_1)^{comp}$ and $I_{P-Breduced}(t_1)^{comp}$ and plasma opacity. The highest U_{max}^{comp} is equal to 25 kV, which is smaller than the maximum for the discharges in D_2. All the r_{pmin}^{comp} (minimum 0.14 cm and maximum 0.36 cm) and the V_{pf}^{comp} (minimum 0.31 cm^3 and maximum 1.82 cm^3) are smaller than the smallest values for discharges in D_2. All the z_{pmax}^{comp} (maximum 5.19 cm and minimum 4.48 cm) and n_{pmax}^{comp} (maximum 7.76x10^{17} 1/cm^3 and minimum 0.93x10^{17} 1/cm^3) are smaller than the highest values for discharges in D_2. Moreover, the highest r_{p0}^{comp} - r_{pmin}^{comp} (0.19 cm) is higher than the highest r_{p0}^{comp} - r_{pmin}^{comp} for discharges in D_2, while the smallest r_{p0}^{comp} - r_{pmin}^{comp} (0.06 cm) is equal to the highest r_{p0}^{comp} - r_{pmin}^{comp} for discharges in D_2. All the z_{pmax}^{comp} - z_{p0}^{comp} (maximum 1.51 cm and minimum 0.81 cm) are smaller than the highest z_{pmax}^{comp} - z_{p0}^{comp} for discharges in D_2. All the V_{p0}^{comp} - V_{pf}^{comp} (maximum 0.93 cm^3 and minimum 0.06 cm^3) are positive and the highest V_{p0}^{comp} - V_{pf}^{comp} is higher than the highest positive value obtained in D_2, while the smallest V_{p0}^{comp} - V_{pf}^{comp} is smaller than the smallest positive value obtained in D_2. All the n_{pmax}^{comp} - n_{p0}^{comp} (maximum 6.32x10^{17} 1/cm^3 and minimum 0.27x10^{17} 1/cm^3) are smaller than the highest n_{pmax}^{comp} - n_{p0}^{comp} for discharges in D_2.

Summarizing, based mainly on the determined r_{pmin}^{comp}, n_{pmax}^{comp}, r_{p0}^{comp} - r_{pmin}^{comp} and n_{pmax}^{comp} - n_{p0}^{comp}, the weak plasma radiative compression phenomenon is stated for the **group I** of computed discharges in the PF-24 operated with the 1.2(±0.1) mbar of initial Ar pressure.

On the other hand, for the **group II** of discharges in about 1.20 mbar of initial Ar pressure (table 8.9.1) the Y_{line}^{comp} are in the range of 221-348 J/discharge – far higher values in comparison to the discharges in D_2 (table 8.8.1) and higher than for the discharges in Ar group I (table 8.9.1). This is followed by the relatively big $I_{P\text{-}B}(t_1)^{comp}$ (minimum 823 kA) and the relatively small $I_{P\text{-}Breduced}(t_1)^{comp}$ (maximum 28 kA) in comparison to the $I_{pp}(t_1)^{comp}$ (minimum 170 kA). Also, the acheived t_Q^{comp} (minimum 0.0007 ns and maximum 0.0008 ns) are always positive and very small in comparison to t_{pl}^{comp} (minimum 58 ns) and t_{rcl}^{comp} (minimum 5 ns). The highest U_{max}^{comp} equal to 41 kV – smaller value than the highest U_{max}^{comp} for discharges in D_2 but higher than the highest U_{max}^{comp} for discharges in Ar group I. All the r_{pmin}^{comp} (minimum 0.11 cm and maximum 0.19 cm) and V_{pf}^{comp} (minimum 0.22 cm^3 and maximum 0.63 cm^3) are smaller than the smallest values for discharges in D_2. And the highest r_{pmin}^{comp} is smaller than the highest r_{pmin}^{comp} for the discharges in Ar group I and the smallest r_{pmin}^{comp} is smaller than the smallest r_{pmin}^{comp} for the discharges in Ar group I. Also the smallest V_{pf}^{comp} is smaller than the smallest V_{pf}^{comp} for discharges in Ar group I. All the z_{pmax}^{comp} (maximum 5.92 cm and minimum 5.50 cm) and all the n_{pmax}^{comp} (maximum 19.76×10^{17} $1/cm^3$ and minimum 12.37×10^{17} $1/cm^3$) are higher than the results for discharges in D_2 and in Ar group I. Moreover, all the r_{p0}^{comp} - r_{pmin}^{comp} (maximum 0.25 cm and minimum 0.18 cm) are higher than the highest r_{p0}^{comp} - r_{pmin}^{comp} for discharges in D_2. And the smallest r_{p0}^{comp} - r_{pmin}^{comp} (0.18 cm) is almost as high as the highest r_{p0}^{comp} - r_{pmin}^{comp} for discharges in Ar group I. All the z_{pmax}^{comp} - z_{p0}^{comp} (maximum 2.29 cm and minimum 1.82 cm), all the V_{p0}^{comp} - V_{pf}^{comp} (maximum 1.27 cm^3 and minimum 0.94 cm^3) and all the n_{pmax}^{comp} - n_{p0}^{comp} (maximum 17.70×10^{17} $1/cm^3$ and minimum 9.18×10^{17} $1/cm^3$) are higher than the highest obtained values for discharges in D_2 and in Ar group I.

Summarizing, based mainly on the determined r_{pmin}^{comp}, n_{pmax}^{comp}, r_{p0}^{comp} - r_{pmin}^{comp} and n_{pmax}^{comp} - n_{p0}^{comp}, the relatively strong plasma radiative compression phenomenon was stated for the **group II** of discharges in the PF-24 operated with the 1.2(±0.1) mbar of initial Ar pressure.

Moreover, the results of investigation, based on the 10 computed discharges in about 1.2 mbar of Ar (table 8.9.1) differ from the results based on the 9 theoretical discharges in 0.50-1.60 mbar and 4.50-5.00 mbar of initial Ar pressure range I (table 8.9.1) in terms of plasma radiative compression phenomenon strength, considering the group II of computed discharges. For the group I of computed discharges in about 1.20 mbar of initial Ar pressure (table 8.9.1) the range of changes of Y_{line}^{comp} (41-108 J/discharge) is within the range of Y_{line}^{comp} (5-530 J/discharge) for Ar range I. The r_{pmin}^{comp}, r_{p0}^{comp} - r_{pmin}^{comp}, z_{pmax}^{comp}, z_{pmax}^{comp} - z_{p0}^{comp}, V_{pf}^{comp}, V_{p0}^{comp} - V_{pf}^{comp}, n_{pmax}^{comp} and n_{pmax}^{comp} - n_{p0}^{comp} parameters describing plasma pinch have similar values for both range I and group I for the most part (ranges of values of parameters mostly overlap) and partially do not exceed the highest or smallest values achived for discharges in D_2 (for example the n_{pmax}^{comp} and n_{pmax}^{comp} - n_{p0}^{comp} parameters for Ar range I and Ar group I do not exceed highest values in D_2). So, the results based on the theoretical discharges in Ar **range I** and computed discharges in Ar **group I** are not so much different in terms of strength of radiative compression – for both only weak or non-existent radiative compression was stated. On the other hand, for the group II of computed discharges also in about 1.20 mbar of initial Ar pressure (table 8.9.1) the range of changes of Y_{line}^{comp} is equal to 221-348 J/discharge – middle region of the Y_{line}^{comp} for range I. The r_{pmin}^{comp}, r_{p0}^{comp} - r_{pmin}^{comp}, z_{pmax}^{comp}, z_{pmax}^{comp} - z_{p0}^{comp}, V_{pf}^{comp}, V_{p0}^{comp} - V_{pf}^{comp}, n_{pmax}^{comp} and n_{pmax}^{comp} - n_{p0}^{comp} parameters for Ar group II are in the most part different from the ones achived for Ar range I (ranges of values of parameters mostly do not overlap) and they exceed all the values of parameters for discharges in D_2 – strong radiative compression was stated for discharges in Ar group II.

So, both **range I** and **group II** differ significantly in terms of strenght of the plasma radiative compression despite the occurrence of discharges in the same initial Ar pressure range. In fact, the computed discharges in about 1.2 mbar from **group II** reassemble more the theoretical discharges in 1.70-4.20 mbar of initial Ar pressures (Ar **range II**) taking into account ranges of values of r_{pmin}^{comp}, r_{p0}^{comp} - r_{pmin}^{comp}, z_{pmax}^{comp}, z_{pmax}^{comp} - z_{p0}^{comp}, V_{pf}^{comp}, V_{p0}^{comp} - V_{pf}^{comp}, n_{pmax}^{comp} and n_{pmax}^{comp} - n_{p0}^{comp} parameters and strength of radiative compression (for the Ar range II strong radiative compression was stated), despite the fact that for the Ar pressure range II the Y_{line}^{comp} changed between 649 J/discharge and 1702 J/discharge (ranges of values of Y_{line}^{comp} for group II and range II do not overlap). This proves that there is no abosolute range of initial Ar pressures and total yields of X-ray line radiation for which strong radiative compression would occure. Neverthless, Y_{line}^{comp} is still stated to be the most important parameter concerning radiative compression investigation during z-pinch discharges but it is not the only one which should be taken into account while investigating plasma pinch compression.

For purposes of further analysis and comparison in table 8.9.2 the highest and smallest values of indicators and parameters are presented for the theoretical discharges in 1.50-1.60 mbar of initial Ar pressure (part of Ar pressure range I) and for the computed discharges in about 1.2 mbar of initial Ar pressure for group II.

Table 8.9.2. Summary of the highest and smallest values of parameters and indicators (see subsection 6.3.3) describing plasma pinch compression for the 2 theoretical discharges in 1.50-1.60 mbar of initial Ar pressure (part of Ar pressure range I) and for the group II (#17101814, #17101816, #17102007, #17102009 and #17102016) of the computed discharges in 1.2 mbar of initial Ar pressure.

Ar Indicator/parameter			**Theoretical**	**Computed**	Unit
			Pressure (mbar)		
			1.5-1.6	1.2	
				group II	
U_{max}^{comp}	maximum voltage	highest	30	41	kV
		smallest	20	23	
$I_{pp}(t_1)^{comp}$	pinch plasma current at t_1	highest	362	216	kA
		smallest	347	170	
$I_{P\text{-}B}(t_1)^{comp}$	P-B current at t_1	highest	774	2605	kA
		smallest	769	823	
$I_{P\text{-}Breduced}(t_1)^{comp}$	reduced P-B current at t_1	highest	32	28	kA
		smallest	29	12	
t_{pl}^{comp}	pinch lifetime	highest	42	70	ns
		smallest	41	58	
t_{rcl}^{comp}	radiative compression lifetime	highest	42	12	ns
		smallest	41	5	
t_Q^{comp}	characteristic radiation depletion time	highest	0.0289	0.0008	ns
		smallest (positive)	0.0185	0.0007	
r_{p0}^{comp}	**initial pinch radius**	**highest**	**0.53**	**0.37**	**cm**
		smallest	**0.53**	**0.35**	
r_{pmin}^{comp}	**minimum pinch radius**	**highest**	**0.34**	**0.19**	**cm**
		smallest	**0.27**	**0.11**	
r_{p0}^{comp} - r_{pmin}^{comp}	**change of pinch radius**	**highest**	**0.26**	**0.25**	**cm**
		smallest	**0.19**	**0.18**	

z_{p0}^{comp}	initial pinch length	highest	3.93	3.7	cm
		smallest	3.93	3.63	
z_{pmax}^{comp}	maximum pinch length	highest	4.96	5.92	cm
		smallest	4.92	5.5	
$z_{pmax}^{comp} - z_{p0}^{comp}$	change of pinch length	highest	1.03	2.29	cm
		smallest	0.99	1.82	
V_{p0}^{comp}	initial pinch volume	highest	3.47	1.59	cm^3
		smallest	3.47	1.4	
V_{pf}^{comp}	final pinch volume	highest	1.79	0.63	cm^3
		smallest	1.14	0.22	
$V_{p0}^{comp} - V_{pf}^{comp}$	change of pinch volume	highest	2.33	1.27	cm^3
		smallest	1.68	0.94	
n_{p0}^{comp}	**initial total pinch density**	**highest**	**0.98**	**3.38**	**10^{17} cm^{-3}**
		smallest	**0.9**	**1.54**	
n_{pmax}^{comp}	**maximum total pinch density**	**highest**	**3.59**	**19.8**	**10^{17} cm^{-3}**
		smallest	**2.22**	**12.4**	
$n_{pmax}^{comp} - n_{p0}^{comp}$	**change of total pinch density**	**highest**	**2.61**	**17.7**	**10^{17} cm^{-3}**
		smallest	**1.32**	**9.2**	
N_{p0}^{comp}	initial total linear pinch density	highest	0.86	1.45	10^{17} cm^{-1}
		smallest	0.79	0.59	
N_{pf}^{comp}	final total linear pinch density	highest	0.82	1.43	10^{17} cm^{-1}
		smallest	0.81	0.63	
$\lvert N_{pf}^{comp} - N_{p0}^{comp}\rvert$	change of total linear pinch density	highest	0.04	0.04	10^{17} cm^{-1}
		smallest	0.01	0.02	
T_{p0}^{comp}	**initial pinch temperature**	**highest**	**0.43**	**0.11**	**keV**
		smallest	**0.4**	**0.08**	
T_{pmin}^{comp}	minimum pinch temperature	highest	0.31	0.1	keV
		smallest	0.27	0.08	
$T_{p0}^{comp} - T_{pmin}^{comp}$	change of pinch temperature	highest	0.13	0.02	keV
		smallest	0.12	< 0.01	
Y_{ohm}^{omp}	total ohmic heating yield	highest	14.7	161	J/discharge
		smallest	11.1	98	
Y_{brem}^{comp}	total X-ray bremsstrahlung yield	highest	3.09	0.13	J/discharge
		smallest	2.45	0.05	
Y_{rec}^{comp}	total X-ray recombination yield	highest	72	3.96	J/discharge
		smallest	53	1.49	
Y_{line}^{comp}	**total X-ray line yield**	**highest**	**530**	**348**	**J/discharge**
		smallest	**356**	**221**	
Y_{totrad}^{comp}	total X-ray yield	highest	605	353	J/discharge
		smallest	411	223	
Y_{eff}^{comp}	effective total X-ray yield	highest	591	192	J/discharge
		smallest	400	124	
Y_{n}^{comp}	total neutron yield	highest	-	-	×10^8 n/discharge
		smallest	-	-	

For the two theoretical discharges in 1.50-1.60 mbar of initial Ar pressures (part of Ar **range I**) the Y_{line}^{comp} is equal to 356-530 J/discharge (table 8.9.2). While for the **group II** of computed discharges in about 1.20 mbar of Ar the Y_{line}^{comp} varied between 221 J/discharge and 348 J/discharge. So, the Y_{line}^{comp} values alone indicate stronger radiative compression for the 2 theoretical discharges, however this is not true. The $I_{P\text{-}Breduced}(t_1)^{comp}$ (29-32 kA) for the 2 theoretical discharges are about 11-12 times smaller than the corresponding $I_{pp}(t_1)^{comp}$ (347-362 kA). Similarly, for the 5 computed discharges the $I_{P\text{-}Breduced}(t_1)^{comp}$ (12-28 kA) are about 8-14 times smaller than the corresponding pinch plasma currents (170-216 kA). Thus, the $I_{P\text{-}Breduced}(t_1)^{comp}$ and $I_{pp}(t_1)^{comp}$ indicators do not show a clear situation – based only on them it is impossible to determine for which group of discharges stronger radiative compression occurs. The t_Q^{comp} (0.02-0.03 ns) for the 2 theoretical discharges are very small in comparison to t_{pl}^{comp} and t_{rcl} (both 41-42 ns). And the ratios of t_{pl}^{comp} / t_Q^{comp} and t_{rcl}^{comp} / t_Q^{comp} are in the range of: 1367-2100. For the 5 computed discharges, the t_Q^{comp} are even smaller (0.0007-0.0008 ns) while the t_{pl}^{comp} are bigger (58-70 ns) and t_{rcl} are smaller (5-12 ns). So, the ratio of t_{pl}^{comp} / t_Q^{comp} for the 5 computed discharges are in the range of about: 72500-100000, while the t_{rcl}^{comp} / t_Q^{comp} are in the range of about: 6250-17143. Thus, the t_{pl}^{comp} / t_Q^{comp} and t_{rcl}^{comp} / t_Q^{comp} ratios are larger for the 5 computed discharges from the Ar **group II** than for the 2 theoretical discharges from Ar **range I**, indicating correctly stronger radiative compression for the 5 computed discharges.

Summarizing, only the time parameters together indicate correctly the stronger radiative compression for the group II of computed discharges. However, the time parameters alone are not always able to determine correctly the strength of radiative compression. For example in the case of the Ar group I of computed discharges, the very low t_Q^{comp} are stated for four discharges (comparable as in the group II) but, no strong radiative compression was determined for them.

The other total yields of X-ray radiation (except the Y_{line}^{comp}) and ohmic heating yield for the 2 theoretical discharges from Ar **range I** and for the 5 computed discharges from Ar **group II** also do not indicate properly about the strength of radiative compression – for example Y_{eff}^{comp} is higher for the 2 theoretical discharges (table 8.9.2). Analyzing further, for the two groups of discharges only the following four parameters describing the initial state of the plasma pinch are significantly different: r_{p0}^{comp}, V_{p0}^{comp}, n_{p0}^{comp} and T_{p0}^{comp} (see table 8.9.2). However, the V_{p0}^{comp} depends only on the r_{p0}^{comp} and z_{p0}^{comp} parameters. So, the initial pinch radius, the initial pinch ion number density and the initial pinch ion temperature must also strongly influence the development of the radiative compression during z-pinch discharges. For the strong radiative compression phenomenon occurrence smaller values of r_{p0} and T_{p0} together with the higher values of n_{p0} appear to be preferable (as was indicated by some of the previous investigators – see section 2.3). In relatively thiner, cooler and denser initial plasma pinches stronger radiative compression can eventually develop. Still, the Y_{line}^{comp} has to be significantly higher than for the discharges in D_2 – at least at the level of 221J/discharge according to the investigated theoretical and computed discharges in the PF-24 (this is also connected with Y_{line}^{comp} and X-ray and ohmic heating yields being dependent on r_{p0}^{comp}, T_{p0}^{comp} and n_{p0}^{comp} – see equations from (2.1.19) to (2.1.21) and (6.2.37) and subsection 8.7.1 – feedback type of relations).

Summarizing, the occurrence of strong plasma radiative compression phenomenon should be dependent and predicted based on the 4 following parameters toogether: $\boldsymbol{Y_{line}}$, $\boldsymbol{r_{p0}}$, $\boldsymbol{T_{p0}}$ and $\boldsymbol{n_{p0}}$ (this is in agreement with the achieved values in table 8.9.1 and table 8.9.2). The: $I_{P\text{-}Breduced}(t_1)$, $I_{pp}(t_1)$, t_Q, t_{rcl} and t_{pl} indicators appear to be less accurate and useful for the predictions concerning radiative compression. This should also apply to the discharges in gas mixtures like in D_2+Ar.

8.10. Summary and comparison of radiative compression indicators and plasma pinch parameters for discharges in D_2+Ar mixtures

Table 8.10.1 lists the indicators and parameters describing the plasma pinch compression for discharges in (100%-*x*)D_2+*x*Ar gas mixtures. The results obtained for the theoretical discharges in the constant initial total pressure of 3.0 mbar are presented separately for 1-45% and 50-95% of Ar in the mixture. The results for the 69 computed discharges in the constant initial total pressure of 2.9(±0.2) mbar are obtained for 3(±0.4)% to 60(±4.2)% of Ar in the gas mixtures.

Table 8.10.1. Summary of the highest and smallest values of parameters and indicators (see subsection 6.3.3) describing plasma pinch compression for the 21 theoretical discharges in 1-95% of Ar in (100%-*x*)D_2+*x*Ar gas mixtures at 3.0 mbar of constant initial total gas pressure and the 69 computed discharges in about 3-60% of Ar in (100%-*x*)D_2+*x*Ar gas mixtures at about 2.9 mbar of constant initial total gas pressure.

(100%-*x*)D_2+*x*Ar Indicator/parameter			**Theoretical**		**Computed**	Unit
			Ar fraction (%)			
			1-45	50-95	3-60	
			range I	**range II**		
U_{max}^{comp}	maximum voltage	highest	56	148	68	kV
		smallest	43	68	19	
$I_{pp}(t_1)^{comp}$	pinch plasma current at t_1	highest	390	393	380	kA
		smallest	360	378	110	
$I_{P\text{-}B}(t_1)^{comp}$	P-B current at t_1	highest	1349	842	19742	kA
		smallest	846	799	793	
$I_{P\text{-}Breduced}(t_1)^{comp}$	reduced P-B current at t_1	highest	1035	26	382	kA
		smallest	27	19	20	
t_{pl}^{comp}	pinch lifetime	highest	40	57	57	ns
		smallest	25	41	21	
t_{rcl}^{comp}	radiative compression lifetime	highest	40	43	42	ns
		smallest	0	19	0	
t_Q^{comp}	characteristic radiation depletion time	highest	43	0.0129	305	ns
		smallest (positive)	0.025	0.0003	0.083	
r_{p0}^{comp}	**initial pinch radius**	**highest**	**0.71**	**0.54**	**0.57**	**cm**
		smallest	**0.54**	**0.53**	**0.36**	
r_{pmin}^{comp}	**minimum pinch radius**	**highest**	**0.66**	**0.26**	**0.53**	**cm**
		smallest	**0.34**	**0.12**	**0.25**	
$r_{p0}^{comp} - r_{pmin}^{comp}$	**change of pinch radius**	**highest**	**0.2**	**0.42**	**0.12**	**cm**
		smallest	**0.04**	**0.27**	**0.04**	
z_{p0}^{comp}	initial pinch length	highest	3.98	3.99	3.76	cm
		smallest	3.92	3.93	3.52	
z_{pmax}^{comp}	maximum pinch length	highest	4.89	5.98	5.1	cm
		smallest	4.8	4.97	3.86	

$z_{pmax}^{comp} - z_{p0}^{comp}$	change of pinch length	highest	0.96	1.99	1.37	cm
		smallest	0.84	1.04	0.24	
V_{p0}^{comp}	initial pinch volume	highest	6.3	3.66	3.84	cm^3
		smallest	3.59	3.47	1.44	
V_{pf}^{comp}	final pinch volume	highest	6.6	1.06	4.25	cm^3
		smallest	1.78	0.27	0.77	
$V_{p0}^{comp} - V_{pf}^{comp}$	change of pinch volume	highest	1.82	3.38	0.8	cm^3
		smallest	negative	2.41	negative	
$\boldsymbol{n_{p0}^{comp}}$	**initial total pinch density**	**highest**	**2.86**	**2.69**	**6.22**	**10^{17} cm^{-3}**
		smallest	**2.04**	**1.83**	**0.21**	
$\boldsymbol{n_{pmax}^{comp}}$	**maximum total pinch density**	**highest**	**7.03**	**37**	**7.42**	**10^{17} cm^{-3}**
		smallest	**2.36**	**12**	**0.27**	
$\boldsymbol{n_{pmax}^{comp} - n_{p0}^{comp}}$	**change of total pinch density**	**highest**	**4.28**	**35.15**	**1.62**	**10^{17} cm^{-3}**
		smallest	**0.32**	**9.04**	**0.06**	
N_{p0}^{comp}	initial total linear pinch density	highest	3.23	2.37	6.13	10^{17} cm^{-1}
		smallest	2.52	1.7	0.12	
N_{pf}^{comp}	final total linear pinch density	highest	3.23	2.49	6.06	10^{17} cm^{-1}
		smallest	2.55	1.61	0.12	
$\lvert N_{pf}^{comp} - N_{p0}^{comp}\rvert$	change of total linear pinch density	highest	0.05	0.13	0.16	10^{17} cm^{-1}
		smallest	< 0.01	0.01	< 0.01	
$\boldsymbol{T_{p0}^{comp}}$	**initial pinch temperature**	**highest**	**0.71**	**0.26**	**0.74**	**keV**
		smallest	**0.27**	**0.18**	**0.16**	
T_{pmin}^{comp}	minimum pinch temperature	highest	0.59	0.19	0.66	keV
		smallest	0.21	0.11	0.09	
$T_{p0}^{comp} - T_{pmin}^{comp}$	change of pinch temperature	highest	0.12	0.07	0.09	keV
		smallest	0.05	0.06	< 0.01	
Y_{ohm}^{comp}	total ohmic heating yield	highest	9	246	3.36	J/discharge
		smallest	0.08	14	0.06	
Y_{brem}^{comp}	total X-ray bremsstrahlung yield	highest	1.262	1.6	0.1355	J/discharge
		smallest	0.003	0.73	0.0001	
Y_{rec}^{comp}	total X-ray recombination yield	highest	35	46	3.7	J/discharge
		smallest	0.0003	23	0.0015	
$\boldsymbol{Y_{line}^{comp}}$	**total X-ray line yield**	**highest**	**396**	**1337**	**40**	**J/discharge**
		smallest	**0.0013**	**633**	**0.0074**	
Y_{totrad}^{comp}	total X-ray yield	highest	432	1360	44	J/discharge
		smallest	0.005	680	0.069	
Y_{eff}^{comp}	effective total X-ray yield	highest	423	1132	41	J/discharge
		smallest	negative	666	negative	
Y_{n}^{comp}	total neutron yield	highest	20.3	110	15.9	×10^8 n/discharge
		smallest	5.5	26	0.04	

The parameters and indicators obtained for the theoretical and computed discharges in Ar are collected in table 8.10.1. The results for theoretical discharges in 1-45% of Ar (Ar fraction range I) differ from the results in 50-95% of Ar (Ar fraction range II) considering the occurrence and strength of plasma radiative compression phenomenon. For the 11 investigated theoretical discharges in the **Ar fraction range I** the Y_{line}^{comp} change in the wide range of 0.001-396 J/discharge. Only the two smallest Y_{line}^{comp} values (0.001-0.03 J/discharge) are smaller or equal to the highest Y_{line}^{comp} calculated for the discharges in D_2 (table 8.8.1), while the most of Y_{line}^{comp} values (6-396 J/discharge) are far higher in comparison to the highest Y_{line}^{comp} for the discharges in D_2. This is followed by the relatively high $I_{P\text{-}B}(t_1)^{comp}$ (minimum 846 kA) and relatively small $I_{P\text{-}Breduced}(t_1)^{comp}$ (27-327 kA) for most of discharges in comparison to the $I_{pp}(t_1)^{comp}$ (360-390 kA), although for two discharges $I_{P\text{-}Breduced}(t_1)^{comp}$ (327-1035 kA) are higher or similar to the corresponding $I_{pp}(t_1)^{comp}$ (360-366 kA). The most of t_Q^{comp} values (0.03-6.51 ns) are positive and far smaller than the corresponding t_{pl}^{comp} (28-40 ns) and t_{rcl}^{comp} (28-40 ns) values, wherein for two discharges t_Q^{comp} are negative and for one discharge t_Q^{comp} (43 ns) is higher than the corresponding t_{pl}^{comp} (26 ns) and t_{rcl}^{comp} (26 ns). This results in the highest U_{max}^{comp} equal to 56 kV, what is smaller than the highest U_{max}^{comp} for discharges in D_2. The smallest r_{pmin}^{comp} (0.34 cm) is smaller than the smallest r_{pmin}^{comp} for discharges in D_2, while the highest r_{pmin}^{comp} (0.66 cm) is higher than the smallest r_{pmin}^{comp} for discharges in D_2. The highest z_{pmax}^{comp} (4.89 cm) is smaller than the highest z_{pmax}^{comp} for discharges in D_2. The smallest V_{pf}^{comp} (1.78 cm^3) is smaller in comparison to smallest V_{pf}^{comp} for discharges in D_2. While the highest V_{pf}^{comp} (6.60 cm^3) is higher than the smallest V_{pf}^{comp} for discharges in D_2. And all the n_{pmax}^{comp} (maximum 7.03×10^{17} 1/cm^3 and minimum 2.36×10^{17} 1/cm^3) are smaller than the highest n_{pmax}^{comp} for discharges in D_2. Moreover, the highest r_{p0}^{comp} - r_{pmin}^{comp} (0.20 cm) is higher than the highest r_{p0}^{comp} - r_{pmin}^{comp} for discharges in D_2. While the smallest r_{p0}^{comp} - r_{pmin}^{comp} (0.04 cm) is equal to the smallest r_{p0}^{comp} - r_{pmin}^{comp} for the discharges in D_2. All the z_{pmax}^{comp} - z_{p0}^{comp} (maximum 0.96 cm and minimum 0.84 cm) are smaller than the highest z_{pmax}^{comp} - z_{p0}^{comp} for discharges in D_2. The highest V_{p0}^{comp} - V_{pf}^{comp} (1.82 cm^3) is positive and higher in comparison to the highest positive V_{p0}^{comp} - V_{pf}^{comp} for discharges in D_2. While the smallest V_{p0}^{comp} - V_{pf}^{comp} is negative. The highest n_{pmax}^{comp} - n_{p0}^{comp} (4.28×10^{17} 1/cm^3) is higher than the highest n_{pmax}^{comp} - n_{p0}^{comp} for discharges in D_2. While the smallest n_{pmax}^{comp} - n_{p0}^{comp} (0.32×10^{17} 1/cm^3) is smaller than the highest n_{pmax}^{comp} - n_{p0}^{comp} for discharges in D_2.

Summarizing, based mainly on the determined r_{pmin}^{comp}, n_{pmax}^{comp}, r_{p0}^{comp} - r_{pmin}^{comp} and n_{pmax}^{comp} - n_{p0}^{comp}, the relatively weak or non-existent plasma radiative compression phenomenon is stated for the theoretical discharges in the PF-24 operated with 1-45% of Ar (**Ar fraction range I**) in $(100\%\text{-}x)D_2\text{+}x\text{Ar}$ gas mixture and at constant initial total pressure of mixtures equal to 3.0 mbar.

On the other hand, for the 10 investigated theoretical discharges in the 50-95% of Ar (**Ar fraction range II**) (table 8.10.1) the Y_{line}^{comp} are in the range of 633-1337 J/discharge – far higher than in D_2 (table 8.8.1) and higher than in 1-45% of Ar fraction (table 8.10.1). This is followed by the relatively big $I_{P\text{-}B}(t_1)^{comp}$ (minimum 799 kA) and the relatively small $I_{P\text{-}Breduced}(t_1)^{comp}$ (maximum 26 kA) in comparison to the $I_{pp}(t_1)^{comp}$ (minimum 378 kA). The acheived t_Q^{comp} (minimum 0.0003 ns and maximum 0.01 ns) are far smaller than the t_{pl}^{comp} (minimum 41 ns) and t_{rcl}^{comp} (minimum 19 ns). This results in the highest U_{max}^{comp} equal to 148 kV – higher value than the highest U_{max}^{comp} for discharges in D_2 and in the Ar fraction range I, although, the smallest U_{max}^{comp} (68 kV) is smaller than the highest U_{max}^{comp} in D_2. All the r_{pmin}^{comp} (minimum 0.12 cm and maximum 0.26 cm) and the V_{pf}^{comp} (minimum 0.27 cm^3 and maximum 1.06 cm^3) are smaller than the smallest r_{pmin}^{comp} and V_{pf}^{comp} in both D_2 and the Ar fraction range I. The highest z_{pmax}^{comp} (5.98 cm) is higher than the highest z_{pmax}^{com} in D_2 and in Ar fraction range I, while the smallest z_{pmax}^{comp} (4.97 cm) is smaller than the highest z_{pmax}^{comp} for discharges in D_2 but also higher than the highest z_{pmax}^{comp} in Ar fraction range I. All the n_{pmax}^{comp} (maximum 37×10^{17} 1/cm^3 and minimum 12×10^{17} 1/cm^3) are higher than the highest n_{pmax}^{comp} for discharges in D_2 and in Ar fraction range I. Moreover, all the r_{p0}^{comp} - r_{pmin}^{comp} (maximum 0.42 cm and minimum 0.27 cm), the z_{pmax}^{comp} - z_{p0}^{comp} (maximum 1.99 cm and minimum 1.04 cm), the V_{p0}^{comp} - V_{pf}^{comp} (maximum 3.38 cm^3 and minimum 2.41 cm^3) and the n_{pmax}^{comp} - n_{p0}^{comp} (maximum 35×10^{17} 1/cm^3 and minimum 9×10^{17} 1/cm^3) are higher or far higher than the highest values of the corresponding parameters obtained in D_2 and in Ar fraction range I.

Summarizing, based mainly on the determined r_{pmin}^{comp}, n_{pmax}^{comp}, r_{p0}^{comp} - r_{pmin}^{comp} and n_{pmax}^{comp} - n_{p0}^{comp}, relativly strong plasma radiative compression phenomenon is stated for the theoretical discharges in the PF-24 operated with 50-95% of Ar (**Ar fraction range II**) in (100%-x)D_2+xAr gas mixtures and at constant initial total pressure of mixtures equal to 3.0 mbar.

For the 69 **computed** discharges in about 2.9 mbar of initial Ar pressure (**3-60% range of Ar fractions**) (table 8.10.1) the Y_{line}^{comp} change in the range of 0.01-40 J/discharge. But the smallest value of Y_{line}^{comp} (0.01 J/discharge) is achieved only for one discharge, while the rest Y_{line}^{comp} varies between 0.04 J/discharge and 40 J/discharge, being much higher than the highest Y_{line}^{comp} value for the discharges in D_2 (table 8.8.1). This is followed by the relatively big $I_{P\text{-}B}(t_1)^{comp}$ (minimum 793 kA) and $I_{P\text{-}Breduced}(t_1)^{comp}$ (109-382 kA), and relatively small $I_{P\text{-}Breduced}(t_1)^{comp}$ (20-106 kA) in comparison to the $I_{pp}(t_1)^{comp}$ (minimum 110 kA and maximum 380 kA). The achieved values of the t_Q^{comp} (minimum 0.1 ns and maximum 305 ns) are not always positive and small in comparison to t_{pl}^{comp} (minimum 21 ns and maximum 57 ns) and t_{rcl}^{comp} (maximum 41 ns and minimum 0 ns). This results in the highest U_{max}^{comp} equal to 68 kV – smaller value than the highest U_{max}^{comp} achieved for discharges in D_2. The smallest r_{pmin}^{comp} (0.25 cm) is smaller than the smallest r_{pmin}^{comp} for discharges in D_2, while the highest r_{pmin}^{comp} (0.53 cm) is slightly higher than the smallest r_{pmin}^{comp} for discharges in D_2. The highest z_{pmax}^{comp} (5.10 cm) is smaller than the highest z_{pmax}^{comp} for discharges in D_2. The smallest V_{pf}^{comp} (0.77 cm^3) is smaller in comparison to smallest V_{pf}^{comp} for discharges in D_2. While the highest V_{pf}^{comp} (4.25 cm^3) is higher than the highest V_{pf}^{comp} for discharges in D_2. All the n_{pmax}^{comp} (maximum 7.42×10^{17} 1/cm^3 and minimum 0.27×10^{17} 1/cm^3) are smaller than the highest n_{pmax}^{comp} for discharges in D_2. Moreover, the highest r_{p0}^{comp} - r_{pmin}^{comp} (0.12 cm) is higher than the highest r_{p0}^{comp} - r_{pmin}^{comp} for discharges in D_2, while the smallest r_{p0}^{comp} - r_{pmin}^{comp} (0.04 cm) is equal to the smallest r_{p0}^{comp} - r_{pmin}^{comp} for the discharges in D_2. All the z_{pmax}^{comp} - z_{p0}^{comp} (maximum 1.37 cm and minimum 0.24 cm) are smaller than the highest z_{pmax}^{comp} - z_{p0}^{comp} for discharges in D_2. The highest V_{p0}^{comp} - V_{pf}^{comp} (0.80 cm^3) is positive and higher in comparison to the highest positive V_{p0}^{comp} - V_{pf}^{comp} for discharges in D_2. While the smallest V_{p0}^{comp} - V_{pf}^{comp} are negative. The highest n_{pmax}^{comp} - n_{p0}^{comp} (1.62×10^{17} 1/cm^3) is higher than the highest n_{pmax}^{comp} - n_{p0}^{comp} for discharges in D_2, while the smallest n_{pmax}^{comp} - n_{p0}^{comp} (0.06×10^{17} 1/cm^3) is smaller than the smallest n_{pmax}^{comp} - n_{p0}^{comp} for discharges in D_2.

Summarizing, based mainly on the determined r_{pmin}^{comp}, n_{pmax}^{comp}, r_{p0}^{comp} - r_{pmin}^{comp} and n_{pmax}^{comp} - n_{p0}^{comp}, the relatively weak or non-existent plasma radiative compression phenomenon is stated for all the 69 **computed** discharges in the PF-24 operated with (100%-x)D_2+xAr gas mixture containg **3-60% of Ar** and at constant initial total pressure of 2.9(±0.2) mbar.

The results obtained for the 69 computed discharges in about 3-60 % of Ar (table 8.10.1) differ from the results based on the 21 theoretical discharges in 1-95% of Ar fraction (table 8.10.1) in terms of plasma radiative compression phenomenon occurrence and strength, considering the computed discharges in 50-95% range of Ar fraction. For the 69 **computed** discharges in **3-60% of Ar** the Y_{line}^{comp} change between 0.007 J/discharge and 40 J/discharge, while for the 1-45% range of Ar (**Ar fraction range I**) Y_{line}^{comp} change between 0.001 J/discharge and 396 J/discharge – Y_{line}^{comp} values for the 69 computed discharges are within the range of Y_{line}^{comp} values for Ar fraction range I. The r_{pmin}^{comp}, r_{p0}^{comp} - r_{pmin}^{comp}, z_{pmax}^{comp}, z_{pmax}^{comp} - z_{p0}^{comp}, V_{pf}^{comp}, V_{p0}^{comp} - V_{pf}^{comp}, n_{pmax}^{comp} and n_{pmax}^{comp} - n_{p0}^{comp} parameters describing plasma pinch have similar values for both 69 computed discharges and discharges from Ar fraction range I for the most part (ranges of values of parameters mostly overlap) and partially do not exceed the highest or smallest values achived for discharges in D_2 (for example the n_{pmax}^{comp} and n_{pmax}^{comp} - n_{p0}^{comp} parameters for 69 computed discharges and Ar fraction range I do not exceed highest values in D_2). So, the results based on the 69 **computed** discharges in **3-60% of Ar** and theoretical discharges in 1-45% of Ar (**Ar fraction range I)** are not so much different in terms of strength of radiative compression – for both 69 computed discharges and Ar fraction range I only weak or non-existent radiative compression was stated. On the other hand, for the theoretical discharges in 50-95% of Ar fraction (Ar fraction range II) (table 8.10.1) the range of changes of Y_{line}^{comp} is equal to 633-1337 J/discharge – the range of Y_{line}^{comp} for the 69 **computed** discharges is completely different from the one for **Ar fraction range II**. The r_{pmin}^{comp}, r_{p0}^{comp} - r_{pmin}^{comp}, z_{pmax}^{comp}, z_{pmax}^{comp} - z_{p0}^{comp}, V_{pf}^{comp}, V_{p0}^{comp} - V_{pf}^{comp}, n_{pmax}^{comp} and n_{pmax}^{comp} - n_{p0}^{comp} parameters for Ar fraction range II are in the most part different from the ones achived for the 69 computed discharges (ranges of values of parameters mostly do not overlap) and they exceed all the values of parameters for discharges in D_2 – strong radiative compression was stated only for theoretical discharges in Ar fraction range II. So, the 69 **computed** discharges in **3-60% of Ar** and theoretical discharges in 50-95% of Ar (**Ar fraction range II**) differ significantly in terms of strenght of the plasma radiative compression despite the occurrence of discharges in the partially same initial Ar fraction range. This proves that there is no abosolute range of initial Ar fractions for which strong radiative compression would occure and that occurrence of plasma radiative compression is mostly dependent on the Y_{line}^{comp} parameter.

Finally, when comparing **all the indicators and parameters** describing the plasma pinch compression, **for the computed and theoretical discharges** and taking into account groups of discharges for which relatively strong plasma radiative compression phenomenon was stated an important observations can be made:

i) The strong plasma radiative compression occurrence was stated only for the theoretical discharges in which Y_{line}^{comp} was higher than about 600 J/discharge (see table 8.9.1 – results for 1.70-4.20 mbar of initial Ar pressure and table 8.10.1 – results for 50-95% of Ar fraction in (100%-x)D_2+xAr gas mixtures). On the other hand, for the first half of computed discharges in about 1.2 mbar of initial Ar pressure the Y_{line}^{comp} is in the range of 221-347 J/discharge (table 8.9.1). However, as was explained at the end ofsection 8.9, the significant changes of the initial pinch parameters: r_{p0}^{comp}, T_{p0}^{comp} and n_{p0}^{comp}, allowed the strong plasma radiative compression phenomenon to develop more easily even below the 600 J/discharge level.

ii) The significant changes of r_{p0}^{comp}, T_{p0}^{comp} and n_{p0}^{comp} must be the result of changes of fitting parameters of the 5-phase Lee model code, enabling different scenarios of discharge development. For all theoretical discharges (including in 1.70-4.20 mbar of initial Ar pressure and 50-95% of Ar fraction) the fitting parameter were always constant (table 8.9.1). Thus, the range of changes of r_{p0}^{comp}, T_{p0}^{comp} and n_{p0}^{comp} for theoretical discharges in 1.70-4.20 mbar of initial Ar pressure (table 8.9.1) and in 50-95% of Ar fraction in (100%-x)D_2+xAr gas mixture (table 8.9.1 and 8.10.1) are similar – when fitting parameters are constant only changes in plasma compressibility can significantly alter the values of initial pinch parameters (changes of SHRs). While, for the second half of computed discharges in about 1.2 mbar of initial Ar pressure (table 8.9.1) the fitting parameters changed (including model parameters decreased with Ar fraction increase) resulting in the significantly smaller initial pinch radii and in the partially smaller initial pinch temperatures and in the significantly higher highest initial pinch densities.

9. Summary and conclusions

The results of investigation of the plasma compression presented in this work are based on the theoretical and coupled experimental-computed discharges. The experimental discharges were obtained using the plasma-focus PF-24 device, the two electric diagnostic systems and the neutron counter. The theoretical discharges and computed discharges were obtained using the 5-phase Lee model code (version RADPFV5.013.9b). The charging voltage of 17 kV and the total energy storage of 16.8 kJ were used during all simulations, computations and experiments. The obtained results of the investigations for pure D_2 (atomic number $Z = 1$) are based on: 12 theoretical discharges for different initial pressures between 0.50 mbar and 5.00 mbar, 10 coupled experimental-computed discharges for different initial pressures between 2.16(±0.01) mbar and 4.71(±0.04) mbar and 34 coupled experimental-computed discharges for constant initial D_2 pressure of 2.9(±0.1) mbar. The results for pure Ar (atomic number $Z = 18$) are based on: 21 theoretical discharges for different initial pressures between 0.50 mbar and 5.00 mbar and 10 coupled experimental-computed discharges for constant initial pressure of 1.2(±0.1) mbar. The results for the $(100\%\text{-}x)D_2\text{+}x\text{Ar}$ gas mixtures are based on: 21 theoretical discharges for various Ar fractions (x) between 1% (corresponding to the total atomic number Z = 1.17) and 95% (corresponding to the total atomic number $Z = 17.15$), and 69 coupled experimental-computed discharges for different Ar fractions (x) between 3% ($Z = 1.51$) and 60% ($Z = 11.20$). All 21 theoretical discharges were performed under constant initial total pressure of gas mixture equal to 3.0 mbar and the 69 coupled experimental-computed discharges were performed under constant initial total pressure of gas mixture of 2.9(±0.2) mbar. This value of initial D_2 pressure and the corresponding mass/density of gas in the experimental chamber of PF-24 were stated as optimal for emission of D-D fusion neutron. Thus, the discharges in $(100\%\text{-}x)D_2\text{+}x\text{Ar}$ gas mixtures were performed in close to neutron-optimized device for smaller Ar fractions (doping) and not optimized device for higher Ar fractions.

9.1. Evaluation of the occurrence of the plasma radiative compression phenomenon

It should be clairyfied that, in this work, the strong plasma radiative compression is stated when almost all investigated parameters describing the plasma pinch (r_{pmin}^{comp}, r_{p0}^{comp} - r_{pmin}^{comp}, z_{pmax}^{comp}, z_{pmax}^{comp} - z_{p0}^{comp}, V_{pf}^{comp}, V_{p0}^{comp} - V_{pf}^{comp}, n_{pmax}^{comp}, n_{pmax}^{comp} - n_{p0}^{comp}) or at least r_{pmin}^{comp}, r_{p0}^{comp} - r_{pmin}^{comp}, n_{pmax}^{comp}, and n_{pmax}^{comp} - n_{p0}^{comp} exceed the highest or smallest values obtained for all theoretical and computed discharges in D_2. On the other hand, the weak plasma radiative compression is stated, when at least one type of investigated parameters describing the compression of plasma pinch exceeds the highest or smallest values for theoretical and computed discharges in D_2 (for example r_{pmin}^{comp} and r_{p0}^{comp} - r_{pmin}^{comp}). Finally, if all investigated parameters describing plasma pinch compression do not exceed the highest or smallest values achieved for theoretical and computed discharges in D_2 then no (or very weak) radiative compression is stated.

Deuterium

The results of investigations based on all 56 discharges (theoretical and coupled experimental-computed) in D_2 showed **no possibility** of plasma radiative compression phenomenon occurrence in the PF-24 device. The main reason of this statement is the significantly **too low computed total yield of X-ray line radiation** during the stable plasma pinch lifetime. The achieved smallest plasma pinch radius and the highest ion number density for the 44 computed discharges were equal to: 0.52 cm and $9.9\text{x}10^{17}$ $1/\text{cm}^3$, respectively.

Argon

The results of investigations based on the 11 theoretical discharges in 0.50-1.60 mbar and 4.50-5.00 mbar of initial Ar pressures (pressure range I) and the group I of 5 computed discharges in 1.2(±0.1) mbar of initial Ar pressure showed only weak or no plasma radiative compression phenomenon. This is due to the too low total yield of X-ray line radiation emission computed during the stable plasma pinch lifetime as well as too big initial pinch radius, too high initial ion temperature and too low initial ion number density of plasma.

On the other hand, for the 10 theoretical discharges in 1.70-4.20 mbar of initial Ar pressures (pressure range II) and the group II of 5 computed discharges in 1.2(±0.1) mbar of initial Ar pressure **strong** plasma radiative compression occurrence was stated. The achieved smallest plasma pinch radius and the highest ion number density during the 11 theoretical discharges were equal to: 0.07 cm and $65\text{x}10^{17}$ $1/\text{cm}^3$, respectively. The achieved smallest plasma pinch radius and highest ion number density during the 5 computed discharges from group II were equal to: **0.11 cm** and $\mathbf{20x10^{17}}$ $\mathbf{1/cm^3}$, respectively.

D_2+Ar mixtures

The results of the investigations based on the 11 theoretical discharges in 1-45% of Ar fraction in $(100\%\text{-}x)D_2\text{+}x\text{Ar}$ gas mixtures (fraction range I) and all the 69 computed discharges in 3-60% of Ar fraction in $(100\%\text{-}x)D_2\text{+}x\text{Ar}$ gas mixtures showed only **weak** or **no** plasma radiative compression. The main reason of this state is again **too low total yield of X- ray line radiation emission** computed during the stable plasma pinch lifetime as well as **too high initial pinch radius**, **too high initial ion temperature** and **too low initial ion number density** of plasma.

On the other hand, for the 10 theoretical discharges in 50-95% of Ar fraction in $(100\%\text{-}x)D_2\text{+}x\text{Ar}$ gas mixtures (fraction range II) the occureance of the strong plasma radiative compression was stated. The achieved smallest plasma pinch radius and the highest ion number density during the 10 theoretical discharges were equal to: 0.12 cm and $37.21\text{x}10^{17}$ $1/\text{cm}^3$, respectively.

Summarizing, since only the computed discharges are belived too actually occure during the PF-24 operation, thus the **weak** plasma radiative compression occurrence was stated for group I of discharges in pure Ar under 1.2(±0.1) mbar of initial Ar pressure and during selected discharges in 15-60% of Ar fraction in $(100\%\text{-}x)D_2\text{+}x\text{Ar}$ gas mixtures. While, the occureance of the **strong** plasma radiative compression phenomenon was stated only for group II of discharges in pure Ar under 1.2(±0.1) mbar of initial Ar pressure.

Moreover, the preformed experiments prove that the phenomenon of plasma radiative compression may or may not appear during discharges in Ar or D_2+Ar mixtures. The increase of Ar content in (100%-x)D_2+xAr gas mixtures at the constant total initial gas pressure, connected mainly with the increase of the total atomic Z number, causes an increase in the **probability of the occurrence** of plasma radiative compression. Still, this will be a relatively **weak** radiative compression until a **sufficiently high level of the total yield of X-ray line emission** (few hundred Joules per discharges) is reached during the stable phase of pinch.

According to the experimental discharges performed in the PF-24 device and the computed discharges, at least **221 J/discharge** is required when $\mathbf{r_{p0} = 0.36}$ **cm**, $\mathbf{n_{p0} = 3.19x10^{17}}$ **1/cm^3** and $\mathbf{T_{p0} = 0.08}$ **keV**. The Y_{line} = 221 J/discharge is about **1.3%** of the initial energy (E_0 = 16.8 kJ) stored in the PF-24 condenser bank. While, r_{p0} = 0.36 cm constitutes about **11.6%** of the anode radius (a_0 = 3.1 cm).

9.2. Assessment of critical indicators and parameters describing strong plasma radiative compression

The main (basic) indicators of plasma radiative compression used in this work are: the P-B current ($I_{P-B}(t_1)^{comp}$), the reduced P-B current ($I_{P-Breduced}(t_1)^{comp}$), the pinch plasma current ($I_{pp}(t_1)^{comp}$), the characteristic time of radiation depletion (t_Q^{comp}) and the pinch lifetime (t_{pl}^{comp}). Additionally, the radiative compression lifetime indicator (t_{rcl}^{comp}) was introduced in this work – if $t_Q^{comp} < t_{rcl}^{comp}$, then the radiative compression should be stated. All the 6 indicators used together for the investigation of each discharge individually correctly predict the occurance of the radiative compression phenomenon **only for some of the discharges**. Especially, taking into account the occurance of the strong radiative compression: the $I_{P-Breduced}(t)^{comp} < I_{pp}(t)$, the $t_Q^{comp} < t_{pl}^{comp}$ and the $t_Q^{comp} < t_{rcl}^{comp}$ conditions are often incorrect. They should be rather changed into: $\mathbf{I_{P-Breduced}(t)^{comp} << I_{pp}(t)}$, $\mathbf{t_Q^{comp} << t_{pl}^{comp}}$ and $\mathbf{t_Q^{comp} << t_{rcl}^{comp}}$ (the most trustworthy in this matter appear to be time indicators). But even then, they would not properly predict the occurance of the strong radiative compression for all investigated discharges (cases). In general it is difficult to predict the strong plasma radiative compression, but the studies presented in this work prove that the main parameters which determine the radiative compression (including its strength) are the: **total yield of X-ray line radiation** (**Y_{line}**), **initial plasma pinch radius** (**r_{p0}**), **initial plasma pinch ion temperature** (**T_{p0}**) and **initial plasma pinch ion number density** (**n_{p0}**). The most important one is the **Y_{line}**. So, these 4 parameters can be used also as the radiative compression indicators and they appear to give in general more accurate predictions than the main (basic) indicators.

The results, based on all the investigated theoretical discharges in D_2, Ar and D_2+Ar mixtures and computed discharges in D_2 in the PF-24, show that the Y_{line}^{comp} should be higher than about 600 J/discharge in order to observe the strong radiative compression taking place during discharges in D_2+Ar gas mixtures (50-95%) or Ar (1.70-4.20 mbar). On the other hand, the results based on computed discharges (1.2 mbar of Ar) in Ar show that 600 J/discharge level can be decreased down to at least 221 J/discharge when the values of r_{p0}^{comp} and/or T_{p0}^{comp} significantly decreased and/or the value of n_{p0}^{comp} significantly increased. As a proof, the 12 theoretical discharges in 1.70-420 mbar of Ar and 10 theoretical discharges in 50-95% of Ar fraction in (100%-x)D_2+xAr mixture have following range of changes of Y_{line}^{comp}, r_{p0}^{comp}, T_{p0}^{comp} and n_{p0}^{comp} parameters: 633-1702 J/discharge, 0.52-0.59 cm, 0.09-0.37 keV, $1.05x10^{17}$-$2.02x10^{17}$ 1/cm^3, respectively. While for the 5 computed discharges in Ar the Y_{line}^{comp}, r_{p0}^{comp}, T_{p0}^{comp} and n_{p0}^{comp} parameters change in the regions: 221-348 J/discharge, 0.35-0.37 cm, 0.08-0.11 keV and $1.54x10^{17}$-$3.38x10^{17}$ 1/cm^3, respectively. As can be seen, all r_{p0}^{comp} values are smaller for computed discharges, some of the T_{p0}^{comp} values is smaller for computed discharges and some of the n_{p0}^{comp} is higher for computed discharges, while all the Y_{line}^{comp} values during computed discharges are smaller than the 600 J/discharge. And for both groups of discharges occurrence of the relatively strong radiative compression was stated.

It should be also mentioned that for the first time in history of investigation of discharges in plasma-focus devices and plasma radiative compression phenomenon such precise analysis with so many plasma parameters and coupled measured-computed discharges (individually fitted) was performed using the 5-phase Lee model code.

9.3. Verification of the increase in total neutron emission by deuterium argon doping.

The experimental data discussed in subsection 8.7.2 (figure 8.7.10) prove that there is **no increase** of the average total neutron yields ($<Y_n^{mea}>$) from D-D fusion with increase of Ar fraction, measured during discharges in $(100\%\text{-}x)D_2\text{+}x\text{Ar}$ mixtures at total gas pressure 2.9(±0.2) mbar. The main reason of this is **decreasing of deuterium ion number density** in plasma pinch (both initial and final) with Ar fraction – see figure 8.5.5. This decrease is connected with the **decrease of initial deuterium fraction and pressure** inside the experimental chamber (decrease of the total number of D ions – fuel for fusion) and with **special changes in the plasma electro-kinetics/dynamics** which also results in **too low total yield of X-ray radiation** preventing the occurance of strong plasma radiative compression. The too low total yield of X-ray line radiation is connected, among others, with the small increase in ion number density of argon (see equation (2.1.19)) due to changes of fitting parameters (L_0^{comp}, R_0^{comp}, f_m, f_c, f_{mr}, f_{cr}) enabling different development of discharge in experimental chamber. Especially, the decrease of model parameters (f_m, f_c, f_{mr}, f_{cr}) with increase of Ar fraction was stated – the lower currents effectively flowing through moving plasma structures and no increase of effective mass sweeping into the pinch for higher Ar fractions (changes in the electro-kinetics/dynamics of discharge). The reason of this state is unknown. It may be probably caused by the **separation of Ar and D species** due to significantly different masses of ions and the penetration of magnetic field into plasma – Ar ions are more likely to be left behind the moving plasma structure [Commisso 1975] [Weingarten 2001]. This would explain only small increase in ion number density of Ar with increase of Ar fraction (figure 8.5.5).

The obtained results are consistent with the experimental results reported by [Aliaga-Rossel 1998], in which, the reduction in Y_n^{mea} with different admixtures of noble gases has been observed for the middle energy plasma-focus (DPF-78, 60 kV/28 kJ) operated with mixtures of D_2 with Ne, Ar and Kr as well as in the sub-kilo-Joule optimized plasma-focus device (FMPF-3, 14 kV/235 J) operated with deuterium–krypton mixtures [Talebitaher 2016] (see also discussion in subsection 3.2).

It should be also mentioned that for the first time in history of investigation of the discharges in plasma-focus devices and the total neutron emission from nuclear fusion of deuterium ions the comparison of measured and computed discharges using Enhanced 5-phase Lee model code (RADPFV5.013.9b) was done for the discharges in gas mixtures. Moreover, the obtained match of the measured and computed Y_n for discharges in gas mixtures is one of the best of investigation of total neutron emission from PF devices (and perhaps also from all z-pinch) operated with gas mixtures.

9.4. Evaluation of the compatibility of results of computations performed with the Lee model code and experimental results

The results of investigation presented in this work are based on the theoretical and computed discharges performed using the 5-phase Lee model code as well as on the experimental discharges performed using the plasma-focus PF-24 device. During all 123 performed and investigated experimental discharges in this work (44 in D_2, 69 in $(100\%\text{-}x)D_2+x$Ar mixtures, 10 in Ar) the electric traces of total discharge current and the total discharge current derivative over time (see example in figure 5.3.1) as well as the number of counts were registered using three different, independent diagnostic systems. Based on the registered electric traces the group of 5 measured parameters – I_{max}^{mea}, I_p^{mea}, t_c^{mea}, t_p^{mea} and v_z^{mea} – was determined for each discharge. The special fitting procedure of measured current traces with the simulated current traces was applied. Thanks to this procedure the computed discharge was generated for each experimental discharge. The computed discharges were analyzed in a similar way as the experimental discharges – 5 computed electro-kinetic parameters were determined: I_{max}^{comp}, I_p^{comp}, t_c^{comp}, t_p^{comp} and v_z^{comp}. The determined 5 measured and computed parameters were compared for each investigated discharge. The results of this comparison are considered to be an evaluation of matching of the measured and computed total discharge current traces. If sufficient matching of coupled experimental-computed current traces is found then the results of investigations of the plasma radiative compression based on the computations are considered **valid in approximation**. And **sufficient match** of most of the 5 measured and computed electro-kinetic parameters was stated for all 123 discharges investigated in this work.

Moreover, an additional 6-th parameter – the total neutron yield (Y_n^{mea}), was measured for each discharge. The computed total neutron yields were also determined (Y_n^{comp}) for each discharge using the 5-phase Lee model code. The comparison of measured and computed Y_n for the discharges in D_2 showed significant differences for the most of discharges. On the other hand, the Y_n^{mea} and Y_n^{comp} were similar for the discharges where the measured total neutron yield was low compared to the highest measured value. This suggests that the computed parameters describing the plasma pinch using the Lee model code are most accurate for the discharges where the measured total neutron yields were lower than about 2.6×10^9 n/discharge (for the PF-24 device). Furthermore, the comparison of measured and computed Y_n for discharges in 3-60% of Ar in $(100\%\text{-}x)D_2+x$Ar mixtures showed relatively **good matching**. This fact further increases confidence that the coupled measured-computed discharges in $(100\%\text{-}x)D_2+x$Ar mixtures in the PF-24 device represent approximately similar state of plasma and discharge.

Finally, the sufficiently well matched computed discharges made using the 5-phase Lee model code are still an approximation of the real experimental discharges and the achieved state of the electron-ion plasma in plasma-focus devices. This is the result of many approximations used in the Lee model code. The most important approximations in view of the plasma compression investigation are: no curvature of the moving current sheet, no generation of the plasma instabilities (although anomalous heating connected with generation of micro-instabilities is in general accounted), the generation of the plasma pinch in form of a perfect cylinder, the computation of only average and unifom values of the plasma density, temperature and current flow along the pinch dimensions, the inability to transform the plasma column into micro-instabilities (hot-spots), the inability of filamentary structures appearance and no possibility of the separation of Ar and D species (although model parameters are sensitive to the total mass losses in general). On the other hand, the mentioned effects are partially, approximately **attuned by the 4 model**

parameters used in the code – f_m, f_c, f_{mr} and f_{cr}. Also, most of the presented electro-kinetic paramters (measured and computed) appear to be in **good agreement with the snow-plow and slug models'** description of PF discharges – see figures: 8.1.4, 8.1.5, 8.1.10 and 8.1.11. Moreover, the Lee model code has been successfully used in the past for example to reconstruct radial piston velocities [Lim 2015], [Akel 2016c], total X-ray radiation emission [Saw 2009], [Saw 2013] or the total neutron yields [Singh 2014], [Akel 2016c], [Singh 2017] from plasma-focus discharges (computed results in reasonable agreement with the experimental results). Especially the measured total neutron yields emitted from different PF devices are usually well matched with the computed ones using the Lee model code – matching of measured and computed Y_n is one of the best in history of investigation of PF discharges (on the level of modern MHD models and fully kinetic/electromagnetic models) [Lee 2017]. Thus, the results concerning plasma radiative compression phenomenon based on the Lee model code may actually represent the real situation during discharges in plasma-focus devices in sufficiently good approximation for investigation of global plasma compression.

Addresing the thesis of work presented in the chapter 4, the plasma radiative compression phenomenon occurrence was stated in the plasma-focus PF-24 device. However, the strong plasma radiative compression occurred only during some of computed discharges in Ar. While for all computed discharges in D_2+Ar mixtures under approximately constant initial total pressure only weak or no plasma radiative compression was stated.

10. References

[Abdallah 1999] J. Abdallah Jr., R. E. H. Clark, A. Ya. Faenov, L. Karpinski, S. A. Pikuz, V. M. Romanova, M. Sadowski, M. Scholz, A. Szydlowski, "Electron beam effects on the spectroscopy of multiply charged ions in plasma focus experiments", Journal of Quantitative Spectroscopy & Radiative Transfer, volume 62, issue 1, pages 85-96, 1999, DOI: 10.1016/S0022-4073(98)00073-9.

[Abdou 2012] A. E. Abdou, M. I. Ismail, A. E. Mohamed, S. Lee, S. H. Saw, R. Verma, "Preliminary Results of Kansas State University Dense Plasma Focus", IEEE Transcation On Plasma Science, volume 40, issue 10, part 2, pages 2741-2744, 2012, DOI:10.1109/TPS.2012.2209682.

[Akel 2013] M. Akel, S. Lee, "Radiative Collapse in Plasma Focus Operated with Heavy Noble Gases", Journal of Fusion Energy, volume 32, issue 1, pages 111–116, 2013, DOI:10.1007/s10894-012-9535-3.

[Akel 2016a] M. Akel, S. Ismael, S. Lee, S. H. Saw, H.-J. Kunze, "Effects of Power Terms and Thermodynamics on the Contraction of Pinch Radius in Plasma Focus Devices Using the Lee Model", Journal of Fusion Energy, volume 35, issue 6, pages 807-815, 2016, DOI:10.1007/s10894-016-0108-8.

[Akel 2016b] M. Akel, J. Cikhardt, P. Kubes, H.-J. Kunze, S. Lee, M. Paduch, S. H. Saw, "Experiments and simulations on the possibility of radiative contraction/collapse in the PF-1000 plasma focus", Nukleonika, volume 61, number 2, pages 145-148, 2016, DOI:10.1515/nuka-2016-0025.

[Akel 2019] M. Akel, Ł. Marciniak, Sh. Ismael, D. Gannom, A. Kulińska, S. Lee, M. Scholz, H.-J. Kunze, S. H. Saw, "Investigation of the Measured and Computed Neutron Yield from the PF-24 device Operated with D2-x%Ar Admixture", IEEE Transactions on Plasma Science, volume 47, issue 9, pages 4301-4311, 2019, DOI: 10.1109/TPS.2019.2932182.

[Al-Hawat 2012] Sh. Al-Hawat, M. Akel, S. Lee, S. H. Saw, "Model Parameters Versus Gas Pressure in Two Different Plasma Focus Devices Operated in Argon and Neon", Journal of Fusion Energy, volume 31, issue 1, pages 13-20, 2012, DOI:10.1007/s10894-011-9414-3.

[Anders 1990] A. Anders, "A Formulary for Plasma Physics", Akademie-Verlag, Berlin, 1990, ISBN 3-05-501263-1.

[Anderson 1958] O. A. Anderson, W. R. Baker, S. A. Colgate, J. Ise Jr., R. U. Pyle, "Neutron Production in Linear Deuterium Pinches", Physical Review, volume 110, issue 6, pages 1375-1387, 1958, DOI: 10.1103/PhysRev.110.1375.

[Antsiferov 1995] P. S. Antsiferov, F. B. Rosmej, O. N. Rosmej, H. Schmidt, D. Schulz, A. Schulz., "X-ray diagnostics of plasma focus DPF-78 discharge with heavy-gas admixtures", Journal of Applied Physics, volume 77, issue 10, pages 4973-4978, 1995, DOI: 10.1063/1.359305.

[Apruzese 1989] J. P. Apruzese, P. C. Kepple, "Effect of line opacity on conditions for radiative collapse in a krypton Z pinch", AIP Conference Proceedings, volume 195, issue 1, pages 108-117, 1989, DOI: 10.1063/1.38882.

[Bailey 1982] J. Bailey, E. Ettinger, A. Fisher, N. Rostoker, "Gas-puff Z pinches with D_2 and D_2-Ar mixtures", Applied Physics Letters, volume 40, issue 6, pages 460-462, 1982, DOI: 10.1063/1.93148.

[Bailey 1986] J. Bailey, A. Fisher, N. Rostoker, "Coupling of radiation and hydrodynamics in a Z-pinch plasma", J. App. Phys., volume 60, issue 6, pages 1939-1945, 1986, DOI: 10.1063/1.337193.

[Bayley 1991] J. M. Bayley, G. Decker, W. Kies, M. Maizig, F. Muller, P. Rowekamp, J. Westheide, Y.V. Sidelnikov, "Observations of soft x-ray production in the speed 2 plasma focus", Journal of Applied Physics, volume 69, issue 2,pages 613-617, 1991, DOI: 10.1063/1.347394.

[Bennett 1934] W. H. Bennett, “Magnetically Self-Focussing Streams”, Physical Review, volume 45, issue 12, pages 890-897, 1934, DOI: 10.1103/PhysRev.45.890.

[Bernal 2002] I. Bernal, H. Bruzonne, “Radiative collapses in Z-pinches with axial mass losses”, Plasma Physics and Controlled Fusion, volume 44, number 2, pages 223–231, 2002, DOI: 10.1088/0741-3335/44/2/306.

[Bernard 1977] A. Bernard, P. Cloth, H. Conrads, A. Coudeville, G. Gourlan, A. Jolas, Ch. Maisonnier, J. P. Rager, “The dense plasma focus — A high intensity neutron source”, Nuclear Instruments and Methods, volume 145, issue 1, pages 191-218, 1977, DOI:10.1016/0029-554X(77)90569-9.

[Bernard 1998] A. Bernard, H. Bruzzone, P. Choi, H. Chacqui, V. Gribkov, J. Herrera, K. Hirano, A. Krejci, S. Lee, C. Luo, F. Mezzetti, M. J. Sadowski, H. Schmidt, K. Ware, C. Wong, V. Zoita, “Scientific status of plasma focus research”, Journal of Moscow Physical Society, volume 8, pages 93-170, 1998.

[Bernstein 1970] M. J. Bernstein “Acceleration Mechanism for Neutron Production in Plasma Focus and z–Pinch Discharges”, Physics of Fluids, volume 13, number 11, pages 2858-2866, 1970, DOI: 10.1063/1.1692871.

[Bienkowska 2014] B. Bieńkowska, R. Prokopowicz, M. Scholz, J. Kaczmarczyk, A. Igielski, L. Karpinski, M. Paduch, K. Pytel, “Neutron counter based on beryllium activation”, AIP Conference Proceedings, volume 1612, issue 1, pages 105–108, 2014, DOI:10.1063/1.4894033.

[Bodin 1971] H. A. Bodin, “Instabilities of high-beta plasmas”, Methods of Experimental Physics: Plasma Physics, volume 9, part A, section 10, pages 395-449, 1971.

[Bogomaz 2008] A. A. Bogomaz, A. V. Budin, S. Yu. Losev, M. E. Pinchuk, A. A. Pozubenkov, Ph. G. Rutberg, A. F. Savvatev, “Attainment of the Pease–Braginskii Current in an Ultra-High-Pressure Discharge”, Plasma Physics Reports, volume 34, number 5, pages 366-375, 2008, DOI: 10.1134/S1063780X08050036.

[Braginskii 1958] S. I. Braginskii, “The behavior of a completelz joniyed plasma in a strong magnetic field”, Journal of Experimental and Theoretical Physics (JETP), volume 6, number 3, pages 494-501, 1958.

[Brzosko 1991] J. S. Brzosko, V. Nardi, “High yield of 12C(d,n)13N and ^{14}N(d,n)^{15}O reactions in the plasma focus pinch”, Physics Letters A, volume 155, issue 2-3, pages 162–168, 1991, DOI: 10.1016/0375-9601(91)90586-W.

[Bures 2009] B. L. Bures, M. Krishnan, Y. Eshaq, “Controlling the Neutron Yield from a Small Dense Plasma Focus using Deuterium-Inert Gas Mixtures”, AIP Conference Proceedings, volume 1088, issue 1, pages 195-198, 2009, DOI: 10.1063/1.3079727.

[Bures 2010] B. L. Bures, M. Krishnan, R. E. Madden, F. Blobner, “Enhancing Neutron Emission From a 500-J Plasma Focus by Altering the Anode Geometry and Gas Composition”, IEEE Transactions on Plasma Science, volume 38, issue 4, pages 667-671, 2010, DOI: 10.1109/TPS.2010.2042621.

[Ching 2010] T. L. Ching, “Simulation Studies of Plasma Dynamics and Radiation Yield in Plasma Focus Device”, master thesis, National Institute of Education, Nanyang Technological University, Singapore, 2010.

[Chittenden 1989] J. P. Chittenden, A. J. Power, M. G. Haines, “Further investigations of radiative collapse in a Z-pinch”, Plasma Physics and Controlled Fusion, volume 31, number 11, pages 1813-1822, 1989, DOI: 10.1088/0741-3335/31/11/006.

[Chittenden 1990] J. P. Chittenden, M. G. Haines, “Processes terminating radiative collapse in a hydrogen fiber Z pinch”, Physics of Fluids B: Plasma Physics, volume 2, issue 8, pages 1889-1897, 1990, DOI: 10.1063/1.859460.

[Cochran 1990] F. L. Cochran, A. E. Robson, “Stability of a Z pinch at the Pease–Braginskii current”, Physics of Fluids B: Plasma Physics, volume 2, issue 9, pages 2270-2272, 1990, DOI: 10.1063/1.859410.

[Commisso 1975] R. J. Commisso, H. J. Kunze, “Estimate of the radial potential jump in a theta−pinch”, Physics of Fluids, volume 18, number 3, pages 392-394, 1975, DOI:10.1063/1.861150.

[Decker 1976] G. Decker, R. Wienecke, “Plasma focus devices”, Physica B+C, volume 82, issue 1, pages 155-164, 1976, DOI: 10.1016/0378-4363(76)90274-6.

[Elton 1971] R. C. Elton, “Atomic processes”, Methods of Experimental Physics: Plasma Physics, volume 9, part A, section 4, pages 115-168, 1971.

[Filippov 1962] N. V. Filippov, T. I. Filippova, V. P. Vinogradov, “Dense, High-Temperature Plasma in a Non-cylindrical Z-pinch Compression”, Nuclear Fusion Supplement, part 2, pages 577-587, 1962.

[Gautam 2017] P. Gautam, R. Khanal, S. H. Saw, S. Lee, “Measurement of Model Parameters Versus Gas Pressure in High-Performance Plasma Focus NX1 and NX2 Operated in Neon”, IEEE Transactions on Plasma Science, volume 45, issue 8, part 3, 2017, DOI:10.1007/s10894-011-9414-3.

[Gribkov 2007] V A Gribkov, A. Banaszak, B. Bienkowska, A. V. Dubrovsky, I. Ivanova-Stanik, L. Jakubowski, L. Karpinski, R. A. Miklaszewski, M. Paduch, M. J. Sadowski, M. Scholz, A. Szydlowski, K. Tomaszewski, “Plasma dynamics in the PF-1000 device under full scale energy storage: II. Fast electron and ion characteristics versus neutron emission parameters and gun optimization perspectives”, Journal of Physics D Applied Physics, volume 40, number 12, pages 3592-3607, 2007, DOI: 10.1088/0022-3727/40/12/008.

[Gribkov 2008] V. A. Gribkov, “Current and Perspective Applications of Dense Plasma Focus Devices”, AIP Conference Proceedings, volume 996, issue 1, 51, pages 1-14, 2008, DOI: 10.1063/1.2917031.

[Gross 1965] R. A. Gross, “Strong Ionizing Shock Waves”, Reviews of Modern Physics, volume 37, pages 724–743, 1965, DOI: 10.1103/RevModPhys.37.724.

[Gross 1971] R. A. Gross, “Plasma heating by strong shock waves”, Methods of Experimental Physics: Plasma Physics, volume 9, part A, section 5, pages 169-212, 1971.

[Haines 1982] M. G. Haines, “The Physics of the Dense Z-Pinch in Theory and in Experiment With Application to Fusion Reactor”, Physica Scripta, volume T2/2, pages 380-390, 1982, DOI: 10.1088/0031-8949/1982/T2B/013.

[Haines 1989] M. G. Haines, “An analytic model of radiative collapse of a Z-pinch”, Plasma Physics and Controlled Fusion, volume 31, number 5, pages 759-778, 1989, DOI: 10.1088/0741-3335/31/5/005.

[Haines 2011] M. G. Haines, Plasma Physics and Controlled Fusion, volume 53, number 9, 093001, pages 1-168, 2011, DOI: 10.1088/0741-3335/53/9/093001.

[Hammel 1989] J. Hammel, “The High Density Z-pinch II experiments”, AIP Conference Proceedings, volume 195, issue 1, pages 303-307, 1989, DOI: 10.1063/1.38879.

[Hebach 1993] M. Hebach, A. EngeI, A. Schulz, R. Lebert, H.-J. Kunze, “Time Evolution of the X-ray Emission from a Micropinch in a Vacuum Spark Discharge”, EPL (Europhysics Letters), volume 21, number 3, pages 311-316, 1993, DOI: 10.1209/0295-5075/21/3/010.

[Hintz 1971] E. Hintz, “6. Collisionless shock waves in laboratory plasmas”, Methods of Experimental Physics: Plasma Physics, volume 9, part A, section 6, pages 213-274, 1971.

[Hussain 2007] S. Hussain, M. Zakaullah, “Reliable Field Distortion Spark Gap for Plasma Focus”, Plasma Science and Technology, volume 9, number 4, pages 504-507, 2007, DOI:10.1088/1009-0630/9/4/27.

[Jach 1991] K. Jach, W. Stępniewski, M. Mroczkowski, Zhurnal Tekhniceskoj Fiziki (Journal of Technical Physics), volume 32, 125, 1991.

[Jager 1987] U. Jäger, H. Herold, “Fast ion kinetics and fusion reaction mechanism in the plasma focus”, Nuclear Fusion, volume 27, number 3, pages 407-423, 1987, DOI: 10.1088/0029-5515/27/3/006/meta.

[Karimi 2017] F. S. Karimi, S. Saviz, M. Ghoranneviss, M. K. Salem, F. M. Aghamir, “The circuit parameters measurement of the SABALAN-I plasma focus facility and comparison with Lee Model”, Results in Physics, volume 7, pages 1859-1869, 2017, DOI:10.1016/j.rinp.2017.05.021.

[Kies 1998] W. Kies, B. Lucas, P. Röwekamp, F. Schmitz, G. Ziethen, G. Decker, “Pinches and micropinches in the SPEED 2 plasma focus”, Plasma Sources Sci. Technol., volume 7, number 1, pages 21-27, 1998 DOI: 10.1088/0963-0252/7/1/004.

[Kies 2000] W. Kies, G. Decker, U. Berntien, Y. V. Sidelnikov, D. A. Glushkov, K.N. Koshelev, D. M. Simanovskii, S. V. Babashev, “Pinch modes produced in the SPEED2 plasma focus”, Plasma Sources Science and Technology, volume 9, number 3, pages 279-287, 2000, DOI: 10.1088/0963-0252/9/3/305.

[Klir 2018] D. Klir, A. V. Shishlov, V. A. Kokshenev, P. Kubes, K. Rezac, R. K. Cherdizov, J. Cikhardt, B. Cikhardtova, G. N. Dudkin, F. I. Fursov, T. Hyhlik, J. Kaufman, B. M. Kovalchuk, J. Krasa, J. Kravarik, N. E. Kurmaev, A. Yu. Labetsky, V. Munzar, H. Orcikova, V. N. Padalko, N. A. Ratakhin, O. Sila, J. Stodulka, K. Turek, V. A. Varlachev, R. Wagner, ”Ion acceleration mechanism in mega-ampere gas-puff z-pinches”, New Journal of Physics, volume 20, 2018, DOI: 10.1088/1367-2630/aac545.

[Koshelev 1985] K. N. Koshelev, Y. V. Sidelnikov, “A micropinch as a spectral source of highly ionized atoms”, Nuclear Instruments and Methods in Physics Research Section B: Beam Interactions with Materials and Atoms, volume 9, issue 4, pages 704-705, 1985, DOI:10.1016/0168-583X(85)90396-9.

[Koshelev 1988] K. N. Koshelev, V. I. Krauz, N. G. Reshetniak, R. G. Salukvadze, Yu. V. Sidelnikov, E. Yu. Khautiev, “The formation of the micropinch structure in plasma focus by the addition of heavy impurities”, Journal of Physics D: Applied Physics, volume 21, number 12, pages 1827-1829, 1988, DOI: 10.1088/0022-3727/21/12/028.

[Koshelev 1991] K. N. Koshelev, N. R. Pereira, “Plasma points and radiative collapse in vacuum sparks”, Journal of Applied Physics, volume 69, issue 10, pages 21-44, 1991, DOI: 10.1063/1.347551.

[Krol 2015] Krzysztof Król, “Optymalizacja numeryczna parametrów elektrycznych układu Plasma-Focus PF-24”, engineering thesis, University of Rzeszów, Faculty of Mathematics and Natural Sciences, 2015.

[Kubes 2010] P. Kubes, M. Paduch, T. Pisarczyk, M. Scholz, D. Klir, J. Kravarik, K. Rezac, T. Chodukowski, I. Ivanova-Stanik, L. Karpinski, E. Zielińska, K. Tomaszewski, M. J. Sadowski, “Transformation of the Pinched Column at a Period of the Neutron Production”, IEEE Transcation On Plasma Science, volume 38, issue 4, pages 672-679, 2010, DOI: 10.1109/TPS.2009.2036623.

[Kubes 2011] P. Kubes, M. Paduch, T. Pisarczyk, M. Scholz, T. Chodukowski, D. Klir, J. Kravarik, K. Rezac, I. Ivanova-Stanik, L. Karpiński, M. J. Sadowski, K. Tomaszewski, E. Zielińska, “Spontaneous Transformation in the Pinched Column of the Plasma Focus”, IEEE Transcation On Plasma Science, volume 39, issue 1, pages 562-568, 2011, DOI: 10.1109/TPS.2010.2086497.

[Kubes 2012] P. Kubes, D. Klir, J. Kravarik, M. Paduch, T. Pisarczyk, M. Scholz, T. Chodukowski, B. Bieńkowska, I. Ivanova-Stanik, L. Karpiński, M. J. Sadowski, K. Tomaszewski, E. Zielińska, “Energy Transformations in Column of Plasma-Focus Discharges With Megaampere Currents”, IEEE Transcation On Plasma Science, volume 40, issue 2, pages 481-486, 2012, DOI: 10.1109/TPS.2011.2178866.

[Kubes 2017] P. Kubes, M. Paduch, J. Cikhardt, B. Cikhardtova, D. Klir, J. Kravarik, K. Rezac, E. Zielinska, M. J. Sadowski, A. Szymaszek, K. Tomaszewski, D. Zaloga, “Filamentation in the pinched column of the dense plasma focus”, Physics of Plasmas, volume 24, issue 3, 032706, 2017, DOI: 10.1063/1.4978558.

[Kubes 2019a] P. Kubes, M. Paduch, M. J. Sadowski, J. Cikhardt, B. Cikhardtova, D. Klir, J. Kravarik, R. Kwiatkowski, V. Munzar, K. Rezac, E. Skladnik-Sadowska, A. Szymaszek, K. Tomaszewski, D. Zaloga, E. Zielinska, “Features of fast deuterons emitted from plasma focus discharges”, Physics of Plasmas, volume 26, issue 3, 032702, 2019, DOI:10.1063/1.5080974.

[Kubes 2019b] P. Kubes, M. Paduch, M. J. Sadowski, J. Cikhardt, B. Cikhardtova, D. Klir, J. Kravarik, V. Munzar, K. Rezac, E. Skladnik-Sadowska, A. Szymaszek, K. Tomaszewski, D. Zaloga, E. Zielinska, “Evolution of a Pinch Column During the Acceleration of Fast Electrons and Deuterons in a Plasma-Focus Discharge”, IEEE Transactions on Plasma Science, volume 47, issue 1, 2019, DOI: 10.1109/TPS.2018.2874288.

[Lebert 1995] R. Lebert, A. Engel, W. Neff, “Investigations on the transition between column and micropinch mode of plasma focus operation”, Journal of Applied Physics, volume 78, number 11, pages 6414-6420, 1995, DOI: 10.1063/1.360524.

[Lee 1970] S. Lee, “Transverse ionizing shock waves in a planar electromagnetic shock tube”, PhD thesis, ANU, Australia, 1970.

[Lee 1971] J. H. Lee, L. P. Shomo, M. D. Williams, and H. Hermansdorfer, “Neutron Production Mechanism in a Plasma Focus”, Physics of Fluids, volume 14, number 10, pages 2217-2223, 1971, DOI: 10.1063/1.1693313.

[Lee 1983] S. Lee, “Radius Ratios of Argon Pinches”, Australian Journal of Physics, volume 36, issue 6, pages 891–896, 1983, DOI: 10.1071/PH830891.

[Lee 2008a] S. Lee, S. H. Saw, “Pinch current limitation effect in plasma focus”, Applied Physics Letters, volume 92, issue 2, 021503, pages 1-3, 2008, DOI: 10.1063/1.2827579.

[Lee 2008b] S. Lee, S. H. Saw, “Neutron Scaling Laws from Numerical Experiments”, Journal of Fusion Fusion Energy, volume 27, issue 4, pages 292-295, 2008, DOI:10.1007/s10894-008-9132-7.

[Lee 2009] S. Lee, S. H. Saw, L. Soto, S. V. Springham, S. P. Moo, “Numerical experiments on plasma focus neutron yield versus pressure compared with laboratory experiments”, Plasma Physics and Controlled Fusion, volume 51, number 7, 075006, pages 1-11, 2009, DOI: 10.1088/0741-3335/51/7/075006.

[Lee 2013] S. Lee, S. H. Saw, J. Ali, ”Numerical Experiments on Radiative Cooling and Collapse in Plasma Focus Operated in Krypton”, Journal of Fusion Energy, volume 32, issue 1, pages 42–49, 2013, DOI: 10.1007/s10894-012-9522-8.

[Lee 2014] S. Lee, “Plasma Focus Radiative Model: Review of the Lee Model Code”, Journal of Fusion Energy, volume 33, issue 4, pages 319-335, 2014, DOI: 10.1007/s10894-014-9683-8.

[Lee 2016] S. Lee, S. H. Saw, M. Akel, J. Ali, H.-J. Kunze, P. Kubes, M. Paduch, “Conditions for Radiative Cooling and Collapse in the Plasma Focus Illustrated With Numerical Experiments on PF1000”, IEEE Transactions on Plasma Science, volume 44, issue 2, pages 165-173, 2016, DOI: 10.1109/TPS.2015.2497269.

[Lee 2017] S. Lee, S. H. Saw, “The Plasma Focus – Numerical Experiments, Insights and Applications”, Plasma Science and Technology for Emerging Economies, pages 113-232, 2017, DOI: 10.1007/978-981-10-4217-1_3, online ISBN: 978-981-10-4217-1, print ISBN: 978-981-10-4216-4.

[Lerner 1980] E. J. Lerner, "Magnetic fusion power", IEEE Spectrum, volume 17, pages 44-50, 1980.

[Liberman 1999] M. A. Liberman, "Physics of High-Density Z-Pinch Plasmas", 1999, DOI: 10.1007/978-1-4612-1424-3, online ISBN: 978-1-4612-1424-3, print ISBN: 978-1-4612-7138-3.

[Marciniak 2016] Ł. Marciniak, A. Wójcik-Gargula, A. Kulińska, J Bielecki, U. Wiącek, "Diagnostic systems for the nuclear fusion and plasma research in the PF-24 plasma focus laboratory at the IFJ PAN", Nukleonika, volume 61, number 4, pages 413-418, 2016, DOI:10.1515/nuka-2016-0068.

[Marciniak 2018] Ł. Marciniak, M. Akel, A. Kulińska, M. Scholz, S. Lee, H.-J. Kunze, S. H. Saw, "Measurements and Simulations of Neutron Emission Versus Deuterium Filling Pressure in Plasma Focus Device PF-24", Journal of Fusion Energy, volume 37, issue 2-3, pages 124-129, 2018, DOI: 10.1007/s10894-018-0157-2.

[Mather 1964] J. W. Mather, "Investigation of the High-Energy Acceleration Mode in the Coaxial Gun", Physics of Fluids, volume 7, issue 11, pages 28-34, 1964, DOI:10.1063/1.1711086.

[Mather 1965] J. W. Mather, "Formation of a High-Density Deuterium Plasma Focus", Physics of Fluids, volume 8, issue 2, pages 366-377, 1965, DOI: 10.1063/1.1761231.

[Mather 1971] J. W. Mather, "Dense Plasma Focus", Methods of Experimental Physics: Plasma Physics, volume 9, part B, pages 187-248, 1971, DOI: 10.1016/S0076-695X(08)60862-5.

[Meierovich 1982] B. E. Meierovich, "Electromagnetic collapse. Equilibrium of a dense pinch", Physics Reports (Review Section of Physics Letters), volume 92, issue 3, pages 83-133, 1982, DOI: 10.1016/0370-1573(82)90144-2.

[Meierovich 1984] B. E. Meierovich, Physics Reports (Review Section of Physics Letters), "Electromagnetic collapse. Problems of stability, emission of radiation and evolution of a dense pinch", volume 104, issue 5, pages 259-346, 1984, DOI: 10.1016/0370-1573(84)90171-6.

[Meierovich 1989] B. E. Meierovich, Fizika Plazmy (Soviet Journal of Plasma Physics), volume 11, 1446, 1985.

[Mohammadi 2011] M. A. Mohammadi, S. Sobhanian, R. S. Rawat, "Neutron production with mixture of deuterium and krypton in Sahand Filippov type plasma focus facility", Physics Letters A, volume 375, issue 33, pages 3002-3006, 2011, DOI: 10.1016/j.physleta.2011.06.025.

[NIST 2019] https://www.nist.gov/pml/atomic-spectra-database, 30-06-2019.

[Pease 1957] R. S. Pease, "Equilibrium Characteristics of a Pinched Gas Discharge Cooled by Bremsstrahlung Radiation", Proceedings of the Physical Society. Section B, volume 70, number 1, pages 11-23, 1957.

[Pereira 1988] N. R. Pereira, J. Davis, "X rays from z-pinches on relativistic electron-beam generators", Journal of Applied Physics, volume 64, issue 3, pages 1-27, 1988, DOI: 10.1063/1.341808.

[Piel 2017] A. Piel, "Plasma Physics: An Introduction to Laboratory, Space and Fusion Plasma, Instabilities", "Instabilties", chapter 8, pages 211-233, 2017, DOI: 10.1007/978-3-319-63427-2_8, online ISBN: 978-3-319-63427-2, print ISBN: 978-3-319-63425-8.

[Piriaei 2015] D. Piriaei, T. D. Mahabadi, , S. Javadi, M. Ghoranneviss, S. H. Saw, S. Lee, "The study of pinch regimes based on radiation-enhanced compression and anomalous resistivity phenomena and their effects on hard x-ray emission in a Mather type dense plasma focus device (SABALAN2)", Physics of Plasmas, volume 22, issue 12, 123507, pages 1-7, 2015, DOI: 10.1063/1.4936801.

[plasmafocus.net 2019] http://plasmafocus.net, 30-06-2019.

[Potter 1971] D. Potter, "Numerical Studies of the Plasma Focus", The Physics of Fluids, volume 14, issue 9, pages 1911-1924, 1971, DOI: 10.1063/1.1693700.

[Potter 1978] D. Potter, “The formation of high-density z-pinches”, Nuclear Fusion, volume 18, number 6, pages 813-823, 1978, DOI: 10.1088/0029-5515/18/6/008.

[RADPF 2019] http://plasmafocus.net/IPFS/modelpackage/File1RADPF.htm, 30-06-2019.

[Rapp 1973] H. Rapp, “Measurements referring to plasma focus scaling laws”, Physics Letters A, volume 43, issue 5, pages 420-422, 1973, DOI: 10.1016/0375-9601(73)90401-5.

[Raspa 2008] V. Raspa, F. Di Lorenzo, P. Knoblauch, A. Lazarte, A. Tartaglione, A. Clausse, C. Moreno, “Plasma focus based repetitive source of fusion neutrons and hard x-rays”, PMC Physics A, 2:5, 2008, DOI: 10.1186/1754-0410-2-5.

[Rawat 2015] R. S. Rawat, “Dense Plasma Focus - From Alternative Fusion Source to Versatile High Energy Density Plasma Source for Plasma Nanotechnology”, Journal of Physics: Conference Series, volume 591, conference 1, 012021, pages 1-25, 2015, DOI: 1088/1742-6596/591/1/012021.

[Robson 1989a] A. Robson, “Radiative collapse of a Z pinch in hydrogen and helium”, Physics of Fluids B: Plasma Physics 1, volume 1, issue 9, pages 1834-1842, 1989, DOI: 10.1063/1.858915.

[Robson 1989b] A. E. Robson, “Anomalous resistivity and the Pease-Braginskii current in a Z-pinch”, Physical Review Letters, volume 63, number 26, pages 2816-2818, 1989, DOI: 10.1103/PhysRevLett.63.2816.

[Robson 1991] A. Robson, “Lower-hybrid-drift instability and radiative collapse of a dense Z pinch”, Physics of Fluids B, volume 3, number 6, pages 1461-1466, 1991, DOI: 10.1063/1.859712.

[Rosenbluth 1954] M. Rosenbluth, R. Garwin, A. Rosenbluth, Los Alamos Report – LA-1850, 1954.

[Rossel 1998] R. Aliaga-Rossel, P. Choi, “Experimental Observations of the Spatial Anisotropy of the Neutron Emission in a Medium Energy Plasma Focus”, IEEE Transactions on Plasma Science, volume 26, issue 4, pages 1138-1145, 1998, DOI:10.1109/27.725143.

[Rudakov 1997] L. I. Rudakov, R. N. Sudan, “MHD turbulence in radiating intense Z-pinches”, Physics Reports, volume 283, issue 1-4, pages 253-263, 1997, DOI:10.1016/S0370-1573(96)00062-2.

[Ryutov 2000] D. D. Ryutov, M. S. Derzon, M. K. Matzen, “The physics of fast Z pinches”, Reviews of Modern Physics, volume 72, number 1, 2000, DOI: 10.1103/RevModPhys.72.167.

[Sadowski 2005] M. J. Sadowski, “Nuclear fusion – energy for future”, Nukleonika, volume 50, supplement 3, pages 41-52, 2005.

[Sadowski 2010] M. J. Sadowski, M. Scholz, “Highlights of dense magnetized plasma research in Poland”, Problems of Atomic Science and Technology, number 6, pages 194-198, 2010.

[Sadowski 2012] M. J. Sadowski, M. Scholz, “Important issues in high-current plasma experiments of the Z-pinch type”, Nukleonika, volume 57, number 1, pages 11-24, 2012.

[Sadowski 2015] M. J. Sadowski, M. Paduch, E. Skladnik-Sadowska, W. Surala, D. Zaloga, R. Miklaszewski, E. Zielinska, K. Tomaszewski, “Soft x-ray studies of plasma-focus pinch structures in PF-1000U experiments”, Plasma Sources Sci. Technol., volume 24, 055003, 2015, DOI: 10.1088/0963-0252/24/5/055003.

[Saw 2014] S. H. Saw, P. L. Chong, R. S. Rawat, L. C. Tan, P. Lee, “The Effect of Specific Heat Ratio on Neutron Yield”, IEEE Transactions on Plasma Science, volume 42, issue 1, pages 99-104, 2014, DOI: 10.1109/TPS.2013.2288945.

[Saw 2016] S. H. Saw, S. Lee, “Measurement of Radiative Collapse in 2.2 kJ PF: Achieving High Energy Density (HED) Conditions in a Small Plasma Focus”, Journal of Fusion Energy, volume 35, issue 4, pages 702-708, 2016, DOI: 10.1007/s10894-016-0095-9.

[Scholz 2004] M. Scholz, B. Bieńnkowska, I. Ivanova-Stanik, L. Karpiński, R. Miklaszewski, M. Paduch, W. Stępniewski, K. Tomaszewski, M. J. Sadowski, “The physics of a plasma focus”, Czechoslovak Journal of Physics, supplement C, volume 54, issue 3, pages 170-185, 2004, DOI: 10.1007/BF03166397.

[Scholz 2006] M. Scholz, B. Bieńnkowska, I. M. Ivanova-Stanik, L. Karpiński, M. Paduch, W. Stępniewski, E. Zielińska, J. Kravarik, P. Kubes, A. Malinowska, M. J. Sadowski, A. Szydłowski, “Studies of Pinch Dynamics and Fusion-Products Emission within a Mega-Joule Plasma-Focus Facility”, proceedings of the 14th International Symposium on High-Current Electronics (SHCE), Tomsk, Russia, 2006.

[Schmidt 2006] H. Schmidt, P. Kubes, M. J. Sadowski, M. Scholz, “Neutron Emission Characteristics of Pinched Dense Magnetized Plasmas”, IEEE Transcations On Plasma Science, volume 34, number 5, pages 2363-2367, 2006, DOI: 10.1109/TPS.2006.878367.

[Sethian 1987] J. D. Sethian, A. E. Robson, K. A. Gerber, A. W. DeSilva, “Enhanced Stability and Neutron Production in a Dense Z-Pinch Plasma Formed from a Frozen Deuterium Fiber”, Physical Review Letters, volume 59, issue 8, pages 892-899, 1987, DOI: 10.1103/PhysRevLett.59.892.

[Sharak 2013] M. N. Sharak, S. Goudarzi, A. Raeisdana, M. Jafarabadi, “Numerical Analysis of Amirkabir Plasma Focus (APF) Device for Neon and Argon Gases”, Journal of Fusion Energy, volume 32, issue 2, pages 258-262, 2013, DOI: 10.1007/s10894-012-9552-2.

[Shearer 1976] J. W. Shearer, “Contraction of Z pinches actuated by radiation losses”, Physics of Fluids, volume 19, issue 9, pages 1426-1428, 1976, DOI: 10.1063/1.861627.

[Sheehey 1992] P. Sheehey, J. E. Hammel, I. R. Lindemuth, D. W. Scudder, J. S. Shlachter, R. H. Lovberg, R. A. Riley Jr., “Two-dimensional direct simulation of deuterium-fiber-initiated Z pinches with detailed comparison to experiment”, Physics of Fluids B: Plasma Physics, volume 4, pages 3698-3706, 1992, DOI: 10.1063/1.860325.

[Singh 2017] A. Singh, S. Lee, S. H. Saw, “Effect of the Variation of Pressure on the Dynamics and Neutron Yield of Plasma Focus Machines”, IEEE Transactions on Plasma Science, volume 45, issue 8, pages 2286-2291, 2017, DOI: 10.1109/TPS.2017.2715802.

[Stepniewski 1995] W. Stępniewski, M. Scholz, A. Gałkowski, “Radiative collapse of a Z-pinch”, Postępy Fizyki, volume 46, notebook 3, pages 235-258, 1995.

[Soto 2014] L. Soto, C. Pavez, F. Castillo, F. Veloso, J. Moreno, S. K. H. Auluck, “Filamentary structures in dense plasma focus: Current filaments or vortex filaments?”, Physics of Plasmas, volume 21, issue 7, 072702, pages 1-6, 2014, DOI: 10.1063/1.4886135.

[Talaei 2010] A. Talaei, S. M. S. Kiai, “Influence of Admixture Gas on the Enhancement of Neutron Production in Plasma Focus Devices”, Journal of Fusion Energy, volume 29, issue 5, pages 427–435, 2010, DOI: 10.1007/s10894-010-9300-4.

[Talebitaher 2016] A. Talebitaher, S. Lee, S. M. P. Kalaiselvi, R. Verma, P. Lee, S. V. Springham, T. L. Tan, R. S. Rawat, “Influence of Krypton Seeding on DD Fusion Neutron Production: Evaluation Methodology for Plasma Focus Optimization”, Journal of Fusion Energy, volume 35, issue 2, pages 370–377, 2016, DOI: 10.1007/s10894-015-0041-2.

[Thornhill 1989] W. Thornhill, J. Giuliani, J. Davies, “The dense radiating deuterium Z-pinch plasma”, Journal of Applied Physics, volume 66, issue 9, pages 4154-4162, 1989, DOI: 10.1063/1.344000.

[Velikovich 2007] A. L. Velikovich, R. W. Clark, J. Davis, Y. K. Chong, C. Deeney, C. A. Coverdale, C. L. Ruiz, G. W. Cooper, A. J. Nelson, J. Franklin, L. I. Rudakov, “Z-pinch plasma neutron sources”, Physics of Plasmas, volume 14, issue 2, 022701, 2007, DOI:10.1063/1.2435322.

[Veloso 2014] F. Veloso, L. Soto, C. Pavez, J. Moreno, “Initial stages in hundreds of Joules plasma focus operating in deuterium – argon mixtures: Preliminary results”, Journal of Physics: Conference Series, volume 511, conference 1, 012027, 2014, DOI: 10.1088/1742-6596/511/1/012027.

[Verma 2008] R. Verma, P. Lee, S. Lee, S. V. Springham, T. L. Tan, R. S. Rawat, M. Krishnan, Applied Physics Letters, volume 93, issue 10, 101501, pages 1-3, 2008, DOI:10.1063/1.2979683.

[Vikhrev 1977] V. V. Vikhrev, Fizika Plazmy (Soviet Journal of Plasma Physics), volume 3, 981, 1977.

[Vikhrev 1978a] V. V. Vikhrev, “Contraction of Z-pinch as a result of losses to radiation”, JETP Letters, volume 27, issue 2, pages 95-98, 1978.

[Vikhrev 1978b] V. V. Vikhrev, K. Gureev, Zhurnal Tekhniceskoj Fiziki (Journal of Technical Physics), volume 48, 2264, 1978.

[Vikhrev 1980] V. V. Vikhrev, S. L. Braginskii, Voprosy Teorii Plazmy (Reviews of Plasma Physics), volume 10, 1980.

[Vikhrev 1982] V. V. Vikhrev, V. Ivanov, K. KosheIev, Fizika Plazmy (Soviet Journal of Plasma Physics), volume 8, 1211, 1982.

[Vikhrev 1986] V. V. Vikhrev, V. Ivanov, V. Prut, Fizika Plazmy (Soviet Journal of Plasma Physics), volume 12, 328, 1986.

[Volobuev 1988] I. V. Volobuev, V. A. Gribkov, D. Denus, N. V. Kalachev, T. A. Kozlova, O. N. Krokhin, S. Sledzinski, S. A. Startsev, S. Czekaj, Fizika Plazmy (Soviet Journal of Plasma Physics), volume 14, 401, 1988.

[Weingarten 2001] A. Weingarten, R. Arad, Y. Maron, A. Fruchtman, “Ion Separation due to Magnetic Field Penetration into a Multispecies Plasma”, Physical Review Letters, volume 87, 115004, pages 1–4, 2001, DOI: 10.1103/PhysRevLett.87.115004.

[Yap 2005] S. L. Yap, C. S. Wong, P. Choi, C. Dumitrescu, S. P. Moo, “Observation of Two Phases of Neutron Emission in a Low Energy Plasma Focus”, Japanese Journal of Applied Physics, volume 44, part 1, number 11, pages 8125, 2005, DOI: 10.1143/JJAP.44.8125.

[Zhang 2019] Y. Zhang, U. Shumlak, B. A. Nelson, R. P. Golingo, T. R. Weber, A.D. Stepanov, E. L. Claveau, E. G. Forbes, Z. T. Draper, J. M. Mitrani, H. S. McLean, K. K. Tummel, D. P. Higginson, C. M. Cooper, “Sustained neutron production from a sheared-flow stabilized Z-pinch”, Physical Review Letters, volume 122, 135001, pages 1-6, 2019, DOI: 10.1103/PhysRevLett.122.135001.

List of tables

List of figures

1. Figure. 2.1.1 16
   Schematic diagram of plasma column (z-pinch discharge). z – axial direction/component in cylindrical system of coordinates (blue arrow), r – the radial direction/component in cylindrical system of coordinates, r_p – the radius of plasma column (pinch), ∇p – the gradient of internal plasma pressure, j_z – current density z component (red arrow), B_φ – magnetic field induction φ component (red circles with arrows) and F_A –Ampere's force extered on the column (green arrows). The $\nabla p, j_z, B_\varphi$ and F_A are constant along z direction.

2. Figure. 2.1.2 21
   a) scheme illustrating the development of MHD a) sausage instability (azimuthal wave number $m = 0$) and b) kink instability (azimuthal wave number $m = 1$) in plasma column [Piel 2017]. j_z – current density z component (black arrow), B_φ – magnetic field induction φ component (circles with arrows) and F_A –Ampere's force extered on the column (gray arrows). The j_z, B_φ and F_A are not constant along z direction.

3. Figure 2.2.1 25
   Phases of discharge in Mather type plasma-focus and basis of operation [Abdallah 1999]. The symbols are: C – the total capacitance of battery, v_z – the velocity of plasma structure (magnetic piston with shock) along z direction, v_r – the velocity of plasma structure (magnetic piston with shock) along r direction, J – the density of current flowing through plasma structure and B_φ – the φ component of magnetic field induction around generated plasma column (plasma pinch).

4. Figure. 2.2.2 26
   Equivalent circuit for a discharge in plasma-focus. The U_{ab} is the total voltage between the electrodes and I is the total current flowing in the circuit. The C_0, L_0, R_0, are the total capacitance, the total inductance and the total resistance of the plasma-focus device, respectively. The L_p is the dynamic plasma inductance and R_p is dynamic plasma resistance [Mather 1971], [Bernard 1998].

5. Figure 3.1.1 38
   Average total D-D neutron yield versus initial deuterium pressure during discharges in linear z-pinch operated with 30 kV of charging voltage [Anderson 1958].

6. Figure 3.1.2 38
   Total D-D neutron yield dependence on initial deuterium pressure for discharges in KSU plasma-focus [Abdou 2012].

7. Figure 3.1.3 40
   Measured discharge current (I) and discharge current derivative over time (dI/dt) for discharges: #17060101, #17052303 and #17063019. The discharge #17052303 was carried at 3.00(±0.01) mbar which was stated as the optimum deuterium pressure under given operation parameters of the PF-24 device.

8. Figure 5.1.1 44
   The front view of the plasma-focus PF-24 device in the laboratory hall in the Institute of Nuclear Physics Polish Academy of Sciences in Cracow in Poland.

9. Figure 5.1.2 45
   a) Projection of the three-dimensional model illustrating connection of the spark-gap IFD-40. b) Projection of the three-dimensional model and diagram showing profile of the electrodes used for construction of the three-electrode spark-gap IFD-40.

10. Figure 5.1.3 46
    The scheme of system of the collector, the vacuum chamber and the electrodes of the PF-24 device (side view).

21. Figure 6.2.5 60
    Scheme of the phase V (expanded column axial) of discharge in the Lee model code. The symbols are: z – the position of the sheet-shock front structure (in reference to the back of experimental chamber). The plasma column has constant radius equal to the anode radius and expands only in axial direction. The arrows indicate: the direction of current flow, the Ampere's force working on the plasma structure and the dimensions.

22. Figure 6.4.1 75
    Exemplary measured (black curve) and simulated (red curve) total discharge current trace. The simulation was performed using: L_0 = 8.5 nH, R_0 = 3.1 mΩ, f_m = 0.1, f_c = 0.6, f_{mr} = 0.2 and f_{cr} = 0.5 input parameters. The numbers indicate parts of the discharge and refer to the computed trace (parts of computed trace). Part 1 (axial 1) is the axial phase. Part 2 (radial) is: the radial inward shock phase, the radial reflected shock phase and the pinch phase. Part 3 (axial 2) is the expanded column axial phase.

23. Figure 6.4.2 77
    The measured discharge current trace is marked with black curve. The 6 computed current traces are marked with colors. The green trace a): L_0^{comp} = 22 nH, R_0^{comp} = 3.1 mΩ, f_m = 0.1, f_c = 0.6, f_{mr}=0.2 and f_{cr} = 0.5. The blue trace b): L_0^{comp} = 22 nH, R_0^{comp} = 10.8 mΩ, f_m = 0.1, f_c = 0.6, f_{mr}= 0.2 and f_{cr} = 0.5. The purple trace c): L_0^{comp} = 22 nH, R_0^{comp} = 10.8 mΩ, f_m = 0.155, f_c = 0.6, f_{mr} = 0.2 and f_{cr} = 0.5. The orange trace d): L_0^{comp} = 22 nH, R_0^{comp} = 10.8 mΩ, f_m = 0.155, f_c = 0.7, f_{mr} = 0.2 and f_{cr} = 0.5. The violet trace e): L_0^{comp} = 22 nH, R_0^{comp} = 10.8 mΩ, f_m = 0.155, f_c = 0.7, f_{mr} = 0.28 and f_{cr} = 0.5. And the pink trace f): L_0^{comp} = 22 nH, R_0^{comp} = 10.8 mΩ, f_m = 0.155, f_c = 0.7, f_{mr} = 0.28 and f_{cr} = 0.64.

24. Figure 7.3.1 86
    Determined (computed) average values of fitting parameters of the 5-phase Lee model code for 113 experimental discharges in (100%-x)D_2+xAr mixtures: a) $\langle L_0^{comp}\rangle$ – nominal inductance, b) $\langle R_0^{comp}\rangle$ – nominal resitance, c) $\langle f_m\rangle$ – axial mass factor, d) $\langle f_c\rangle$ – axial current factor, e) $\langle f_{mr}\rangle$ – radial mass factor, f) $\langle f_{cr}\rangle$ – radial current factor. Roman numerals mark given series of discharges.

25. Figure 8.1.1 90
    The computed theoretical compression time (t_c^{comp}) and pinch time (t_p^{comp}) versus initial D_2 pressure (p_0).

26. Figure 8.1.2 90
    The computed theoretical compression time (t_c^{comp}) and pinch time (t_p^{comp}) versus initial Ar pressure (p_0).

27. Figure 8.1.3 90
    The computed theoretical compression time (t_c^{comp}) and pinch time (t_p^{comp}) versus Ar fraction (x) in (100%-x)D_2+xAr mixture.

28. Figure 8.1.4 91
    The measured (t_c^{mea}) and computed (t_c^{comp}) compression time and the measured (t_p^{mea}) and computed (t_p^{comp}) pinch time versus initial D_2 pressure (p_0).

29. Figure 8.1.5 92
    a) The average measured ($\langle t_c^{mea}\rangle$) and computed ($\langle t_c^{comp}\rangle$) compression time and b) the average measured ($\langle t_p^{mea}\rangle$) and computed ($\langle t_c^{comp}\rangle$) pinch time versus Ar fraction ($\langle x\rangle$) in (100%-x)D_2+xAr mixture. Roman numerals mark given series of discharges.

30. Figure 8.1.6 94
    a) The measured (t_c^{mea}) compression time, b) the measured (t_p^{mea}) pinch time versus series ID for all single discharges in 0%Ar (discharges in D_2 in the four experimental series).

31. Figure 8.1.7 95
    The computed theoretical average axial velocity (v_z^{comp}), maximum axial velocity (v_{zmax}^{comp}) and maximum radial velocity (v_{rmax}^{comp}) versus initial D_2 pressure (p_0).

List of publications of Łukasz Marciniak

1) **Ł. Marciniak**, M. Akel, A. Kulińska, S. Lee, H.-J. Kunze, M. Scholz, S. H. Saw, “Initial results of plasma radiative compression investigation in the PF-24 device operated with D_2, Ar and D_2-x%Ar admixtures”, 2020, in preparation.
2) M. Akel, **Ł. Marciniak**, Sh. Ismael, D. Gannom, A. Kulińska, S. Lee, M. Scholz, H.-J. Kunze, S. H. Saw, “Investigation of the Measured and Computed Neutron Yield From the PF-24 Device Operated With D_2-x%Ar Admixture”, IEEE Transactions on Plasma Science, volume 47, issue 9, pages 4301-4311, 2019, DOI: 10.1109/TPS.2019.2932182.
3) **Ł. Marciniak**, M. Akel, A. Kulińska, M. Scholz, S. Lee, H.-J. Kunze, S. H. Saw, “Measurements and Simulations of Neutron Emission Versus Deuterium Filling Pressure in Plasma Focus Device PF-24”, Journal of Fusion Energy (Springer), volume 37, issue 2-3, pages 124-129, 2018, DOI: 10.1007/s10894-018-0157-2.
4) J. Bielecki, K. Drozdowicz, D. Dworak, A. Igielski, W. Janik, A. Kulińska, **Ł. Marciniak**, M. Scholz, M. Turzański, U. Wiącek, U. Woźnicka, A. Wójcik-Gargula, „Experimental and Monte Carlo investigations of Bcf-12 small-area plastic scintillation detectors for neutron pinhole camera”, Radiation Protection Dosimetry (Oxford University Press), volume 180, issue 1-4, pages 427-431, 2017, DOI: 10.1093/rpd/ncx277.
5) **Ł. Marciniak**, A. Wójcik-Gargula, A. Kulińska, J. Bielecki, U. Wiącek, “Diagnostic systems for the nuclear fusion and plasma research in the PF-24 plasma focus laboratory at the IFJ PAN”, Nukleonika, volume 61, number 4, pages 413-418, 2016, DOI: 10.1515/nuka-2016-0068.